UNIVERSITY OF
BIRMINGHAM

NUMERICAL AND EXPERIMENTAL EVALUATION OF ADVANCED METAL-ORGANIC FRAMEWORK MATERIALS FOR ADSORPTION HEAT PUMPS

By

Eman Mohamed Elsayed Aly Hussein

Thesis Submitted in Partial Fulfilment of Requirements for the Degree of

DOCTOR OF PHILOSOPHY

Department of Mechanical Engineering
School of Engineering
College of Engineering and Physical Sciences
The University of Birmingham
August- 2018

خذيني ،إذا عدت يوما وشاحا لهدبك

و غطّي عظامي بعشب تعمّد من طهر كعبك

و شدّي وثاقي بخصلة شعر..بخيط يلوّح في ذيل ثوبك

إلي روح أبي الطاهرة

إلي كل مأملك في دنياي: إمي

لكما كل الحب والفخر والاعتزاز

'A smooth sea never made a skilled sailor'

Franklin D. Roosevelt (1882- 1945)

ACKNOWLEDGEMENT

I would like to express my deepest appreciation and gratitude to my PhD supervisors **Dr. Raya Al-Dadah**, **Dr. Saad Mahmoud** (School of Mechanical Engineering) and **Dr. Paul A. Anderson** (School of Chemistry) for giving me the opportunity to study at the University of Birmingham in their research groups. Their valuable guidance, ideas and reviewing are undeniable in both my scientific papers and thesis.

I will always be indebted to my brother **Dr. Ahmed Elsayed** for his emotional and scientific support during the last 4 years, I would not have reached this stage without you. Also, I will be forever grateful for **Salwa** and **Mayada** for their support, encouragement and being always there for me. Special thanks go to my two pearls, **Arwa** and **Abdelrhman,** I am immensely blessed for having you both in my life.

Many thanks go to all the adsorption group members; late and present for all the valuable discussions, laughs and support. Thanks to all my friends in Egypt and Birmingham for their continuous support.

ABSTRACT

Adsorption technology has gained considerable research interest in the last few years as it offers a good solution for many energy problems facing our world today. It can be used to generate cooling/heating effects without CO_2 emissions using environmentally friendly refrigerants such as water. Also, the system can be operated using low grade heat sources such as industrial waste heat or renewable energy sources. Additionally, adsorption systems can be used for water desalination to solve the water scarcity problem particularly in countries with good solar radiation. Adsorption has also been proposed for energy storage where for instance solar energy can be stored during the day to be used at night.

Conventional adsorption systems are mainly using silica gel and zeolite as the adsorbent materials. Both materials suffer from problems such as the lower hydrophilicity of the former and the high regeneration temperature required for the latter lowering the efficiency of the system. To overcome these drawbacks, metal-organic framework materials were suggested as an alternative to the conventional adsorbents. Metal-organic frameworks (MOFs) are a class of materials with high porosity and tunable properties.

In this study the potential of a number of metal-organic framework materials namely; MIL-101(Cr), MIL-100(Fe), CPO-27(Ni) and aluminium fumarate, was investigated in various adsorption applications such as heat pump, water desalination and heat storage. Two MOFs, MIL-101(Cr) and MIL-100(Fe), were successfully synthesized at University of Birmingham (UoB) with developing a technique to scale up the synthesis process while the other two MOFs were commercially available. The properties of MIL-101(Cr) in terms of thermal conductivity and water vapour capacity were further improved through synthesizing a number of novel composites with graphene oxide (GrO), calcium chloride ($CaCl_2$). The MIL-101(Cr)/GrO composite showed an improved water vapour capacity and an enhanced thermal conductivity

depending on the preparation method and the GrO concentration in the composite. The addition of $CaCl_2$ to MIL-101(Cr) significantly improved the water adsorption uptake in the low relative pressure range making the new composite a promising candidate for adsorption cooling applications unlike the neat MIL-101(Cr) which require high relative pressure to operate. Also, the adsorption isotherm shape and capacity of MIL-100(Fe) were tuned through synthesizing two core-shell mechanism composites. The core-shell composites of MIL-101(Cr)/MIL-100(Fe) and CPO-27(Ni)/MIL-100(Fe) were synthesized to use the advantage of the high-water vapour uptake of MIL-101(Cr) in the high relative pressure (above 0.5) and of CPO-27(Ni) in the low relative pressure range (below 0.1).

Also, integrating the MOF material as a coated layer instead of the granular form was investigated showing a high durability and improvement in the heat transfer properties which highlight the potential of testing coated heat exchangers as an alternative for conventional packed adsorption beds.

A lumped SIMULINK model was developed to simulate a two-bed adsorption system. The model was used to investigate the potential of using MOF materials and their composites in standard cycles of adsorption heat pump, desalination and heat storage. It was found that for the different adsorption applications, the performance of all the adsorbent materials depends significantly on the operating conditions. In the cooling application and at a chilled water inlet temperature of 10ºC, it was found that adsorbents exhibiting type I adsorption isotherm such as CPO-27(Ni) outperform other neat adsorbents even though it requires high desorption temperatures. It was followed by MIL-100(Fe), MIL-101(Cr) and aluminium fumarate. As the performance of the composites was compared to that of the neat MOFs, it was found that the MIL-101(Cr)/$CaCl_2$ composites have outperformed all neat MOFs and their composites producing an SCP of 246 W kg^{-1} compared to 146 W kg^{-1} for CPO-27(Ni). Also, it was found that the performance of CPO-27(Ni)/MIL-100(Fe) was improved compared to that of neat MIL-

100(Fe). MIL-101(Cr) and its GrO composites were found to require long cycle times and are only suitable for applications working at high relative pressure ranges. Increasing the chilled water temperature to 20ºC was found to significantly enhance the performance of all the adsorbents except CPO-27(Ni).

Due to unavailability of MIL-101(Cr) and its composites in large quantities to be tested in real systems and as MIL-100(Fe) and aluminium fumarate showed good performance at the different adsorption applications and under various operating conditions, the two MOFs were chosen to be experimentally tested in a two-bed adsorption system. The effect of various operating conditions such as chilled water inlet temperature, cycle time, adsorption bed cooling water inlet temperature, desorption bed heating water inlet temperature and condenser cooling water inlet temperature was investigated. It was found that aluminium fumarate performance depends mainly on the chilled water inlet temperature and the adsorption bed cooling water temperature but insignificantly on the desorption bed heating water temperature, while in case of MIL-100(Fe) it was found that it profoundly depends on the desorption bed heating temperature. For a typical adsorption air conditioning system, MIL-100(Fe) was found to produce an SCP of 200-220 W kg^{-1} with the potential of producing an SDWP of 4-10 m^3 ton^{-1} day^{-1} in case of using the system as a dual effect desalination system. Aluminium fumarate was found to produce SCP of 60-140 W kg^{-1} and SDWP of 3-4.5 m^3 ton^{-1} day^{-1}. In other applications such as energy storage, aluminium fumarate was found to store 800 W h kg^{-1} during a cycle of 5400 s while MIL-100(Fe) stored almost 1200 W h kg^{-1} within the same time. This work highlights the potential of using MOF material in adsorption applications like cooling, heating, water desalination and energy storage.

TABLE OF CONTENTS

LIST OF FIGURES

LIST OF TABLES

ABBREVIATIONS

Adsorption heating density	***AHD***
Aluminumphosphates	***$AlPO_4$s***
Aqua SOrb adsorbent	***AQSOA***
Avogadro's number	***NA***
Benzene dicarboxylate	***BDC***
Benzene tricarboxylate	***BTC***
Brunauer–Emmett–Teller	***BET***
Coefficient of performance	***COP***
Chlorofluorocarbons	***CFCs***
Co-ordination Polymer of Oslo	***CPO***
Density functional theory	***DFT***
Differential scanning calorimetry	***DSC***
Differential thermal analysis	***DTA***
Dynamic vapour sorption	***DVS***
Electro-dialysis	***ED***
Energy dispersive X-ray spectroscopy	***EDS***
Energy storage density	***ESD***
European Union	***EU***

Expanded natural graphite	***ENG***
Fourier transform infrared spectroscopy	***FTIR***
Functional Adsorption Material Type Z02	***FAM-Z02***
Greenhouse gases	***GHG***
Graphene oxide	***GrO***
Graphite oxide	***GO***
High density	***HD***
Hong Kong University of Science and Technology	***HKUST***
Hydrochlorofluorocarbons	***HCFCs***
Hydroxyethyl Cellulose	***HEC***
Institute for Solar Energy	***ISE***
International Union of Pure and Applied Chemistry	***IUPAC***
Laser flash analyser	***LFA***
Linear driving force	***LDF***
Low density	***LD***
Materials Institute Lavoisier	***MIL***
Metal-organic framework	***MOF***
Mitsubishi Plastic Incorporation	***MPI***
Mobil Composition of Matter	***MCM***
Mobil Thirty-Nine	***MTN***

Multi-Effect Distillation	***MED***
Multi-Stage Flash	***MSF***
Mutli-wall carbon nano-tubes	***MWCNT***
Outer diameter	***OD***
Part per million	***PPM***
Phase change materials	***PCM***
Polytetrafluoroethylene	***PTFE***
Polyvinyl alcohol	***PVA***
Powder X-ray diffraction	***PXRD***
Regular density	***RD***
Resistance temperature detectors	***RTD***
Reverse Osmosis	***RO***
Scanning electron microscopy	***SEM***
Secondary building units	***SBUs***
Selective water sorbent	***SWS***
Silicoaluminumphosphates	***SAPOs***
Specific cooling power	***SCP***
Specific daily water production	***SDWP***
Tetramethyl ammonium hydroxide	***TMAOH***
Thermal energy storage	***TES***

Thermogravimetric analysis	***TGA***
Total dissolved solids	***TDS***
Transmission Electron Microscopy	***TEM***
Universitetet i Oslo	***UiO***
University of Birmingham	***UoB***
Unsaturated metal centres	***UMCs***
Vapour compression	***VC***
World Health Organization	***WHO***
X-Ray Fluorescence	***XRF***
Zeolitic Imidazolate Framework	***ZIF***

NOMENCLATURE

Symbols	*Description*	Unit
A	***Surface area***	m^2
A	***Adsorption potential***	J mol^{-1}
A_{cs}	***Cross-section area of adsorbate molecule***	m^2
A_s	***BET surface area***	m^2 g^{-1}
AHD	***Adsorption heating density***	kJ kg^{-1}
C	***Constant***	–
COP	***Coefficient of performance***	–
C_p	***Specific heat capacity***	J $(kg\ K)^{-1}$
d_{hkl}	***d-spacing***	Å
D_s	***Surface diffusion coefficient***	m^2 s^{-1}
D_{so}	***Pre-exponential constant***	m^2 s^{-1}
E	***Adsorption characteristic parameter***	J mol^{-1}
E_a	***Activation energy***	J mol^{-1}
ESD	***Energy storage density***	Wh kg^{-1}
F	***Constant***	–
h_{fg}	***Specific enthalpy of vaporization***	J kg^{-1}
i	***Intercept***	g^{-1}

I	***Sample thickness***	mm
K_0	***LDF model empirical constant***	s^{-1}
$K_s a_v$	***Overall mass transfer coefficient***	s^{-1}
M	***Molecular weight of adsorbate in nitrogen adsorption***	g mol^{-1}
M	***Mass***	kg
$\dot{m}$	***Mass flowrate***	kg s^{-1}
n	***Exponent fitting parameter***	–
$\dot{n}$	***Flag***	–
N_A	***Avogadro's number***	6.02E23
P_1	***Initial pressure in sample chamber, pycnometer***	psi
P_2	***Final pressure in sample chamber, pycnometer***	psi
P_a	***Ambient pressure, nitrogen adsorption***	mmHg
$P_{sat\ (Tbed)}$	***Saturation pressure at the bed temperature***	kPa
$P_{sat\ (Tref)}$	***Saturation pressure corresponding to condenser or evaporator***	kPa
$\frac{P}{P_0}$	***Relative pressure***	–
Q	***Rate of heat transfer***	W
Q_{st}	***Isosteric heat of adsorption***	J kg^{-1}
R	***Ideal gas constant***	J $(mol\ K)^{-1}$
R_p	***Particle radius***	m
S	***Slope***	g^{-1}

SDWP	***Specific daily water production***	$m^3\ ton^{-1}\ day^{-1}$
SCP	***Specific cooling power***	$W\ kg^{-1}$
t	***Time***	s
$t_{0.5}$	***Time at 50% of the temperature increase***	s
T	***Temperature***	K
T_{bed}	***Bed temperature***	K
TDS	***Total dissolved solids***	$mg\ L^{-1}$
U	***Overall heat transfer coefficient***	$W\ (m^2\ K)^{-1}$
V_{ads}	***Volume of nitrogen adsorbed***	cm^3
V_C	***Volume of sample chamber***	cm^3
V_{liq}	***Volume of liquid nitrogen contained in the pores***	cm^3
V_m	***Volume of gas corresponding to one monolayer***	cm^3
V_R	***Volume of reference chamber***	cm^3
V_S	***Volume of sample***	cm^3
X	***Amount of adsorbed gas in nitrogen adsorption***	g
X_m	***Amount of the adsorbed gas forming the monolayer***	g
X	***Equilibrium uptake***	$g_{H_2O}\ g_{ads}^{-1}$
x_0	***Maximum uptake***	$g_{H_2O}\ g_{ads}^{-1}$

Greek symbols	***Description***	**Unit**

λ	***Wavelength***	Å
θ	***Scattering angle***	°
ϕ	***Thermal conductivity***	W $(m\ K)^{-1}$
α	***Thermal diffusivity***	$mm^2\ s^{-1}$
ε	***Total porosity***	–
ρ	***Compact density***	$kg\ m^{-3}$
ρ_{bulk}	***Bulk density***	$kg\ m^{-3}$
ρ_{true}	***True density***	$kg\ m^{-3}$

Subscripts	***Description***
a	***Adsorbent***
ads	***Adsorption***
Al,ads	***Aluminium in adsorption bed***
chill	***Chilled***
cond	***Condenser***
Cu,ads	***Copper in adsorption bed***
des	***Desorption***
eff	***Effective***
evap	***Evaporator***
g	***Gas***

h	***Heating***
HX	***Heat exchanger***
in	***Inlet***
l	***Liquid***
out	***Outlet***
ref	***refrigerant***
s	***solid***
sw	***seawater***
v	***vapour***
w	***water***

LIST OF PUBLICATIONS

Journal papers

1. **E. Elsayed**, H. Wang, P. A. Anderson, R. Al-Dadah, S. Mahmoud, H. Navarro, Y. Ding, and J. Bowen, “Development of MIL-101 (Cr)/GrO composites for adsorption heat pump applications,” Microporous and Mesoporous Materials, vol. 244, pp. 180-191, 2017.
2. **E. Elsayed**, R. Al-Dadah, S. Mahmoud, P. A. Anderson, A. Elsayed, and P. G. Youssef, "CPO-27 (Ni), aluminium fumarate and MIL-101 (Cr) MOF materials for adsorption water desalination," Desalination, vol. 406, pp. 25-36, 2017.
3. A. Elsayed, **E. Elsayed**, R. Al-Dadah, S. Mahmoud, A. Elshaer, and W. Kaialy, “Thermal energy storage using metal–organic framework materials,” Applied Energy, vol. 186, pp. 509-519, 2017.
4. **E. Elsayed**, R. Al-Dadah, S. Mahmoud, A. Elsayed, and P. A. Anderson, "Aluminium fumarate and CPO-27 (Ni) MOFs: characterization and thermodynamic analysis for adsorption heat pump applications," Applied Thermal Engineering, vol. 99, pp. 802-812, 2016.
5. B. Shi, R. Al-Dadah, S. Mahmoud, A. Elsayed, and **E. Elsayed**, "CPO-27 (Ni) metal–organic framework based adsorption system for automotive air conditioning," Applied Thermal Engineering, vol. 106, pp. 325-333, 2016.

Conference papers and posters

6. Poster at 2nd International Conference on Desalination and Environment, Qatar, 2016.
7. Enhancement of MIL-101(Cr) thermal conductivity and water adsorption with graphene oxide, 7th Heat Powered Cycles Conference, 2016.

8. Numerical investigation of MIL-101(Cr)/GrO composite performance in adsorption cooling systems, 9th International Conference on Applied Energy, ICAE 2017.
9. Numerical Investigation of aluminium fumarate MOF adsorbent material for adsorption desalination/cooling application, 9th International Conference on Applied Energy, ICAE 2017.
10. Poster at 'A COOL WORLD' international clean cooling congress, University of Birmingham, 2018.
11. Iron(III) trimesate (MIL-100(Fe)) in adsorption desalination, 8th Heat Powered Cycles Conference, 2018.

Book Chapters

12. M. B. Elsheniti, O. A. Elsamni, R. K. Al-dadah, S. Mahmoud, **E. Elsayed**, and K. Saleh, "Adsorption Refrigeration Technologies," IntechOpen Publisher, 2018.
13. **E. Elsayed**, R. Al-Dadah and S. Mahmoud, Metal-Organic Frameworks (MOFs) for Adsorption Heat Pump Applications, Nova Science Publisher, 2018.

CHAPTER 1

INTRODUCTION

1.1. Background

Over the past 50 years, a significant increase of almost 22% in the CO_2 emissions was observed causing the increase of the average global temperature at the fastest rate in the recorded history (**Fig. 1-1a**) [1-3]. According to the EU statistics, this rise is expected to increase by 72% over the next 15 years [1] causing the demand for cooling and air conditioning to dramatically increase in the next decades as shown in **Fig. 1-1b** [4]. It can be noticed that currently the demand for cooling is still lower than the heating but is expected to increase significantly to surpass the heating demand after 2060.

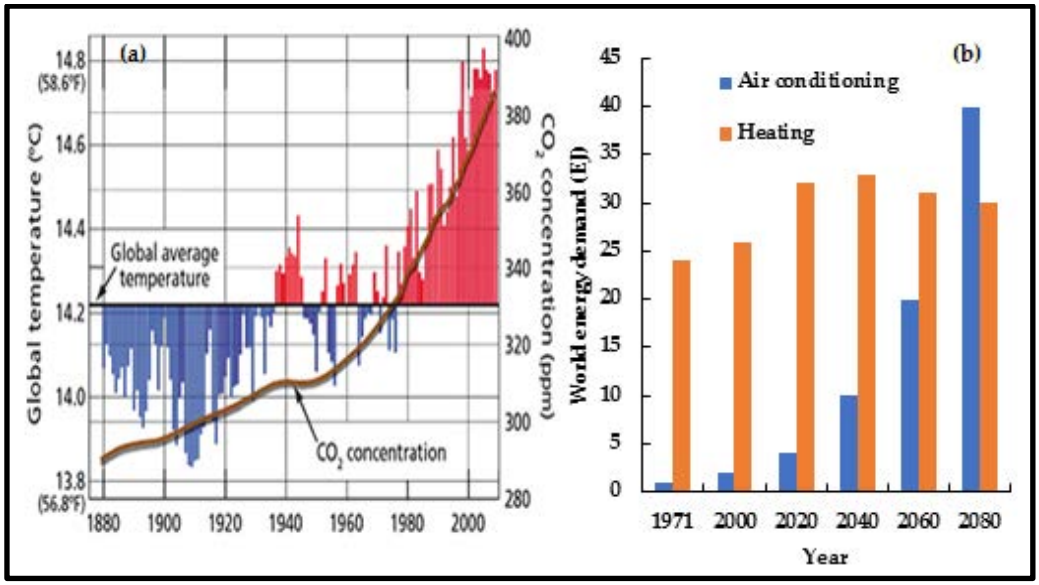

Fig. 1-1 a. Global temperature and carbon dioxide emissions [2] and b. global air conditioning and heating energy demand [5].

According to the published data, the air conditioning and refrigeration account for more than 20% of total electricity consumption in the UK and 17% of the worldwide consumption (**Fig. 1-2**) [1, 3].

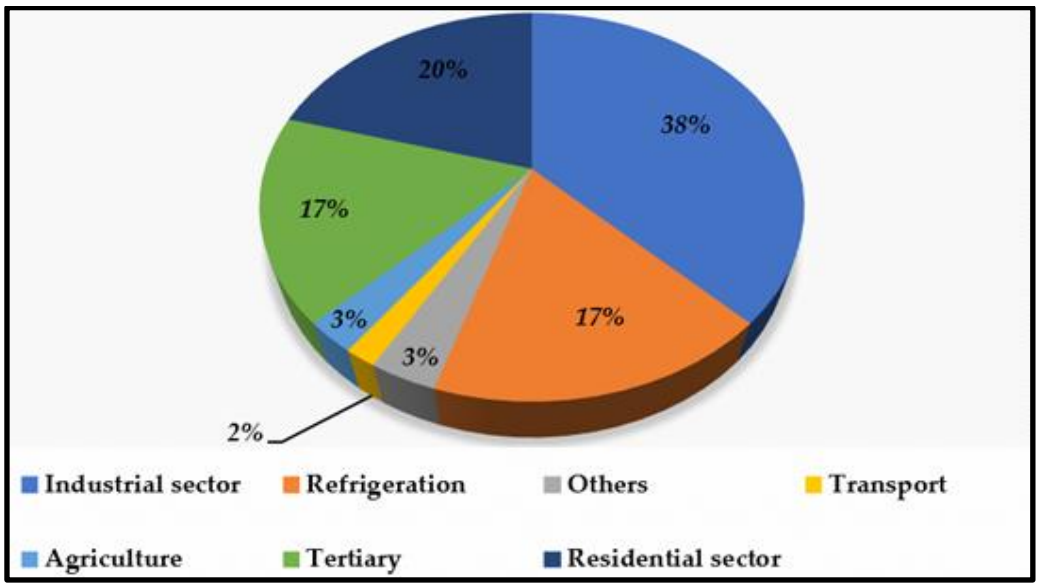

Fig. 1-2 Global energy consumptions in different sectors [1, 3].

This high demand of cooling is mainly supplied by systems that utilise chlorofluorocarbons (CFCs) and hydrochlorofluorocarbons (HCFCs) refrigerants and driven by electricity generated using fossil fuels. It was found that the direct leaks of such refrigerants is responsible for 20% of the global warming impact of refrigeration while the remaining 80% is due to the emissions from the consumed electricity generated by fossil fuels [1, 3]. Not only that, but the above-mentioned refrigerants are a direct cause of the depletion of the ozone layer and the global warming phenomenon.

To rectify the situation, the use of chlorofluorocarbons has been prohibited in 2010 while the hydrochlorofluorocarbons are to be phased out by 2040 according to Montreal and Kyoto protocols [6]. Another step was taken in 2015 as the European Union (EU) countries committed to limit the temperature increase to 1.5°C above pre-industrial levels through the Paris Agreement [7]. This agreement aims to decrease the CO_2 emissions by at least 20% in the EU

by 2020 compared to the 1990 levels. It was proposed that this can be done through increasing the use of renewable energy by 20% and achieving a 20% increase in energy efficiency [7].

An effective alternative to the common vapour compression (VC) cooling systems is the adsorption technology. The adsorption technology can be operated using waste heat or renewable energy sources such as solar and geothermal energy. Also, this technology uses environmentally friendly refrigerants such as water [8]. In a basic adsorption system (**Fig. 1-3**), the refrigerant (adsorbate) is evaporated, gaining its heat of evaporation from the surroundings producing useful cold (for refrigeration application), when the evaporator is connected to the adsorption bed, the vapour is adsorbed into the porous adsorbent material, generating the heat of adsorption. This heat can be either released to the surrounding in case of cooling applications or used as useful heat in heating application. In the desorption process, the porous adsorbent is dried through applying heat from an external heat source (low grade heat source). As the desorption bed is connected to the condenser, the desorbed refrigerant is condensed releasing its heat of condensation. This heat can be used in the heating application or is released to the surrounding in cooling applications [9].

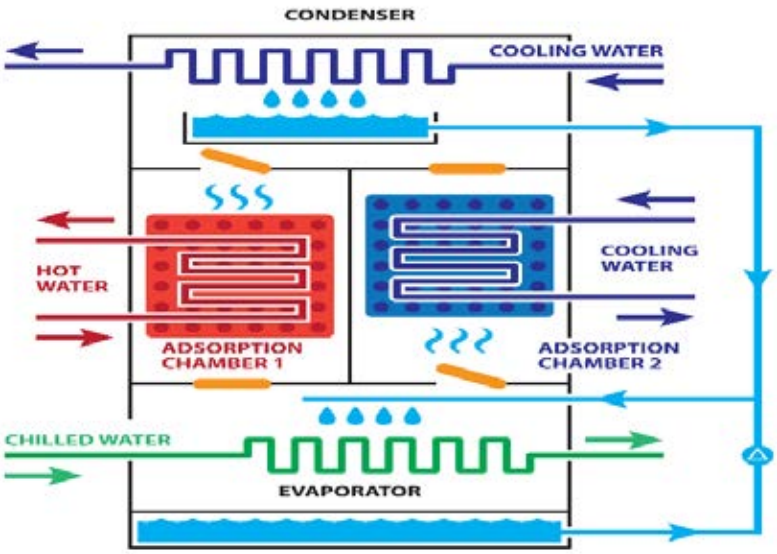

Fig. 1-3 Adsorption system.

Adsorption technology can also offer an innovative solution to another global crisis which is water scarcity. Globally, there are seven hundred million people who are suffering from water scarcity, while another 500 million are approaching this situation as shown in **Fig. 1-4**. This situation is expected to worsen by 2025 as 1.8 billion people will be living in regions with absolute water scarcity [10].

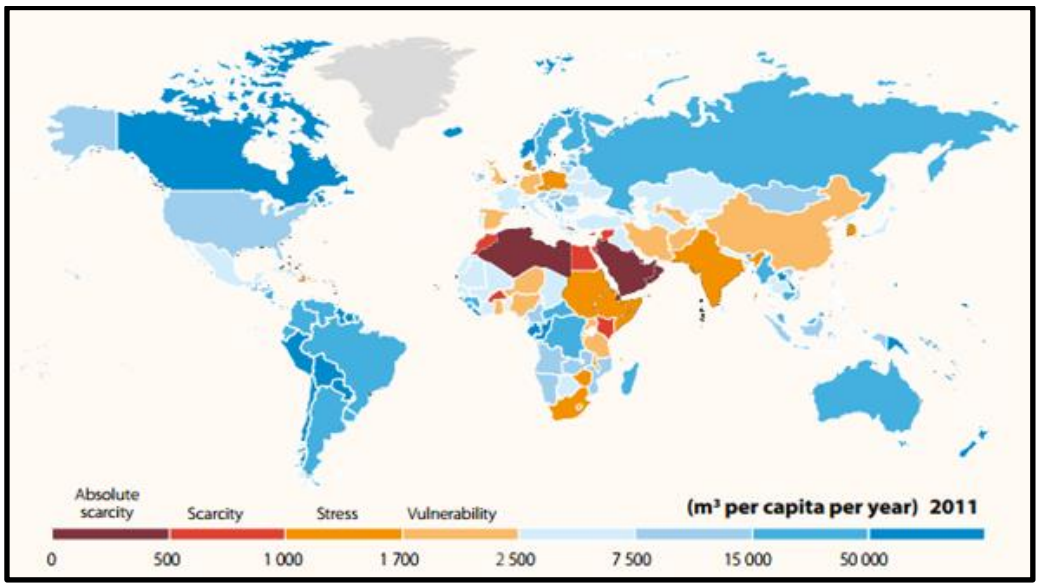

Fig. 1-4 Water scarcity across the world [11]
(If the annual water supply is less than 1,700 m^3 per capita, the area is experiencing water stress. If it is less than 1,000 m^3 per person then the area is facing water scarcity [12])

Fig. 1-5 shows that more than 70% of the earth's surface is covered with water but only 1% of this percentage can be directly used for producing potable water. With 97% of the water body being salty water, an important approach to face the water scarcity problem is using seawater to produce fresh water using desalination processes. Adsorption desalination is a promising technology that has recently gained significant attention due to its many advantages such as the low energy consumption (1.38 kWh m^{-3}) [13], being environmentally friendly, driven by low-grade heat sources, low evaporator temperature and hence reduced fouling (formation of scales which may cause damage to the evaporation units) effect. Also, such system can produce not only high-grade distilled water but also cooling effect using the same heat source [14].

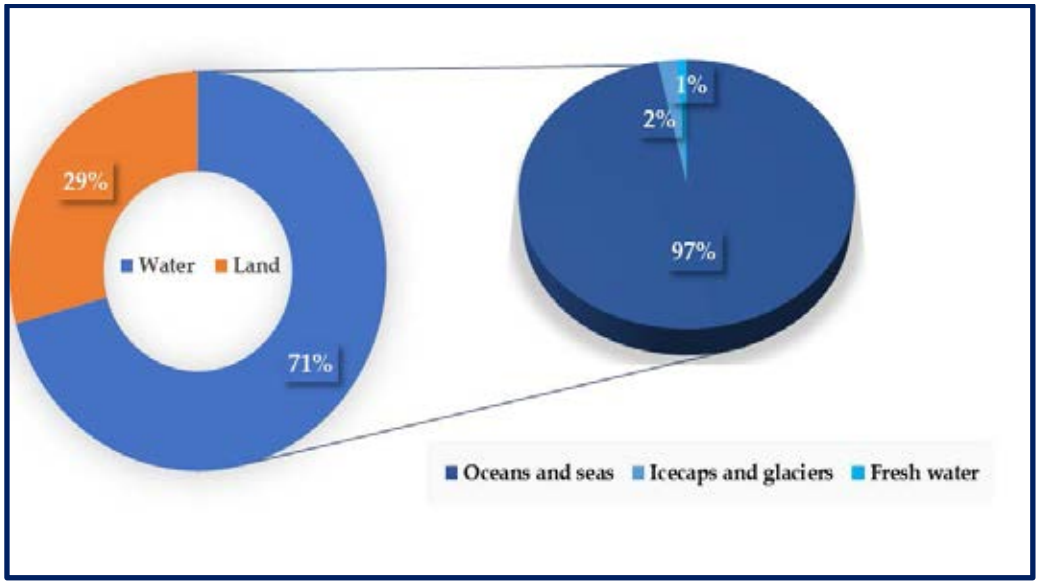

Fig. 1-5 Water body on earth [15].

Another promising application of adsorption is thermal energy storage which offers high energy storage density and has the potential for long-term energy storage [16].

Generally, adsorption systems suffer from several drawbacks (**Fig. 1-6**) such as the low coefficient of performance (COP) and specific cooling power (SCP) due to the limited circulated refrigerant and low water uptake of currently used adsorbent materials at low relative pressure range which limit their applications. The poor thermal conductivity of the adsorbent material, the complicated production technique and the low yield are also challenges facing commercialization of adsorption systems. As all the published studies are mainly focusing on conventional adsorbents such as silica gel and zeolites which suffer from previously highlighted problems, this work aims to fill the gap in knowledge shaped by the previous problems through investigating the potential of advanced metal-organic framework (MOF) materials in different adsorption applications. MOFs are crystalline porous materials with exceptional properties such as high surface area, versatile pore size and volume, and tunable pore geometry thus providing high adsorption capacity compared to conventional silica gel. Using such materials in adsorption system is expected to significantly improve the performance of the system due to their superior adsorption capacity.

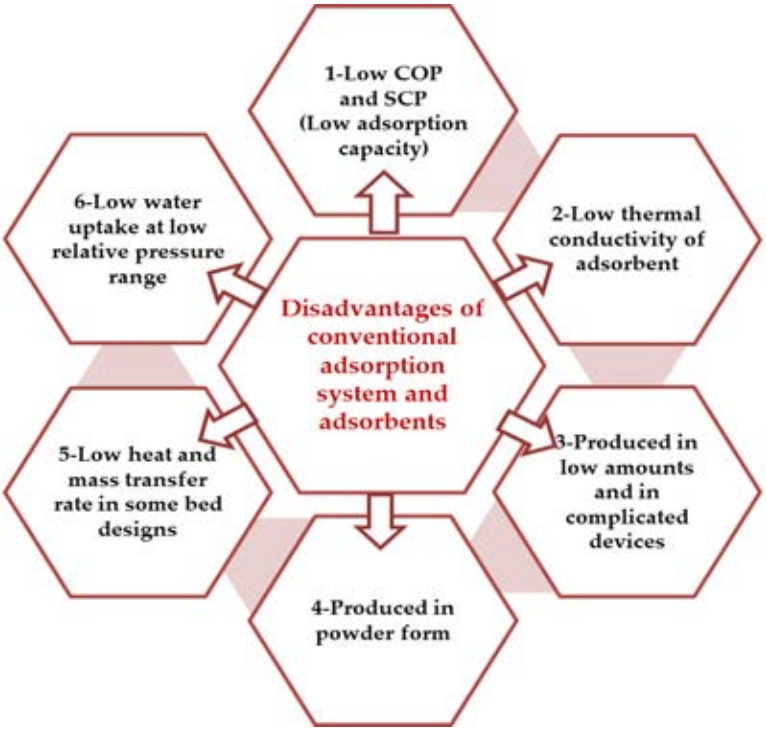

Fig. 1-6 Main drawbacks in current adsorption systems shaping the research gap of knowledge.

1.2. Aims and objectives

This research aims to investigate the potential of using metal-organic framework (MOF) materials as alternatives for conventional silica gel in adsorption applications such as heating/cooling, desalination and energy storage. This was achieved through the following objectives:

1. Reviewing different MOFs and their water vapour capacity to determine their potential in adsorption systems.

2. Synthesis and characterization of four MOFs, two of them are commercially available (aluminium fumarate and CPO-27(Ni)) in addition to two synthesized MOFs, MIL-101(Cr) and MIL-100(Fe), in terms of their XRD patterns, water adsorption isotherm, SEM images, density, thermal stability and thermal conductivity.

3. Investigating means to enhance the performance of MIL-101(Cr) through the synthesis of different novel composites using $CaCl_2$ salt or graphene oxide (GrO).

4. Developing novel MOF core-shell composites of MIL-101(Cr)/MIL-100(Fe) and CPO-27(Ni)/MIL-100(Fe).

5. Developing a synthesis technique to scale up the production of MIL-100(Fe) that can be used at atmospheric pressure and a reduced temperature compared to conventional techniques.

6. Integrating the MOF materials as a coated layer with testing its water uptake and durability to investigate its potential in adsorption system.

7. Developing isotherm and kinetic equations to numerically investigate the performance of the above MOF materials and their composites through SIMULINK model.

8. Experimentally investigating the performance of different MOFs at different operating conditions.

1.3. Thesis outline

This thesis has been organized in eight chapters (**Fig. 1-7**). The literature review of the adsorption technology including; applications and operating conditions, working pair (representing the adsorbent materials and adsorptive gas) and methods to enhance the heat and mass transfer rates was described in chapter two. Different techniques and test facilities used to characterize the MOF materials were described in chapter three. Chapter four includes full characterization of the various neat MOFs under study, while chapter five discusses the synthesis and characterization of a number of MOFs composites and how MOFs can be integrated as a coated layer instead of granules. The measured properties and developed kinetics and isotherms equations from chapter four and five were used in thermodynamic modelling of the MOF materials for different applications in chapter six. Based on the results from chapter four and six, two MOFs, aluminium fumarate and MIL-100(Fe), were chosen to be experimentally tested in a two-bed adsorption system and the results are discussed in chapter seven.

Finally, a summary of the main point discussed in each chapter and recommendations for future work are presented in chapter eight.

Numerical and Experimental Evaluation of Advanced Metal-Organic Framework Materials for Adsorption Heat Pumps

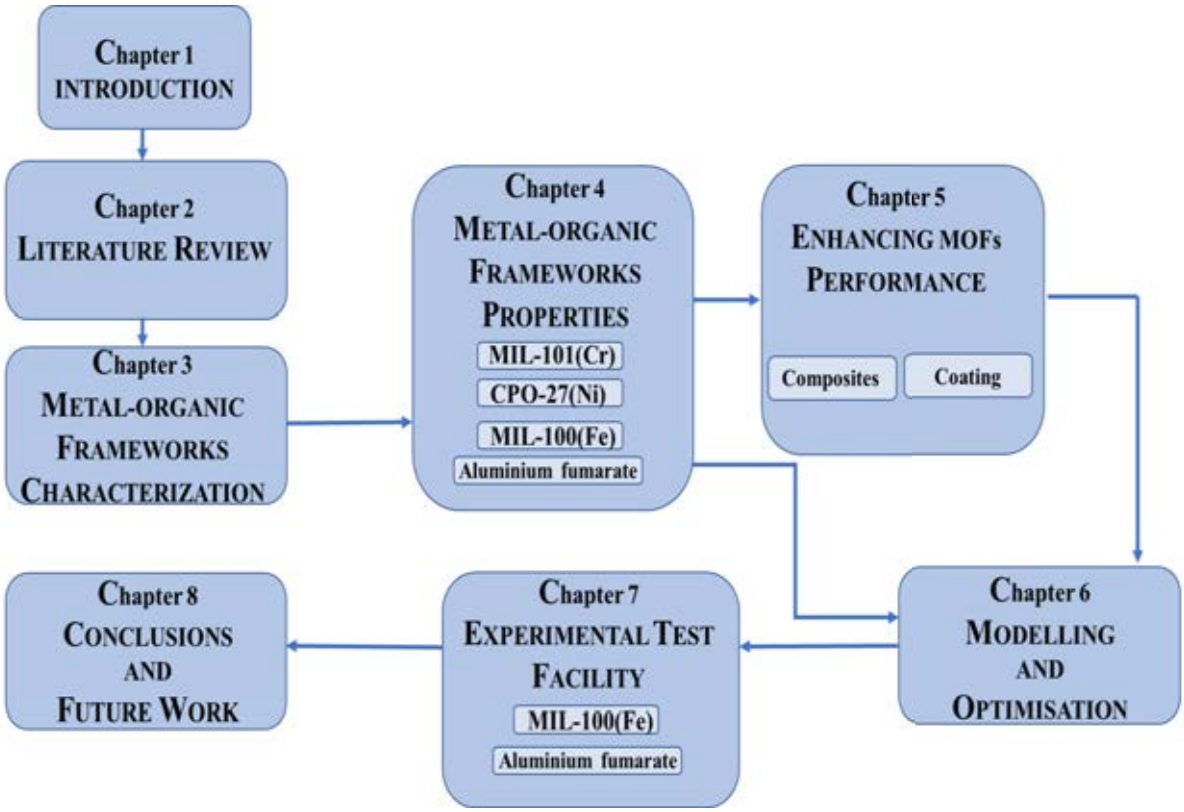

Fig. 1-7 Thesis outline diagram.

CHAPTER 2

LITERATURE REVIEW

2.1. Introduction

This chapter reviews the concept of adsorption, the most common adsorbents used and the different adsorption applications such as heat pumps, desalination and energy storage. As the adsorption system depends mainly on the adsorbent material capacity, a new class of materials which is metal-organic frameworks that has significantly higher adsorption capacity is also comprehensively reviewed. Techniques that may affect and enhance the adsorption system heat and mass transfer rates are also reviewed.

2.2. Adsorption: Theory [17-19]

Adsorption is a very old phenomenon, it was firstly observed by Scheele in 1773 [20] and Fontana in 1777 [21] reporting the adsorption of gases on charcoal and clays [19]. Later in time, de Saussure noticed that heat evolved during the process and that the porosity of the solid material is the main reason for the adsorption process to take place [22] and since then adsorption has been a prolific field with countless research studies.

Adsorption is defined as the phenomenon taking place when a porous material is in contact with gas. According to IUPAC (International Union of Pure and Applied Chemistry), porous materials are classified into macroporous, mesoporous or microporous. Microporous are materials with pores of an internal diameter less than 2 nm. If the pores are between 2 and 50 nm, then it would be a mesoporous material. Pores with diameter higher than 50 nm characterize macroporous materials. As the gas molecules are adsorbed on the surface, they change from the gas state to the liquid state and the duration that the molecules stay in their adsorptive state

without being desorbed depends basically on the interaction forces between the adsorbent surface and the adsorptive gas.

The adsorption process is categorized into physisorption (physical sorption) and chemisorption (chemical sorption). In physical adsorption, the adsorbate (adsorptive gas) and the adsorbent (porous solid) are bonded through the Van der Waals interactions to form multilayers of the adsorbate. This means that applying a certain amount of energy can convert the trapped molecules back to the original gas phase. On the other hand, the chemisorption is characterized by that the adsorptive gas is bonded to the adsorbent material through much stronger chemical bonds. **Table. 2-1** shows the main differences between the physisorption and chemisorption.

Table. 2-1 Main differences between physisorption and chemisorption

	Physisorption	**Chemisorption**
Forces	Weak Van der Waals	Strong chemical bonds
Heat of adsorption	20-40 kJ mol^{-1}	80-240 kJ mol^{-1}
No. of adsorbed layers	Multi-layers	Uni-layer
Temperature required	Low	High
Effect of temperature	Decrease with increasing temperature	Increase with increasing temperature
Activation energy required	Low	High

2.2.1. Adsorption isotherms and hysteresis [17-19]

Adsorption isotherms are defined as the relation between the mass of the adsorbed adsorbate and the relative pressure at a constant temperature. The uptake which is the ratio between the amount of gas adsorbed and the mass of the adsorbent material was found to be a function of the equilibrium pressure, the adsorption temperature, the surface area of the porous material and the nature of the gas–solid system. Characteristic shapes of adsorption isotherms are shown in **Fig. 2-1a.** The isotherm shape can give valuable information about the pore size and the interaction between the adsorbate and adsorbent.

Type I isotherm is obtained in case of microporous materials where the observed steep rise at the low relative pressure range is an evidence of the enhanced adsorbent–adsorbate interaction and the high adsorption energy. The plateau shows that the material has a small external surface area and the knee point is an indication that the monolayer is completed, and the multilayer formation is beginning. Type II adsorption isotherm is obtained when the solid is either non-porous or a macroporous material. The high uptake at the high relative pressure is due to the formation of the multilayer of multi-molecules where the adsorbed layers are bulk liquid. The uncommon type III isotherm usually shows the weak adsorbent–adsorbate interactions on a non-porous or macroporous adsorbent without the formation of a monolayer. The type IV isotherm is associated with mesoporous materials where the steep increase after the completion of the monolayer formation is due to the capillary condensation phenomenon. Capillary condensation takes place when the critical diameter of the adsorbate is much smaller than the diameter of the pore diameter of the adsorbent. The phenomenon is foregone by cluster-based adsorption step [23, 24]. The type V isotherm is rarely found just as the type III. It also shows the weak interaction between the adsorbent and the adsorbate with the only difference is that it can identify microporous or mesoporous materials. Finally, the type VI isotherm which is also a rare type of isotherm where a layer by layer adsorption mechanism is evident.

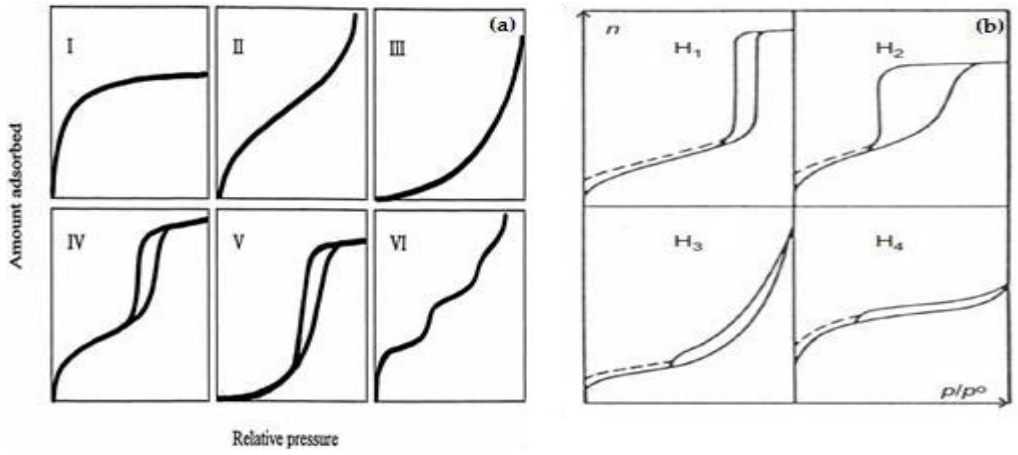

Fig. 2-1 The IUPAC classification of adsorption a. Isotherms and b. Hysteresis loops [25, 26].

In some of the above-mentioned isotherms, adsorption hysteresis takes place when the concentration of the adsorbate in the pores during desorption phase fails to reach the same level as it was during the adsorption phase at the same relative pressure. This phenomenon usually happens in mesoporous materials. From **Fig. 2-1b** there are mainly four types of hysteresis. Type H_1 loop takes place in case of adsorbents with a narrow and uniform pore distribution. Type H_2 loop takes place in materials with different shape and size. In case of particles aggregates, type H_3 loop takes place while when the pores of the porous material are macro slit-shaped pores, type H_4 loop is obtained.

2.2.2. Applications of adsorption phenomenon in heat transformation

2.2.2.1. Adsorption heat pumps for cooling and heating applications

As described in chapter 1, the demand for cooling has been remarkably increasing and is expected to surpass heating demand by 2080. This cooling demand is currently met mostly by systems that utilise harmful refrigerants and driven by electricity generated using fossil fuels causing the depletion of the ozone layer and the global warming phenomenon, respectively. To meet the previous demands while preventing the situation from aggravating and at the same time control the average global temperature rise, cleaner and more energy efficient technologies must be used. An effective alternative to the common vapour compression (VC) systems is the adsorption technology. The adsorption technology has proven to be a sustainable system that has important advantages such as being driven by waste heat and low-grade heat sources such as solar energy and using environmentally friendly refrigerants such as water [8]. This technology can significantly participate in reducing the CO_2 emissions because it can be operated using the abundant renewable thermal energy sources. The system also has no moving parts and hence low maintenance costs.

Generally, the adsorption system consists of an evaporator, a condenser and adsorption/desorption beds which are packed with the porous material (**Fig. 2-2a**). In this

system, the refrigerant (adsorbate) is evaporated, gaining its heat of evaporation from the surroundings producing useful cold (for refrigeration application). As the evaporator is connected to the adsorption bed, the vapour is adsorbed into the porous adsorbent material, generating the heat of adsorption. This heat can be either released to the surrounding in case of the cooling application or used as useful heat in the heating application. In the desorption process, the porous adsorbent is dried through applying heat from an external heat source (low grade heat source). As the desorption bed is connected to the condenser, the desorbed refrigerant is condensed releasing its heat of condensation. This heat can be used in the heating application or released to the surrounding in the cooling application [9, 27].

The previous steps can be explained on the Dühring diagram shown in **Fig. 2-2b**. The cycle consists of four processes which are isosteric heating (1─2), isobaric desorption (2-3), isosteric cooling (3-4) and isobaric adsorption (4-1) [28].

In the **isosteric heating** process (1─2): All the valves in the system are closed and the temperature of adsorber is increased from T_1 to T_2 through heating the bed. This process increases the pressure of the bed from P_{eva} to P_{cond}.

In the **isobaric desorption** process (2─3): The valve between the adsorbent bed and condenser is opened while external heating is applied and due to the elevated temperature, the water vapour is removed from the porous media and then condensed in the condenser releasing latent heat of condensation. The heating fluid is circulated to supply the heat and keep the temperature of the bed at T_3.

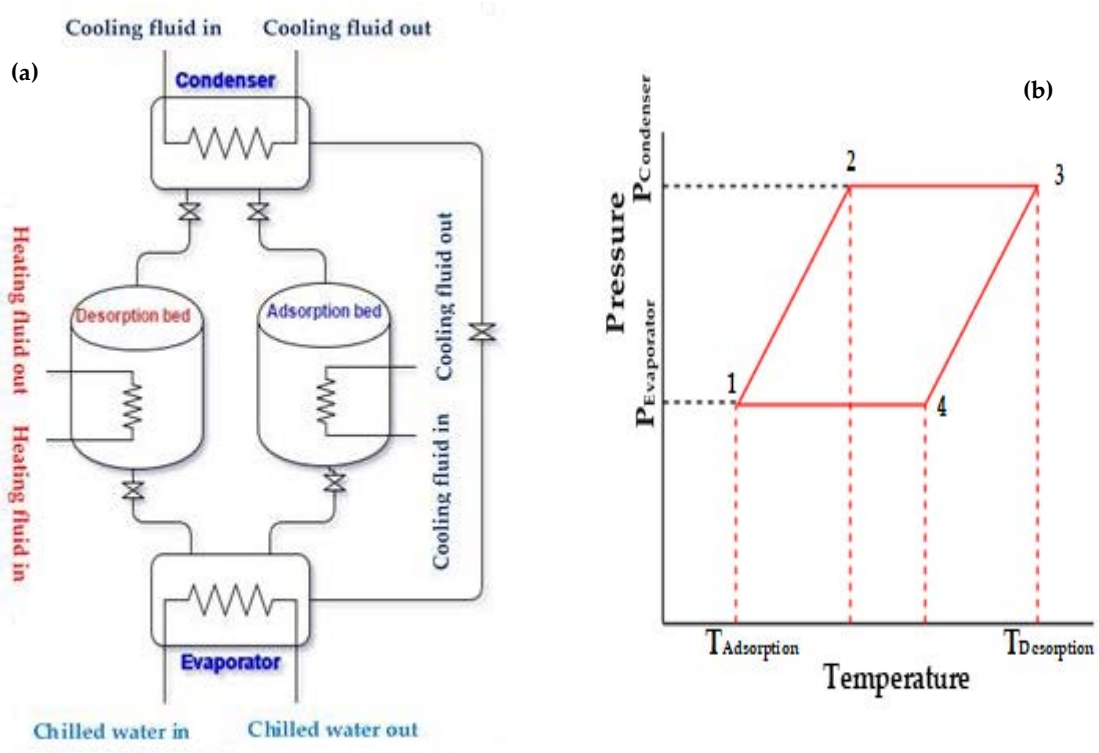

Fig. 2-2 a. Adsorption system and b. Dühring diagram.

In the **isosteric cooling** process (3─4): Again, all the valves in the system are closed and the temperature of the bed is decreased from T_3 to T_4 causing the pressure of the adsorption bed to decrease from P_{cond} to P_{eva}.

In the **isobaric adsorption** process (4─1): After the pressure and temperature of the adsorption bed are decreased, the valve between the adsorption bed and evaporator is opened causing the evaporation of the adsorbate and the adsorption of the vapour by the porous media. Heat in the form of heat of adsorption is released. Cooling fluid is circulated to remove this heat and keep the temperature of the bed at T_1.

Using a system of two adsorption beds ensure continuous cooling/heating as the two beds are working in opposite modes that are reversed every half cycle time.

2.2.2.2. Adsorption desalination: Background and operating conditions

Desalination has become a well-known technology across the world (**Fig. 2-3**). It is the process by which seawater with high total dissolved solids content (>35,000 ppm) is used to produce potable water. The desalination technologies can be categorised into (1) membrane technologies which include pressure activated systems such as the Reverse Osmosis (RO) or electrical activated systems such as Electro-dialysis (ED); (2) thermal energy systems (distillation processes) such as the Multi-Stage Flash (MSF), Multi-Effect Distillation (MED), Mechanical Vapour Compression (MVC) and Solar Distillation (SD) and (3) chemical methods such as Ion-Exchange Desalination and Gas Hydrate [14]. The most used technologies are the RO, ED, MSF and MED (**Fig. 2-4**).

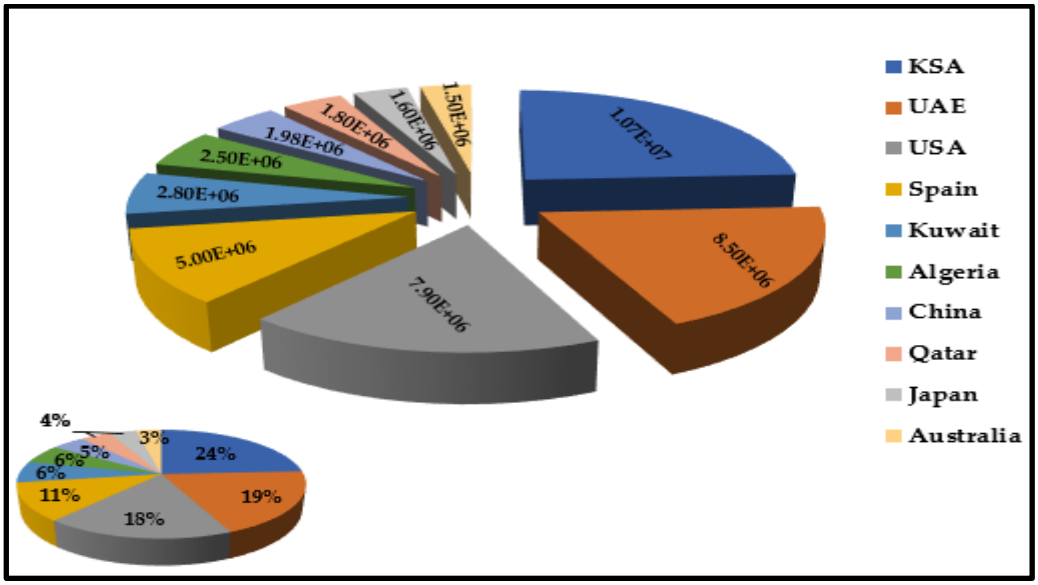

Fig. 2-3 Desalination across the world in m^3 per day and the global percentage share of each country [29, 30].

The multi-stage flashing desalination is basically carried out through boiling the seawater and then condensing the vapour. After pre-treating the feed seawater, the stream passes through pipes as preheating step before entering the heating chamber where it is heated using thermal energy (usually steam). The heated stream is then introduced to the first stage, where the pressure is reduced leading to boiling and flashing of the seawater. Number of stages is used to

increase the efficiency of the flashing process and usually between 18 to 25 stages are used. The vapour formed is then condensed on pipes carrying feed seawater [31].

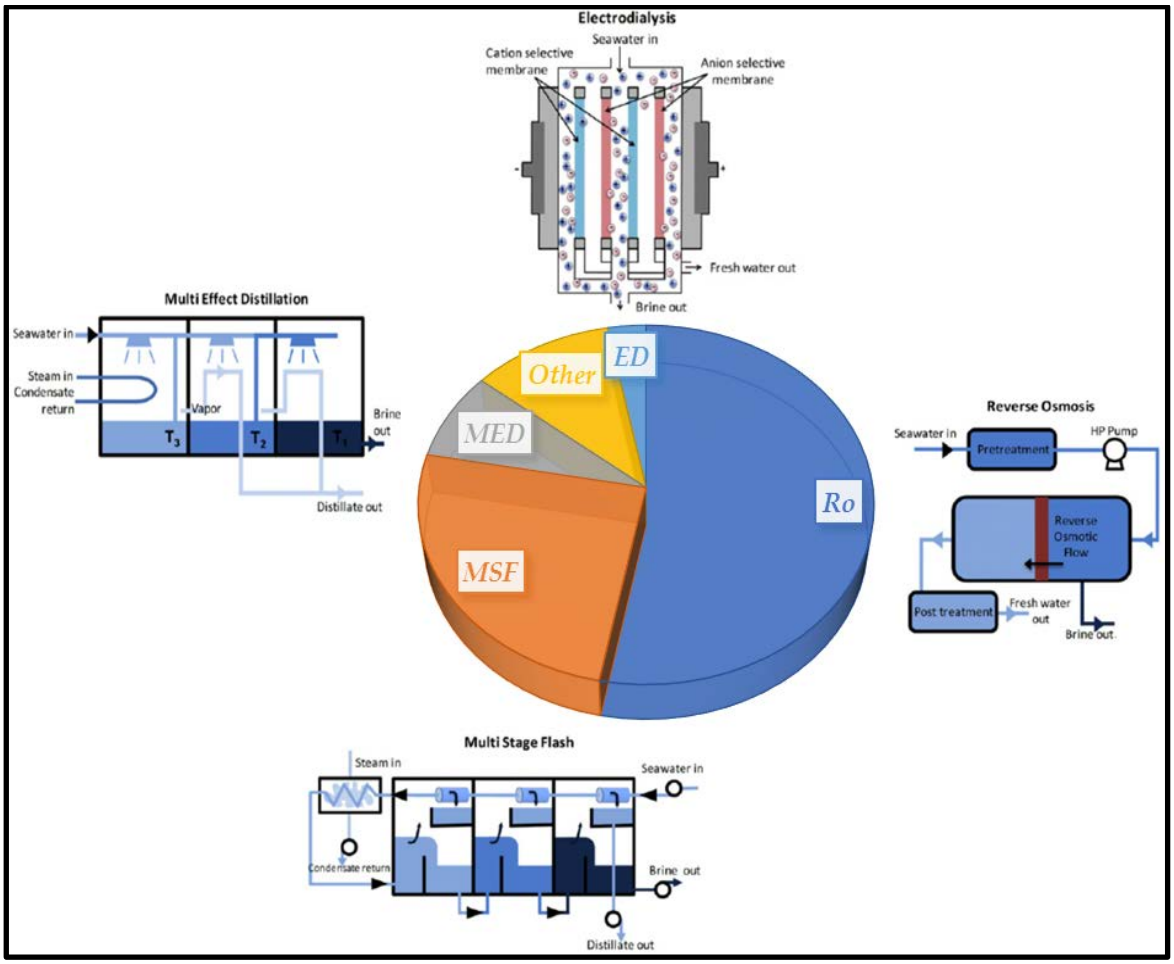

Fig. 2-4 Desalination technology shares across the world [31, 32].

The multiple-effect distillation is very similar to the MSF technology as it employs the concept of evaporation and condensation under reduced pressure. The main difference between the two techniques is the method of evaporation of the seawater. In MED, the evaporation takes place as the droplets of seawater is in contact with the hot pipes while in MSF, the water is vaporized due to the convection heat transfer [31].

Due to the extensive energy consumption of the MSF and MED compared to the RO techniques (**Table. 2-2**), hybrid desalination systems that combine thermal and membrane processes were proposed. Such systems offer the operation flexibility and lower energy consumption which would result in lower greenhouse gas (GHG) emissions [13, 31]. Combining RO with MED

and MSF systems compensates the inflexibility of MSF and MED and reduces the post-treatment costs [31].

Table. 2-2 Energy consumption and GHG emissions of desalination techniques

	Thermal energy consumption (kWh m^{-3})	Electrical energy consumption (kWh m^{-3})	CO_2 emissions (kg m^{-3})	Cost ($ m^{-3})	Ref.
RO	0	4–8	2.79	0.76	[31, 33]
MED	41.67–61.11	1.5–5	11.8–17.6	0.83	
MSF	69.44–83.33	3.5–5	20.4–25.0	1.07	
Adsorption	39.8	1.38	11.2	0.3	[34]

Due to the high GHG emissions of the conventional desalination methods and its effect on the global warming phenomenon, new technologies with lower energy consumption and CO_2 emissions are needed. Recently, adsorption desalination has gained significant attention due to its many advantages such as the low energy consumption as shown in **Table. 2-2** [13, 34], using environmentally friendly refrigerants, being operated by waste or renewable heat sources, using low evaporation temperature hence reducing the fouling (formation of scales which may cause the evaporation unit damage) effect. Also, adsorption desalination system can produce not only high-grade distilled water but also cooling effect using the same heat source [14].

The desalination adsorption system consists of adsorption/desorption beds, a condenser and an evaporator. Each bed contains finned tube heat exchangers with the adsorbent material packed between the fins [14]. For a two-bed system, the first bed works as an adsorption bed while the other works as a desorption bed. After the half cycle time, the operation mode is reversed. At the beginning of the cycle, an evaporation–adsorption process takes place where the seawater is evaporated due to the affinity of the adsorbent resulting in the cooling effect from the evaporator. Heat of adsorption is evolved and transferred to the cooling water in the adsorption bed. During the desorption–condensation processes, the low-grade heat is supplied to the desorption bed to remove the adsorbed water vapour. As the desorption bed and condenser are

connected, the water vapour migrates to the condenser where the vapour is condensed and the desalinated water is collected [35].

As shown in **Table. 2-3**, numerous studies of adsorption desalination have been conducted since its appearance in 2006 [36]. It can be noticed that most of the systems use silica gel as the adsorbent material giving a maximum SDWP of 10 m^3 $(ton\ day)^{-1}$ for a 4-bed system. A heat recovery cycle was later developed where the latent heat of condensation was recovered into the evaporator through building the two units inside each other. This approach increased the SDWP to 26 m^3 $(ton\ day)^{-1}$. *Kim et al.* [37] assessed the water quality produced from a silica gel adsorption desalination system. The results showed that the total dissolved solids decreased from more than 40,000 ppm to almost zero while other parameters such as turbidity, pH, hardness, alkalinity, conductivity and elemental analysis proved the production of high quality distilled water from the system. A feasibility study of the system was held by *Ng et al.* [34] showing that adsorption desalination required less unit production cost, electrical energy and total primary energy than other conventional desalination systems [14].

The long dominating silica gel was replaced by AQSOA-ZO2 (Aqua SOrb adsorbent) in a SIMULINK model for a two-bed adsorption system developed by *Youssef et al.* [38] showing that at high chilled water temperature (>20°C), silica-gel outperformed AQSOA-ZO2 while at chilled water temperature < 20°C, the situation was reversed [14].

Another technique that was recently proposed to enhance the performance and water production of the adsorption system is hybridization where the system can be a combination of two systems such as adsorption desalination and multi-effect distillation [39]. Also, another proposed solution is replacing the conventional adsorbent materials with advanced adsorbents that exhibit higher water capacity and hence a higher distilled water production and better system performance is expected. This solution will be further investigated in this study.

Table. 2-3 SDWP and SCP of some of previously developed adsorption desalination systems

Adsorbent	No. of beds	SDWP m^3 (ton day)$^{-1}$	SCP Rton ton^{-1}	T_{eva} (°C)	T_{reg} (°C)	Half cycle time (s)	Ref.
Silica gel	2	4.2	27.5	15	85	600	[40]
Silica gel	2 and 4	8.8 and 10	-	30	85	600-500	[41]
Silica gel	4	7.8	51	30	85	480	[42]
Silica gel	4	2.4	18	30	85	600	[43]
Silica gel	2	9.3	-	<32	70	570	[44]
Silica gel	4	26	-	<42	85	300	[45]
AQSOA-Z02	4	7.5	58	30	85	300	[46]

2.2.2.3. Adsorption heat storage: Background and operating conditions

Thermal energy storage (TES) has proved to be a potential solution for the high-energy consumption problem. Such systems can reduce the power consumed as it can reduce the electric power demands in buildings through utilizing waste heat and renewable energy [47]. TES systems has recently participated in reducing the CO_2 emissions as it is operated on the previous power sources. The main types of thermal storage systems are sensible heat storage, latent heat storage and thermochemical heat storage [48]. The first type is the sensible heat storage (water tanks) where the heat is exchanged through using a storage media such as ceramics, concrete or an exchange fluid such as oil or water. The main drawback of this type is the relatively low specific energy stored (40–60 kW h m^{-3}), leading to large storage volume but remains to be a low cost technique [47, 48]. The second type is the latent heat storage where a phase change material absorbs the heat. This type utilizes phase change materials (PCM) such as $Na_2SO_4.10H_2O$, Paraffin wax (P116) or $CaC1_2.6H_2O$ where heat is charged or discharged according to the phase of the material. During the charging process the phase change material (PCM) stores the energy till the discharging process in which the PCM crystallizes giving the stored energy [49, 50]. The efficiency of the latent heat storage system depends mainly on the type of the PCM used which is selected based on the charging temperature and the design of the storage system [51, 52]. Even though this type suffers from problems such as crystallization of the storage materials and being operated only in the temperature range of the phase transition, it has a higher energy storage density than the sensible heat storage [47]. Generally, the previous storage systems were found to give relatively low storage density and high energy loss [53]. A solution for the previous problems has appeared in the adsorption heat storage system which offers numerous advantages such as being a green technology, high energy storage density, negligible heat loss, long-term heat storage ability and ease of operation [54, 55]. The adsorption process is a reversible reaction as shown in **Fig. 2-5** because as soon as the adsorbate

is in contact with the adsorbent material, heat is released (exothermic process) while to regenerate (separate) the adsorbate, heat should be applied. The heat released can then be stored with negligible loss because the heat is stored as potential energy and not in the form of sensible or latent heat [56].

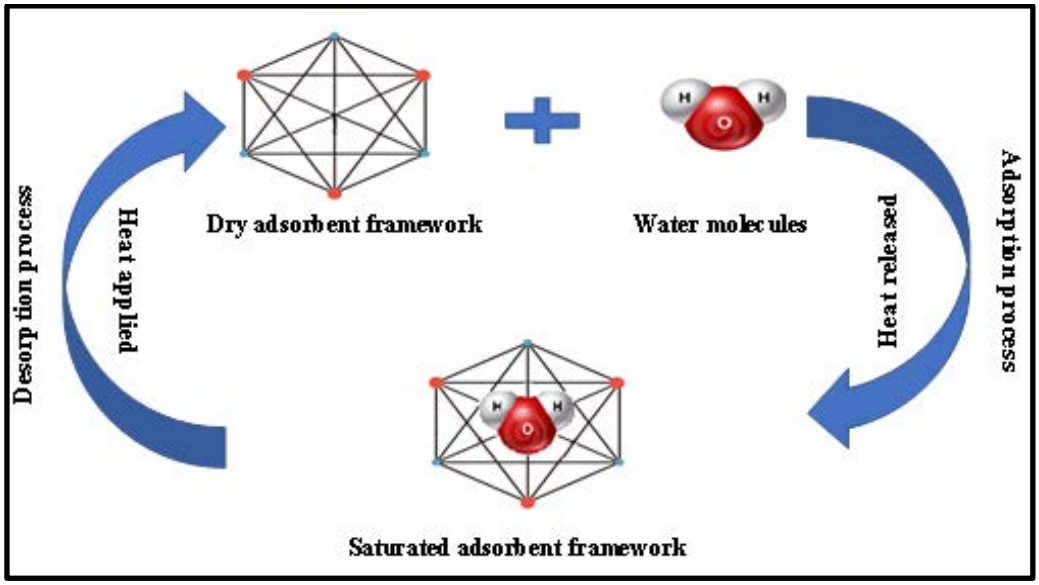

Fig. 2-5 Reversible process of adsorption.

Generally, adsorption heat storage systems can be classified into open and closed systems [50]. As any adsorption system, the cycle is divided into adsorption phase and desorption phase. In adsorption heat storage application, the adsorption phase is called discharging process while the desorption phase is called charging process. In open systems, air is working as a carrier gas in the adsorption phase and as a heating fluid in the desorption phase. Moist air flows through the dry adsorbent and as the adsorption process starts, the water vapour concentration in the adsorbent increases but decreases in the outlet air. As the adsorption process proceeds and the heat of adsorption is released, the air temperature increases. By the end of the adsorption phase, the material is fully saturated, and the desorption process is initiated. The process is carried out through flowing a stream of hot air (at a temperature higher than the temperature of the adsorbent) [57].

In a closed system and at the start of the process, the fully saturated adsorption bed is ready to be charged. During the desorption process, the valve between the condenser and the bed is open and as the hot fluid go through the heat exchanger, the temperature and the pressure of the bed increase allowing the flow of the adsorbate (normally water) from the bed to the condenser. The adsorbate vapour is converted from its gas state into liquid losing an amount of heat equal to its latent heat of condensation which can be utilized. After the end of the charging process (the adsorbent material is fully dry or contains the minimum amount of adsorbate), the valve between the bed and the condenser is closed. Now the bed is ready for the discharging process and can be kept in such state as long as required. When the energy stored is needed to be recovered, the adsorption process takes place. The valve between the evaporator and the bed is open allowing the flow of the vapour of the adsorbate from the evaporator to the pores of the adsorbent in the adsorption bed. Once the adsorbate comes in contact with the adsorbent, the heat of adsorption is released and recovered. Once the bed is fully saturated, the valve between the bed and the evaporator is closed and the cycle is repeated (**Fig. 2-6**).

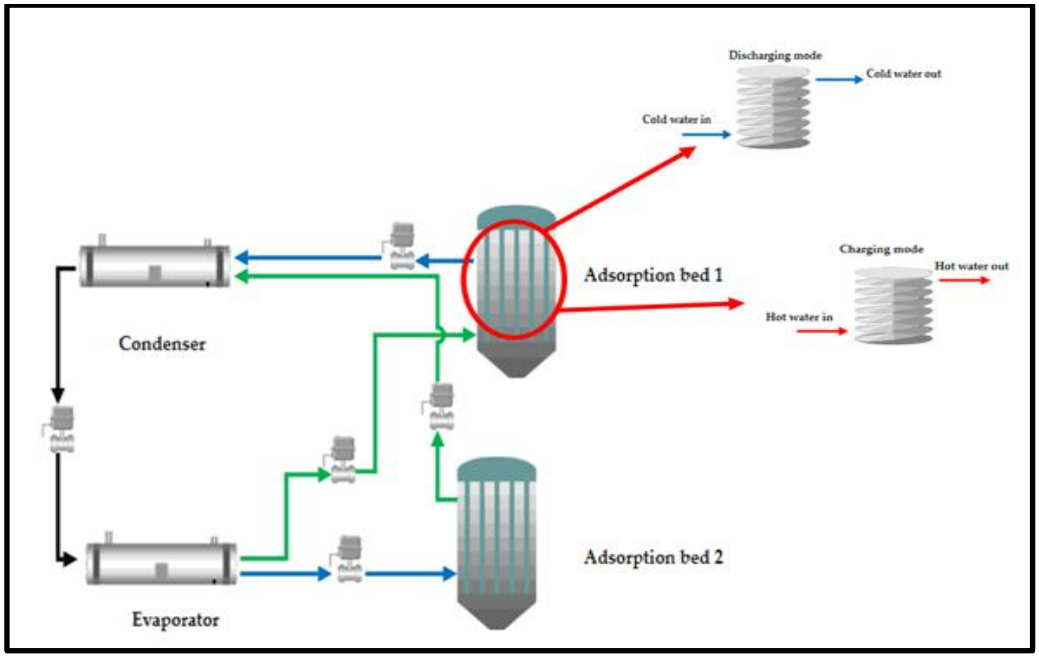

Fig. 2-6 Operation modes of adsorption energy storage system.

The key factors controlling the performance of the adsorption energy storage are the same as any other adsorption application which are the bed design, the recovery strategies (heat and mass) and most importantly the adsorbent material. Conventional adsorbents such as silica gel and zeolite usually suffer from low thermal conductivity, low permeability and low adsorption capacity. These properties cause the low heat and mass transfer properties in the bed resulting in low specific cooling power, COP or energy density according to the application [58]. The previously reported studies on the use of conventional adsorbents (silica gel and zeolite) in adsorption energy storage systems are summarized in **Table. 2-4**. Previous studies concluded that the system performance strongly depends on the evaporator temperature [59], the adsorbate vapour pressure, the adsorption capacity, the adsorbent porosity, adsorbent particle size [60] the flow rate [48]. To be able to judge on the performance of the previous systems, the specific energy storage densities and the half cycle times used are listed in **Table. 2-4**.

Table. 2-4 Energy storage density, half cycle time and desorption temperature of different adsorbents in adsorption energy storage

Ref.	Adsorbent material	Desorption temperature (°C)	Specific energy storage density (kWh kg^{-1})	Half cycle time (min)
[61]	MWCNT-LiCl composite	100	0.2	–
[62]	FAM-Z01	70	0.08	50
[16]	Zeolite 13X	175	0.015	120
[63, 64]	NaX SAPO-34 NaY Silica gel	97-277	0.156 0.13 0.155 0.123	–
[65]	Sodium aluminosilicate (HX-13)	93	0.09	1440
[66]	Silica gel	95	0.051	360
[67]	Silica gel Silica gel/30% $CaCl_2$ composite	90	0.097 0.283	–
[47]	FAM-Z01	70	0.22	18

[68]	Zeolite 5A	103	0.063	833
[69]	Silica gel/10% $CaCl_2$ composite Silica gel/20% $CaCl_2$ composite Silica gel/30% $CaCl_2$ composite Silica gel/40% $CaCl_2$ composite	100	0.111 0.194 0.277 0.361	–
[70]	Sr- ion exchanged zeolite 13X Zn- ion exchanged zeolite 13X	150	0.142 0.160	–
[71]	Zeolite 13X	220	0.3	240

As shown above, all the previously reported adsorption energy storage systems used conventional adsorbents such as zeolite and silica gel or their composites. It can be noted that most of the systems suffer from the low energy density. Such performance is attributed to the low adsorption capacity of silica gel and zeolite as highlighted previously.

There is very limited information on using new adsorbent materials such as metal–organic frameworks (MOFs) in energy storage applications and its performance in adsorption energy storage compared to conventional adsorbents. *Elsayed et al* numerically investigated the viability of CPO-27(Ni) for adsorption energy storage for the first time [49]. Compared to silica gel, CPO-27(Ni) outperformed silica gel when the half cycle time was longer than 30 min. An energy storage density 0.17 kW h kg^{-1} was obtained which outperformed all the previously reported densities from dynamic models except zeolite 13X system which was attributed to the high desorption temperature used [71]. Also, it was highlighted that the performance of the CPO-27(Ni) was almost constant regardless of the chiller inlet water temperature but more profoundly dependent on the desorption heating water and the adsorption cooling water temperatures.

2.2.3. Adsorbent materials in adsorption heating/cooling application

Physical adsorbents are porous materials with different pore size and topologies that adsorb gases through Van der Waals forces and retain their original properties during the adsorption and desorption processes. The criteria in the selection of the adsorbent/adsorbate pair include affinity of the pair for each other, pore size, surface area, toxicity, thermal and chemical stability, corrosiveness, thermal conductivity, diffusivity, heat of adsorption, heat of evaporation, availability and cost. Activated carbon, silica gel, zeolites and zeolite-like materials (aluminumphosphates ($AlPO_4$s) and silicoaluminumphosphates (SAPOs)) are the most common commercially available adsorbents [72].

2.2.3.1. Silica gel

Silica gel is the most commonly used adsorbent material in different adsorption applications. The amorphous material consists of a continuous network of SiO_4 with surface area in the range of 100-1000 $m^2\ g^{-1}$. Different types of silica gel include silica gel regular density (RD) with pore diameter of 2 nm, the silica gel low density (LD) with pore width in the range of 15-20 nm and silica gel high density (HD) with pore size of 1-2 nm [73]. Silica gel has many advantages such as low desorption temperature range, availability, performance stability, hydrophilic properties and the lack of toxicity. Silica gel has been paired with different adsorbates such as water (which is considered as the most common adsorbate) [74, 75], methanol [76, 77] and ethanol [78].

2.2.3.2. Activated carbon

Activated carbon is produced through the activation of organic substances with high carbon content at very high temperatures in the presence of steam to remove all volatile substances and produce char. The final step is to wash all the acid soluble ash and then it is water washed to remove the traces of the acid through water washing. This process gives a carbon skeleton with high internal surface area (500- 1500 $m^2\ g^{-1}$) [79]. Due to the high affinity of activated carbon

for high vapour pressure adsorbates such as ammonia [80], ethanol [81], methanol [82] and carbon dioxide [83], such pairs have been used mainly in adsorption cooling and ice making applications.

2.2.3.3. Zeolites

Zeolites are microporous aluminosilicate minerals. One of the main advantages of zeolites is the high-water affinity in the low relative pressure range which is attributed to the silicon/aluminium ratio (the higher the ratio, the lower hydrophilicity). The high affinity for water comes with the price of the high regeneration temperatures (150-300°C) due to the high interaction between the material framework and water molecules. Zeolites (**Fig. 2-7**) are considered as the most used adsorbents along with silica gel and are mainly used with water [84] and rarely with methanol [85].

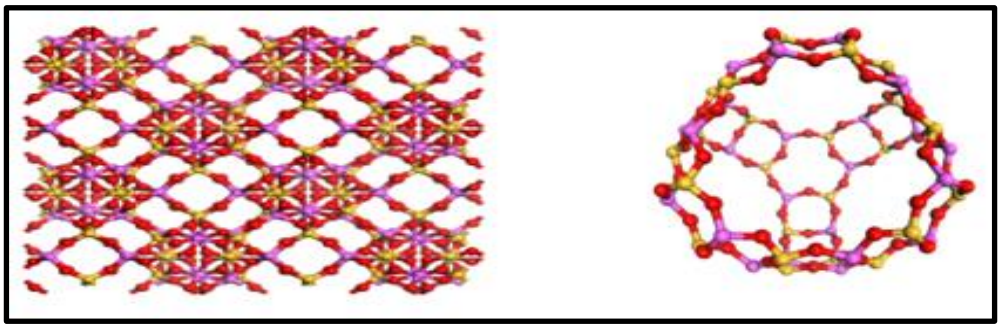

Fig. 2-7 Crystal structure and single super cage of Faujasite zeolite.
(The atoms highlighted are, O red, Si yellow and Al pink)
(Figure was developed using Materials Studio software)

2.2.3.4. Aluminophosphate ($AlPO_4$)

$AlPO_4$ is a zeolite-like material (possess framework like zeolites). The main difference between the two materials is that the Si atoms in the zeolite framework are substituted with Al and P (**Fig. 2-8**). The most used $AlPO_4$ type is $AlPO_4$-5 and AlPO-18 which can be used with methanol, ammonia and water [86].

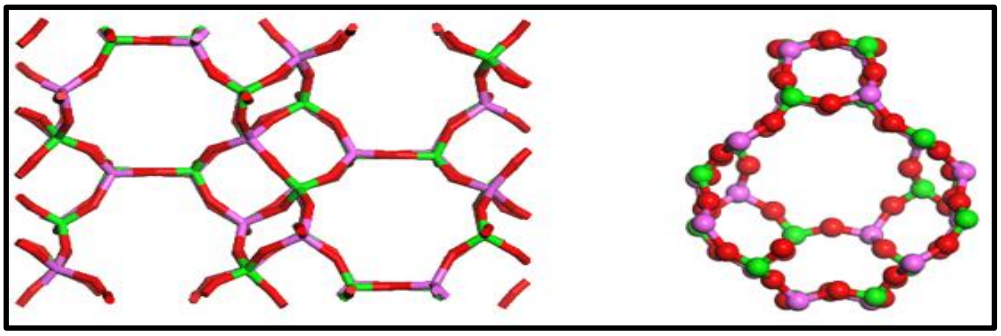

Fig. 2-8 Crystal structure and single cage of AlPO-18.
(The atoms are highlighted, O red, P green and Al pink)
(Figure was developed using Materials Studio software)

2.2.3.5. Silicoaluminumphosphate (SAPO)

SAPO is another zeolite-like material which adopt similar structure to zeolite [87]; SAPO-34 or AQSOA™-FAM-Z02 (AQSOA stands for Aqua SOrb adsorbent while FAM is for Functional Adsorption Material Type Z02) [88] is the most common type. SAPO-34 (**Fig. 2-9**) which is usually paired with water in heating and cooling applications [89, 90].

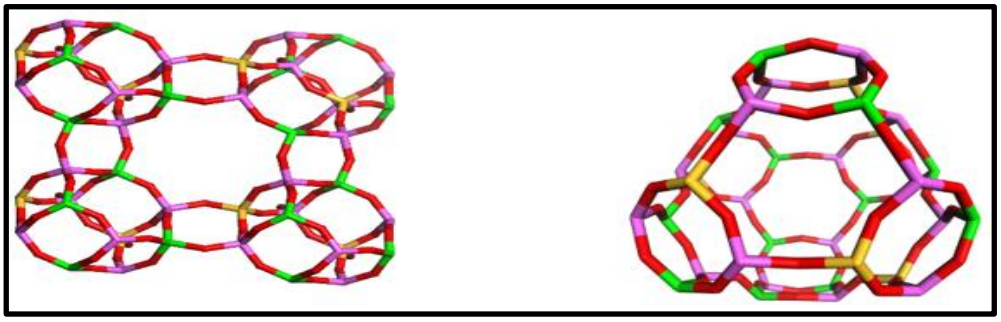

Fig. 2-9 Crystal structure and single cage of SAPO-34.
(The atoms are highlighted, O red, Si yellow, P green and Al pink)
(Figure was developed using Materials Studio software)

Table. 2-5 lists the research work conducted on adsorption systems using silica gel, zeolite, activated carbon, $AlPO_4$s and SAPOs showing the application, mass of adsorbent used, the cooling power in case of cooling and coefficient of performance (COP) of each system.

Table. 2-5 Adsorption systems using conventional adsorbents

I. Silica gel- Water

Ref.	Application	Mass of adsorbent (kg)	Specific cooling power (W kg^{-1})	COP
[75]	Heating and Cooling	130	115 and 61	1.3 and 0.5
[91]	Cooling	13.9	288	0.275
[92]	Cooling	56	80	0.3
[93]	Cooling	-	-	0.6

II. Silica gel- Methanol

Ref.	Application	Mass of adsorbent (kg)	Specific cooling power (W kg^{-1})	COP
[77]	Cooling	0.6	100	0.3

III. Activated Carbon-Methanol

Ref.	Application	Mass of adsorbent (kg)	Specific cooling power (W kg^{-1})	COP
[94]	Ice making	-	-	0.12
[95]	Cooling	52	170	0.5

IV. Activated Carbon-Ammonia

Ref.	Application	Mass of adsorbent (kg)	Specific cooling power (W kg^{-1})	COP
[96]	Cooling	2	800	0.22
[80]	Ice making	-	-	0.34-0.46
	Heating	-	-	1.36-1.5
	Cooling	-	-	0.39-0.52

V. Activated carbon- Carbon dioxide

Ref.	Application	Mass of adsorbent (kg)	Specific cooling power (W kg^{-1})	COP
[83]	Cooling	-	-	0.083-0.15

VI. SAPO-34- Water

Ref.	Application	Mass of adsorbent (kg)	Specific cooling power (W kg^{-1})	COP
[97]	Cooling	1.5	113	0.34

VII. Zeolite- Water

Ref.	Application	Mass of adsorbent (kg)	Specific cooling power (W kg^{-1})	COP
[72]	Heating and Cooling	-	-	0.34 and 1.33
[98]	Cooling	10	135	0.68
[99]	Energy storage	13.2	-	0.43–0.61

As shown in the above table, water is the most used adsorbate. This is attributed to the fact that water has high latent heat of vaporization, being environmentally friendly, being thermally stable at a wide range of operating conditions and with a wide range of adsorbent materials, and also its availability is an essential advantage [70, 100]. **Fig. 2-10** shows the water vapour uptake by different adsorbent materials. It can be noticed that all the materials possess an uptake less than 0.3 while Zeolite 13X is the only material with an uptake of 0.35 $g_{H_2O}\, g_{ads}^{-1}$ at a relative pressure of 0.5.

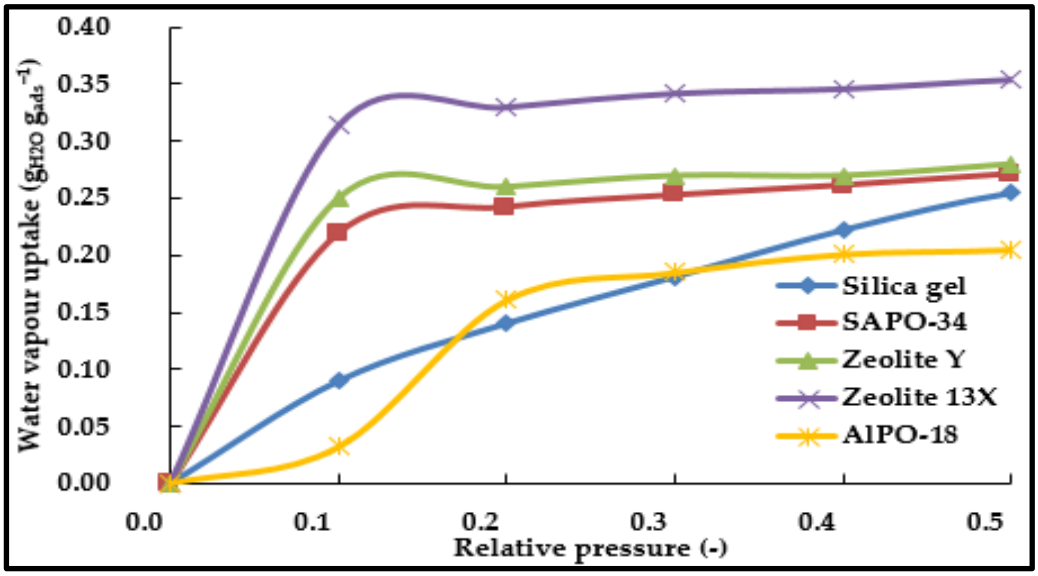

Fig. 2-10 Water adsorption isotherms of conventional adsorbents such as silica gel RD [101], SAPO-34 [102], Zeolite Y [103], Zeolite 13X [104] and AlPO-18 [104] at 25°C.

It can be noticed from **Table. 2-5** that adsorption system suffers from low coefficient of performance (COP) (an indication of the cycle efficiency) and specific cooling power (SCP) due to the limited amount of the adsorbed refrigerant circulated in the system [8, 105, 106]. To solve such problems, new adsorbent materials with improved adsorption properties [107, 108] and/or new adsorption bed designs [109] need to be developed. Metal-organic frameworks (MOFs) are new class of adsorbent materials with significantly enhanced properties compared to conventional adsorbents. **Fig. 2-11** compares the surface area of conventional adsorbents to a number of MOF materials to show their exceptional properties over conventional adsorbents. This class of adsorbent materials will be discussed in detail through the next section.

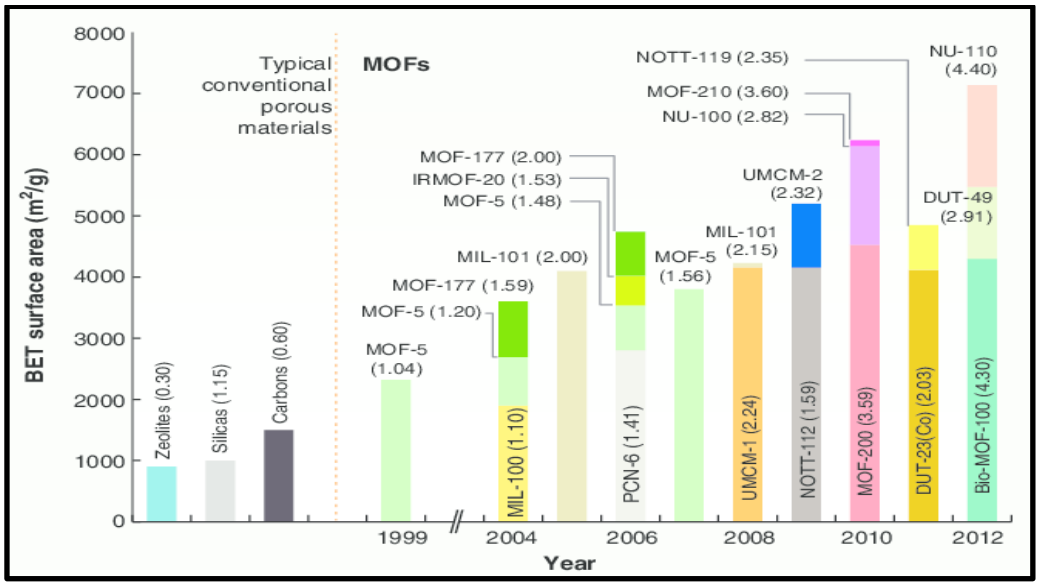

Fig. 2-11 The surface area and pore volume comparison for conventional adsorbents and MOFs [110].

2.2.3.6. Metal-organic frameworks (MOFs): Historical background and applications

Metal–organic frameworks (MOFs) are considered to be one of the fastest growing class of materials since the development of MOF-2 back in 1998 which was found to maintain its porosity and crystallinity [111]. This class of materials has been based on the reports of coordination polymers back in the 1930s [112, 113]. Nevertheless, co-ordination polymers are believed to have low stability and weak bonds while MOFs are materials built by assembling poly-atomic secondary building units (SBUs) by strong covalent metal-ligand bonding, hydrogen-bonding or π-π interactions [114, 115].

MOF crystals are formed in a two-step process: the first part is the nucleation followed by the crystal growth step. In the nucleation step, the ions are assembled to form a cluster or precursors. In the case of MOFs, these precursors are either the inorganic building units or the deprotonated organic ligand molecules. Below a certain size, the cluster is not stable and re-dissolves or breaks down. Once the cluster attains a minimum size, the so called critical nucleus size, the next step starts which is the crystal growth (**Fig. 2-12**)

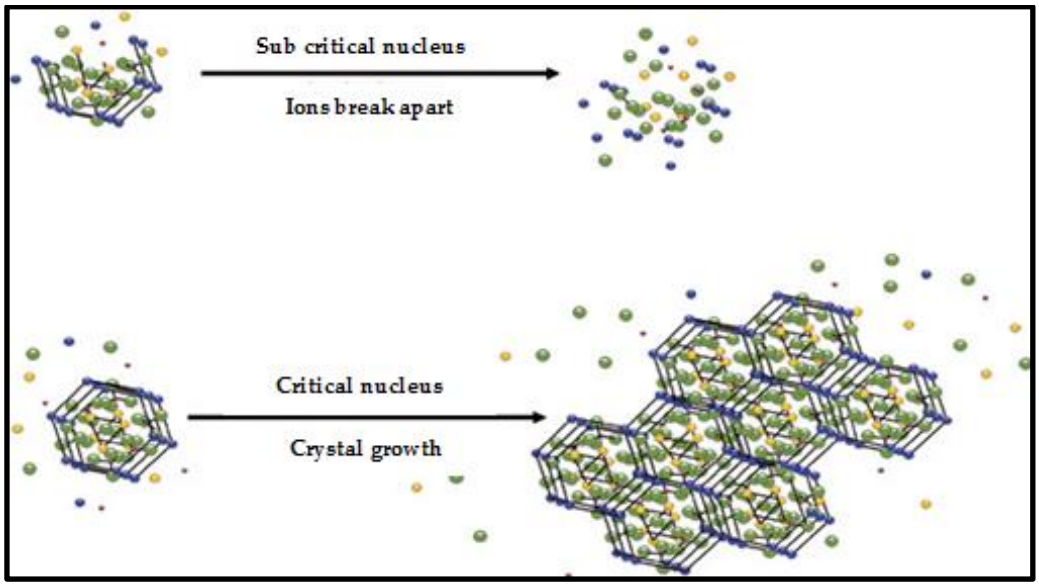

Fig. 2-12 Illustration of nucleation and crystal growth processes [116].

2.2.3.6.1. Strategies for designing metal-organic frameworks

One of the most advantageous design approaches for the synthesis of MOFs is the assembly of extended frameworks from molecular building blocks. In this concept, MOFs are designed based on the assembly of multi-topic organic units and metal clusters (two or more metal atoms of the same or different types) as secondary building units (SBUs) to build 1D, 2D or 3D robust complex structures (**Fig. 2-13**) [117].

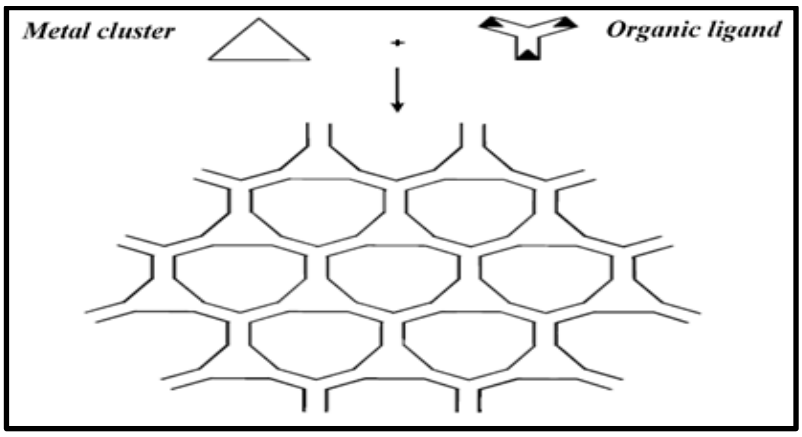

Fig. 2-13 Schematic representation of how the framework is formed [115].

Nevertheless, such approach faces different challenges such as the difficulty to control the building blocks orientation and thus predict the resulting structure. The crystallinity and porosity of the produced structures are also critical parameters to look at as in some structures, the removal of guest molecules from the open pores may lead to the collapse of the framework [115, 118]. Several strategies have been followed to study MOF synthesis and designing new MOFs [119, 120].

I. **High-throughput (HT) methods** where the reactors are miniaturized to a few microlitres or a few millilitres reducing the amount and costs of the reactants. The parameters that may affect the produced structure are the reaction time, reaction temperature, metal salt, the salt hydration, stirring and the reactants concentrations [121]. Such parameters are studied in parallel giving large amounts of data that can give

a better understanding of the effect of each of the reaction parameters on the reaction and its product formation.

II. **Ex-situ and in-situ studies of MOF crystallization** allows the study of the reaction rate constants and activation energies and gives a comprehensive description of the crystallization mechanism through studying the crystalline intermediates. This information may be used to control the crystal size of the final product.

III. **One-pot approach** is done through subjecting the reactants to a number of chemical reactions in one reactor, regardless of the intermediate chemicals. Usually, the organic linker used in the synthesis of MOFs is either pre-synthesized or commercial linkers. An alternative approach is generating organic linkers during the reaction which can give better crystalline materials with different crystal size.

IV. **The iso-reticular approach** enables researchers to build several crystalline structures with the same framework structure but with different functionalities and dimensions. Through using this approach, the IRMOF-n (**Fig. 2-14**) series was obtained through changing the di-topic carboxylate links giving the same type of frameworks with diverse surface area, pore sizes and functionalities just by changing the organic linker [122, 123]. The same is expected to happen when changing the metal clusters to new ones which are topologically similar or identical [124].

2.2.3.6.2. Metal-organic framework synthesis methods

Fig. 2-15 and **Fig. 2-16** show the most common synthesis techniques of MOF materials, most notably the **hydrothermal synthesis**. In this method, a mixture of the organic ligand and the metal salt is heated usually in autoclaves with Teflon liners at temperatures higher than their boiling points to generate autogenous pressure; the solvent used is water. The second most used synthesis method is **solvothermal synthesis** which differs from the hydrothermal method only in the solvent used. In this technique, dimethyl formamide, diethyl formamide, acetonitrile,

acetone, ethanol and methanol are the most used solvents [124]. Even though these two methods produce high crystalline material, they are slow processes where they might take days to complete. Also, such methods are not suitable for reactants that are not thermally stable [125].

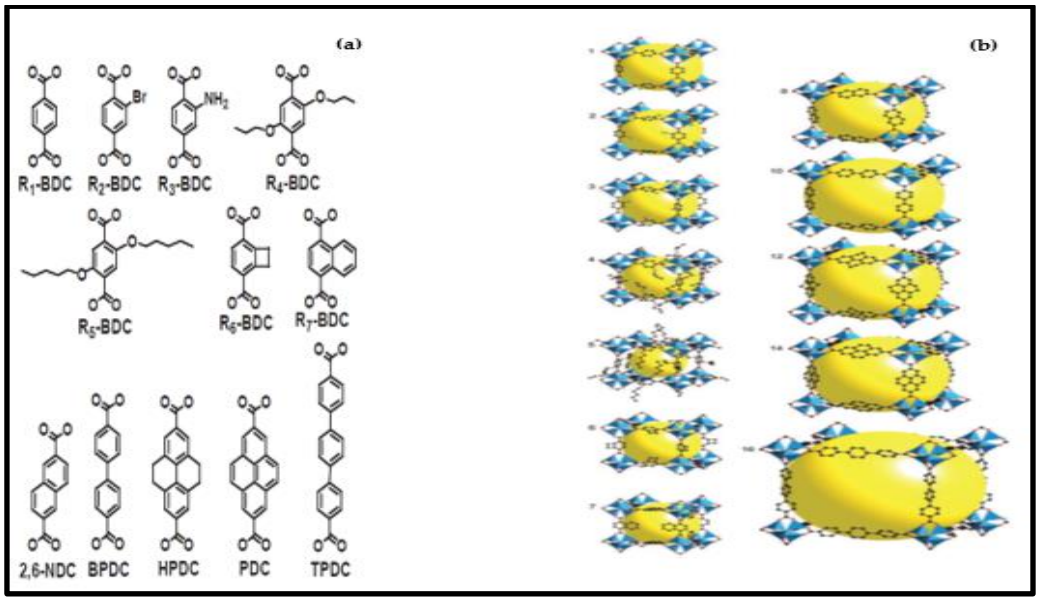

Fig. 2-14 a. Di-topic carboxylate linkers and b. Structures of IRMOF-n [122].

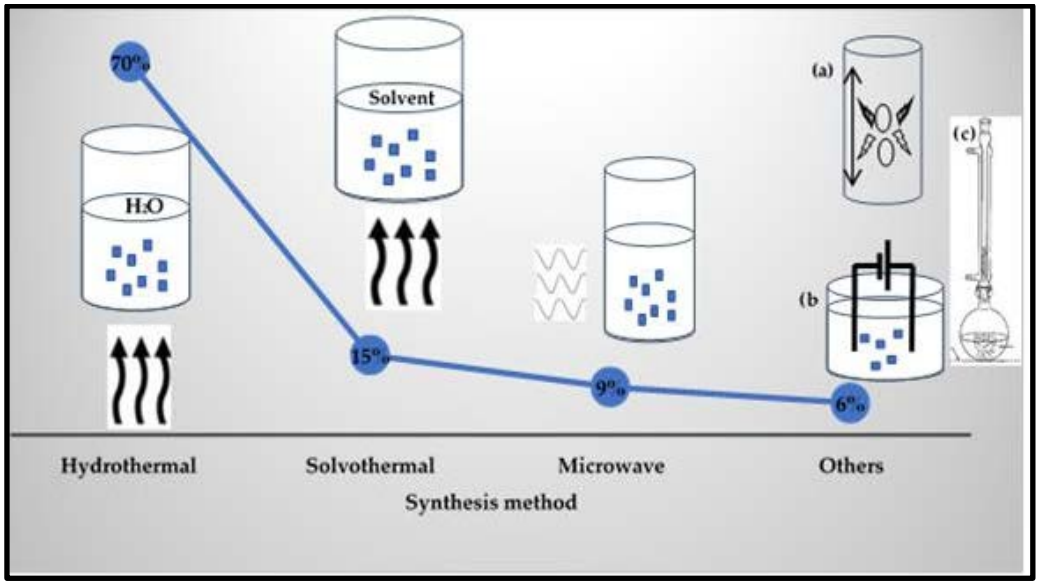

Fig. 2-15 The main MOFs synthesis routes [124].
(a. Mechano-chemical, b. electrochemical and c. low temperature synthesis using reflux)

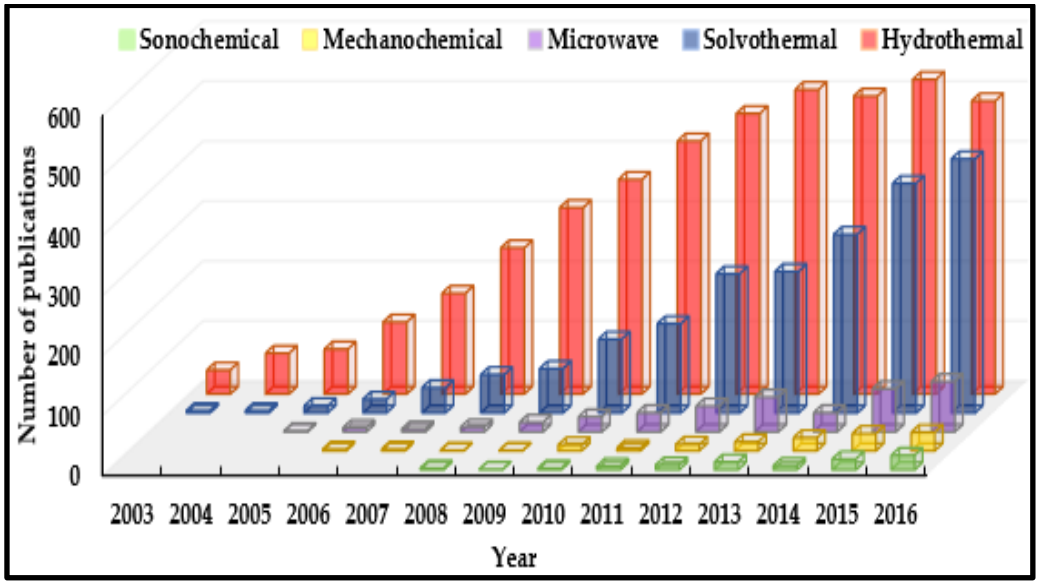

Fig. 2-16 Most common synthesis methodologies of MOFs.
(Data extracted from Web of Science)

Microwave synthesis has managed to solve the long period synthesis problem as it can take only minutes or hours what would usually take days using conventional thermal methods. In the solvothermal and hydrothermal methods, heat is conducted through the walls of the autoclave while in this method the microwave radiation generates high temperature spots which heat up the entire reaction volume and significantly accelerate the rate of the nucleation step and gives crystals in the scale of nanoparticles [126, 127]. A more recent method is **mechano-chemical synthesis**. This can be neat-grinding, grinding-annealing or liquid-assisted grinding and kneading. Unlike the previous synthesis methods, neat grinding and grinding-annealing are solvent free methods. The organic ligand and the metal salt are mixed together, and then mechanical force is applied on the mixture. Such force is transformed into the heat required to accomplish the chemical reaction. The main difference between the previous two methods and the liquid-assisted grinding and kneading is the addition of a small quantity of a solvent to assist the mechano-chemical reaction in the latter [128]. In 2008, a new method was introduced which is **sonochemical synthesis**. The concept used in this method is similar to the one used in the microwave-assisted synthesis except that ultrasound is used. Bubbles are formed which create areas with high temperature and pressure accelerating mainly the nuclei formation step.

The exceptional properties of high surface area, pore size and volume, the tunable functionality and structural flexibility make MOFs suitable for a wide range of interesting applications, including gas storage [129-131], liquid phase separation [132], heterogeneous catalysis [133], photo-catalysis [134], drug delivery [135], sensing [136], luminescence sensing [137], proton conductivity [138] and MOF membranes [139]. Despite the numerous applications of metal-organic frameworks, adsorption and gas storage remains one of the most important applications as shown in (**Fig. 2-17**) which proves the increasing interest in MOFs as a host for gases such as methane, hydrogen and carbon dioxide [140, 141].

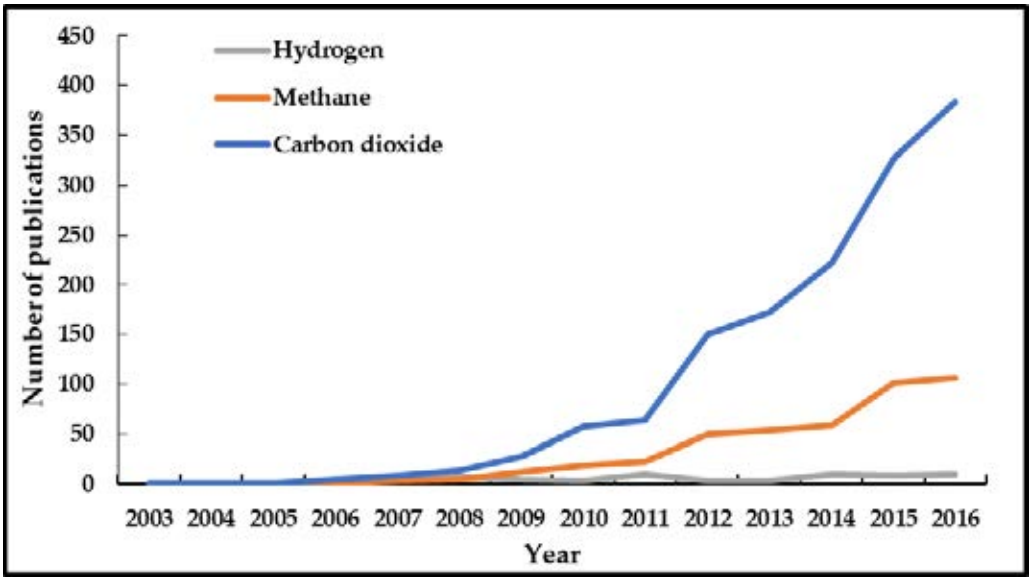

Fig. 2-17 Adsorption and storage of different gases on MOFs.
(Data extracted from Web of Science)

A different adsorption application that has attracted a significant amount of research over the last decade is the adsorption of water vapour on different MOFs and its potential in adsorption heat pumps.

2.2.3.7. MOFs in heat pumps

(This section is based on the author's contribution in the published book chapter "Adsorption Refrigeration Technologies" by M. B. Elsheniti, O. A. Elsamni, R. K. Al-dadah, S. Mahmoud, E. Elsayed, and K. Saleh, 2018.)

With over 10,000 MOF materials reported to date [110, 142], only a small number of frameworks have proven their stability and suitability in applications involving water vapour. **Fig. 2-18** shows the water vapour capacity of a number of MOF materials. It can be noticed that each of the MOF materials had a different shape of adsorption isotherm which is based on the strength and distribution of the adsorption sites for the water interaction determined by the chemical composition and the pore structure of the MOF material [64]. A more limited number of MOFs was investigated for adsorption heat pump systems.

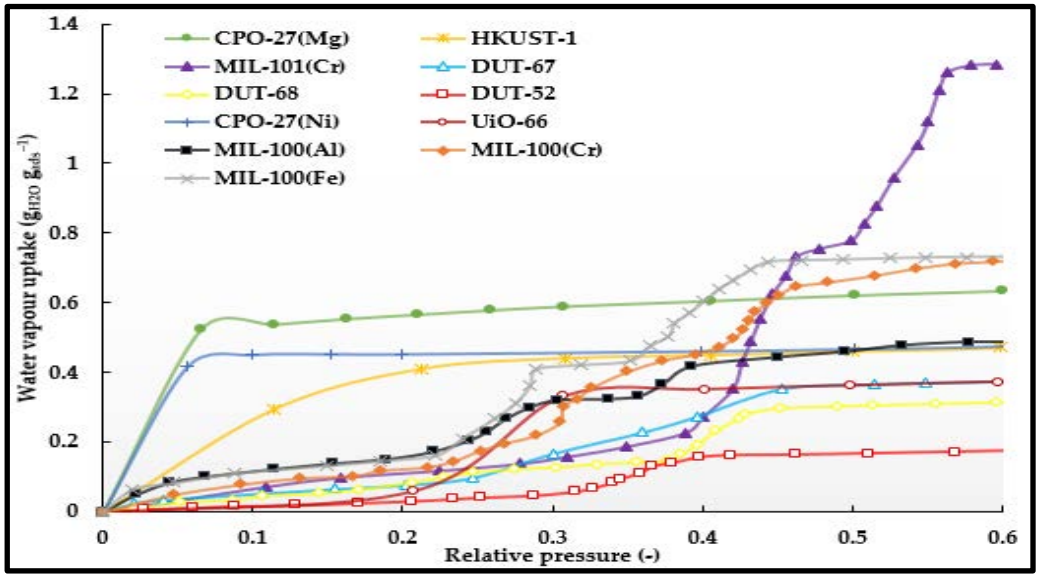

Fig. 2-18 Water adsorption isotherms on different MOFs [24, 143].

The performance of adsorption cooling systems was improved through substituting conventional adsorbent materials with metal-organic framework (MOF) materials due to the high adsorption capacity and the relatively low regeneration temperatures required.

Most of the published data are using water as a refrigerant with limited work conducted on MOFs-ethanol/methanol working pair due to the hazards of the two adsorbates. However, *Rezk et al* [144] experimentally investigated the adsorption affinity of six MOF materials namely CPO-27(Ni), MIL-101(Cr), HKUST-1, MIL-100(Fe), MIL-53(Cr) and MIL-100(Cr) for ethanol compared to that of silica gel. MIL-101(Cr) showed exceptional performance having the highest ethanol uptake and maintaining its performance over 20 successive adsorption/desorption cycles. Methanol was used by *Jeremias et al* [145] showing that it can be utilized as a working fluid for hydrothermally unstable or not sufficiently hydrophilic materials like HKUST-1 or MIL-101(Cr), respectively in low temperature applications. Also, *Saha et al* [146] experimentally and numerically investigated the potential of MIL-101(Cr) in adsorption cooling applications using ethanol as the adsorbate. Results showed promising performance for the working pair [147].

Water has numerous advantages as a refrigerant; it is an environmentally friendly working fluid with high latent heat of vaporization and good heat and mass transfer properties. The water adsorption capacity of different metal-organic framework materials has been previously studied over the last few years. **Fig. 2-19** shows the maximum water vapour capacity of a number of MOF materials at 25°C. MIL-101(Cr) was studied by *Ehrenmann et al* [148] showing that the material has a water vapour capacity of 1 $g_{H_2O}\, g_{ads}^{-1}$ with high performance stability and low regeneration temperature. *Khutia et al* [9] investigated the water adsorption of four nitro and amino-functionalized MIL-101(Cr) materials showing that the fully aminated MIL-101(Cr)-NH_2, and partially aminated MIL-101(Cr)-pNH_2, gave the highest water loadings (1.0 $g_{H_2O}\, g_{ads}^{-1}$) and proving a lower regeneration temperature is required. A MIL-101(Cr) and graphite oxide (GO) composite synthesized by *Yan et al* [149] increased the adsorption capacity from 1.22 to 1.58 $g_{H_2O}\, g_{ads}^{-1}$. The effect of moulding on the water adsorption properties of MIL-101(Cr) was

studied by *Rui et al* [150] where it was found that the compression pressure has a significant effect on the capacity of MIL-101(Cr) [147].

Another MOF, aluminium fumarate, was studied by *Jeremias et al* [151] through synthesizing a MOF coating layer on a metal substrate via the thermal gradient approach. The study showed that aluminium fumarate has a potential in adsorption applications as it can be regenerated at a significantly low temperature and it has a water loading difference of 0.5 $g_{H_2O}\, g_{ads}^{-1}$.

CPO-27(Ni) was used by *Shi et al* [152] in automotive air conditioning where it outperformed SAPO-34 giving higher cooling power. CPO-27(Ni) produced 440 W kg^{-1} while SAPO-34 gave a specific cooling power of 310 W kg^{-1} at the same operating conditions [147].

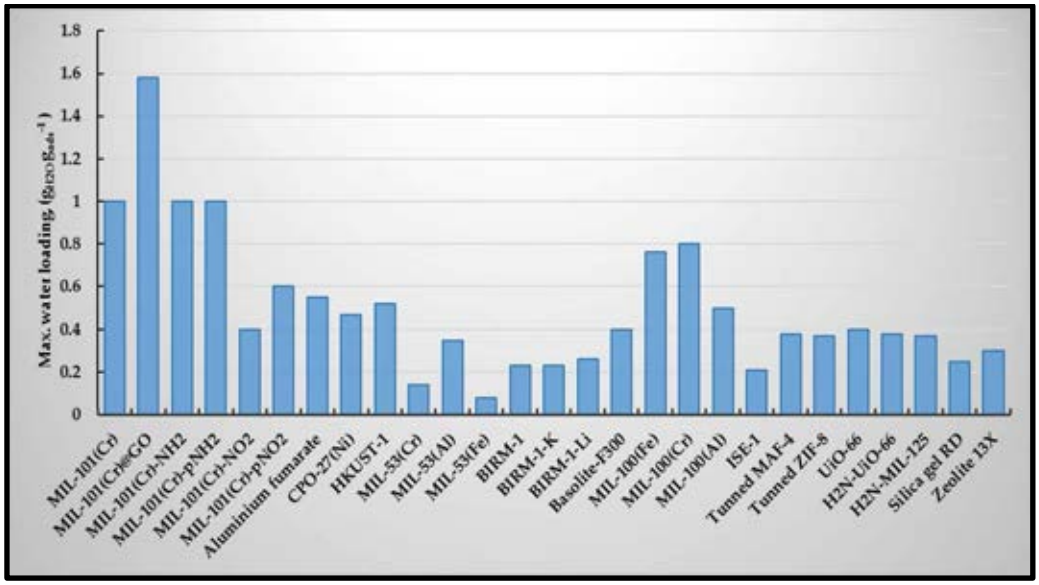

Fig. 2-19 Metal-organic frameworks in adsorption heat pumps [9, 101, 106, 148-158].

Other MOFs such as HKUST-1 and MIL-100(Fe) were studied and compared to silica gel RD-2060 by *Rezk et al* [106]. Results showed that HKUST-1 had a 93.2% higher water vapour uptake than silica gel RD-2060. This improvement can lead to a considerable increase in the refrigerant flow rate, cooling capacity and/or reducing the size of the adsorption system. MIL-53(Cr), MIL-53(Fe), Birm-1, Birm-1(K) and Birm-1(Li) showed water uptake between 0.14 to 0.35 $g_{H_2O}\, g_{ads}^{-1}$ which are lower than that of HKUST-1 [101].

MIL-100 (Fe and Al) had a water vapour uptake of 0.76 and 0.5 $g_{H_2O}\, g_{ads}^{-1}$, respectively. The high adsorption capacity made the two MOFs promising candidates for heat pump applications [154, 155].

In another study, a MOF material, ISE-1, had a water vapour uptake of 0.21 $g_{H_2O}\, g_{ads}^{-1}$ which was higher than other zeolites and silica gel showing the potential of the MOF material in adsorption applications [156]. MIL-53(Al), MIL-100(Fe) and ZIF-8 had a water vapour uptake higher than 0.3 $g_{H_2O}\, g_{ads}^{-1}$ which makes them promising candidates for heat pumping/cooling processes [157, 158]. Other functionalized MOF materials such as H_2N-UiO-66 and H_2N-MIL-125 showed a promising potential for adsorption heat pump application due the enhanced hydrophilicity improving the water adsorption isotherm shape [147, 153].

Out of the numerous known MOFs, four MOF materials with different adsorption isotherm shapes were chosen to be further studied, namely MIL-101(Cr), MIL-100(Fe), aluminium fumarate and CPO-27(Ni). MIL-101(Cr) was chosen due to its high-water vapour capacity while MIL-100(Fe) was chosen due to its scalable synthesis procedures. Aluminium fumarate and CPO-27(Ni) were chosen due to their commercial availability and water vapour characteristics.

2.2.3.7.1. MIL-101(Cr)

The MIL- family is a group of metal carboxylates porous materials that were firstly synthesized at the Materials Institute Lavoisier (MIL) by G. Férey [159]. In this group of MOFs, the metal moiety is trivalent cations of vanadium, chromium, iron, aluminium, gallium or indium [159]. MIL-101(Cr) is the most known MOF in the MIL family due to its exceptional properties. This MOF which is also known as chromium terephthalate or chromium-benzenedicarboxylate was reported to have a giant cell volume of 702,000 $Å^3$ and Langmuir surface area of 5900± 300 $m^2\, g^{-1}$ due to the large pore sizes of 29 and 34 Å [160]. The structure is built up from super tetrahedra shape that is formed from the linkage of organic linker

(terephthalic acid) and inorganic trimers (chromium (III) cations). The super tetrahedra is connected and arranged in a Mobil Thirty-Nine (MTN) [161] topology to form two types of mesoporous cages with an internal diameter of 29 and 34 Å, respectively. The large cage exhibits two types of pentagonal and hexagonal windows with openings of 14.5 and 16.0 Å while the smaller cage possess a pentagonal window with an opening of 12 Å (**Fig. 2-20**) [160, 162].

MIL-101(Cr) is usually synthesized through hydrothermal reaction of chromium salt (nitrate or chloride) and terephthalic acid for 8 hr at 220°C in case of using conventional heating [160] or 15-60 min at 210°C in case of using microwave heating [163].

The very large windows and enormous volume allow the introduction and confinement of new species such as gases into the cages easily [160]. This explains why the material have been widely used in numerous applications such as dehumidification [164], adsorption of natural gas [165], CO_2 [166], H_2 [167], catalysis [168] and many other applications. One of the potential interesting applications of MIL-101(Cr) is adsorption heat pumps. MIL-101(Cr) was always considered as an interesting candidate in such application due to the high capacity of water vapour which was reported to be 1-1.6 $g_{H_2O}\, g_{ads}^{-1}$ [148, 164]. Nevertheless, serious challenges such as the low thermal conductivity as a result of the enormous free volume and the remarkable low water vapour uptake at the low relative pressure range (IV type isotherm, also known as S shape isotherm) limit its use and remain unsolved till the current moment.

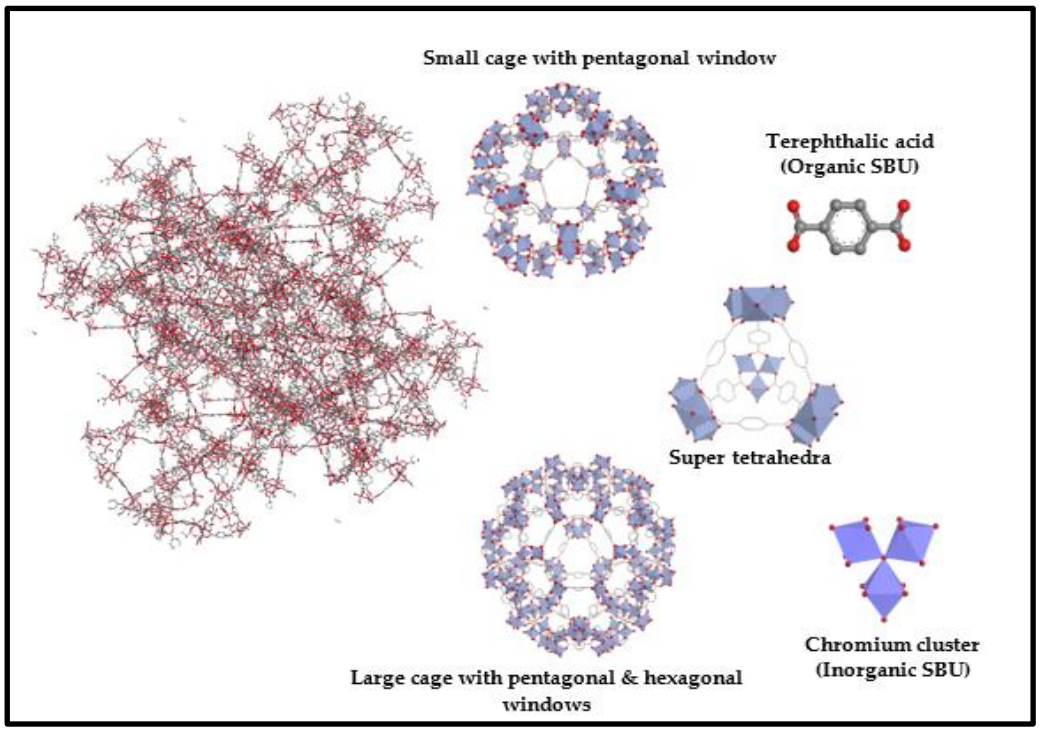

Fig. 2-20 Crystal, mesoporous cages, super tetrahedra and secondary building units of MIL-101(Cr).
(Figure was developed using Materials Studio software)

2.2.3.7.2. MIL-100(Fe)

Another MOF of the MIL family is MIL-100(Fe) which is also known as iron trimesate or iron-benzenetricarboxylate and commercially known as Basolite F300. Advantage of choosing iron as the inorganic SBU includes being environmentally benign and a non-toxic low cost component [169]. The MOF material is built out from trimesate as the organic moiety and iron (III) cluster as the inorganic moiety. Similarly, to MIL-101(Cr), the organic and inorganic linkers are connected together to form super tetrahedra that is joined in a MTN topology to form two mesoporous cages.

Nevertheless, the cages in the MIL-100(Fe) are smaller compared to those of MIL-101(Cr) as the cages diameters are 25 and 29 Å, respectively. The cages exhibit two types of pentagonal and hexagonal windows with openings of 5.5 and 8.6 Å (**Fig. 2-21**). The MOF material exhibits a high Langmuir surface area of more than 2800 $m^2\ g^{-1}$, pore volume of 1.2 $cm^3\ g^{-1}$ and a cell volume of 394,481 $Å^3$ [169].

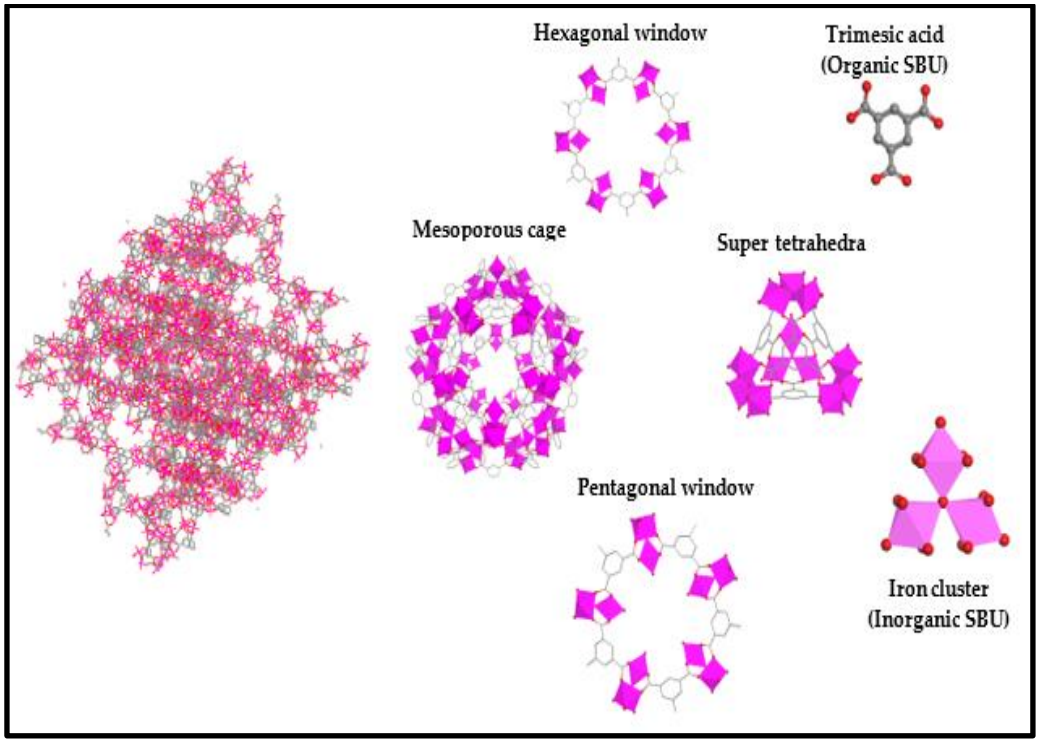

Fig. 2-21 Crystal, mesoporous cage, pentagonal and hexagonal windows, super tetrahedra and secondary building units of MIL-100(Fe).
(Figure was developed using Materials Studio software)

The material can be synthesized through either hydrothermal reaction of iron (III) cluster (metal powder or nitrate) and trimesic acid at 150-160°C for 8-12 hr in case of using conventional heating [169-171], at 95°C and atmospheric pressure for 12 hr [172] or at 130°C for 6 min in case of using microwave heating [173]. MIL-100(Fe) with a maximum water vapour uptake of 0.76 $g_{H_2O}\, g_{ads}^{-1}$ and hydrothermal cyclic stability is considered as a good candidate for adsorption heat pump application [154, 155]. Though, the material still suffers as MIL-101(Cr) from the limited water vapour uptake at the low-pressure range which limit its use to certain operating conditions and being produced in lab-scale only.

2.2.3.7.3. CPO-27(Ni)

CPO-27 (Ni) (Co-ordination Polymer of Oslo) [142], also known as MOF-74(Ni) or nickel(II) dihydroxyterephthalate is an isostructural MOF in which the same ligands is used with different divalent metal ions (Ni, Mg, Mn, Zn or Co). The metal organic or the linker (dihydroxyterephthale) are connected to the metal cation to form a 1D hexagonal channel (**Fig. 2-22**) with a pore size of 11-12 Å [174]. CPO-27(Ni) has been known for its many advantages such as its thermal stability and its high open metal sites density [175]. The metal ions in the honeycomb structure are co-ordinately bonded to solvent molecules, these molecules are removed by heating leaving open coordination sites that can be occupied by the adsorbed gas molecules [176].

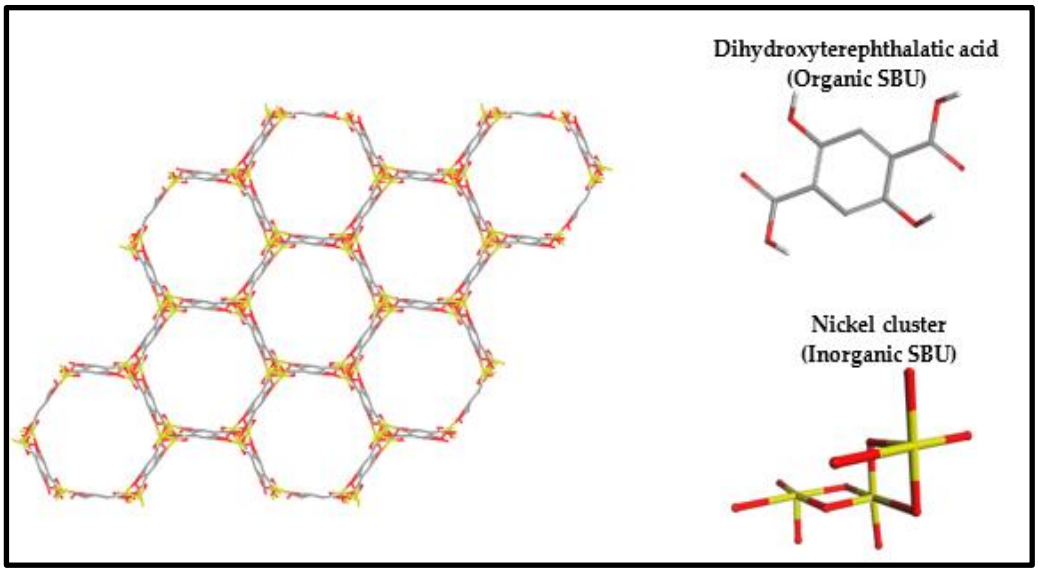

Fig. 2-22 Crystal structure and secondary building units of CPO-27(Ni).
(Figure was developed using Materials Studio software)

CPO-27 (Ni) is synthesized from nickel acetate or nitrate and 2,5-dihydroxyterephthalic acid at 110°C for 3 days using conventional heating [177], 90°C for 1hr using microwave heating [175], 70°C for 120 min using ultrasound irradiation [178] or 160°C and atmospheric pressure for 1 hr [179].

2.2.3.7.4. Aluminium fumarate

Aluminium fumarate is a microporous MOF material that is also known as Basolite™ A520. The Al–OH–Al nodes are linked to the fumarate moiety to form a rhombohedral channels that structurally resembles MIL-53 [151] (**Fig. 2-23**). The material is synthesized from aluminium chloride or nitrate and fumaric acid at 130°C for 4 days at atmospheric pressure [151, 180] or 130°C for 15 min using microwave irradiation [181]. With its hydrothermal stability, low desorption temperature and maximum water vapour uptake of 0.53 $g_{H_2O}\, g_{ads}^{-1}$, aluminium fumarate is considered as a candidate for adsorption heat pump applications.

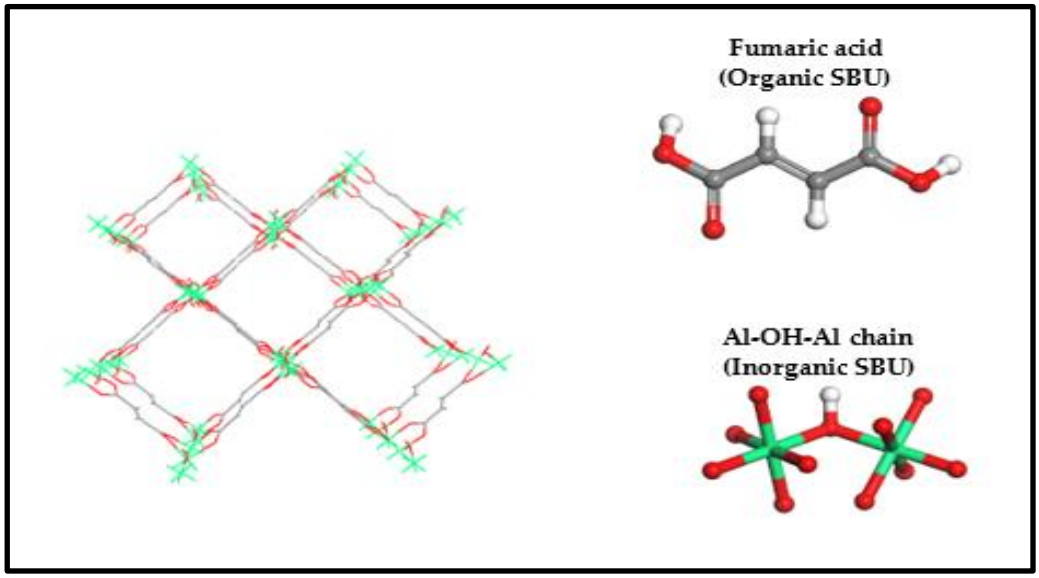

Fig. 2-23 Crystal structure and secondary building units of aluminium fumarate.
(Figure was developed using Materials Studio software)

The performance of any adsorption system is mainly evaluated through the coefficient of performance (COP) and specific cooling power (SCP). A main disadvantage of adsorption systems compared to the conventional mechanical vapour compression cycle is the low COP and SCP values. Low system SCP will lead to a bulky system and preventing it from being commercially available [182] while low COP means an increase in the consumed energy and hence the system operating cost [183]. The selection of the adsorbent material along with the bed design and its configuration are crucial factors affecting the performance of the adsorption system. Inappropriate bed design may cause low heat and mass transfer rates and hence long cycle time that may contribute to the poor performance.

2.2.3.8. Adsorption bed designs

As mentioned above, the bed design and its configuration is an important parameter as it can strongly affect the mass and heat transfer rates in the system and hence the performance of the whole system [109]. Mainly there have been 3 different bed designs that have been utilized in adsorption related applications which are plate heat exchanger, finned tube heat exchanger and annulus tube heat exchanger [102].

2.2.3.8.1. Plate heat exchanger

The plate heat exchanger consists of thin metal plates forming channels where the porous media is packed. The heating/ cooling fluid passes through small channels between the plates (**Fig. 2-24**). This type of heat exchanger has compact size and high heat transfer which are essential features for any adsorption system [184]. *Critoph et al.* [96] investigated the potential of a stainless steel plate heat exchanger for a car air-conditioning system using activated carbon and ammonia as the working pair giving a COP of 0.22 and SCP of 800 W kg^{-1}. Another study was conducted but the exchanger was made of copper and the working pair was SWS-1L/water. The system once again proved the potential of plate heat exchanger in the heat pump application as it produced a system COP and SCP of 0.51 and 662.8 W kg^{-1}, respectively [184].

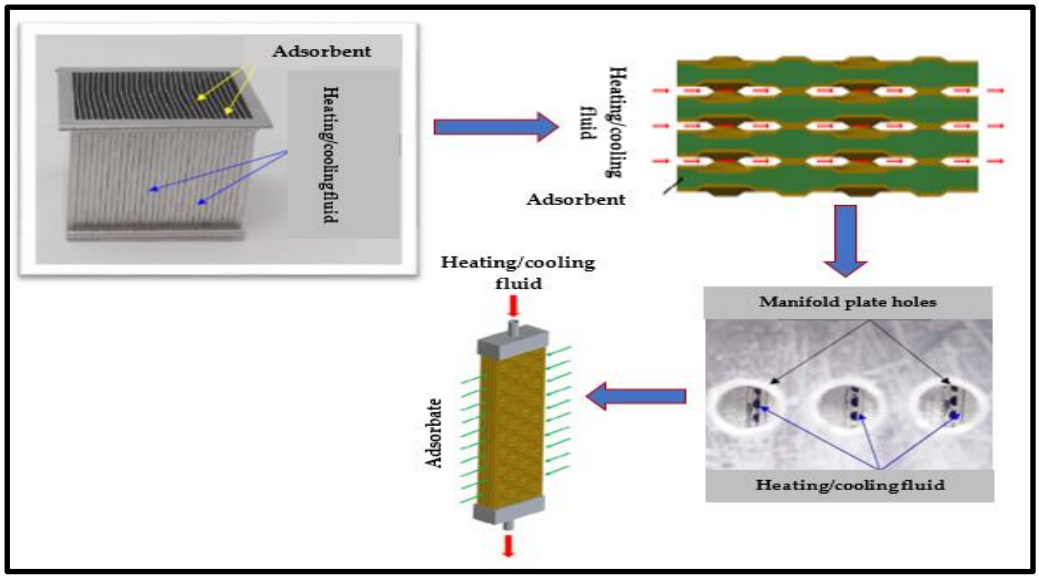

Fig. 2-24 Plate heat exchanger [96, 184].

2.2.3.8.2. Finned tube heat exchanger

The finned tube heat exchanger consists of metal fins (rectangular or annular) where the porous media is placed in between [185]. The heating/ cooling fluid passes through tubes across the bed (**Fig. 2-25)**. Finned tube heat exchanger is considered to be the most common used heat exchanger type in adsorption applications. This is attributed to the high fin surface area that enhances the heat transfer and mass transfer through the bed. Such enhancement contributes in decreasing the cycle time and increasing both COP and SCP of the system. Generally, the fin-tube heat exchanger may provide a COP of 0.5−0.7 and SCP of 100−600 W kg^{-1} with a half cycle time less than 1000 s [184]. This shows that the finned tube heat exchangers perform better than other bed designs [186]. The bed performance can be further improved through optimizing the bed configuration such as the fin spacing, fin height and the fin length [185].

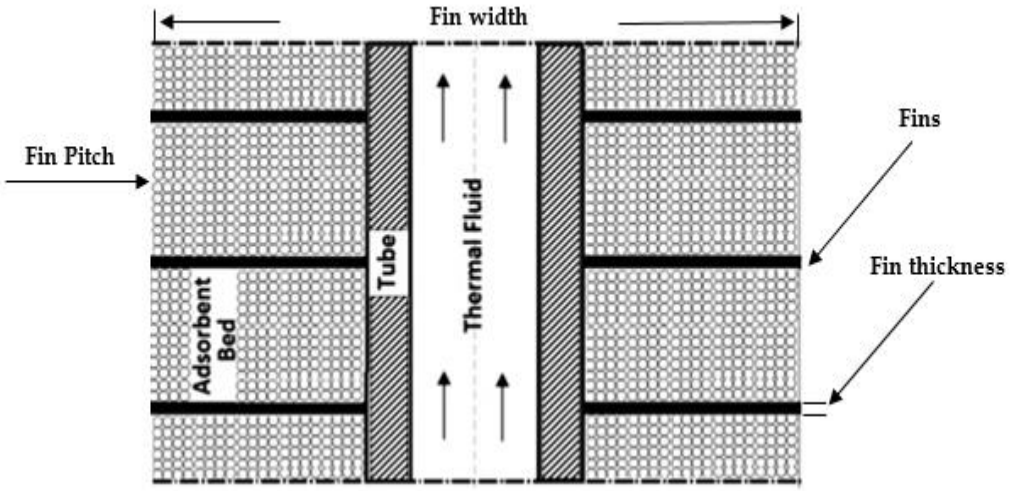

Fig. 2-25 Fin-tube heat exchanger [185].

2.2.3.8.3. Annulus tube heat exchanger

The main advantage of this heat exchanger is its simplicity [102]. The bed consists of tube and radial fins placed in a circular shell (**Fig. 2-26**). *Zhang et al.* [187] used zeolite and water as a working pair in an annulus tube heat exchanger for a car cooling system. The cycle produced a COP of 0.38 and SCP of 25.7 W kg^{-1}. The poor performance was attributed to the long cycle time.

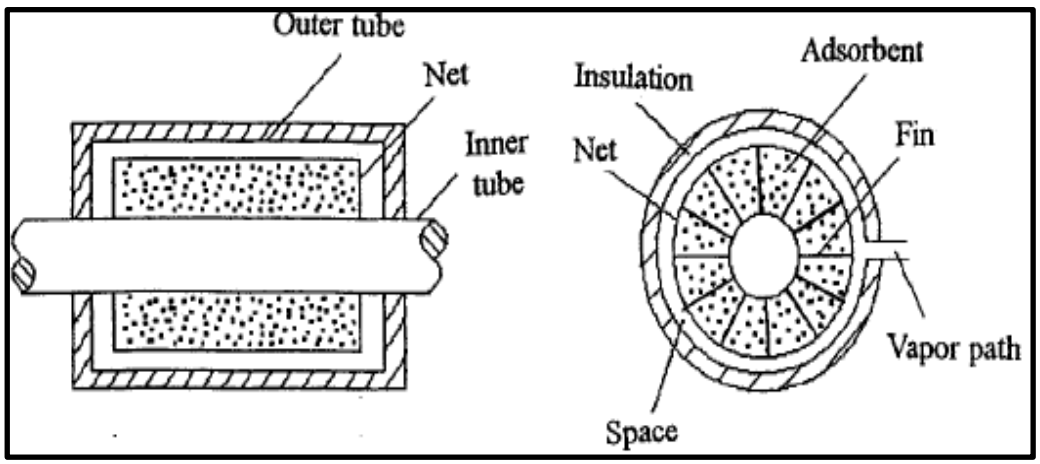

Fig. 2-26 Annulus tube heat exchanger [187].

This shows that the performance of the adsorption system is strongly related to design of the bed which means that different designs and configurations may result in different heat and mass transfer rates and hence different performances [182].

2.2.3.9. Improving the adsorption bed performance

A number of strategies have been suggested to improve the COP and SCP of adsorption systems including mass and heat transfer rates improvement, heat and mass recovery schemes and new types of efficient adsorbents [182].

2.2.3.9.1. Composites

Improving the heat and mass transfer rates may result in increasing the refrigerant capacity and shortening the cycle time [182] that is why composites are one of the routes that have been proposed to enhance the mass and heat transfer of adsorbent materials. According to the IUPAC (International Union of Pure and Applied Chemistry), composites are "multicomponent materials comprising multiple different phase domains in which at least one type of phase domains is in a continuous phase" [188]. The main advantage of composites is improving the heat and mass transfer performance of the system through improving the thermal conductivity and adsorption capacity.

2.2.3.9.1.1. Improving thermal conductivity

Due to the free volume in the porous media, adsorbent materials suffer from poor thermal conductivity. This low conductivity can hinder the heat transfer process during the adsorption and desorption processes causing longer heating/cooling times to reach the required operating temperatures [189].

Enhancing the thermal conductivity of conventional adsorbents like silica gel, zeolites and activated carbons was carried out through using metal powder, metal foam or expanded graphite. Also introducing the adsorbent material in the consolidated form was found to improve the heat transfer performance. The thermal conductivity of the unconsolidated silica gel was improved through introducing metal additives to adsorption beds. Pieces of copper, brass, aluminium and stainless steel were added showing that as the metal pieces' size increased, the heat transfer rate increased due to the higher contact area. Also, increasing the

amount of the metal significantly enhanced the heat transfer rate as 15wt% of aluminium pieces enhanced the effective thermal conductivity of a pure silica gel bed by 242% [190]. A similar study on activated carbon showed that using 30wt% aluminium pieces reduced the cycle time by 50% and increased the specific cooling power (SCP) by 100% [191].

To further improve the thermal performance of adsorbents, consolidated sorbent composites were made through using silica gel and 20-30wt% expanded graphite. This can be done through compacting the adsorbent with a thermally conductive material into a solid matrix. The thermal conductivity of silica gel was reported to be 10-20 W (m K)$^{-1}$ when it was incorporated with expanded graphite. The reported values are significantly higher than the value of 0.17 W (m K)$^{-1}$ of the silica-gel packed bed. It was concluded that optimum conditions of graphite fraction and moulding pressure should be obtained to give the maximum heat and mass transfer [192]. The performance of the composite was experimentally investigated using 30wt% graphite and 8 MPa as the optimum conditions for graphite concentration and moulding pressure. The composite blocks showed an enhanced heat and mass transfer rates giving a higher performance of the cooling systems [193]. Another study on incorporating silica gel with graphite flakes has been conducted [194] while activated carbon showed enhanced performance when combined with expanded graphite [183]. **Table. 2-6** shows the enhancement in the thermal conductivity of activated carbon and silica gel.

Table. 2-6 Thermal conductivity enhancement in activated carbon and silica gel through consolidated composites

Adsorbent	Thermal conductivity (W (m K)$^{-1}$)	Ref.
Granular activated carbon	0.24	[183]
Consolidated activated carbon + expanded natural	2.47	[183]
Granular silica gel	0.17	[192]
Consolidated silica gel + expanded natural graphite	10 to 20	[192]
Consolidated silica gel + graphite flakes	0.57 to 0.78	[194]

The first attempt to estimate the thermal conductivity of a MOF was done for MOF-5. The thermal conductivity of MOF-5 was numerically predicted in the temperature range of 200 K (-73°C) to 400 K (127°C) by *Huang et al* [195]. The crystal thermal conductivity was found to be 0.31 W (m K)$^{-1}$ at 300 K. This study was followed by an experimental measurement over a wider temperature range of 6 to 300 K (-267 to 27°C). At temperatures higher than 100 K (-137°C), the thermal conductivity was 0.32 W (m K)$^{-1}$ [196]. A more recent simulation study on the thermal conductivity of zeolitic imidazolate framework-8 (ZIF-8) predicted that the thermal conductivity was 0.165 W (m K)$^{-1}$ [32].

With such low thermal conductivity, few attempts were done to **enhancing the thermal conductivity of MOFs**. The first composite was based on MOF-5 and through adding expanded natural graphite (ENG) to the MOF powder producing a series of composites containing from 1 to 10wt% of expanded natural graphite (ENG). The thermal conductivity measurement revealed that for pellets with density of 500 kg m^{-3}, the addition of 10wt% ENG resulted in an improvement of five times compared to MOF-5 as it increased from 0.10 to 0.56 W (m K)$^{-1}$ at room temperature. It was also highlighted that ENG partially protected the MOF-5 crystals from deformation [197].

The effect of the pressing direction, the ENG content and the ENG distribution (homogeneous or layered) was investigated in a later study (**Fig. 2-27**) suggesting that the nature and direction of the second-phase addition controls the magnitude of thermal transportation in MOF compacts [198].

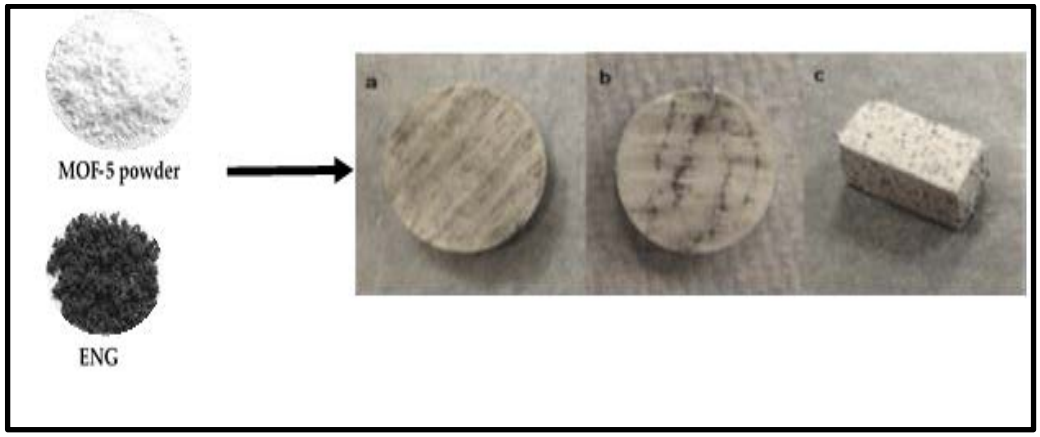

Fig. 2-27 MOF-5/ENG composites a. cylindrical pellet with a homogeneous ENG distribution, b. cylindrical pellet with a layered ENG distribution and c. Rectangular sample [198].

2.2.3.9.1.2. Improving the adsorption capacity

As highlighted earlier, the uptake of conventional adsorbents does not exceed 0.3 g_{H_2O} g_{ads}^{-1} which has a strong influence on the performance of the adsorption system. This uptake is almost a quarter of that of calcium chloride which was reported to be 0.9-1.2 $g_{H_2O}\, g_{ads}^{-1}$ [183, 199]. Calcium chloride is a hygroscopic salt that have a strong affinity for water. It was found that using $CaCl_2$ as a main adsorbent material may face some limitations such as the extremely low thermal conductivity and tendency to form agglomerates around the salt particles [200]. The poor thermal conductivity was enhanced through introducing expanded graphite to the salt for the application of ice making on fishing boats. The consolidated composite of 80% $CaCl_2$ and 20% of expanded graphite showed an enhancement of 353% in the SCP of the system compared to using $CaCl_2$. Such performance was attributed to the shorter cycle time due to the improved composite thermal conductivity [200].

It was also reported that a significant improvement was observed when the salt was incorporated with other porous material (hosting matrix) such as activated carbon, silica gel and zeolites to form composites. One of the earliest studies was conducted by *Aristov et al.* [201] discussing a composite of silica gel/$CaCl_2$ known as selective water sorbent (SWS-1L) (**Fig. 2-28**) which later became a subject of extensive studies due to the enhanced adsorption capacity up to 0.7 g

$_{H_2O}$ g_{ads}^{-1}. It was found that the anhydrous salt of $CaCl_2$ attracts the water molecules to form a $CaCl_2.0.33H_2O$ salt at higher relative pressures. As the adsorption process continues, a solid crystalline hydrate $CaCl_2.2H_2O$ is formed. The enhancement in the water vapour capacity increased the COP from 0.48 to 0.7 when using a desorption temperature of 90ºC [202]. In another study the potential of the SWS-1L at low desorption temperature was highlighted as the material can be desorbed at temperatures as low as 60°C sustaining almost the same performance as at 90°C (**Fig. 2-29**) [203].

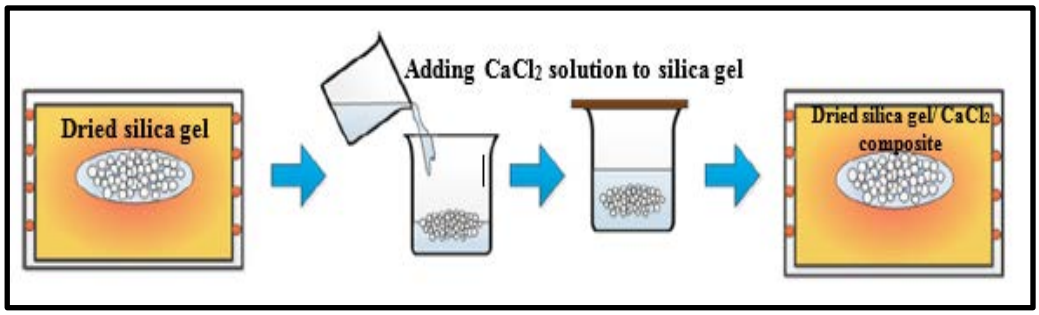

Fig. 2-28 Procedures of preparing silica gel/$CaCl_2$ composite (SWS-1L) [204].

Tso et al [199] showed that the uptake was significantly improved through impregnating activated carbon with silica-gel and different concentration of $CaCl_2$ solutions as shown in **Fig. 2-30**. This enhancement significantly improved the COP from 0.37 using activated carbon to 0.7 when using S3 composite while the SCP was increased from 65 to 387 W kg^{-1} using the same composite. While a composite of activated carbon fibre felts (ACF FELT) and 30% calcium chloride had a water uptake of 1.7 g $_{H_2O}$ g_{ads}^{-1} which is higher than the uptake of activated carbon, silica gel and even the silica gel/$CaCl_2$ composite that had a maximum uptake of 0.5 g $_{H_2O}$ g_{ads}^{-1} [204].

Soaking zeolite 13X in 46% $CaCl_2$ solution showed a similar improvement as a 0.4 g $_{H_2O}$ g_{ads}^{-1} difference in the maximum capacity was observed between 25 and 75°C at 870 Pa. It was mentioned that this was equal to an improvement of 420% in the uptake between the synthesized composite and neat zeolite 13X [84].

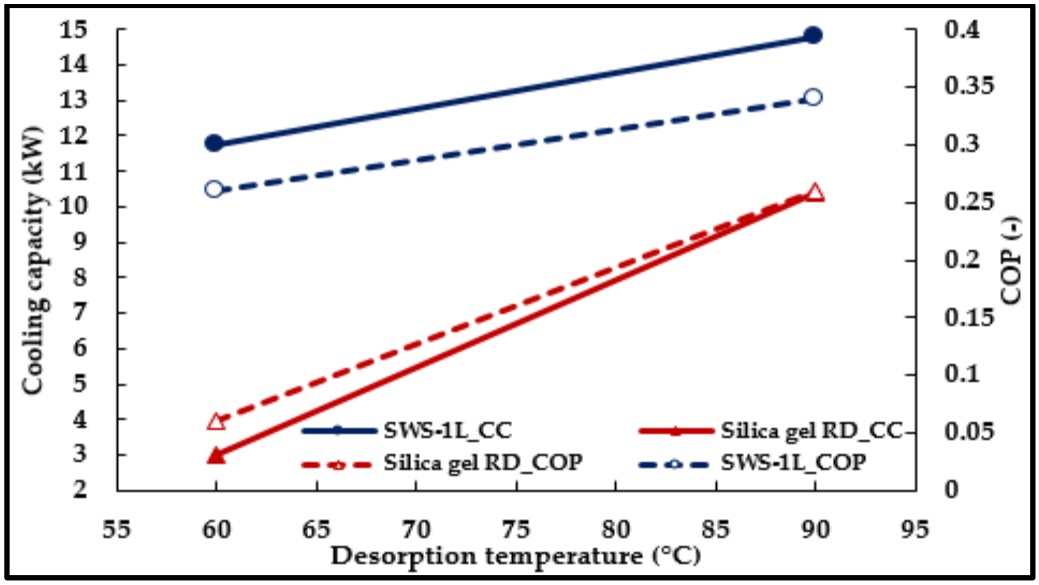

Fig. 2-29 Enhancement and effect of desorption temperature on silica gel RD and SWS-1L [203].
(Silica gel: cycle time 420 s, switching time 30 s and for SWS-1L: cycle time 630 s, switching time 30 s)

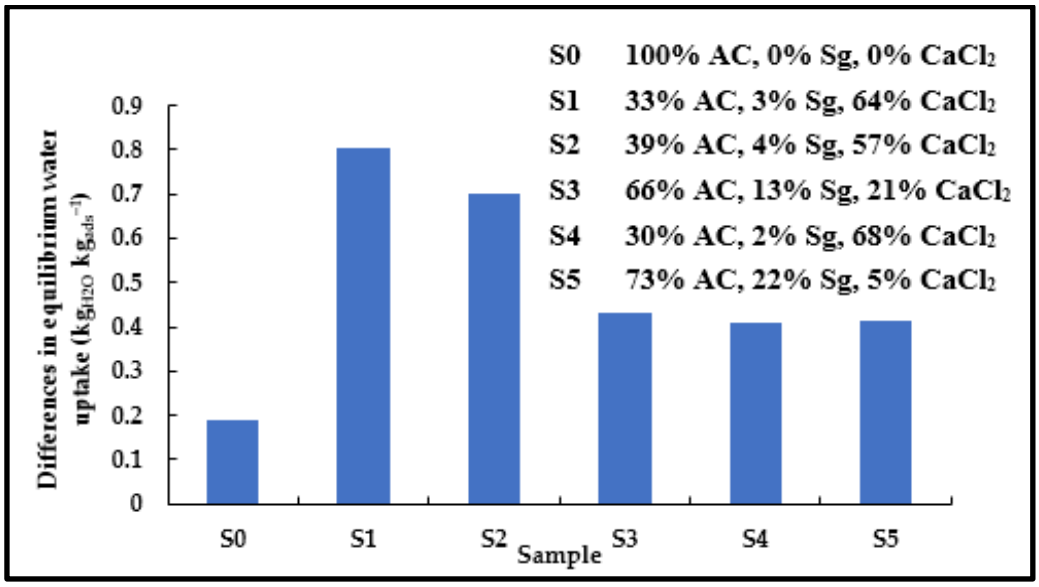

Fig. 2-30 Improvement in the equilibrium water uptake difference through incorporating activated carbon with silica gel and $CaCl_2$ (between 25°C and 115°C) [199].

MIL-101(Cr) is a MOF material that has gained considerable attention in the gas storage technology due to its numerous advantages such as the extra high surface area, high pore volume giving it an outstanding adsorption capacity of different solvents and the high thermal and chemical stability [160]. Nevertheless, there have been very limited studies focusing on improving the water vapour adsorption performance of MIL-101(Cr). One of the studies was performed by *Yan et al.* [149] synthesizing composites of MIL-101(Cr) using the carbonous material of graphite oxide (GO). A number of composites were synthesized with different GO concentration 2, 4, 6 and 8wt%. It was found that due to the hydrophilic properties of the graphite oxide, the composites showed an enhanced water adsorption performance at high relative pressure range (>0.5) with the highest water vapour capacity of 1.58 $g_{H_2O}\, g_{ads}^{-1}$, which improved from 1.22 $g_{H_2O}\, g_{ads}^{-1}$.

One of the main drawback of using of MIL-101(Cr) is that it does not adsorb any significant amount of water vapour at the low relative pressure range (<0.5). *Akiyama et al*. [205] showed that this problem can be solved and that the shape of the adsorption isotherm can be tuned through changing the substituent group in the ligand. Three functional groups, $-SO_3H$, $-NO_2$ and NH_2, were in situ incorporated to the structure (**Fig. 2-31**).

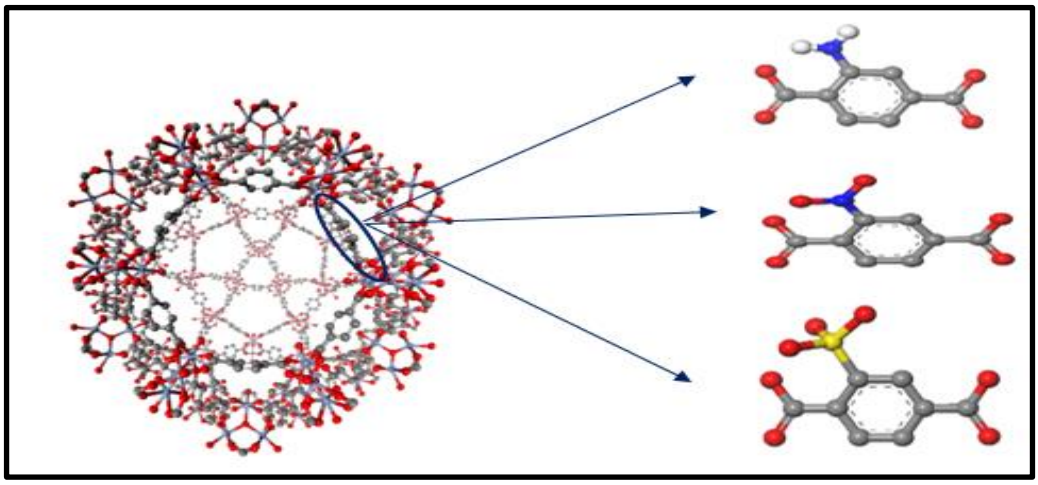

Fig. 2-31 Modification of MIL-101(Cr) to MIL-101(Cr)-NH_2, MIL-101(Cr)-NH_2 and MIL-101(Cr)-SO_3.
(O: red, C: grey, S: yellow, N: blue and H: white)
(Figure was developed using Materials Studio software)

Fig. 2-32 shows the adsorption isotherm of the four materials. It can be noted that the isotherm of MIL-101(Cr)-NH_2 and MIL-101(Cr)-SO_3H were shifted to lower relative pressure which was attributed to the highly hydrophilic incorporated groups while the MIL-101(Cr)-NO_2 showed almost no improvement due to the lower hydrophilicity [205]. Similar studies were later conducted to introduce functional groups through post synthesis approach instead of the direct synthesis [9, 206].

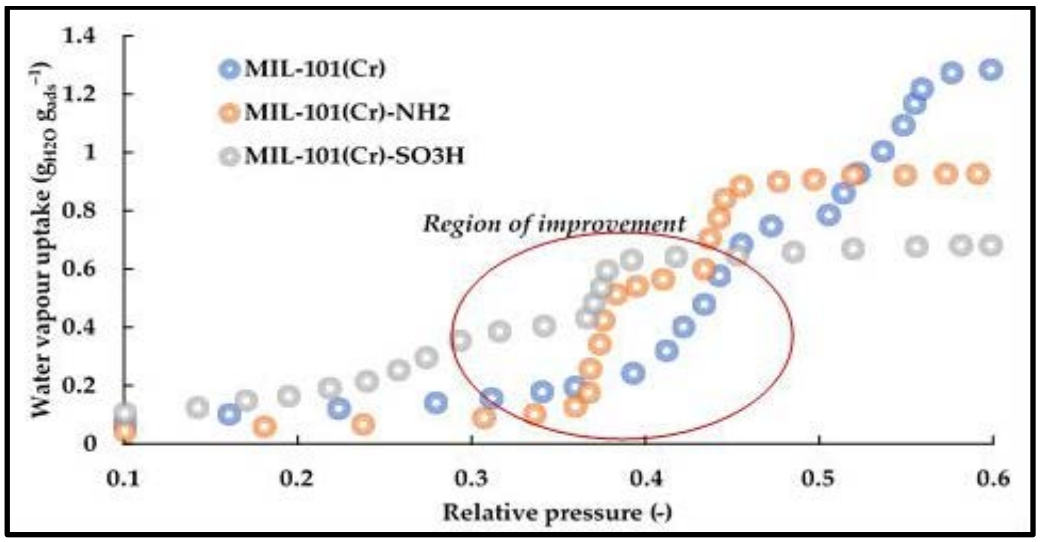

Fig. 2-32 Water adsorption isotherm of MIL-101(Cr), MIL-101(Cr)-NH_2, MIL-101(Cr)-SO_3H [205].

2.2.3.9.2. Mass and heat recovery

Another route to improve the performance of the adsorption system is using heat and mass recovery concept. The two techniques are applied after the adsorption/desorption processes. In the heat recovery process, the heating fluid flows through the two adsorption beds to recover the heat. The heating fluid from the desorption bed is used to pre-heat the adsorption bed while the cooling fluid from the adsorption bed is used to pre-cool the desorption bed. Such technique can enhance the heat usage and energy efficiency of the cycle and hence the COP of the system is improved. An improvement in the COP of 25% was achieved by *Wang et al.* [207] through applying heat recovery to a two-bed adsorption cooling system.

In the mass recovery process (**Fig. 2-33**), the two adsorption beds (in the adsorption and in the desorption phase) are connected. This allows the refrigerant vapour to flow from the high-pressure bed (desorption bed) to the low-pressure adsorption bed causing almost pressure equalization between the two beds. This scheme removes the adsorbate from the desorption bed and enables the porous material in the adsorption bed to adsorb more adsorbate vapour. This strategy improves both the adsorption and desorption processes through increasing and decreasing the pressure respectively. The mass recovery step is usually done before the heat recovery process to accelerate the circulation of refrigerant and enhance the cycle cooling power hence a higher SCP is achieved [73, 208, 209]. **Fig. 2-34** shows the enhancement in the system COP when using heat and mass recovery strategies.

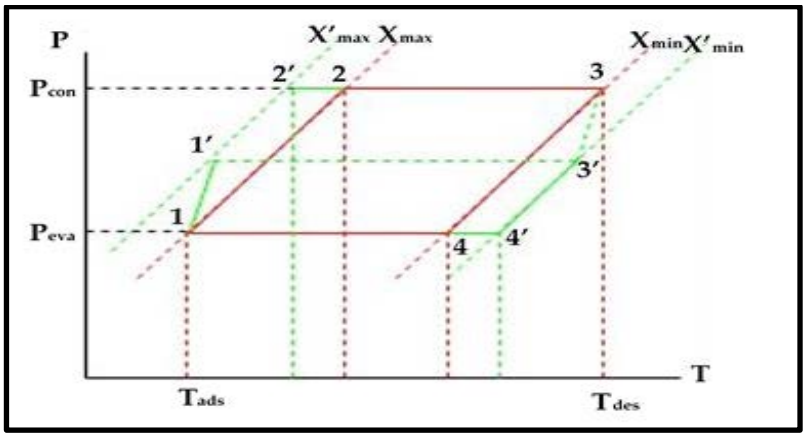

Fig. 2-33 Dühring diagram of the basic adsorption cycle (red) and improvement through mass and heat recovery (green).

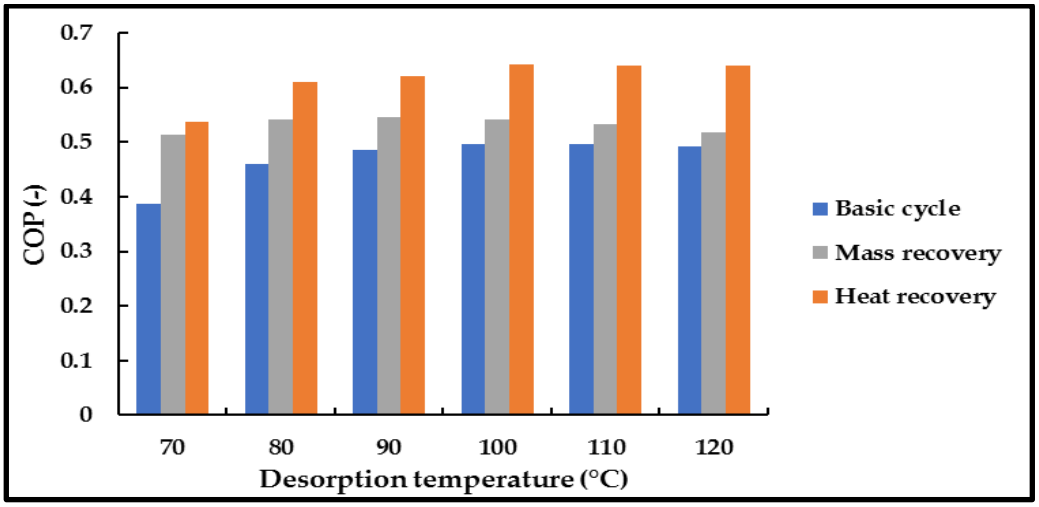

Fig. 2-34 Effect of heat and mass recovery strategies on the system COP [207].

2.2.3.9.3. Adsorbent material integration in the bed

Packed adsorption beds usually suffer from poor heat transfer rates which may be attributed to high contact thermal resistance because of the low contact area between the adsorbent grains and the metal surface. One proposed technique that has gained attention within the last few years is coating the surface of the heat exchanger instead of packing it with the adsorbent granules (**Fig. 2-35**). The technique was numerically investigated by *Rezk et al* [100] through combining an adsorbent coating layer with silica gel granules and metal additives of 15% copper, brass, aluminium or stainless steel. This technique was used to remove the contact resistance between silica gel granules and the heat exchanger metal keeping the same bed permeability. Results showed that the system cooling capacity and coefficient of performance (COP) were enhanced. It was reported that the coated layers should offer some specifications such as the high adsorption capacity, suitable permeability to facilitate the mass transfer process and the high lifetime [47]. Also, an optimum coating layer thickness usually must be obtained so no decrease in the mass and heat transfer rates takes place. Such strategy can be achieved either by using a binding agent or through direct coating. The most common technique is using binding agents such as polyvinyl alcohol (PVA), bentonite clay, Polytetrafluoroethylene (PTFE), N-propyltrimethoxy-silane, aluminium hydroxide and silicone resins with adsorbents such as silica gel, AQSOA-Z02, zeolite 4A, zeolite Y and AlPO-18 [103, 210-214]. This method has the advantages of easily controlling the coating thickness, the mild operating condition, the simplicity and potential of implementing the technique.

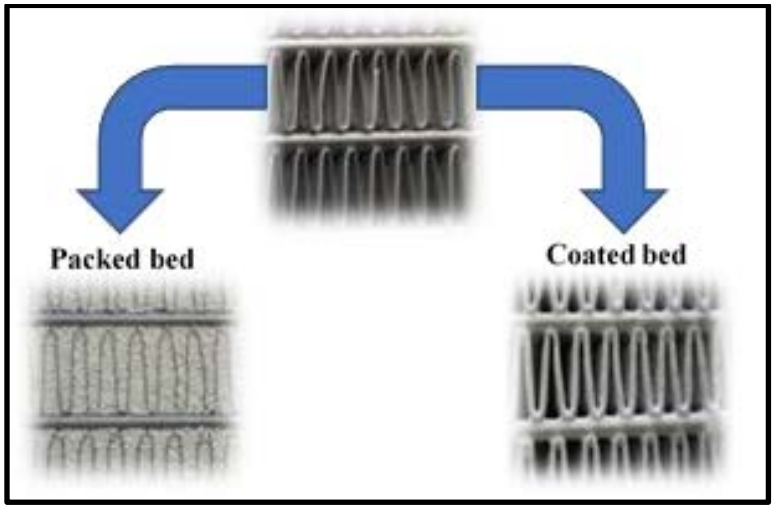

Fig. 2-35 Methods to introduce adsorbents to the adsorption system [212].

Fig. 2-36 shows the effect of integrating SAPO-34 as a coating layer instead of loose particles. It can be noticed that the specific cooling power was significantly enhanced, while the COP was reduced.

On the other hand, the direct coating technique is usually done through the temperature gradient approach. This method offers the advantage of not using any additional binding substance and not affecting the mass transfer rate and adsorption capacity of the adsorbent material. The coated layer is usually obtained through immersing the metal substrate into the reactants mixture where the metal substrate is the only medium with the suitable temperature to form the desired material on. Such method was used to deposit zeolite A [215] and zeolite X [216]. **Table. 2-7** summarizes the work done on adsorbent coating through listing the adsorbent used, the thickness developed, and the method used.

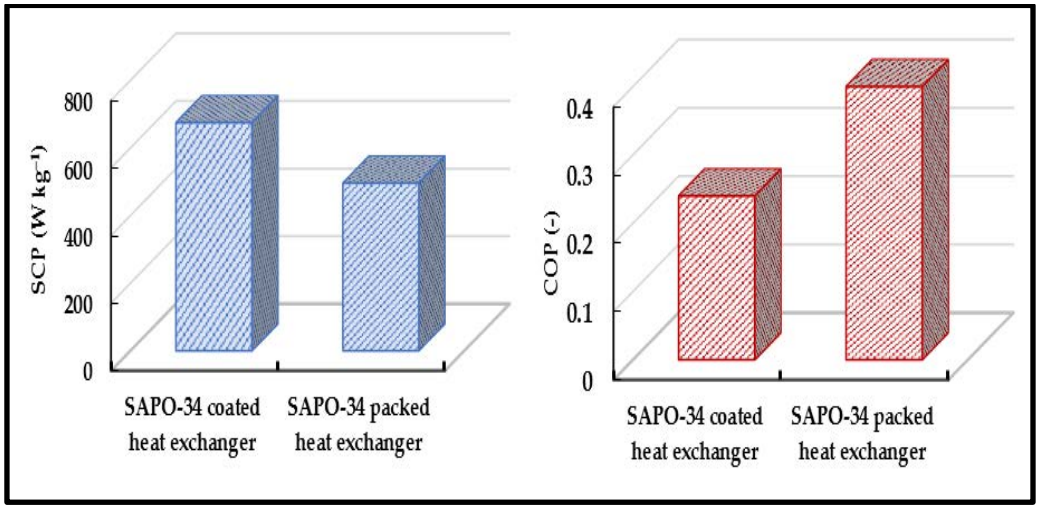

Fig. 2-36 Comparison between packing and coating of SAPO-34 on the performance of adsorption system [212].

Table. 2-7 Summary of adsorbent coating and its thickness

Material	Thickness (mm)	Method of coating	Ref.
SAPO-34	0.2-0.8	Dip coating	[210]
Zeolite A	0.27	Temp. gradient	[215]
Zeolite A and X	0.038-0.23	Temp. gradient	[216]
SAPO-34	0.12	Dip coating	[212]
Zeolite Y	0.102-0.135	Dip coating	[103]
SAPO-34	0.23-0.29	Dip coating	[103]
Zeolite A	0.13-0.14	Temp. gradient	[217]
SAPO-34	0.6	Dip coating	[218]
Zeolite	4	Dip coating	[219]

With the intensive research on performance of adsorbent coating, there are very limited studies on the mechanical strength of the developed coating layers. One of the very few and most detailed studies was the one conducted by *Freni et al* [210] where they compared the mechanical stability of two coated samples of AQSOA-Z02 using clay based binder, one prepared by the group and the other by Mitsubishi Plastic Incorporation (MPI) through different tests such as micro-hardness, shear, bending strength, vibrations and impact strengths.

2.3. Summary

Based on the previously published work, it can be concluded that:

1. There are serious problems that endanger the existence of mankind such as water scarcity, global warming and ozone layer depletion.
2. The world is heading to using technologies that has lowered its dependency on electricity and fossil fuel and hence lower CO_2 emissions are expected.
3. Adsorption technology can be an alternative to conventional cooling technologies.
4. It can also be an excellent solution to water scarcity through the adsorption desalination or storing energy through adsorption energy storage application.
5. The performance of the adsorption system depends significantly on the adsorbent material, its properties, the bed design and its configuration.
6. The performance of the system can be further improved through using advanced adsorbent materials such as MOFs or through enhancing techniques to improve the heat and mass transfer rates.
7. Techniques such as coating, composites and heat/mass recovery can significantly enhance the performance of the adsorption system.

CHAPTER 3

METAL-ORGANIC FRAMEWORKS CHARACTERIZATION

3.1. Introduction

MOF materials can be characterized through an array of techniques to identify their properties. Basic MOF characterization include powder X-ray diffraction (PXRD) to establish crystallinity and phase purity of the material in addition to nitrogen adsorption to confirm their porosity and calculate their surface area. Additional characterization techniques and protocols may include thermogravimetric analysis (TGA) to determine the thermal stability of the materials, the water vapour uptake and the performance stability of the materials in the presence of humidity through dynamic vapour sorption (DVS), scanning electron microscopy (SEM) to show the crystal size and morphology which can be coupled with energy dispersive X-ray spectroscopy (EDX) to further understand their elemental composition, Fourier transform infrared spectroscopy (FTIR) to show the presence of functional groups in the materials structures and X-Ray Fluorescence (XRF) to give the elemental composition of the materials [220]. The different equipments' testing parameters used to characterize different materials have been optimised based on previous study in the literature.

3.2. Powder X-Ray Diffraction (PXRD)

X-Ray diffraction is used for structural characterization of solid state materials. All crystalline solids have their own characteristic patterns which are used as their fingerprints. Also, the position, shape and intensity of the peaks in X-ray diffraction pattern can be used for

the determination of unit cell parameters, crystal size measurement and phase purity. A crystal structure is constructed of a unique arrangement of atoms exhibiting long range order and symmetry in three dimensions. The infinite repeating of that array of points in space is called a crystal lattice.

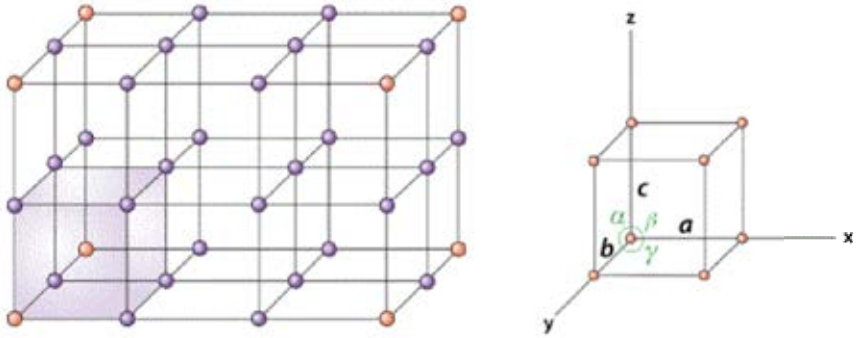

Fig. 3-1 Crystal lattice and unit cell.

The smallest repeating unit in a lattice that represents the atomic arrangement and reveals the symmetry of the crystal structure is called unit cell. The lattice parameters are the unit cell's three lengths (a, b and c) and the angles in between (α, β and γ) (**Fig. 3-1**).

Fig. 3-2 shows a schematic representation of diffraction of X-rays in a crystalline material. The X-rays are produced by bombarding copper with a beam of electrons generated from a hot tungsten filament. The beam will ionize the target atom K-shell electrons and X-rays are emitted. A crystalline material is composed of parallel planes or layers of atoms described in terms of three integers (hkl), known as Miller Indices. The perpendicular distance between such two planes is known as the d-spacing (d_{hkl}). As the X-rays hit the crystal, the first layer of atoms will partially reflect the X-rays, the remaining rays will go through to the second layer where the process continues. The reflected rays form the X-ray diffraction pattern which can be plotted in the form of the measured intensity and angle of the diffracted rays. This can only happen when the Bragg law (**Eq. 3-1**) is satisfied. This means that the path difference between the incident X-rays must be equal to a multiple of their wavelength (nλ).

Path length difference= $n\lambda = 2d_{hkl}\sin\theta$ **(3-1)**

Where n is an integer, λ is the wavelength of X-rays, d_{hkl} is the spacing between the planes in the atomic lattice, and θ is the angle between the incident ray and the scattering planes.

Important information can be extracted from the XRD pattern based on the position, shape and intensity of the peaks. Peak position is a fundamental factor generated from the scattering within lattices. Based on the Bragg equation (**Eq. 3-1**), diffraction peaks appear at specific angles determined by the wavelength of the incident radiation and the unit cell dimensions. Peak shape profile is a factor to describe the broadening of the diffraction peaks. It is important because this parameter contains information of the crystallite size which is of interest in materials characterization.

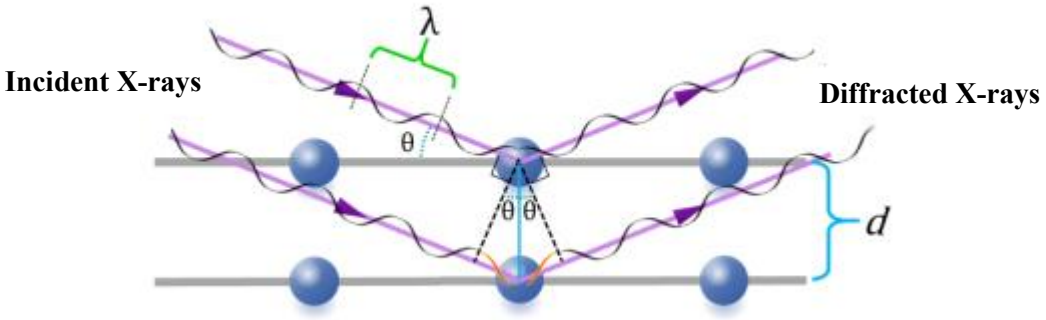

Fig. 3-2 Diffraction X-rays in a crystalline material in the derivation of Bragg's law.

In this study, aluminium fumarate and CPO-27(Ni) samples were characterized using a Bruker D8 Advance Reflection Diffractometer (**Fig. 3-3a**) with Cu Kα radiation (1.5418 Å). The aluminium fumarate sample was scanned from 8 to 45° 2θ while the CPO-27(Ni) sample was scanned from 10 to 75°, with a step size of 0.02° and both were spun at 15 rpm [14, 221].

As the characteristics peaks of MIL-101(Cr) and MIL-100(Fe) are positioned at much lower 2θ angle, Siemens D5005 diffractometer (**Fig. 3-3b**) using CuKα radiation (λ = 1.5418 Å) was used to scan the samples from 2.5 to 30° with a step size of 0.02° [14].

Fig. 3-3 a. D8 Advance-Bruker and b. Siemens D5005.
((a) X-ray source, (b) monochromator, (c) sample holder and (d) detector).

3.3. Nitrogen adsorption at 77 K [18]

Important features of porous materials such as the surface area, pore volume and pore size distribution cannot be determined based on their other characteristics such as the particle size but is rather determined at the atomic level by the adsorption of an inert gas. The adsorption isotherm shows the change in the adsorbed gas amount with relative pressure at a constant temperature. The most commonly used gas is nitrogen as it is readily available in high purity. Also, the molecular size and the interaction of nitrogen with most solid surfaces is relatively strong. Other gases such as Krypton or Argon maybe used in case of low specific surface area.

3.3.1. Surface area

a. Monolayer Adsorption: The Langmuir Model [222]

Typically, the Langmuir model refers to the adsorption on a surface having only one kind of space in which this space can hold only one adsorbed layer of molecules. This means that

the monolayer is the limit of the adsorption which usually causes an overestimation of the material surface area.

b. Multilayer Adsorption: The Brunauer–Emmett–Teller (BET) Model [223]

According to the BET theory, the Langmuir mechanism was extended to multilayer adsorption (**Fig. 3-4**). The first layer of adsorbed molecules acts as adsorption sites for the next layers untill the saturation vapour pressure is reached. It was found that the amount of the gas adsorbed depends on the interaction between the adsorbed layer and adsorbent, pressure and temperature as shown in **Eq. 3-2**.

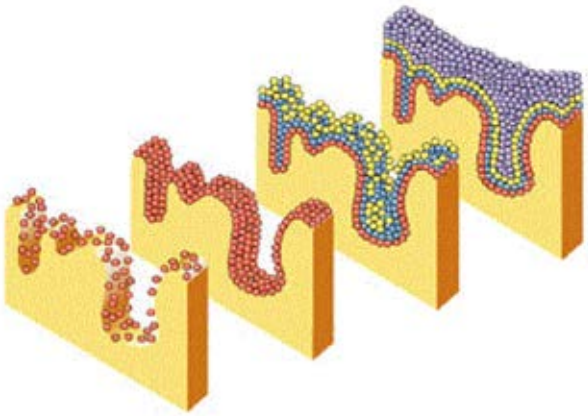

Fig. 3-4 Multilayer adsorption.

$$\frac{1}{X\left[\frac{P_0}{P}-1\right]}=\frac{1}{X_m C}+\frac{C-1}{X_m C}\left[\frac{P}{P_0}\right] \qquad \textbf{(3-2)}$$

Where X is the amount of adsorbed gas, P/P_0 is the relative pressure, C is a constant depending on the interaction between gas and porous material and X_m is the amount of the adsorbed gas forming the monolayer. The BET equation requires a linear plotting of $1/[X((P/P_0)-1)]$ against the relative pressure (P/P_0), such plot gives slope (S) and intercept (i) as shown in **Eq. 3-3** and **Eq. 3-4**.

$$S = \frac{C-1}{X_m C} \quad \textbf{(3-3)}$$

$$i = \frac{1}{X_m C} \quad \textbf{(3-4)}$$

X_m is then calculated through **Eq. 3-5**

$$X_m = \frac{1}{S+i} \quad \textbf{(3-5)}$$

The surface area A can then be derived from **Eq. 3-6**

$$A = \frac{X_m N_A A_{cs}}{M} \quad \textbf{(3-6)}$$

Where X_m is the amount of adsorbed gas to form a monolayer, N_A is Avogadro's number, A_{cs} is the cross-section area of adsorbate molecule and M is molecular weight of adsorbate.

Finally, the BET surface area is

$$A_s = \frac{A}{m} \quad \textbf{(3-7)}$$

Where A is the surface area of the adsorbent and m is the mass of the adsorbent sample.

3.3.2. Total pore volume

The total pore volume is calculated based on the amount of gas adsorbed at a relative pressure close to unity where it is assumed that the pores of the adsorbent material are filled with liquid nitrogen. The volume of liquid nitrogen (V_{liq}) is calculated using the volume of nitrogen adsorbed (V_{ads}) (**Eq. 3-8**)

$$V_{liq} = \frac{P_a V_{ads} V_m}{RT} \quad \textbf{(3-8)}$$

Where P_a is ambient pressure, V_m is the volume of gas corresponding to a monolayer, R is the universal gas constant and T is the ambient temperature.

In this study, the nitrogen adsorption/desorption measurements were carried out at 77 K (-196°C) using a Quantachrome NOVA surface area analyser (**Fig. 3-5**). All samples were

evacuated at 393 K (120°C) under vacuum except CPO-27(Ni) which was dried at 666 K (150°C). The BET surface area was calculated in the relative pressure range from 0.03 to 0.3, the total pore volume was calculated at a relative pressure close to unity (0.95) and the pore size distribution was calculated using DFT method [224].

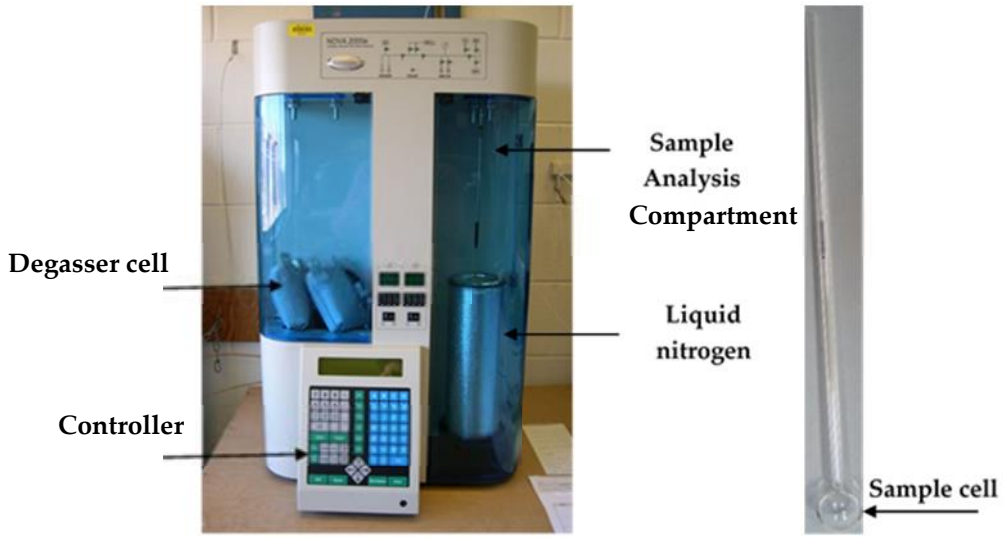

Fig. 3-5 Quantachrome NOVA surface area analyser.

3.4. Thermogravimetric Analysis (TGA)

Thermal gravimetric analysis or thermogravimetric analysis (TGA) is a technique to observe the change in a sample mass as a function of temperature or time. The sample is subjected to a pre-set temperature program in an atmosphere of argon, nitrogen, oxygen or air. Such technique is normally used as indication of the thermal stability of the material and changes in sample composition. Differential thermal analysis (DTA) can be used to determine the temperature at which weight loss or the phase change is most apparent. The sample to be tested and a reference sample undergo an identical thermal program.

In this study, the thermal stability of the materials were investigated using a Perkin Elmers Pyris 1 (**Fig. 3-6**) in the temperature range of 23°C to 650°C, under a nitrogen flow (60 ml min^{-1}) and using a heating rate of 10°C min^{-1} [225].

Fig. 3-6 Perkin Elmers Pyris 1.

3.5. Scanning Electron Microscopy (SEM)

Scanning Electron Microscopy is an optical technique where electrons are used instead of light to form an image of a sample. The technique is used for studying the topography and morphology of samples. Also, the X-rays emitted from the sample surface can provide elemental information which is called Energy-dispersive X-ray Spectroscopy (EDX).

Scanning electron microscopy (SEM) images of all the MOFs under investigation were taken using a CFEI Quanta 3D FEG FIB-SEM [27].

3.6. Fourier Transform Infrared Spectroscopy (FTIR)

This technique is used to check for the presence of functional groups in a given structure. The Fourier Transform Infrared Spectroscopy is carried out by passing an infrared (IR) radiation (wavenumber of 10-12800 cm^{-1}) through a sample. As the sample is irradiated, it will stretch through absorbing part of the radiation of specific wavelengths and transmit the rest.

The absorbed radiation causes a change in the dipole moment of molecules. As a result, the sample vibrational energy level transfers from the ground state to the excited state. The spectrum is formed of absorption peaks which correspond to the frequencies of energy gap between the vibrational states of the molecules making up the material. The resulting spectrum represents unique molecular fingerprint which cannot be repeated for another structure.

FTIR measurements carried out in this study were recorded on a Perkin Elmer Spectrum 100 FTIR spectrometer (**Fig. 3-7**) in the wavenumber range of 650 cm^{-1} to 4000 cm^{-1}.

Fig. 3-7 Perkin Elmer Spectrum 100 FTIR spectrometer.

3.7. X-Ray Fluorescence (XRF)

When an X-ray beam is produced and allowed to be in contact with a sample, the beam interacts with the atoms and knocks out the electrons in the inner orbital shells of the atom (k-shell electrons). Such process causes the instability of the atom; hence the vacancies must be re-filled with electrons from higher orbits. The further the electrons are from the nucleus, the higher binding energy they have. This means that, when the electrons move from the higher orbit to a lower one, it loses some energy (equivalent to the energy difference and distance between the two shells). Each element in the periodic table has a unique distance between its orbital shells. This means that the energy lost is unique for each element and hence this process can be used to identify the elements present in a sample. To achieve quantitative analysis, the

detected energies are analysed through the instrument and a software. Elemental analysis of different samples was carried out in this study using an S8 Tiger XRF Spectrometer (**Fig. 3-8**).

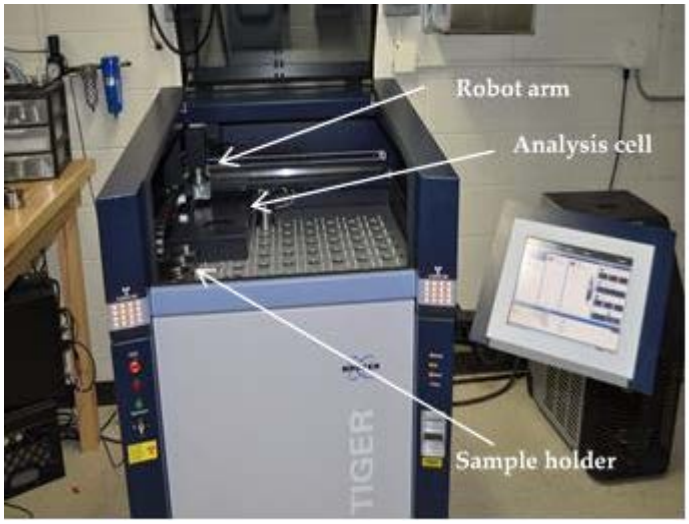

Fig. 3-8 S8 Tiger XRF Spectrometer.

3.8. Helium Pycnometer

For a porous material, there are mainly two types of densities to determine. The first is the bulk density (envelope density), in which the volume of the pores and spaces are included in the sample volume. For a dried powder, measuring the bulk density can be done simply by weighting a known volume of a sample.

The second type is the true density (skeletal or apparent), where the voids volume is not taken into account in measuring the volume. Measuring true density is not as easy as bulk density. Gas pycnometers are used based on the gas displacement method to measure the volume of a given sample. The displacement medium can be an inert gas such as helium. The true volume of a porous sample is calculated through measuring the pressure drop before and after opening a valve between the sealed sample chamber and the expansion chamber based on **Eq. 3-9**.

$$V_S = V_C + \frac{V_R}{1 - \frac{P_2}{P_1}} \qquad \textbf{(3-9)}$$

Where:

V_S is the sample volume, V_C is sample chamber volume, V_R is reference chamber volume, P_2 is final pressure in the sample chamber while P_1 is the initial pressure.

The true density of all the samples was measured using an Accupyc II 1340 Helium Pycnometer (**Fig. 3-9**).

Fig. 3-9 Helium Pycnometer.

The measured true density was used to estimate the porosity of each material. The bulk density which is also known as the packing density, was measured through weighing a known volume of each material. Finally the porosity is calculated using **Eq. 3-10** [226]

$$\varepsilon = 1 - \frac{\rho_{bulk}}{\rho_{true}} \qquad \textbf{(3-10)}$$

Where ε is the total porosity, ρ_{bulk} is the bulk density in kg m^{-3} and ρ_{true} is the true density in kg m^{-3}.

3.9. Thermal conductivity

Thermal conductivity is a crucial property of porous materials as it shows the ability to conduct heat. The thermal conductivity is measured through measuring the density, specific heat capacity and thermal diffusivity as shown in **Eq. 3-11**

$$\phi = \alpha . C_p . \rho \qquad \textbf{(3-11)}$$

Where ϕ is the thermal conductivity, α is the thermal diffusivity, C_p is the specific heat capacity and ρ is the compact density.

3.9.1. Thermal diffusivity

The thermal diffusivity is a thermo-physical property that describes the rate of heat propagation of a material due to a change in temperature. The common technique for measuring the thermal diffusivity is the laser flash analysis (LFA). The technique is based on that when a beam of laser is focused on the sample allowing it to absorb the energy, an IR detector measures the temperature increase on the rear face of the sample as a function of time. The sample is usually coated with graphite to improve light absorption [225].

The thermal diffusivity (α) is determined by **Eq. 3-12**.

$$\alpha = 0.1388 \frac{I^2}{t_{0.5}} \qquad \textbf{(3-12)}$$

Where I is thickness of the sample and $t_{0.5}$ is time at 50% of the temperature increase.

The thermal diffusivity of the different MOFs was measured using a NETZSCH-LFA 427 (**Fig. 3-10**) in the temperature range of 303-473 K (30-200°C) which represent the temperature range for adsorption and desorption phases in real systems. Samples were dried at 453 K (180°C) under vacuum for 6 hr before being pressed under 20 MPa pressure to form pellets with an average diameter of 12.9 mm and thickness of 1.6 mm. The produced pellets were then coated with graphite to improve the absorption of light [225].

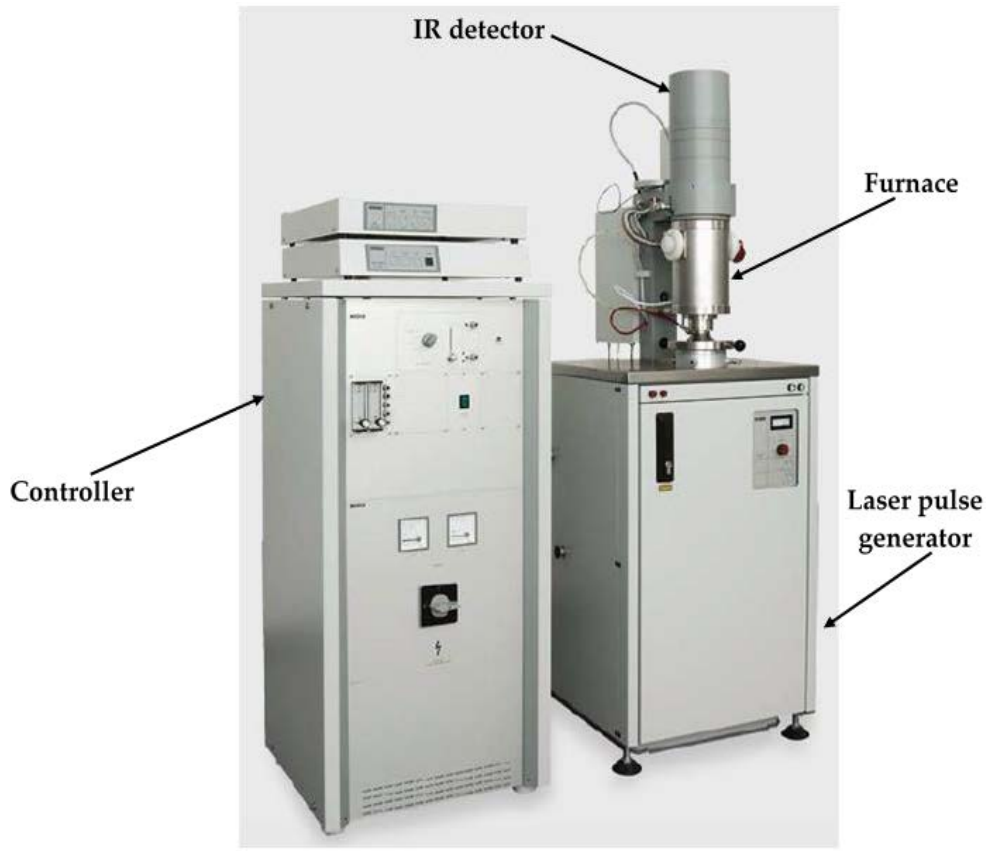

Fig. 3-10 NETZSCH-LFA 427.

3.9.2. Specific heat capacity

The specific heat capacity (Cp) is an indication of the thermal energy storing ability of a material. It is defined as the amount of heat required to raise the temperature of a unit mass of a material by one degree. The Cp is usually measured through differential scanning calorimetry (DSC) technique. Such technique provides information about thermal changes based on the sample mass. This technique not only provides the specific heat capacity of a substance but also can provide the melting point, the enthalpy, the purity and the phase change reaction of a sample. This is done through connecting the sample and a reference (Sapphire) by a low-resistance heat flow path. The temperature difference and changes between a sample and the reference is measured by thermocouples. The temperature difference is then used to calculate the heat flow and the specific heat capacity.

The specific heat capacity was measured in the temperature range of 303 K-473 K (30-200°C) using a METTLER TOLEDO DSC2 [225].

After calculating the thermal conductivity of materials' pellets using **Eq. 3-11**, the effective thermal conductivity of the packed bed (the thermal conductivity of the adsorbent material and water vapour inside its pores) was calculated using the measured thermal conductivity and the calculated porosity using the modified Zehner–Schlunder model (**Eq. 3-13** to **Eq. 3-15)** [227].

$$\phi = \frac{\phi_g}{\phi_s} \tag{3-13}$$

$$b = \left(\frac{1-\varepsilon}{\varepsilon}\right)^{0.9676} \tag{3-14}$$

$$\frac{\phi_{eff}}{\phi_g} = (1-\sqrt{1-\varepsilon}) + \frac{1-\sqrt{\varepsilon}}{\phi} + (\sqrt{1-\varepsilon}+\sqrt{\varepsilon}-1)\times\left[\frac{b(1-\phi)}{(1-\phi b)^2}\ln\frac{1}{\phi b} - \frac{b-1}{1-\phi b}\right] \tag{3-15}$$

Where ϕ_g is the water vapour thermal conductivity W (m K)$^{-1}$, ϕ_s is the thermal conductivity of solid (adsorbent without voids) W (m K)$^{-1}$, ε is the total bed porosity and ϕ_{eff} is the effective thermal conductivity W (m K)$^{-1}$.

3.10. Dynamic Vapour Sorption (DVS)

The Dynamic Vapour Sorption analyser (**Fig. 3-11**) is designed to estimate the uptake of an adsorbent based on measuring the change in its mass as it sorbs. The apparatus consists of two weighting chambers (**Fig. 3-12**), one for the sample to be tested and the other is for the empty reference. A sample pan is placed in each chamber and the two pans are hung on thin wires that are connected to an ultra-sensitive microbalance. First, the sample is evacuated (dried) at the desired temperature and for the preferred time through setting a heating program that controls a heating coil (**Fig. 3-13**). Nitrogen, which is used as a purge gas, carry the adsorbate vapour to pass over the sample at the desired flowrate and temperature. The desired relative humidity (vapour pressure) is adjusted through mixing a stream of dry nitrogen with the adsorbate vapour at the correct ratios by controlling the mass flowrates of both streams

based on the signals received from an optical vapour sensor. The change in the mass is then recorded through the microbalance. The change in the sample mass shows the adsorption/desorption behaviour of the material. After recording the mass of the sample at a series of different relative humidities, the equilibrium water vapour uptake was calculated at each relative humidity step giving the water vapour isotherm at the set temperature. The adsorption rate (adsorption kinetic) curves are obtained through plotting the change in the sample weight versus time.

The water adsorption characteristics of the investigated MOFs were measured using a dynamic vapour sorption (DVS) gravimetric analyser (Advantage DVS, Surface Measurement Systems, UK) by placing 10 mg in the sample pan. Each sample was evacuated for 6 hrs before starting the measurements. The measurements were carried out in a relative pressure range from 0 to 0.9 [14, 221, 225].

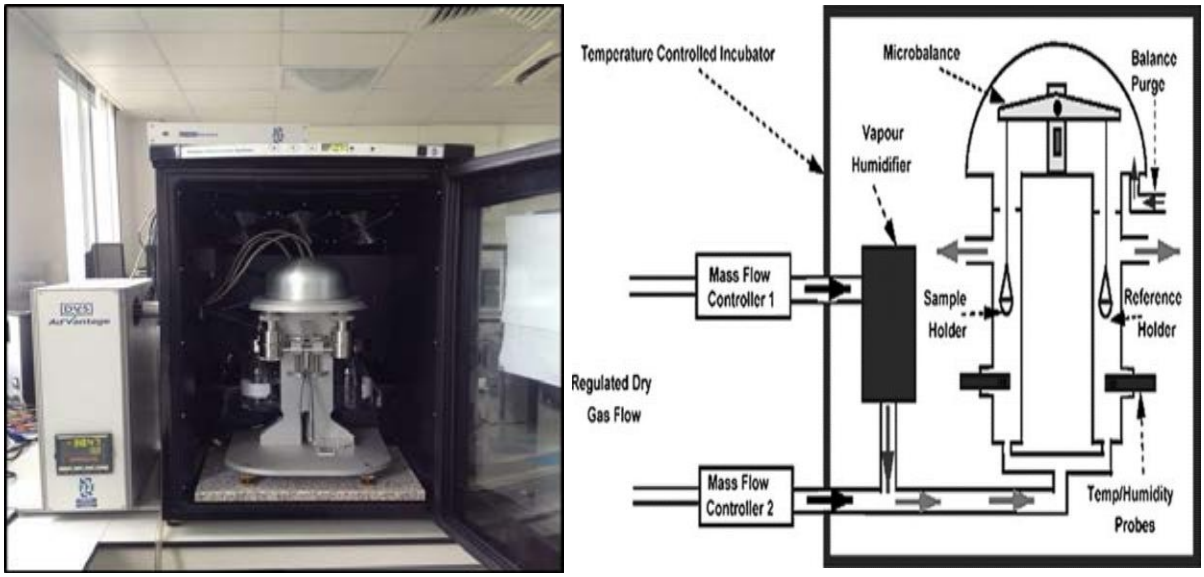

Fig. 3-11 Schematic diagram and picture of DVS analyser.

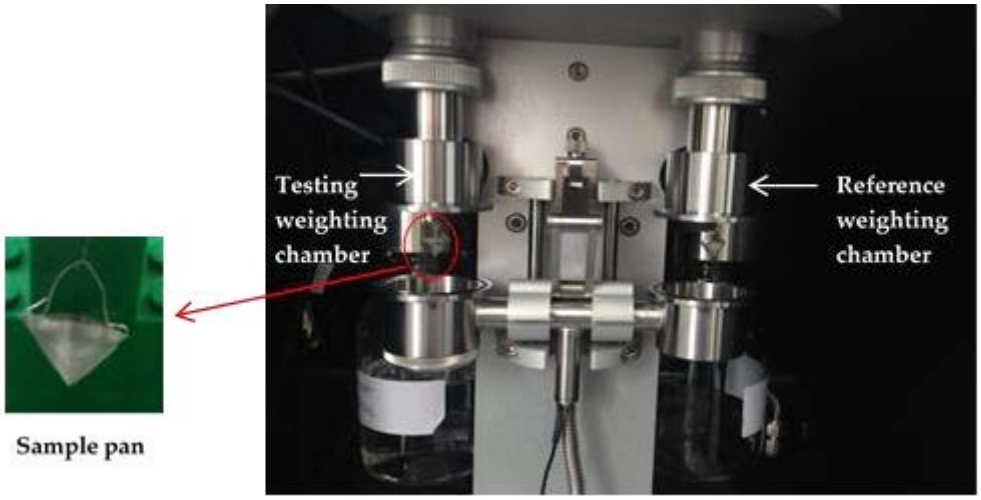

Fig. 3-12 Two weighting chambers of the DVS.

Fig. 3-13 DVS heating coil.

To develop models to simulate the experimental adsorption isotherms and kinetics generated from the DVS test facility, the adsorption isotherm and kinetics models described below were used.

3.10.1. Adsorption isotherm models

3.10.1.1. Dubinin– Astakhov isotherm

Dubinin– Astakhov isotherm (D-A) is an empirical model used to describe the adsorption of vapours onto microporous solids [18]. The model was based on the adsorption potential theory of *Polanyi*.

$$A = -RT\ln(\frac{P}{P_0}) \qquad \textbf{(3-16)}$$

$$X = x_0 exp(-(\frac{A}{E})^n) \quad \textbf{(3-17)}$$

Where X is equilibrium uptake in $g_{H_2O}\ g_{ads}^{-1}$, x_0 is maximum uptake in $g_{H_2O}\ g_{ads}^{-1}$, A is adsorption potential in J mol^{-1}, R is the ideal gas constant in J (mol K) $^{-1}$, E is adsorption characteristic parameter in J mol^{-1}, n is exponent fitting parameter and P/P_0 is the relative pressure. It was reported that the value of n can be between 2 and 6 with the value of 3 for some molecular sieve, carbons and zeolites [228].

3.10.1.2. Modified Freundlich isotherm

A modified Freundlich model was used to produce more accurate fitting of the adsorption of water vapour on silica gel [229] using the following equations:

$$X = A_{(T_{bed})}\left[\frac{P_{sat(T_{ref})}}{P_{sat(T_{bed})}}\right]^{B_{(T_{bed})}} \quad \textbf{(3-18)}$$

$$A_{(T_{bed})} = A_0 + A_1 T_{bed} + A_2 {T_{bed}}^2 + A_3 {T_{bed}}^3 \quad \textbf{(3-19)}$$

$$B_{(T_{bed})} = B_0 + B_1 T_{bed} + B_2 {T_{bed}}^2 + B_3 {T_{bed}}^3 \quad \textbf{(3-20)}$$

Where $P_{sat\ (Tbed)}$ is saturation pressure at the bed temperature, $P_{sat\ (Tref)}$ is saturation pressure at the condenser or evaporator temperature in desorption or adsorption phases, respectively and T_{bed} is the bed temperature. The model was used to fit the adsorption isotherm data of water vapour on silica gel [230, 231] with the constants values given in **Table. 3-1**

Table. 3-1 Modified Freundlich equation constants

A_0	-6.53
A_1	0.72E-1
A_2	-0.24E-3
A_3	0.25E-6
B_0	-15.58
B_1	0.16
B_2	-0.51E-3
B_3	0.53E-6

The Dubinin– Astakhov model was successfully used to fit the experimental adsorption isotherms of CPO-27(Ni). The adsorption isotherm models of other MOF materials such as aluminium fumarate, MIL-101(Cr), MIL-100(Fe) and their composites were developed in terms of the adsorption potential (A) (**Eq. 3-16**) to show the effect of temperature on the adsorption capacity based on the work of *Polanyi* [232, 233]. The proposed approach employed to fit the measured isotherms in different 'A' regions has been previously employed by Schicktanz and Núñez [234] and Tokarev, Okunev, Safonov, Kheifets and Aristov [235].

3.10.2. Adsorption kinetics model

Adsorption kinetics is the rate of adsorption determining how quickly the adsorption/desorption process is taking place as it is controlling the residence time required for the completion of the adsorption cycle. Improving the adsorption kinetics will lead to a better system performance as the refrigerant flow rate circulated in the system will increase [73]. The kinetics depends mainly on the heat and mass transfer performance of the adsorption bed and the interaction between the adsorbent and the adsorbate [193]. Enhancing the heat transfer performance of the adsorption bed results in improving the adsorption rate and hence increasing the cycle cooling performance [236-238]. The porosity of the adsorbent material was also found to affect the adsorption kinetics. As the adsorbent porosity increased, the adsorbent thermal conductivity decreased resulting in a decrease in the adsorption kinetics [74]. There are two types of mass transfer in the adsorption bed. The first type is the intra-particle mass transfer which controls the mass transfer rate of the adsorbate through the pores of the adsorbent material. This resistance affects the rates of heat and mass transfers to or from the particles [239]. The second is the inter-particle mass transfer resistance which controls the mass transfer rate of the adsorbate through the voids between the adsorbent particles. This resistance affects the rates of the heat and mass transfer of the whole bed [239].

The linear driving force (LDF) approach is usually chosen to describe the adsorption rate as it has been widely known for being simple and analytically and physically consistent [240, 241]. The model was firstly proposed by *Glueckauf* in the period between 1947-1955 [242, 243] assuming that the uptake profile within a particle is parabolic. This model assumes that the rate of adsorption rate is proportional to the concentration difference between the outer and inner adsorbate concentrations of adsorbent particle [204] and that the rate of adsorption on the surface is much faster than the rate of inner diffusion that is why the LDF model ignores the inter-particle mass transfer resistance and only accounts the intra-particle mass transfer resistance as the kinetics on the surface are not considered rate-limiting [60, 244, 245]. Linear driving force model is one of the most used kinetics models as it can be applied to a wide range of adsorbents for the previously mentioned reasons [245]. **Eq. 3-21** to **Eq. 3-24** represent the LDF model.

$$\frac{dx}{dt} = K_s a_v (x - x_0) \quad \textbf{(3-21)}$$

$$\frac{dx}{dt} = K_0 \exp\left[-\frac{E_a}{RT}\right](x - x_0) \quad \textbf{(3-22)}$$

$$K_0 = \frac{FD_{So}}{R_p^2} \quad \textbf{(3-23)}$$

$$D_s = D_{so} \exp\left[-\frac{E_a}{RT}\right] \quad \textbf{(3-24)}$$

Where F is a constant depending on the shape of the adsorbent particles and equals 15 for spherical particles. The LDF model constants are evaluated at each adsorption step and the average values are evaluated at conditions suitable for adsorption chiller operation. Arrhenius equation is then used to investigate the effect of temperature on the diffusion time constant. The constants were calculated according to previously published procedures [246-249].

As mentioned above, this approach accounts only the intra-particle mass transfer resistances and hence it is only acceptable for large-sized particles or small thicknesses adsorbent beds [250].

The adsorbent particle size is an effective parameter influencing the adsorbent bed as it directly affects the mass transfer resistances in the bed [244]. When adsorbent particle size is increased, the mass transfer rate inside the particle is decreased (intra-particle mass transfer resistance is increased) and hence the adsorption/desorption rates in the adsorbent bed are decreased. At the same time, increasing the particle size, increase the voids or channels between the granules which decrease the resistance and facilitate the vapour flow through the adsorbent bed. Opposite effects are expected for smaller sized particles and that is why for the large particles the inter-particles resistance is neglected while it is the opposite case for small particles. The particle size also can affect the heat transfer as it affects the thermal resistances between the porous materials and heat transfer surfaces. As the particle size is decreased, the contact thermal resistance is decreased and hence once again the adsorption kinetics can be indirectly affected by the particle size [239, 244, 251].

To validate the DVS measurements and ensure that the data produced is consistent with published data and the carrier gas has no effect on the adsorption kinetics, silica gel isotherm was measured at 20°C and compared to published kinetic and isotherm models [252]. **Table. 3-2** shows the LDF constants of silica gel used to produce the published kinetics model curve while **Fig. 3-14** shows the good agreement between the DVS measured data and the published kinetics model which highlight that the nitrogen (purge gas) has low effect on the adsorption rate and that the DVS test facility can successfully measure both adsorption isotherms and kinetics.

Table. 3-2 Silica gel LDF model constants [252]

Material	R_p (m)	E_a (J mol^{-1})	D_{so} (m^2 s^{-1})
Silica gel RD	0.16E-3	42,000	2.54E-4

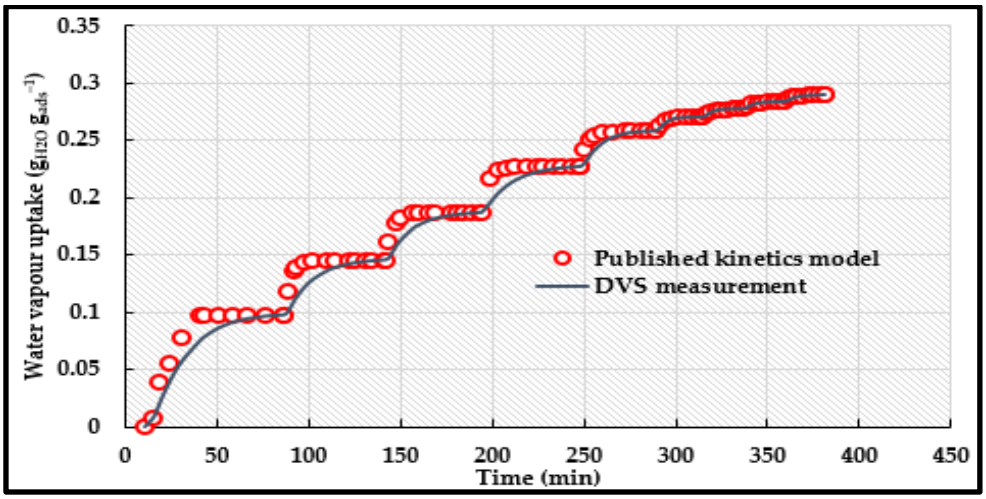

Fig. 3-14 Comparing DVS measuring data at 20°C and published kinetics model [252].

3.11. Instron Environmental Mechanical Analyser

The mechanical properties of the MOF coated samples were measured using the Instron environmental mechanical analyser (**Fig. 3-15**). Compression tests and 3-points bending tests were performed using a 2kN load. After the compression test, optical images of samples were taken using Alicona InfiniteFocus (**Fig. 3-16**) with an objective magnification of 5x.

Fig. 3-15 Instron Environmental Mechanical Analyser.

Fig. 3-16 Alicona InfiniteFocus.

3.12. Micro-hardness test

The hardness of the coating layer was measured using a Beuhler MMT-7 micro-hardness tester (**Fig. 3-17**). The samples were grinded with abrasive papers (4 stages 300, 600, 1200, 2000). A Vickers indenter with 100g load for 15 s was used.

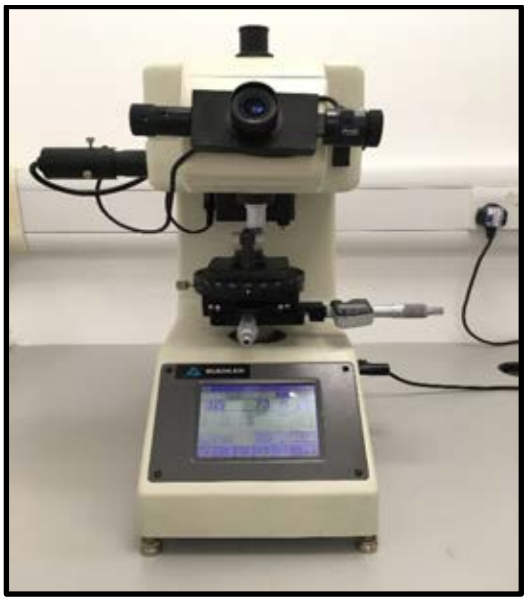

Fig. 3-17 Beuhler MMT-7 micro-hardness tester.

3.13. Total dissolved solids and conductivity of distilled water

One of the main parameter to judge the potential of adsorption desalination as a successful desalination technique is its water quality. The distilled water produced from the adsorption desalination system was analysed based on the total dissolved solids (TDS) and conductivity using a JENWAY 3540 pH and conductivity meter (**Fig. 3-18)**. The TDS and conductivity measurement of the adsorption desalination water was compared to those of filtered water and tap water to correctly judge on the quality of water produced from the adsorption system.

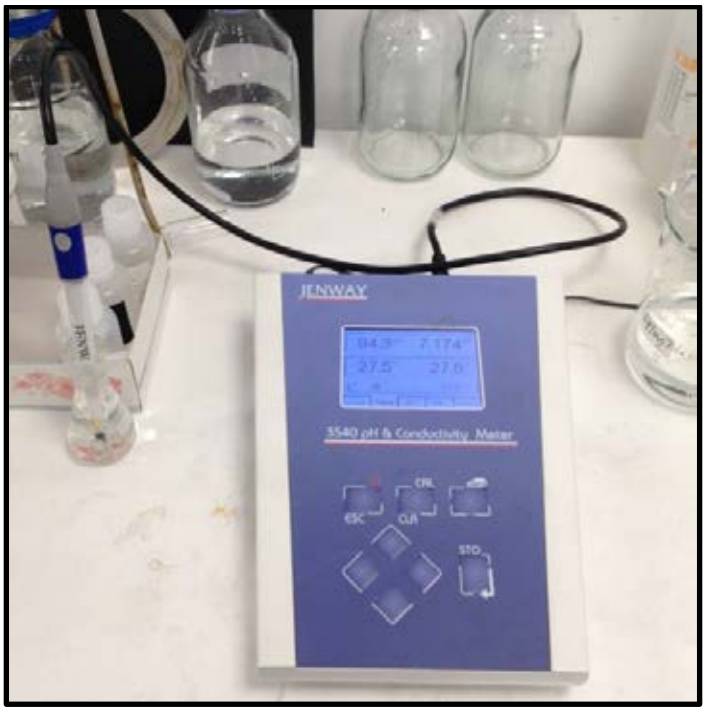

Fig. 3-18 JENWAY 3540 pH and conductivity meter.

3.14. Summary

Various techniques were used to fully characterize the various MOF materials under study. X-ray diffraction, FTIR, SEM images were used to judge the quality and crystallinity of each material, while other properties such as the thermal conductivity and water vapour adsorption properties are crucial to determine their performance in adsorption systems. Other techniques were used to test the durability and mechanical strength of the developed MOF coatings. Finally, the distilled water produced from the adsorption desalination system was analysed based on its total dissolved solids and conductivity.

CHAPTER 4
METAL-ORGANIC FRAMEWORKS PROPERTIES

4.1. Introduction

A crucial parameter that significantly affects the performance of the adsorption system is the adsorbent material used. As highlighted earlier most systems employ zeolites or silica gel as adsorbent materials which may decrease the performance due to their limited adsorption capacity. Therefore, using an advanced adsorbent with higher specific and volumetric capacity can lead to a more compact system with an improved performance. This study discusses the potential of metal-organic frameworks in various adsorption applications as an alternative to conventional adsorbents when using water as a refrigerant. This chapter investigates the synthesis and characterization of two MOF materials that have superior water adsorption properties, namely MIL-101(Cr) and MIL-100(Fe). Also, two commercial MOFs, namely, CPO-27(Ni) and aluminium fumarate, were characterized and compared to the performance of the other two MOFs.

(This chapter is based on the previously published papers: E. Elsayed, A.-D. Raya, S. Mahmoud, A. Elsayed, and P. A. Anderson, "Aluminium fumarate and CPO-27 (Ni) MOFs: characterization and thermodynamic analysis for adsorption heat pump applications," Applied Thermal Engineering, vol. 99, pp. 802-812, 2016. E. Elsayed, A.-D. Raya, S. Mahmoud, P. A. Anderson, A. Elsayed, and P. G. Youssef, "CPO-27 (Ni), aluminium fumarate and MIL-101 (Cr) MOF materials for adsorption water desalination," Desalination, vol. 406, pp. 25-36, 2017.

E. Elsayed, H. Wang, P. A. Anderson, R. Al-Dadah, S. Mahmoud, H. Navarro, Y. Ding, and J. Bowen, "Development of MIL-101 (Cr)/GrO composites for adsorption heat pump applications," Microporous and Mesoporous Materials, vol. 244, pp. 180-191, 2017).

4.2. MIL-101(Cr)

As previously mentioned, MIL-101(Cr) is a highly stable MOF material that was chosen to be investigated due to its exceptional properties and high-water vapour capacity that can reach 1.47 g_{H_2O} g_{ads}^{-1}. Various synthesis approaches have been used to synthesize metal-organic frameworks in their pure forms. Such methods include hydrothermal, microwave, electrochemical and mechano-chemical [253]. The hydrothermal synthesis approach is considered as the main synthesis method of MOFs as more than 70% of the MOFs are produced through this approach [253] as highlighted earlier in the literature review chapter. The reaction takes place in autoclaves under autogenous pressure.

4.2.1. Synthesis

One of the most commonly used MIL-101(Cr) synthesis procedures is the one reported by *Férey et al.* [160] where hydrofluoric acid (which has a severe toxicological effect) was used as a mineralizer. That is why in this work MIL-101(Cr) was synthesized using the hydrothermal method reported by *Yang et al.* [254] without the use of hydrofluoric acid and where 1 mmol terephthalic acid (1,4-Benzene dicarboxylic acid (H_2BDC)) was added to 5 ml of solution of tetramethyl ammonium hydroxide (TMAOH). The reactants were stirred at room temperature for 10 min, then 1 mmol of chromium nitrate nonahydrates ($Cr(NO_3)_3.9H_2O$) was added to the mixture and stirred for another 20 min [225]. The effect of reaction temperature and time was investigated based on the reported information [160, 254]. As the water vapour adsorption characteristics are the most crucial parameters to judge the potential of any adsorbent in adsorption applications, the time and temperature of the reaction were optimized according to their water vapour capacities and their crystallinity through using XRD patterns.

Fig. 4-1 shows the XRD patterns of the synthesized MIL-101(Cr) at two temperatures (which were chosen based on the literature) and different reaction times to optimize the reaction conditions. It can be observed that all the samples showed the correct peak positions which highlight that the MIL-101(Cr) crystals can be formed at a reaction time as short as 4 hr or as long as 24 hr. It can be also noticed that as the temperature increased from 180°C to 220°C, a new phase was formed which suggests that the quality of the material formed might be reduced, a similar behaviour was observed by *Zhao et al.* [255]. **Fig. 4-2** shows the water adsorption isotherm of the synthesized samples where it can be observed that high capacity MIL-101(Cr) crystals were able to form at a reaction time as short as 4 hr and that the reaction time had almost no effect on the water vapour adsorption capacity. This suggests that the nucleation process is faster compared to the crystal growth step meaning that the synthesis is a crystal growth-controlled process. It can also be noticed that as the temperature increased, the water adsorption capacity decreased. This is consistent with the observation from the XRD patterns that an unknown phase is formed decreasing the purity of MIL-101(Cr).

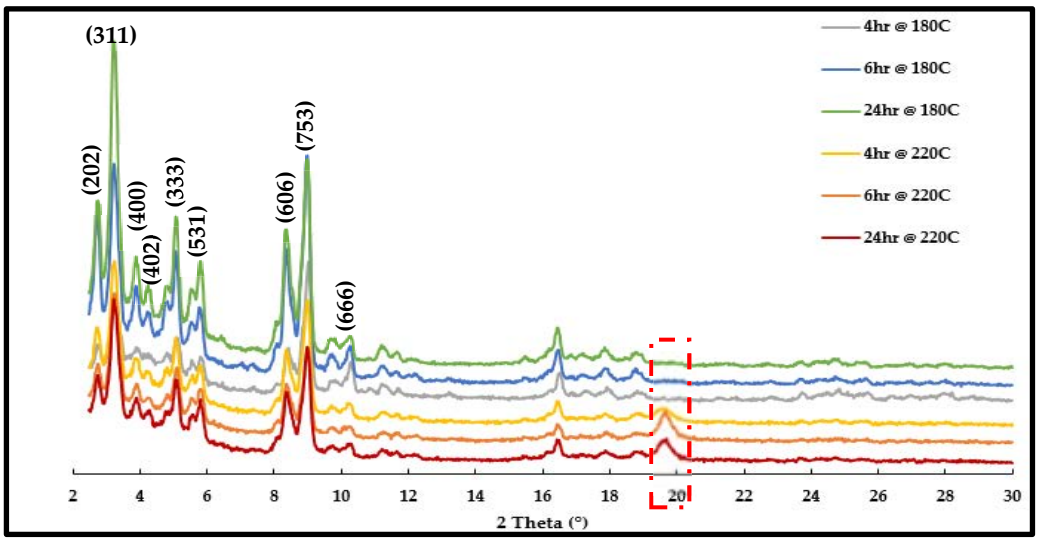

Fig. 4-1 Powder XRD patterns of synthesized MIL-101(Cr) at different reaction times and temperatures.
(Peaks corresponding to reflection planes are indexed [256] and additional peaks of the unknown phase are highlighted)

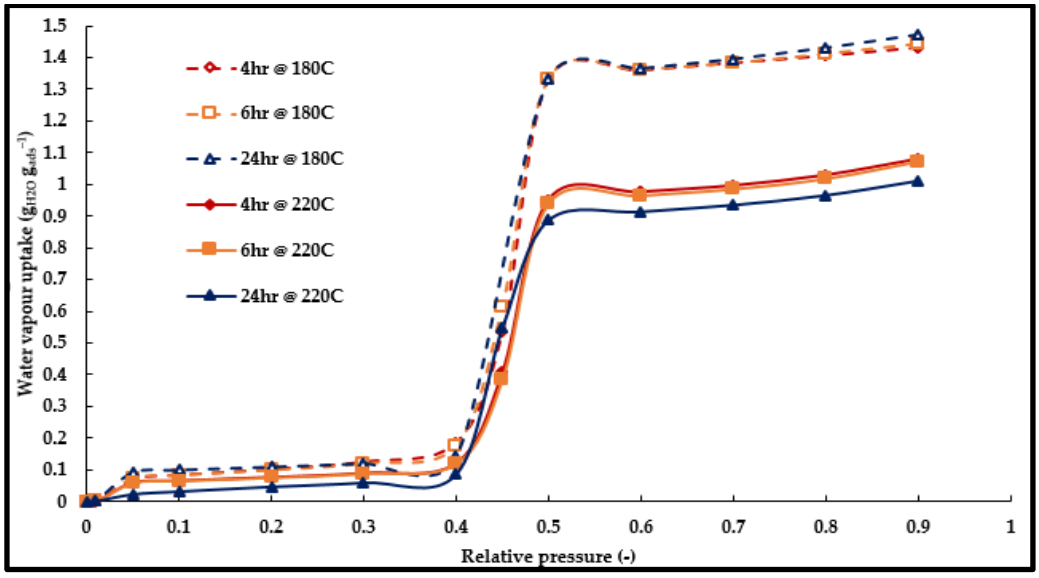

Fig. 4-2 Water vapour adsorption capacity of synthesized MIL-101(Cr) at different reaction times and temperatures.

The conclusion of these experiments is that a reaction temperature of 180°C is preferred while an optimum time of 24 hr was used to obtain the highest yield. This means that in the optimum procedures, the reactants mixture was placed in a 23 ml Teflon-lined autoclave and heated for 24 hr at 180°C. After cooling down, MIL-101(Cr) was obtained as a fine green powder with a notable amount of terephthalic acid (H_2BDC). To eliminate the crystalized H_2BDC, the suspension was filtered using a glass filter. The fine powders of MIL-101(Cr) and water pass through the glass filter while the crystallized acid remains on the glass filter. The suspension was then centrifuged to separate the MIL-101(Cr) particles from the liquid. The MIL-101(Cr) solids were suspended in absolute ethanol, stirred at 60°C for 1 hr and then centrifuged again. The process was repeated at least twice. After that, the green MIL-101(Cr) particles were suspended in water, stirred at 60°C for 1 hr. Finally, the MIL-101(Cr) powder was separated from the solution using a small pore filter paper and the product was dried in air at room temperature [225]. The reaction was scaled up using a 45 ml Teflon lined autoclave.

4.2.2. Characterization

4.2.2.1. Powder XRD

Fig. 4-3 shows the powder XRD pattern of the synthesized MIL-101(Cr) and the reactants; terephthalic acid and chromium nitrate nonahydrate. The diffraction peak positions of MIL-101(Cr) were found to be in agreement with previously reported data [160, 254] which indicates that the material was successfully synthesized. Also, the absence of the reactant peaks indicates that the washing procedures used have effectively removed any traces of both reactants.

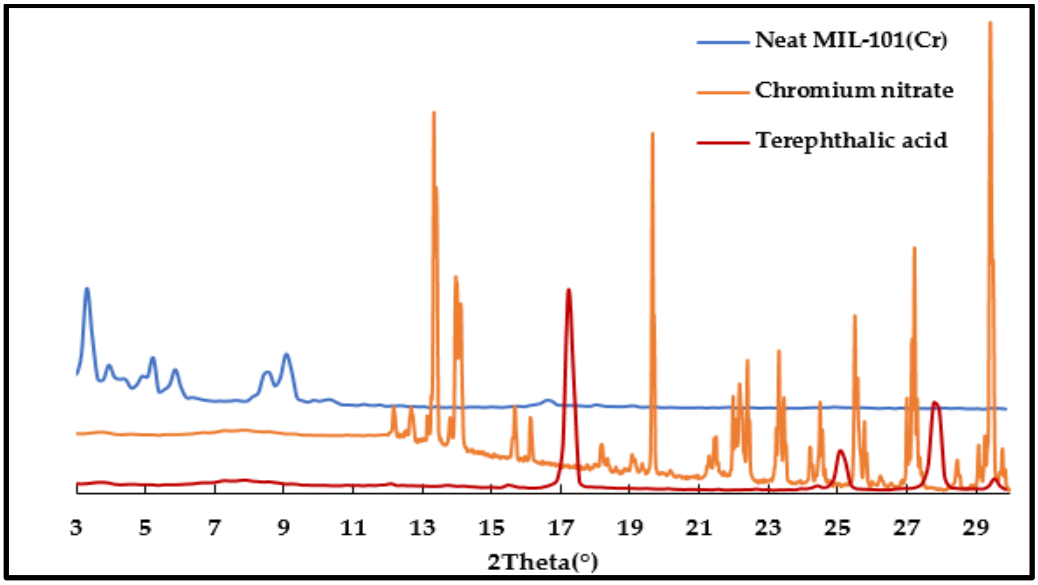

Fig. 4-3 Powder XRD patterns of synthesized MIL-101(Cr), chromium nitrate and terephthalic acid.

4.2.2.2. Nitrogen adsorption

To achieve a high adsorption capacity, it is always preferable for the adsorbent material to exhibit high accessible surface area to accommodate the adsorbate molecules. MIL-101(Cr) has been reported to have a high BET surface area of 3197-4100 $m^2 g^{-1}$ and a pore volume of 1.73-1.9 $cm^3 g^{-1}$ [160, 254]. The surface area and pore characteristics of the synthesized MIL-101(Cr) were evaluated using the nitrogen adsorption technique at 77 K. **Fig. 4-4** shows the nitrogen adsorption isotherm of MIL-101(Cr). It was found that the surface area of the

synthesized MIL-101(Cr) batches ranged between 3355-3460 $m^2 g^{-1}$ and its pore volume was 1.73-1.75 $cm^3 g^{-1}$. The measured values are in good agreement with the previously reported values using the same synthesis procedures which were 3197 $m^2 g^{-1}$ and 1.73 $cm^3 g^{-1}$, respectively [254]. **Fig. 4-5** shows the pore size distribution calculated using the density functional theory (DFT) method which are in good agreement with the previously reported measurement [257].

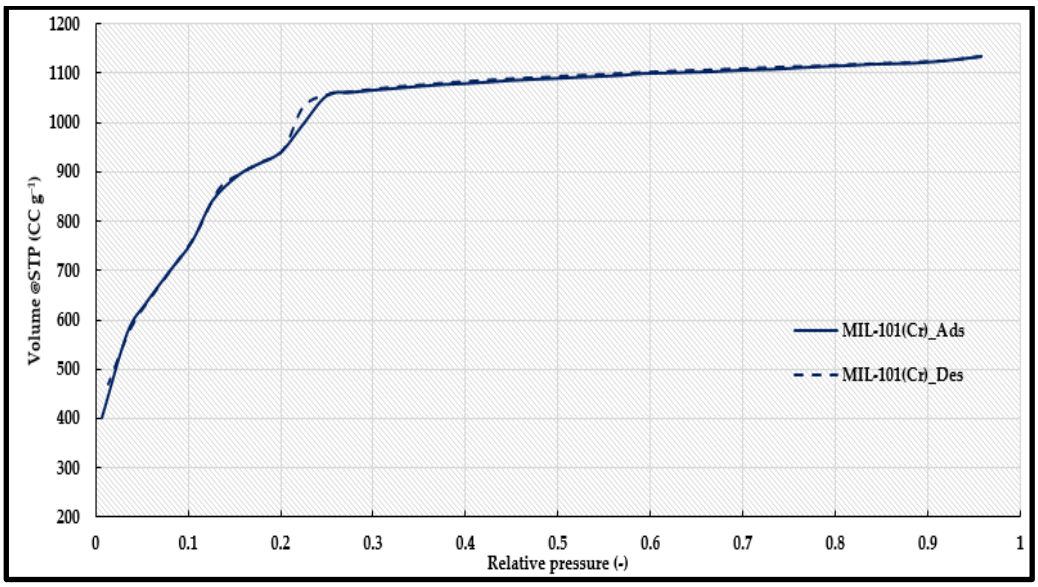

Fig. 4-4 Nitrogen adsorption isotherms of MIL-101(Cr) at 77 K [225].

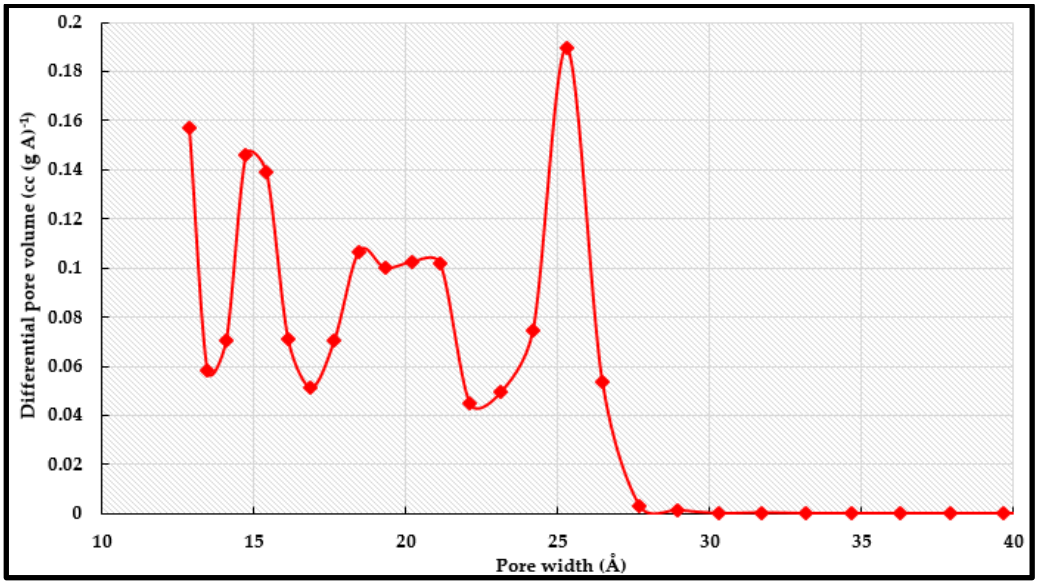

Fig. 4-5 Pore size distribution of MIL-101(Cr) [225].

4.2.2.3. Thermogravimetric analysis (TGA)

The thermal stability of MIL-101(Cr) was assessed using the thermal gravimetric technique where the change in mass was recorded as the temperature increased in a flow of nitrogen. **Fig. 4-6** shows the TGA traces of the MIL-101(Cr) where it can be noticed that there were three stages of weight loss.

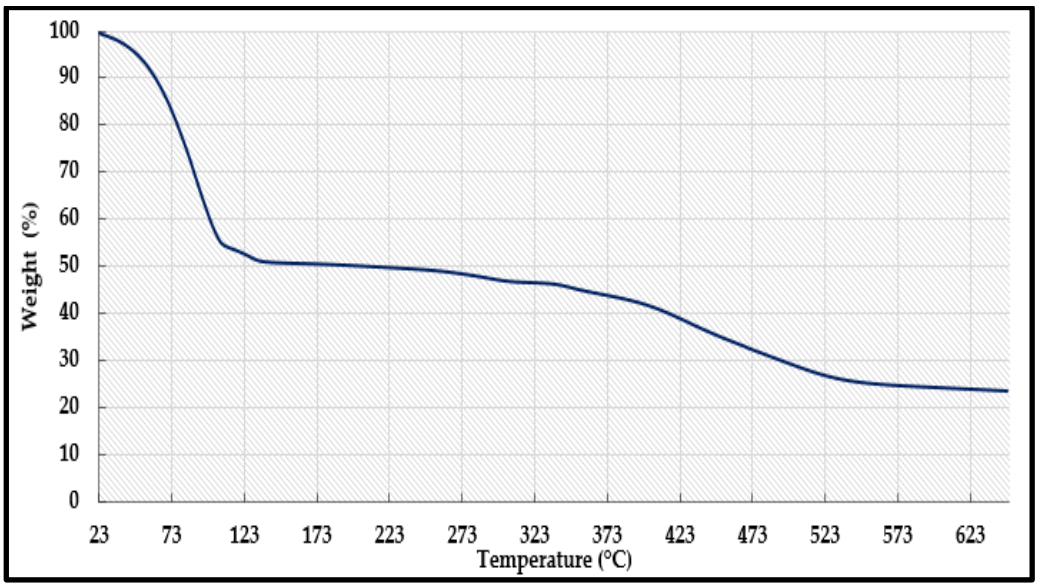

Fig. 4-6 Thermogravimetric analysis of MIL-101(Cr) [225].

In the first stage, MIL-101(Cr) lost almost 50% of its weight at 137°C due to the removal of the free water trapped in its pores. As the temperature increases (137–337°C), the second stage starts where the co-ordinated water molecules are removed hence a relatively low weight loss is expected. The decomposition of the structure and the combustion of the terephthalic acid takes place in the final stage [225].

4.2.2.4. Scanning Electron Microscopy (SEM)

The morphology of MIL-101(Cr) was investigated using SEM. **Fig. 4-7** shows that the synthesized MIL-101(Cr) had well defined octahedral crystals [225].

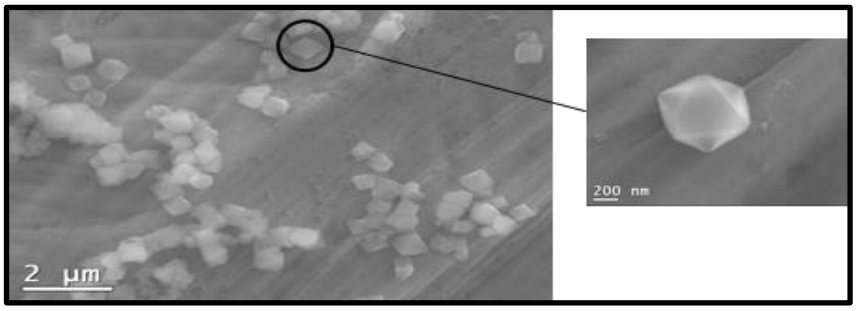

Fig. 4-7 SEM images of MIL-101(Cr) crystals [225].

4.2.2.5. Fourier Transform Infrared Spectroscopy (FTIR)

The presence of functional groups in MIL-101(Cr) was examined using the FTIR technique. **Fig. 4-8** shows that the presence of the characteristic vibrational bands of the carboxylate group (O-C-O)- at 1400 and 1620 cm^{-1} which confirms the presence of the dicarboxylate ligand within the MIL-101(Cr) framework while the absorbance band between 3250 and 3500 cm^{-1} confirms the presence of water. The band at 1500 cm^{-1} is for the vibration of (C=C) while the bands between 600-1600 cm^{-1} confirms the presence of the benzene ring (C-H) [160, 258].

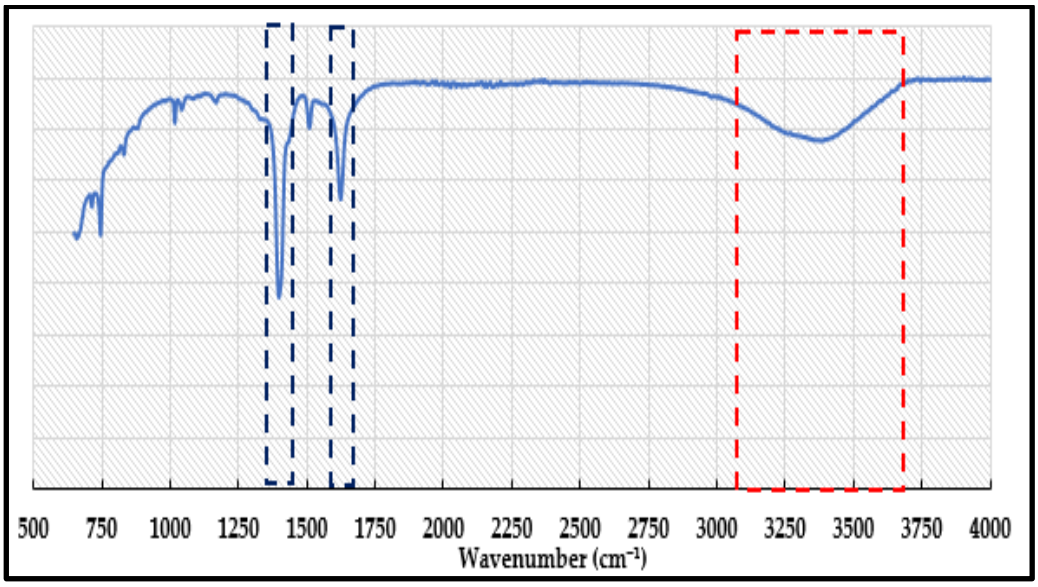

Fig. 4-8 FTIR spectra of MIL-101(Cr).

4.2.2.6. True density

The true density of MIL-101(Cr) was measured using helium pycnometer. Also, the material porosity was calculated using **Eq. 3-10**. **Table. 4-1** shows the values of the true, bulk densities and porosity of MIL-101(Cr).

Table. 4-1 True, bulk densities and porosity of MIL-101(Cr).

Material	True density ($kg\ m^{-3}$)	Bulk density ($kg\ m^{-3}$)	Porosity (–)
MIL-101(Cr)	1733	295.9	0.82

4.2.2.7. Thermal conductivity

As there are no previous studies showing the thermal conductivity of MIL-101(Cr), it was evaluated through measuring thermal diffusivity, specific heat capacity and density of the formed pellets as described in chapter 3. The measured specific heat capacity was 1.1 kJ (kg K) $^{-1}$. **Fig. 4-9** shows the thermal conductivity of MIL-101(Cr) pellet as a function of temperature. It can be noticed that the MIL-101(Cr) pellet thermal conductivity increased linearly from 0.05 W (m K)$^{-1}$ at 303 K (30°C) to 0.103 W (m K)$^{-1}$ at 473 K (200°C) [225].

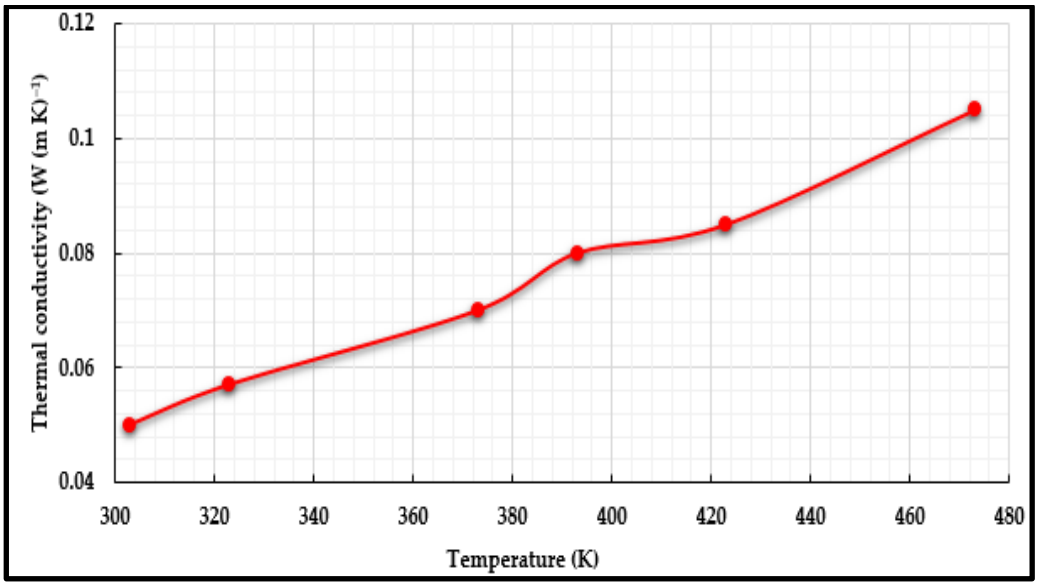

Fig. 4-9 Measured thermal conductivity of MIL-101(Cr) [225].

Table. 4-2 shows an empirical equation to estimate the effective thermal conductivity of MIL-101(Cr) determined using **Eq. 3-13** to **Eq. 3-15**.

Table. 4-2 Effective thermal conductivity of MIL-101(Cr).

Material	Effective thermal conductivity ($W\ (m\ K)^{-1}$)
MIL-101(Cr)	$-2.155E-2+1.7E-4T_{bed}$

4.2.2.8. Water adsorption characteristics

4.2.2.8.1. Adsorption isotherms

One of the most important features of MIL-101(Cr) that make it a good candidate as an adsorbent in various adsorption applications is its high-water vapour capacity. In this study the adsorption isotherms were measured using a dynamic vapour sorption (DVS) test facility. The change in mass with relative pressure and time were then fitted with equations to predict the adsorption behaviour at different temperatures, pressures and time. **Fig. 4-10** shows the water adsorption isotherms of MIL-101(Cr) which exhibited type IV isotherm. At relative pressure ≤0.4, the presence of unsaturated metal centres (UMCs) is responsible for the water vapour adsorption as they attract and offer extra binding sites for water molecules. Nevertheless, the low water uptake is due to the hydrophobic effect of the organic linker [225].

At relative pressure 0.4-0.5, the water uptake showed a steep increase as a result of the capillary condensation phenomenon [18] which also causes the hysteresis loop between the adsorption and desorption processes [24, 259]. At a relative pressure >0.5, MIL-101(Cr) exhibited a stable uptake as the pores were almost filled. It can be concluded that due to the shape of the adsorption isotherm of MIL-101(Cr), the material is more suitable for adsorption applications working at high relative pressures, which may include heat storage, desalination and moderate temperature cooling [225].

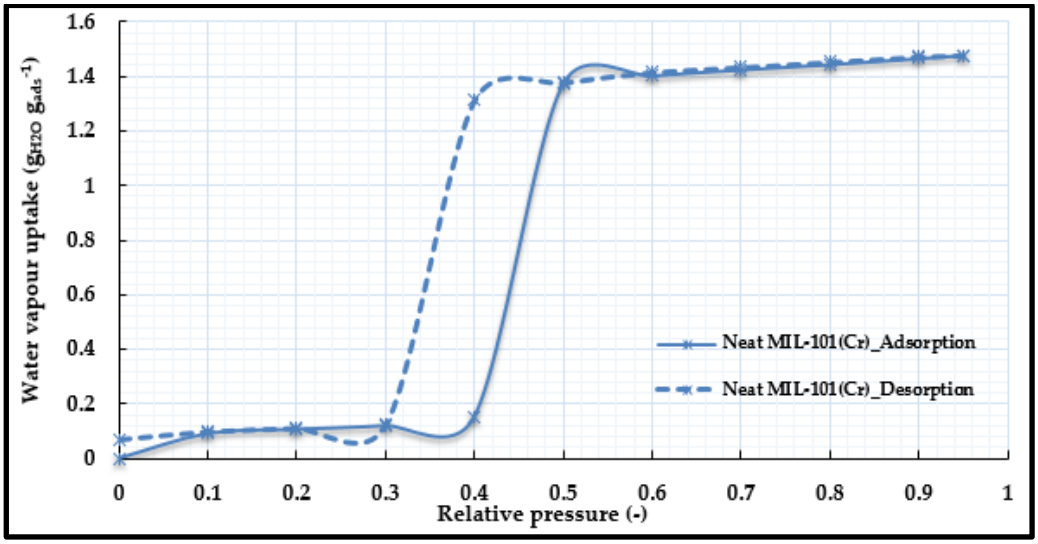

Fig. 4-10 Water adsorption isotherms of neat MIL-101(Cr) at 25°C [225].

The performance stability of MIL-101(Cr) was investigated through subjecting the material to ten successive adsorption/desorption cycles (**Fig. 4-11**); showing great stability in terms of the water vapour adsorption capacity. Also, the adsorption capacity of water vapour was measured at three different temperatures (15, 25 and 35°C). The data measured were used to develop a series of empirical equations in terms of the adsorption potential A (**Eq. 4-1** to **Eq. 4-5**) to predict the water uptake at a wide range of operating conditions [260].

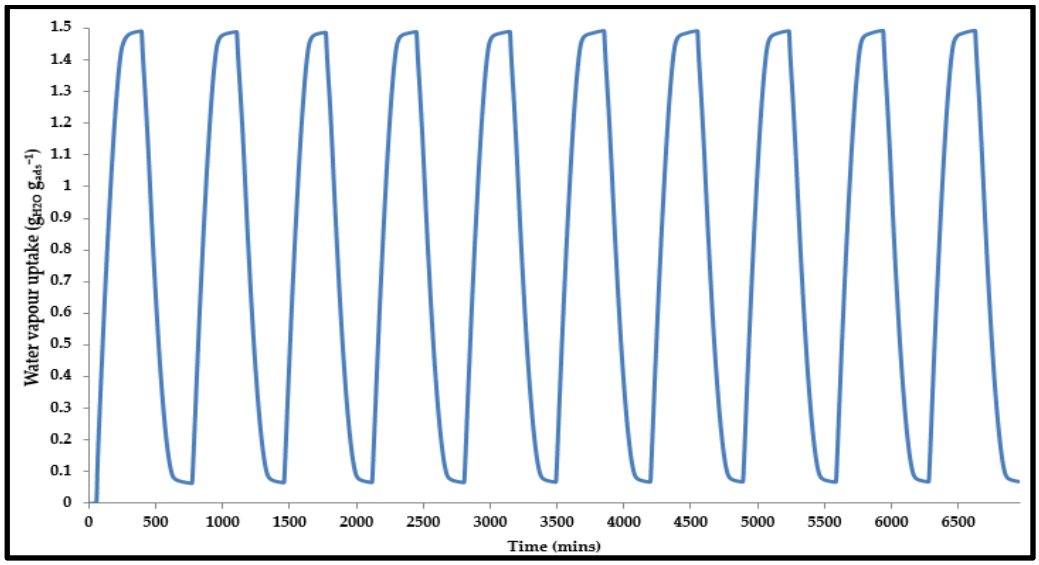

Fig. 4-11 Cyclic performance of MIL-101(Cr) for 10 adsorption/desorption cycles at a relative pressure range of 0.9 [14].

$$A = -RT\ln\left(\frac{P}{P_0}\right) \quad \textbf{(4-1)}$$

$$X = 0.424\exp(-2.825E-4A) \qquad A \geq 5300 \quad \textbf{(4-2)}$$

$$X = 0.4636 - 2.4E-4A + 5.4E-08A^2 - 4.06E-12A^3 \qquad 2100 \leq A < 5300 \quad \textbf{(4-3)}$$

$$X = -11802.6 + 29.5A - 2.9E-2A^2 + 1.4E-5A^3 - 3.6E-9A^4 + 3.5E-13A^5 \qquad 1600 < A < 2100 \quad \textbf{(4-4)}$$

$$X = 1.51 - 2.66E-4A + 0.363E-6A^2 - 1.77E-10A^3 \qquad A \leq 1600 \quad \textbf{(4-5)}$$

The good agreement between the developed equations and the experimental data is shown in **Fig. 4-12**.

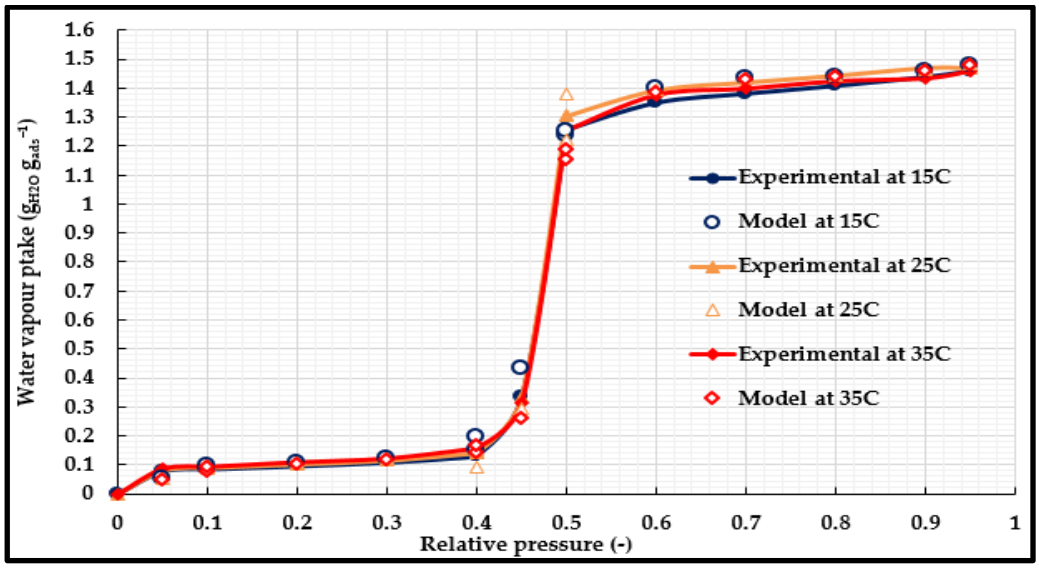

Fig. 4-12 Proposed isotherm model fitting of water vapour adsorption on MIL-101(Cr).

4.2.2.8.2. Adsorption Kinetics

The rate of water adsorption was predicted through applying the linear driving force (LDF) model (**Eq. 3-21** to **Eq. 3-24)**. **Table. 4-3** gives the values of parameters E_a and k_0 for MIL-101(Cr), while **Fig. 4-13** highlights the validity of the LDF model in fitting the experimental data.

Table. 4-3 Values of LDF equation parameters

Material	Relative pressure range	E_a (J mol^{-1})	k_0 (s^{-1})
MIL-101(Cr)	>0.4&≤0.5	30,872	1.5E3
	≤0.4&>0.5	31,148	42.4

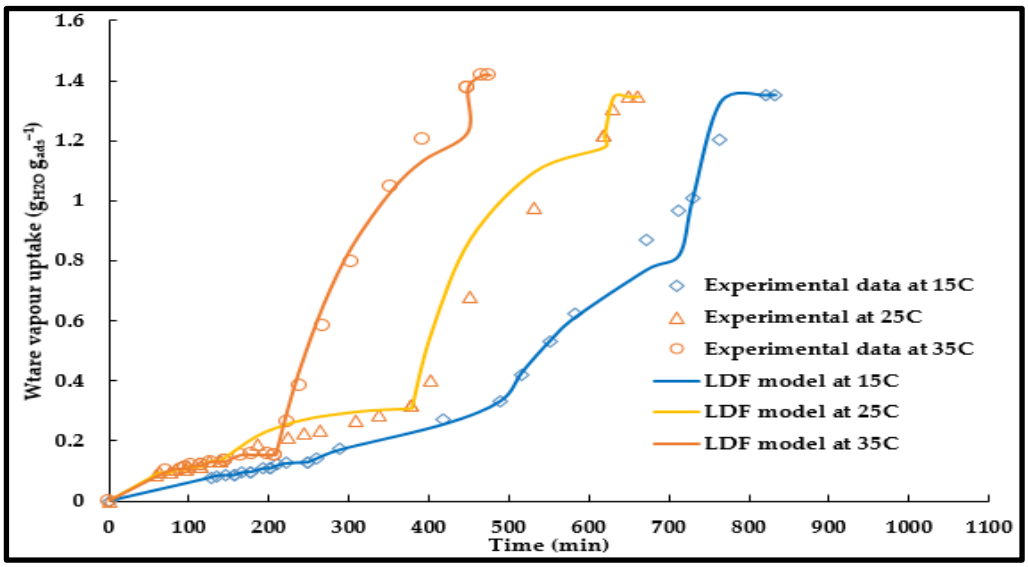

Fig. 4-13 LDF model fitting of water adsorption on MIL-101(Cr) at 15°C, 25°C and 35°C.

4.3. CPO-27(Ni)

CPO-27(Ni) known as MOF-74(Ni) is a MOF material that was synthesized and commercially produced by Johnson Matthey, UK.

4.3.1. Characterization

4.3.1.1. Powder XRD

Fig. 4-14 shows the powder XRD patterns of CPO-27(Ni). The diffraction peak positions were in agreement with the previously reported data [261], while the sharp peaks of the CPO-27(Ni) pattern highlight the high crystallinity of the material [221].

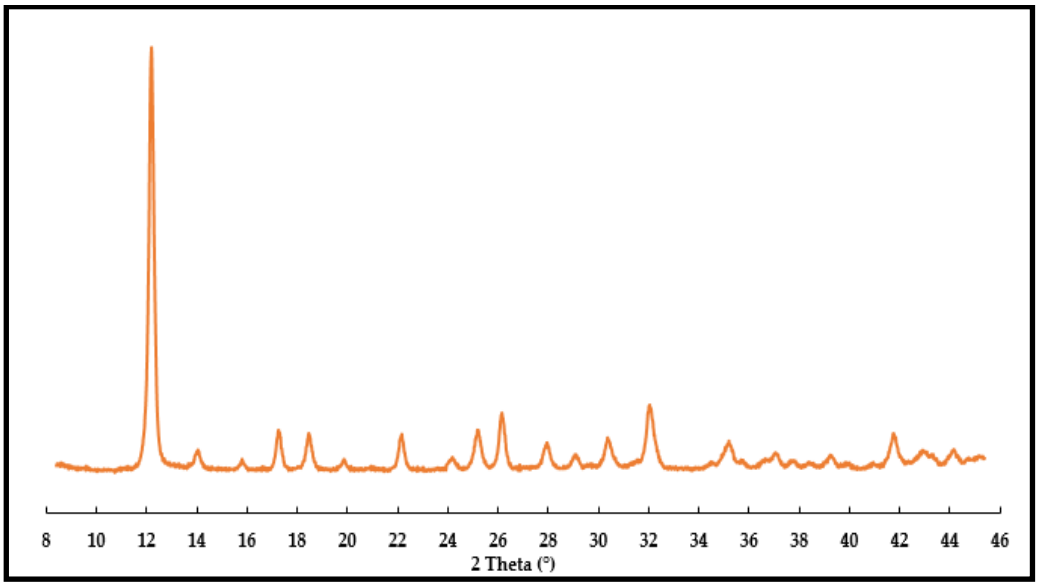

Fig. 4-14 Powder XRD patterns of CPO-27(Ni) [221].

4.3.1.2. Nitrogen adsorption

The CPO-27(Ni) was characterized by nitrogen adsorption at 77 K (**Fig. 4-15**), a BET surface area of 469.7 $m^2 g^{-1}$ was measured [221]. The total pore volume was found to be 0.258 $cm^3 g^{-1}$.

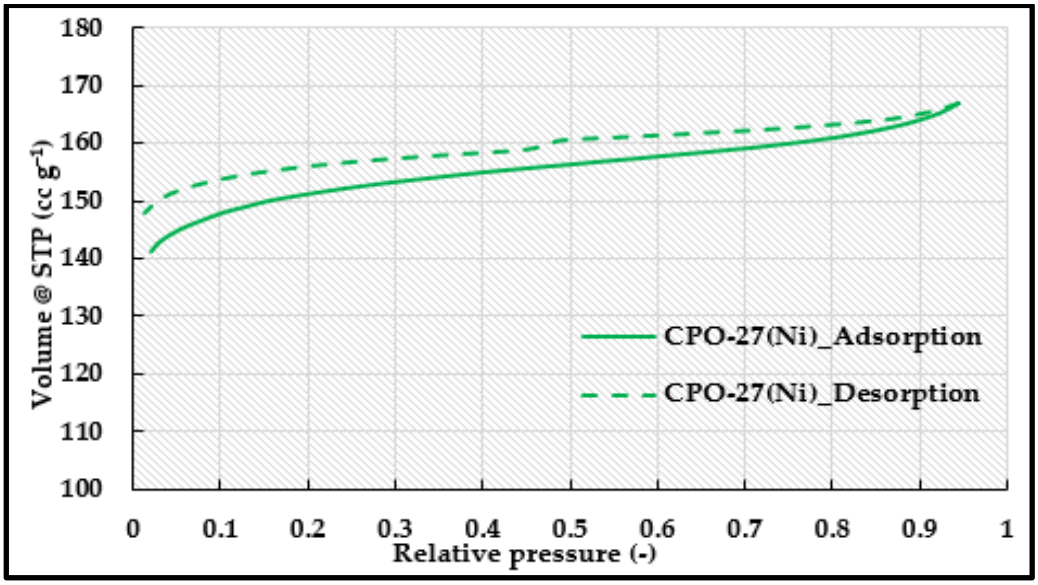

Fig. 4-15 Nitrogen adsorption isotherm of CPO-27(Ni) at 77 K [221].

4.3.1.3. Thermogravimetric analysis (TGA)

The thermal stability of CPO-27(Ni) was assessed using the thermal gravimetric technique where the change in mass was recorded as the temperature increased under a flow of nitrogen. **Fig. 4-16** shows the TGA traces of the MOF material. It can be noticed that there are three stages of weight loss. In the first stage, CPO-27(Ni) lost almost 30% of its weight at 173°C due to losing the free water trapped in its pores. In the temperature range of 173°C –350°C, the second stage took place due to the loss of the coordinated water molecules. As the temperature increased, the weight loss in the final stage took place due to the destruction of the structure and the decomposition of the dihydroxyterephthalic acid.

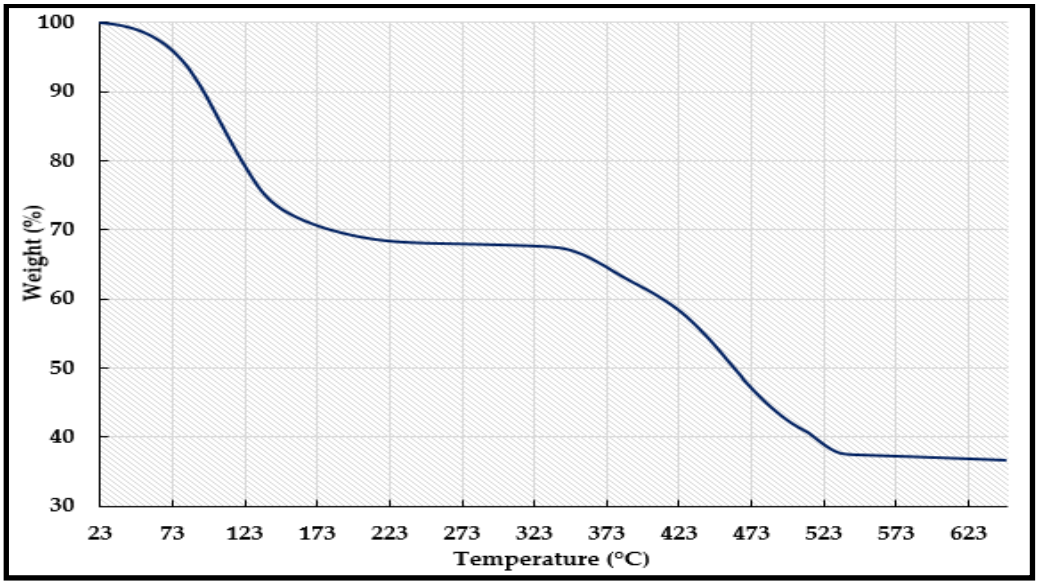

Fig. 4-16 Thermogravimetric analysis of CPO-27(Ni).

4.3.1.4. Scanning Electron Microscopy (SEM)

The morphology of the CPO-27(Ni) crystals was investigated using SEM. **Fig. 4-17** shows SEM images of the MOF material indicating that it possesses a needle and flake-like crystals. This is in agreement with the previously published data [178].

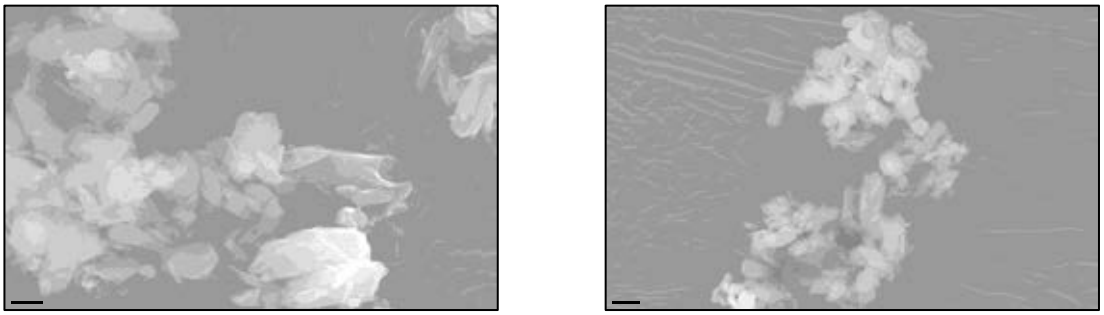

Fig. 4-17 SEM images of CPO-27(Ni).

4.3.1.5. Fourier Transform Infrared Spectroscopy (FTIR)

The presence of functional groups in CPO-27(Ni) was examined using the FTIR technique (**Fig. 4-18**). The presence of the characteristic vibrational bands at 1400 and 1550 cm^{-1} confirms the presence of the carboxylate (O-C-O) and (C=C) groups within the framework. The vibration band at 816 cm^{-1} is attributed to the bending C–H group. Also, the band at 1244 cm^{-1} can be attributed to the presence of (C–O) from the deprotonated species derived

from the hydroxyl group while the band between 3250 and 3500 cm^{-1} confirms the prescence of water [262].

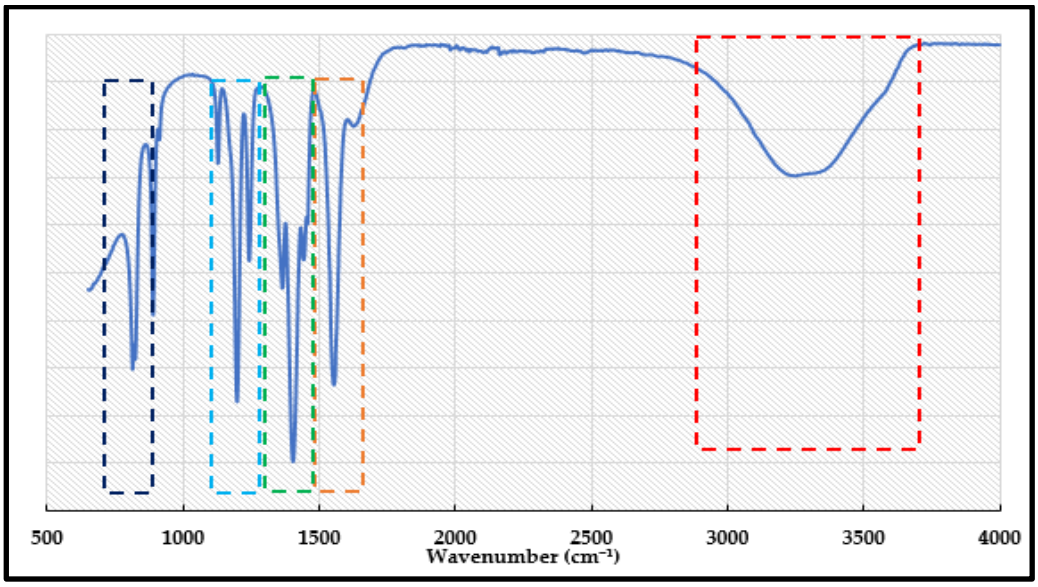

Fig. 4-18 FTIR spectrum of CPO-27(Ni).

4.3.1.6. True density

The true density of CPO-27(Ni) was measured using helium pycnometer. **Table. 4-4** shows the values of the true, bulk densities and porosity of this MOF material

Table. 4-4 True, bulk densities and porosity of CPO-27(Ni)

Material	True density ($kg\ m^{-3}$)	Bulk density ($kg\ m^{-3}$)	Porosity (–)
CPO-27(Ni)	1882.9	440.06	0.76

4.3.1.7. Thermal conductivity

The thermal conductivity of CPO-27(Ni) was evaluated through measuring thermal diffusivity, specific heat capacity and density of the formed pellets. The variation of thermal conductivity of the CPO-27(Ni) pellet with temperature is shown in **Fig. 4-19** while an emepirical equation of the effective thermal conductivity is shown in **Table. 4-5**. It can be noticed that the material has a higher thermal conductivity compared to MIL-101(Cr) due to the lower free volume. The thermal conductivity of CPO-27(Ni) was 0.086 W $(m\ K)^{-1}$ at 303

K (30°C) and increased to 0.156 W (m K)$^{-1}$ at 423 K (150°C) compared to 0.05 W (m K)$^{-1}$ and 0.086 W (m K)$^{-1}$ for MIL-101(Cr). The measured specific heat capacity was 0.97 kJ (kg K) $^{-1}$.

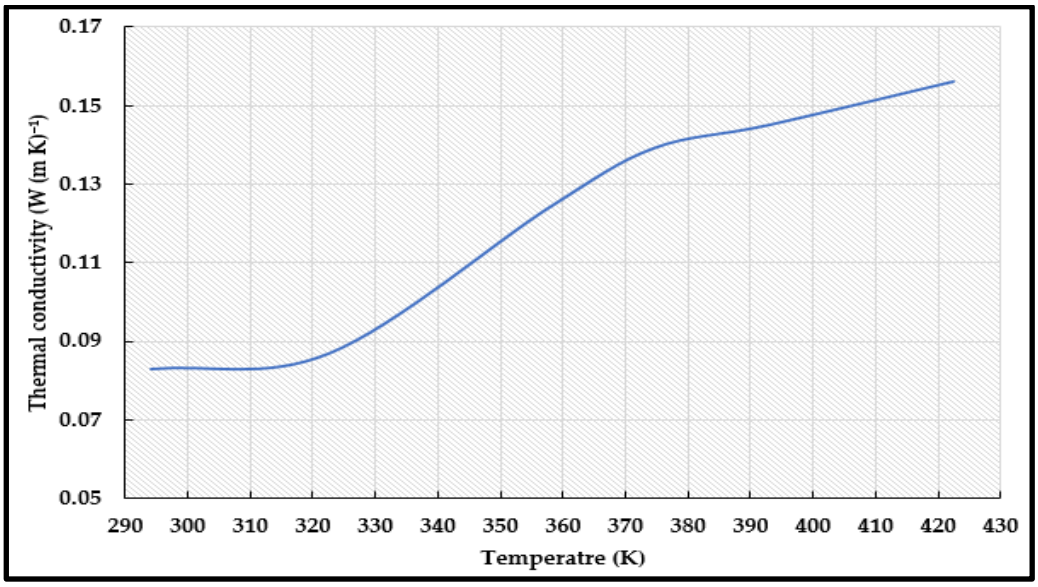

Fig. 4-19 Thermal conductivity of CPO-27(Ni).

Table. 4-5 Effective thermal conductivity of CPO-27(Ni)

Material	Effective thermal conductivity (W (m K)$^{-1}$)
CPO-27(Ni)	$4.6E-4T_{bed}-0.077$

4.3.1.8. Water adsorption characteristics

4.3.1.8.1. Adsorption isotherms

Fig. 4-20 shows the measured water adsorption/desorption isotherm of CPO-27(Ni) at 25°C. It is evident that the CPO-27(Ni) exhibited a type I adsorption isotherm where it reached 81% of its maximum capacity at a very low relative pressure with a final uptake of 0.47 g_{H_2O} g_{ads}^{-1} at a relative pressure of 0.9. At the low relative pressure, the water vapour adsorption is due to the presence of unsaturated metal centres (UMCs) (**Fig. 4-21)**. These UMCs attracts and offers extra binding sites for water molecules. Another factor contributing to high capacity of CPO-27(Ni) is the hydrophilic nature of the organic ligand due to the presence of the hydroxyl group. Nevertheless, the strong interaction between the UMCs and the adsorbed water

molecules causes the material to require very high regeneration (desorption) temperatures as shown in the hysteresis between the adsorption and desorption phases [14, 221].

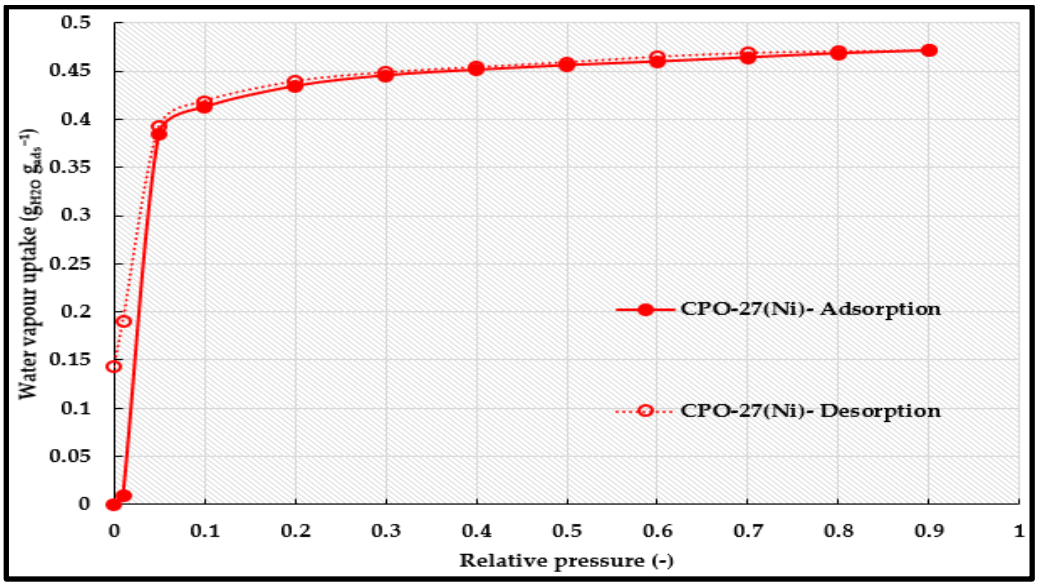

Fig. 4-20 Water adsorption isotherm of CPO-27(Ni) at 25°C [14, 221].

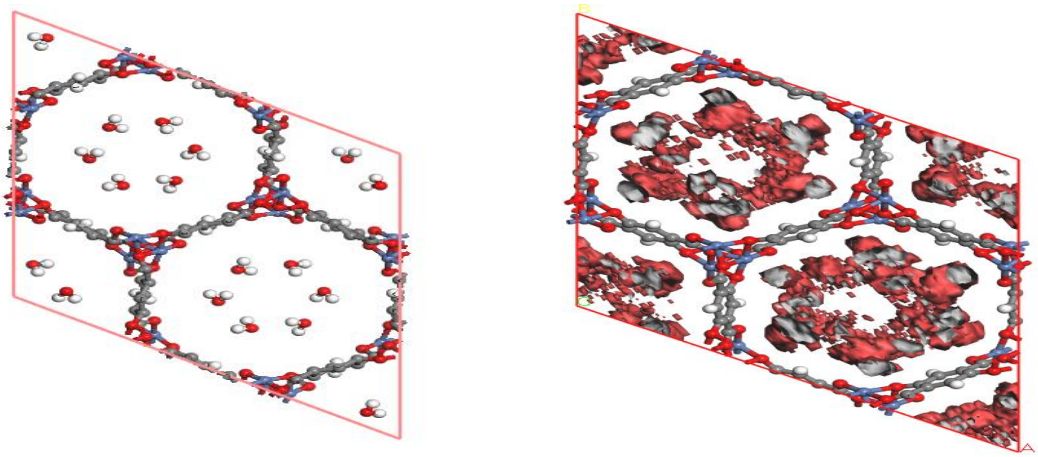

Fig. 4-21 water adsorption sites and the water adsorption field at 25°C [14].
(Figure was developed using Materials Studio software)

This concludes that CPO-27(Ni) is suitable for adsorption applications working at very low relative pressure with high desorption temperatures where low evaporation temperature is used such as adsorption cooling [221] or even freeze desalination using seawater as a refrigerant [263].

To further investigate the performance of CPO-27(Ni) at different temperatures, the water adsorption isotherms of the material were measured at 35°C and 55°C (**Fig. 4-22**). The material showed a temperature independent performance [221].

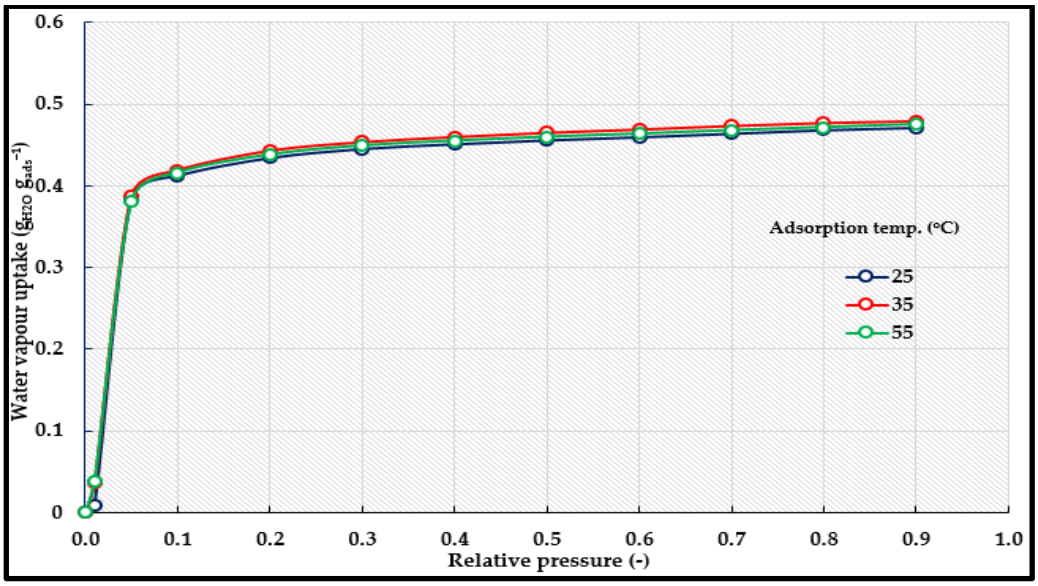

Fig. 4-22 Water adsorption isotherm of CPO-27(Ni) at different adsorption temperatures [14, 221].

The measured data were fitted using the Dubinin-Astakhov equation (**Eq. 3-16** and **Eq. 3-17**) [14, 221]. The values of the Dubinin-Astakhov equation parameters are shown in **Table. 4-6**. **Fig. 4-23** shows good agreement between the experimental data and the proposed model.

Table. 4-6 Values of Dubinin-Astakhov equation parameters [14, 221]

x_0 (g_{H2O} g_{ads}^{-1})	E (J mol^{-1})	n (-)
0.462	10,014	4

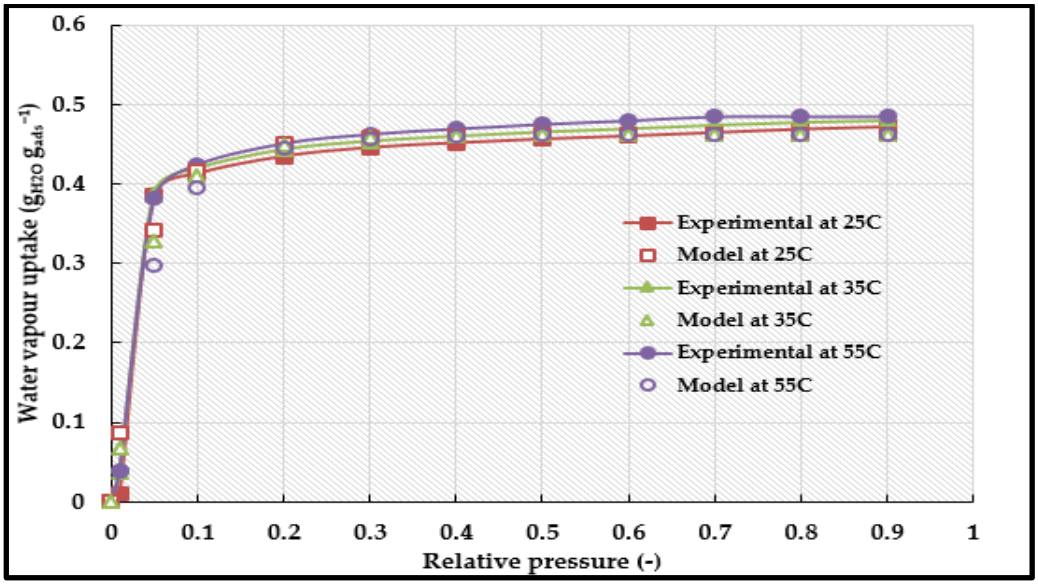

Fig. 4-23 Proposed isotherm model fitting of water adsorption on CPO-27(Ni) [221].

The performance stability of CPO-27(Ni) was confirmed through subjecting the material to ten successive adsorption/desorption cycles (**Fig. 4-24**); the material showed good performance stability [221].

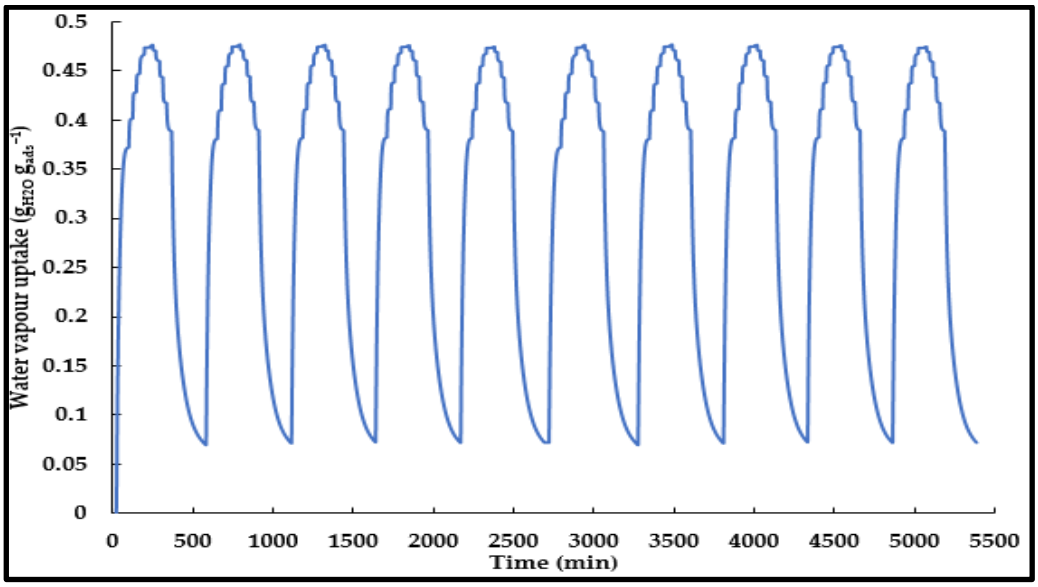

Fig. 4-24 Cyclic performance of CPO-27(Ni) for 10 full adsorption/desorption cycles [221].

4.3.1.8.2. Adsorption Kinetics

The rate of water adsorption was predicted through using the LDF model (**Eq. 3-21** to **Eq. 3-24**). **Table. 4-7** gives the values of parameters E_a and k_0 fitting CPO-27(Ni) experimental data. **Fig. 4-25** highlights the validity of the LDF model in fitting the experimental data of the material under investigation [14, 221].

Table. 4-7 Values of LDF equation parameters

Adsorbent	E_a (J mol^{-1})	K_0 (s^{-1})
CPO-27(Ni)	25,125	5.1

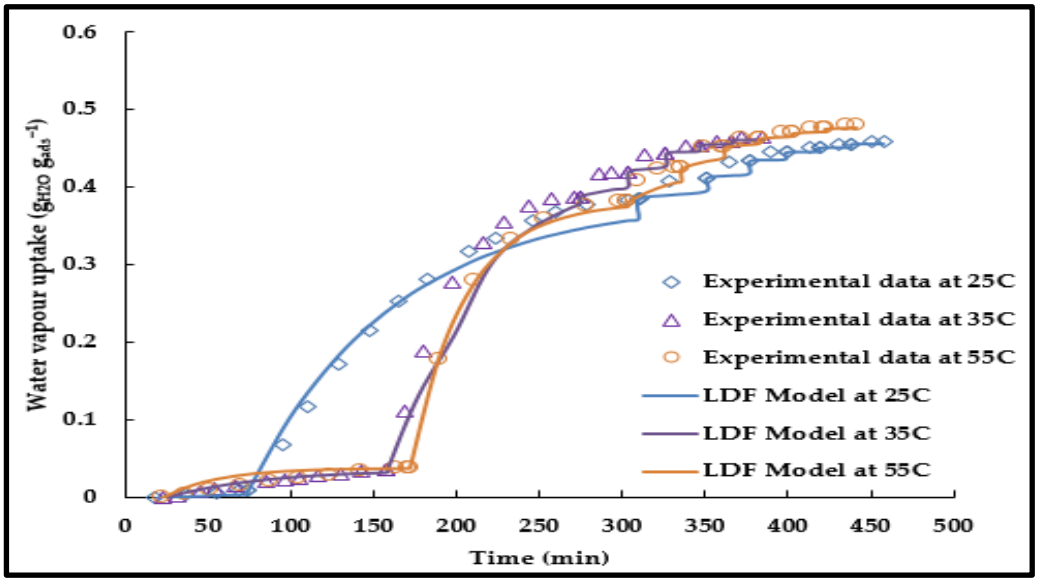

Fig. 4-25 LDF model fitting of water adsorption on CPO-27(Ni) at 25°C, 35°C and 55°C.

4.4. MIL-100(Fe)

4.4.1. Synthesis

4.4.1.1. Hydrothermal synthesis

MIL-100(Fe) was synthesized using a hydrothermal method reported by *Yoon et al.* [264] with the modification of not using hydrofluoric (HF) acid. Typically, the material was produced using the following reactants: trimesic acid with metallic iron, nitric acid, and H_2O. The molar composition of the reaction mixture is 1.0 Fe^0: 0.67 1,3,5-BTC: 0.6 HNO_3: 277 H_2O (1, 3, 5-BTC = 1,3,5-benzenetricarboxylic acid or trimesic acid). The reactant mixture was loaded into a Teflon autoclave, which was heated up to reaction temperature and kept at 160^{o}C for 8 hr. The light orange solid product was recovered by centrifugation, and the separated solids were further purified by a two-step process using equal volumes of water and ethanol. The purification was performed at 80^{o}C for 1 hr each time. After centrifugation for the last time, the solids were finally dried overnight in air. Due to the difficulty in scaling up the autoclave hydrothermal synthesis, another synthesis route was developed.

4.4.1.2. Development of low-temperature synthesis optimization

The hydrothermal synthesis approach is only feasible in pressure vessels under high temperature and autogenous pressure, where the yield is limited by the volume of the autoclave. Therefore, the low-temperature synthesis concept was adopted from the work of *Shi et al.* [265] with modifications and initially with the same molar ratio employed in the hydrothermal synthesis. The optimum reaction time and reactants concentrations were chosen based on the MOF water vapour capacity. **Fig. 4-26** shows the effect of the reaction time on the water vapour adsorption. It can be noticed that as the time increased from 16 hr to 48 hr, the water vapour capacity increased insignificantly. When the time was further increased to 72 hr, the capacity significantly decreased. This may be attributed to the prolonged reaction time caused partial destruction of the framework [120]. Based on the water vapour capacity, a reaction time of 16

hr was chosen as the optimum reaction time. The molar ratios of trimesic acid and nitric acid were also investigated. **Fig. 4-27** shows the effect the trimesic acid concentration on the water adsorption characteristics. It can be noticed that as the molar ratio of Fe^0: trimesic acid increased above or decreased below 1:0.67, the water vapour adsorption capacity would decrease. This is a direct consequence of the stoichiometric ratio of reactants where excess trimesic acid would lead to the unreacted acid to block the accessible pores and hence reduce the water vapour uptake, while a lower quantity of acid would lead to incomplete reaction and hence the excess of other reactants would block the pores. Hence, the molar ratio of Fe^0: trimesic acid of 1:0.67 was chosen as an optimum ratio.

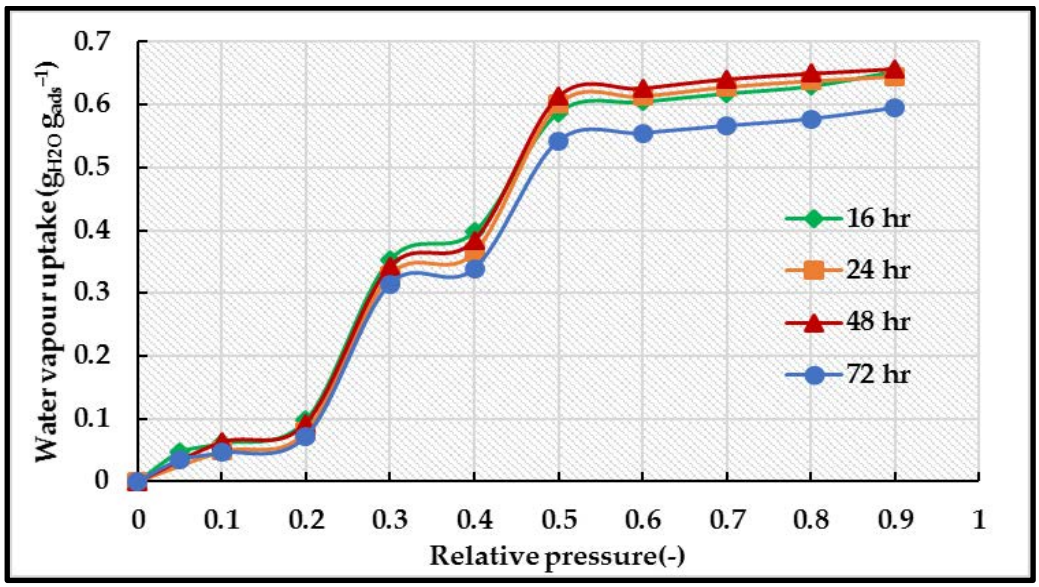

Fig. 4-26 Effect of reaction time on water adsorption capacity of MIL-100(Fe) at 25°C.

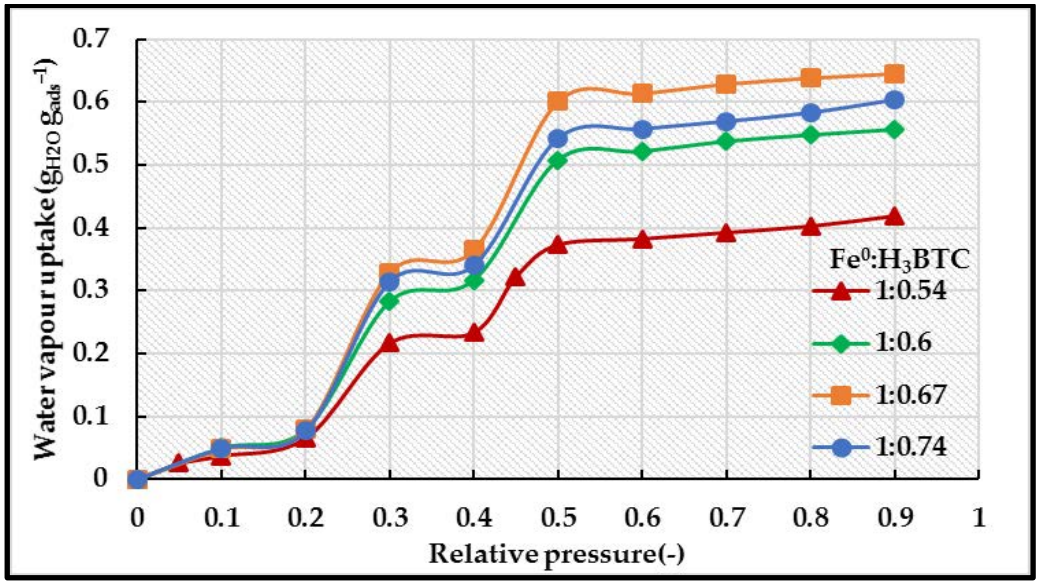

Fig. 4-27 Effect of trimesic acid molar ratio on water adsorption capacity of MIL-100(Fe) at 25°C.

Fig. 4-28 shows the effect of the nitric acid concentration on the water adsorption characteristics. It can be noticed that as the molar ratio of Fe^0: nitric acid decreased below 1:0.6, the water vapour capacity decreased. This is attributed to the ratio of reactants where lower nitric acid concentration could lead to incomplete oxidation of the metallic iron to Fe^{3+} and hence unreacted acid and metal may block the accessible pores and reduce the water vapour uptake. Higher concentrations of nitric acid had no effect and hence a molar ratio of Fe^0: nitric acid of 1:0.6 was chosen as an optimum ratio.

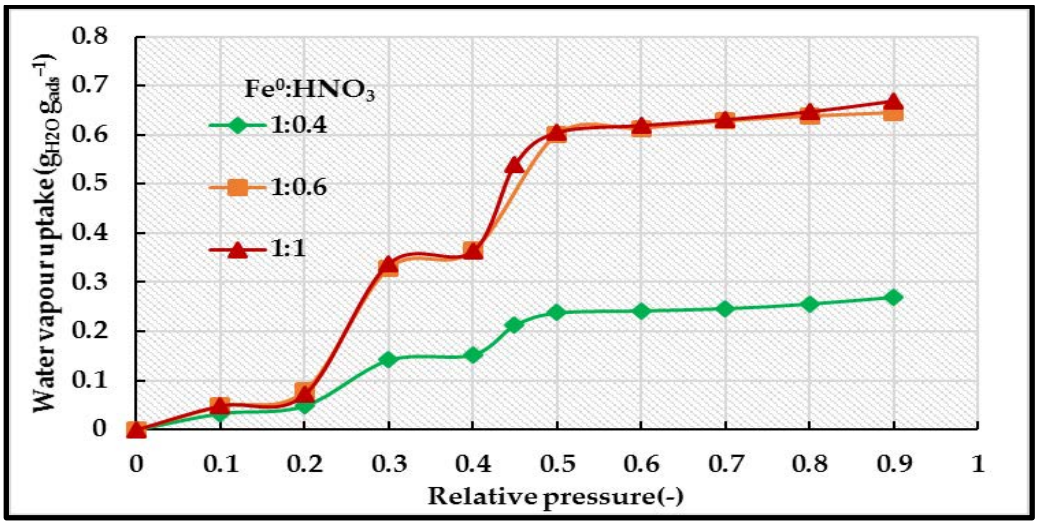

Fig. 4-28 Effect of nitric acid molar ratio on water adsorption capacity of MIL-100(Fe) at 25°C.

As a conclusion from the previously shown experiments, the material was produced using the following reactants; trimesic acid with metallic iron, nitric acid, and H_2O. The composition of reaction mixture was 1.0 Fe^0: 0.67 1,3,5-BTC (1, 3, 5-BTC = 1,3,5-benzenetricarboxylic acid or trimesic acid): 0.6 HNO_3: 277 H_2O. The reactant mixture was loaded in a 100ml round-bottomed flask, and the flask was heated up to the reaction temperature and kept at 90-95^oC for 16 hr. The light orange solid product was recovered by centrifugation, and the separated solids were further purified by a two-step process using an equal volume of water and ethanol. The purification was performed at 80^oC for 1 hr each time. After the last centrifugation for the last time, the solids were finally dried overnight in air.

The reaction was scaled up using a 1 L round-bottomed flask, where increasing the volume of the reactants by 10 times produced 25 g of MIL-100(Fe) per batch.

4.4.2. Characterization

4.4.2.1. Powder XRD

Fig. 4-29 shows the powder XRD pattern of the synthesized MIL-100(Fe) using both autoclave and low-temperature (LT) synthesis, and its reactants: trimesic acid and iron powder. The diffraction peak positions of the synthesized MOF were found to be in agreement with the previously reported data [266] which indicates that the material was successfully synthesized by the two techniques. Also, the absence of the trimesic acid peaks indicates the complete removal of the acid traces through the washing procedures.

As both synthesis methods produced MIL-100(Fe) and with the potential of scaling up the low temperature synthesis method, MIL-100(Fe) produced from this technique will be further investigated.

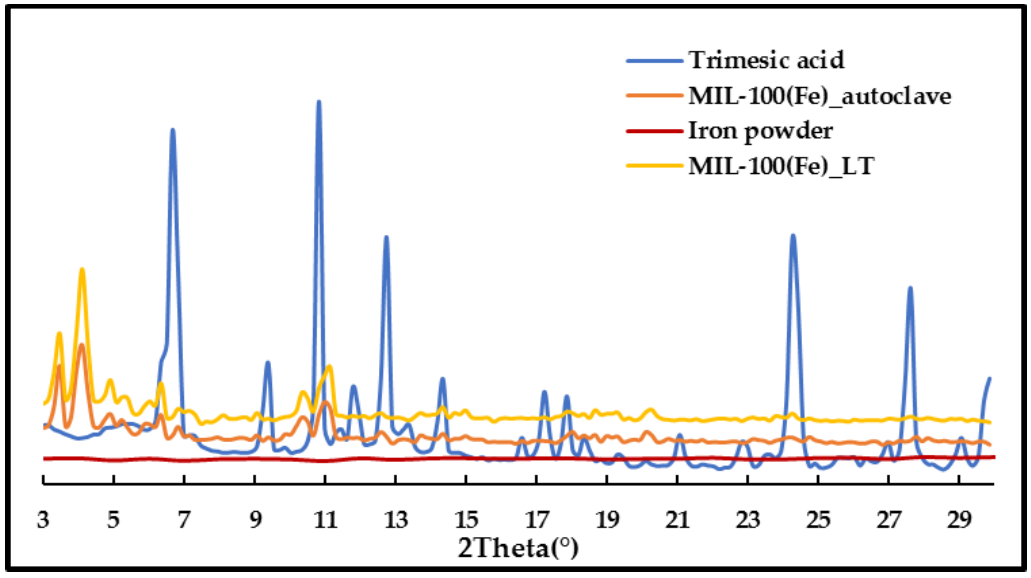

Fig. 4-29 Powder XRD patterns of synthesized MIL-100(Fe) (low temperature and autoclave), iron powder and trimesic acid.

4.4.2.2. Nitrogen adsorption

The surface areas and pore volumes of MIL-100(Fe) was measured using nitrogen adsorption technique at 77 K. **Fig. 4-30** shows the adsorption isotherm of MIL-100(Fe) where the measured BET surface area was 1481.6 m^2g^{-1}, while the pore volume was 0.83 cm^3g^{-1}. The pore size distribution of MIL-100(Fe) is shown in **Fig. 4-31**.

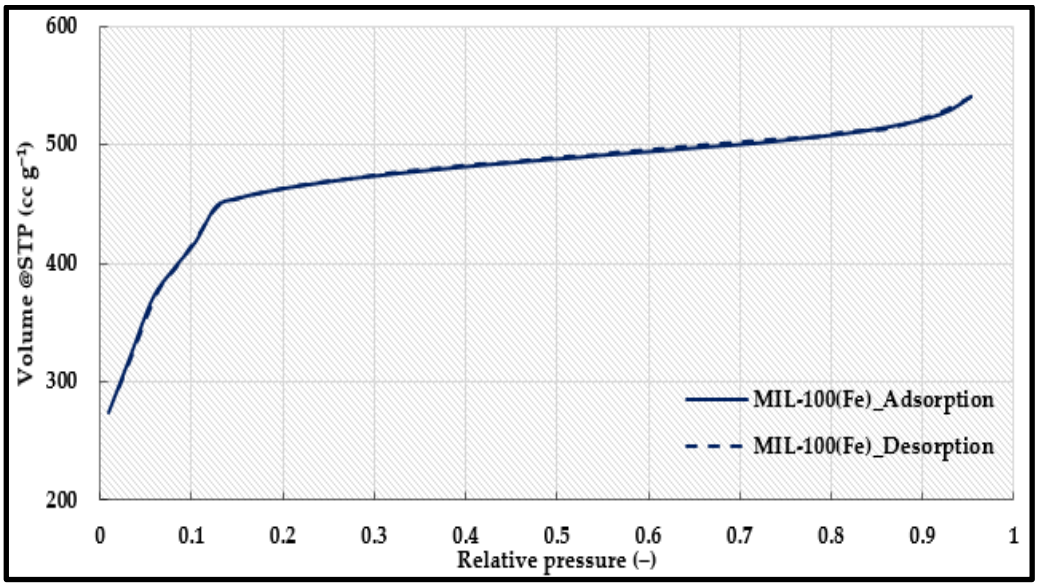

Fig. 4-30 Nitrogen adsorption isotherms of MIL-100(Fe) at 77 K.

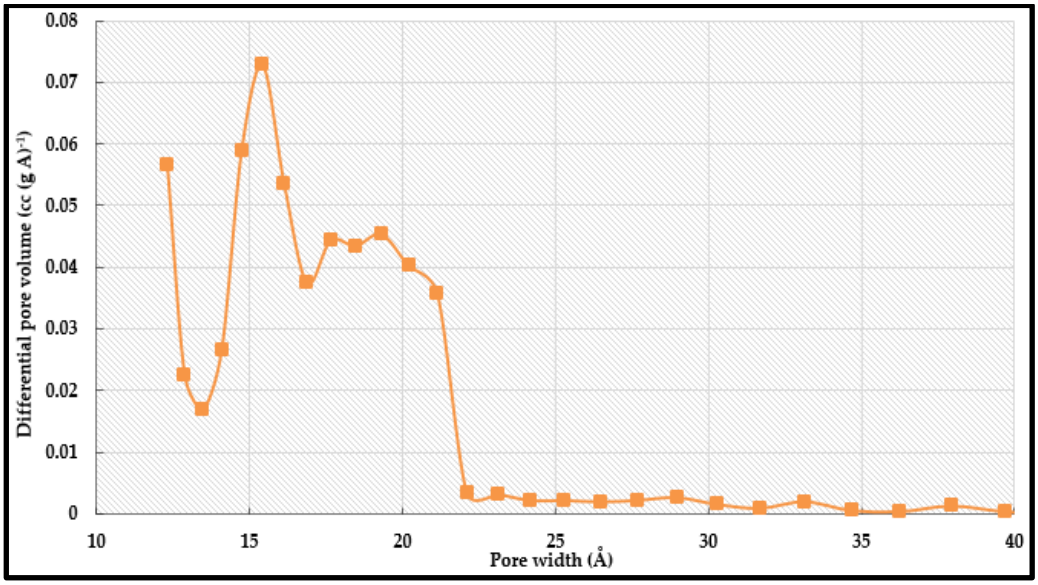

Fig. 4-31 Pore size distribution of MIL-100(Fe).

4.4.2.3. Thermogravimetric analysis (TGA)

The thermal stability of MIL-100(Fe) was assessed using the thermal gravimetric technique where the change in mass was recorded at various temperatures under a flow of nitrogen. **Fig. 4-32** shows the TGA traces of MIL-100(Fe) where the material lost 20% of its initial weight at 73°C due to the removal of the free water trapped in the pores. At the temperature range of 73°C – 400°C, the weight loss was due to the loss of co-ordinated water molecules. As the temperature increased, the final stage took place where the weight loss was due to the decomposition of the trimesic acid and the destruction of the structure.

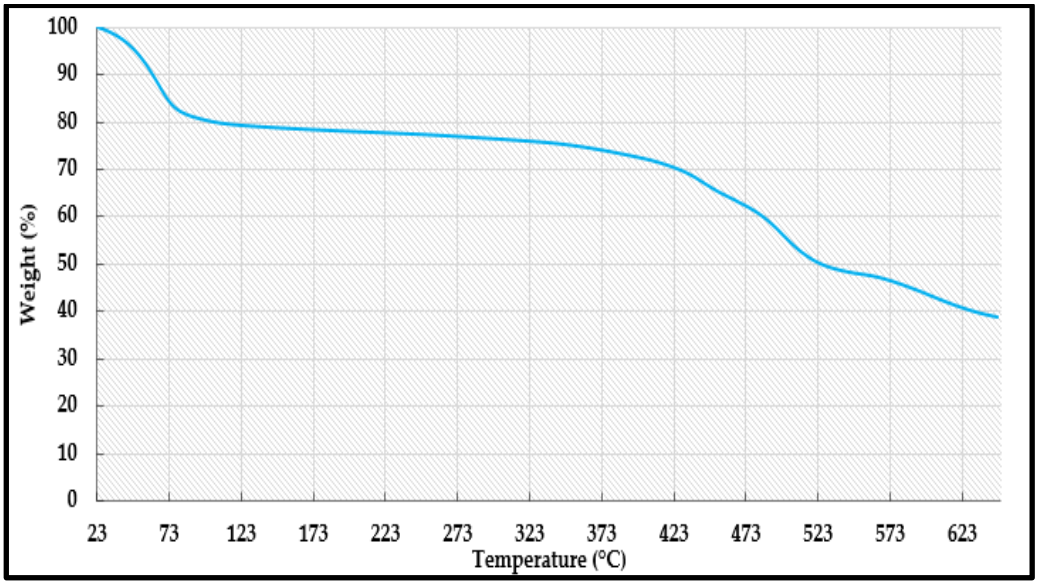

Fig. 4-32 Thermogravimetric analysis of MIL-100(Fe).

4.4.2.4. Scanning Electron Microscopy (SEM)

The morphology of MIL-100(Fe) was investigated using SEM. **Fig. 4-33** shows SEM image of the synthesized MIL-100(Fe) crystals where it was found that the produced crystals did not have a definite shape.

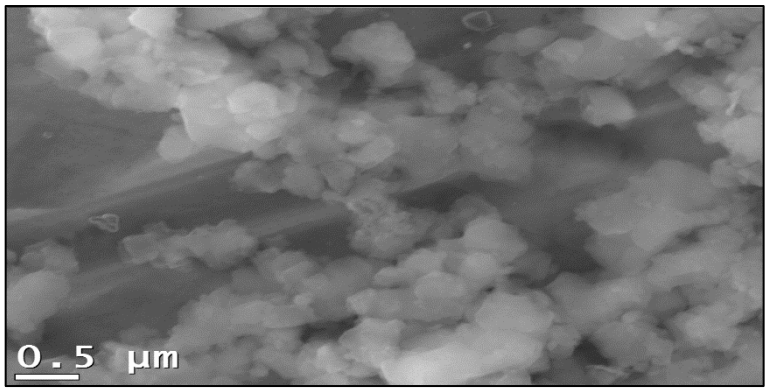

Fig. 4-33 SEM images of MIL-100(Fe).

4.4.2.5. Fourier Transform Infrared Spectroscopy (FTIR)

The presence of functional groups in MIL-100(Fe) was examined using the FTIR technique (**Fig. 4-34**). The vibration at 1628 cm^{-1} is attributed to the interaction between the O-C-O and the Fe^{3+} ion in the structure while the band at 1385 cm^{-1} is due to carboxylate group stretching.

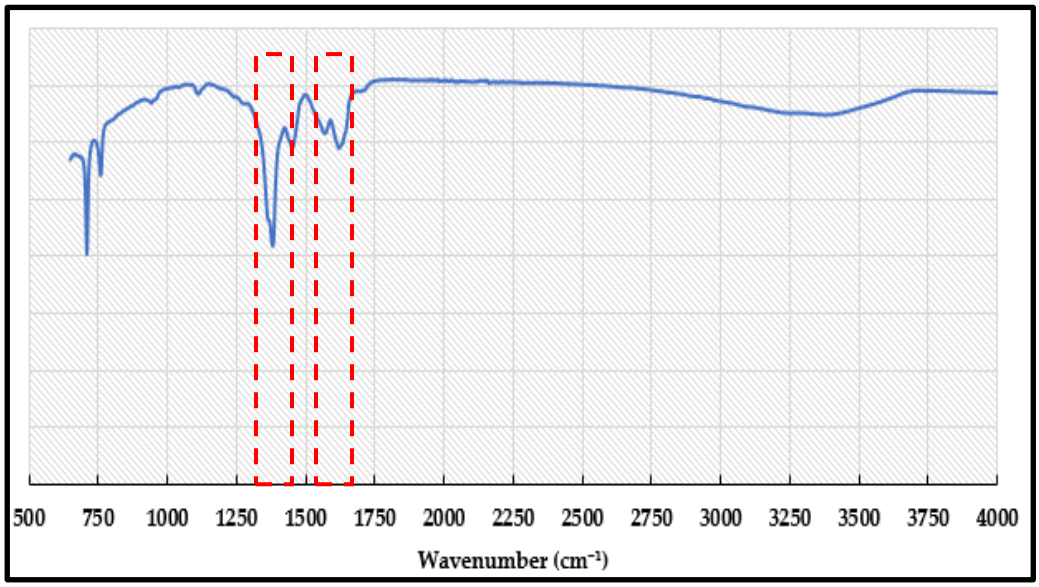

Fig. 4-34 FTIR spectra of MIL-100(Fe).

4.4.2.6. True density

The true density of MIL-100(Fe) was measured using helium pycnometer. **Table. 4-8** shows the values of the true, bulk densities and porosity of MIL-100(Fe).

Table. 4-8 True, bulk densities and porosity of MIL-100(Fe)

Material	True density (kg m^{-3})	Bulk density (kg m^{-3})	Porosity (–)
MIL-100(Fe)	2094.7	442	0.79

4.4.2.7. Thermal conductivity

The thermal conductivity of MIL-100(Fe) is shown in **Fig. 4-35**. It can be noticed that MIL-100(Fe) has a thermal conductivity lower than CPO-27(Ni) and higher than MIL-101(Cr). The measured thermal conductivity and the calculated porosity were used to develop an empirical equation to predict the effective thermal conductivity at different temperatures as shown in **Table. 4-9**. Also, the measured specific heat capacity was 0.99 kJ (kg K) $^{-1}$.

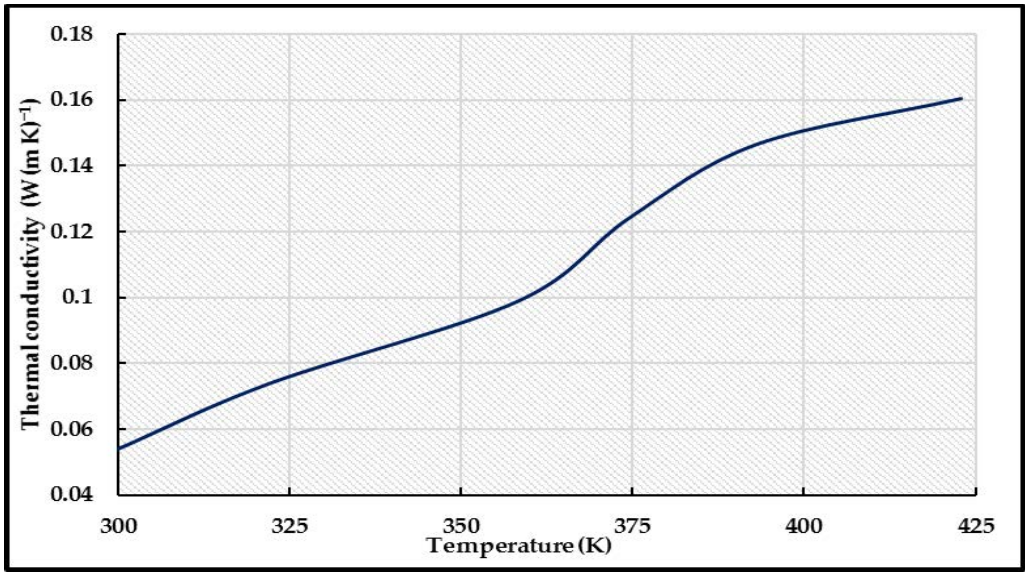

Fig. 4-35 Thermal conductivity of MIL-100(Fe).

Table. 4-9 Effective thermal conductivity of MIL-100(Fe)

Material	Effective thermal conductivity (W (m K)$^{-1}$)
MIL-100(Fe)	$6.5E-4T_{bed}-0.155$

4.4.2.8. Water adsorption characteristics

4.4.2.8.1. Adsorption isotherms

Fig. 4-36 shows the measured water adsorption/desorption isotherm of MIL-100(Fe) at 25°C. It can be noticed that the material exhibits a two-steps type IV isotherm. Also, it can be noticed that at low partial pressure range and similar to MIL-101(Cr), the material is characterized by its low uptake. Once the water molecules are introduced to the structure, it starts to fill the smaller pores first and then the larger ones [143]. The presence of two types of pores justify the two-step isotherm shape [154].

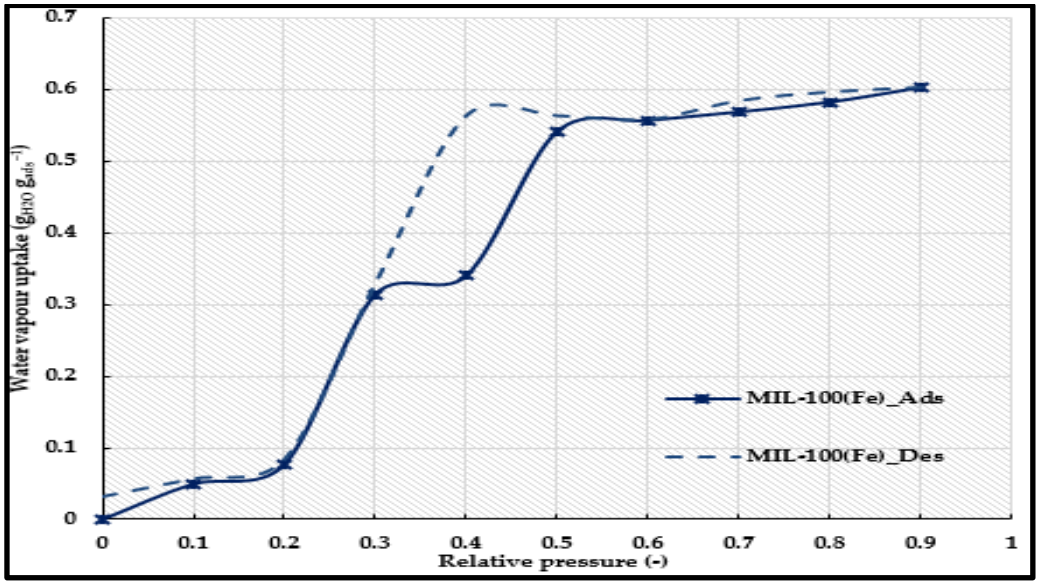

Fig. 4-36 Water adsorption isotherm of MIL-100(Fe) at 25°C.

The water adsorption uptake of the MIL-100(Fe) was measured at 15°C, 25°C and 35°C (**Fig. 4-37**). The measured data were fitted using a series of equations in terms of adsorption potential (A) (**Eq. 4-6** to **Eq. 4-8**).

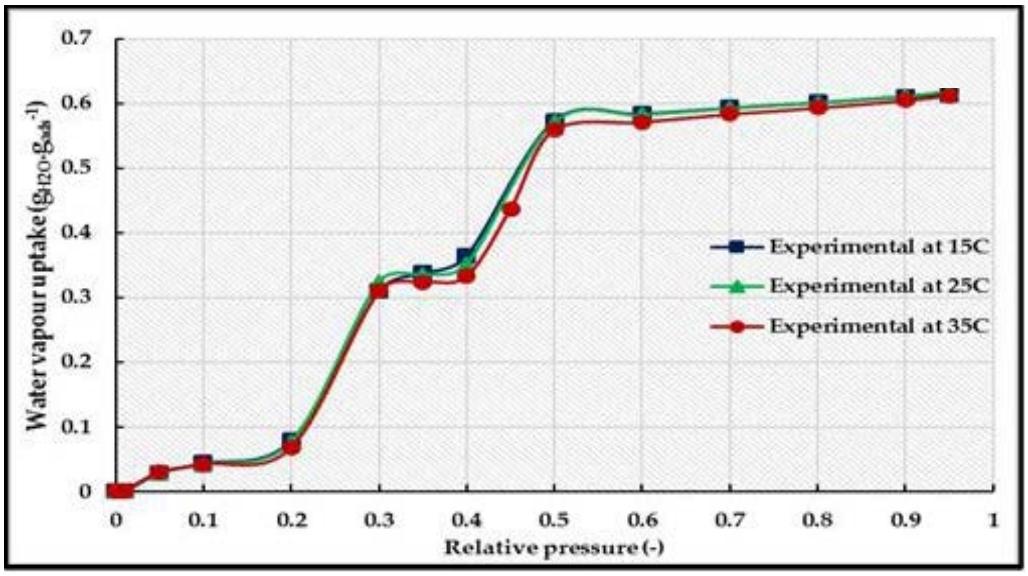

Fig. 4-37 Water adsorption isotherm of MIL-100(Fe) at different adsorption temperatures.

$$X = 1.59\exp(-6.4E - 4A) \qquad \text{A}\geq 5300 \qquad \text{(4-6)}$$

$$X = -3.82 + 4.7E - 3A - 1.8E - 6A^2 + 2.9E - 10A^3 + 1.7E - 14A^4 \qquad \text{2100} \leq \text{A} < \text{5300} \qquad \text{(4-7)}$$

$$X = 0.64 - 0.2E - 3A + 2.4E - 7A^2 - 9.4E - 11A^3 \qquad \text{A} < \text{2100} \qquad \text{(4-8)}$$

Fig. 4-38 shows the good agreement between the experimental data and the proposed models for the neat MIL-100(Fe).

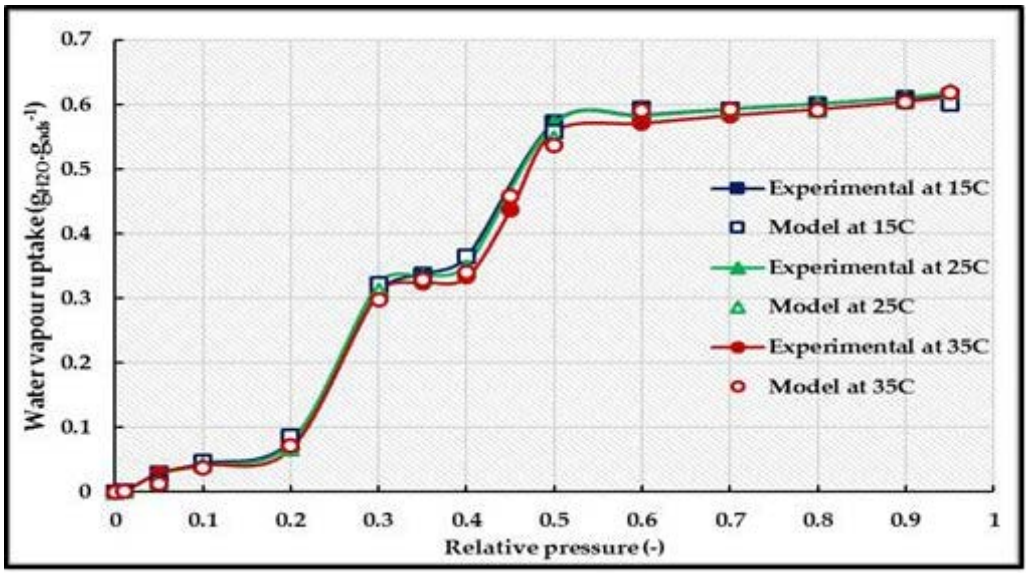

Fig. 4-38 Proposed isotherm model fitting of water adsorption on MIL-100(Fe) at different adsorption temperatures.

In order to evaluate the performance stability, MIL-100(Fe) was subjected to ten successive adsorption/desorption cycles (**Fig. 4-39**), the test was held in the relative pressure range of 0 to 0.9. The material showed a steady performance over the investigated range which emphasize the stability of MIL-100(Fe).

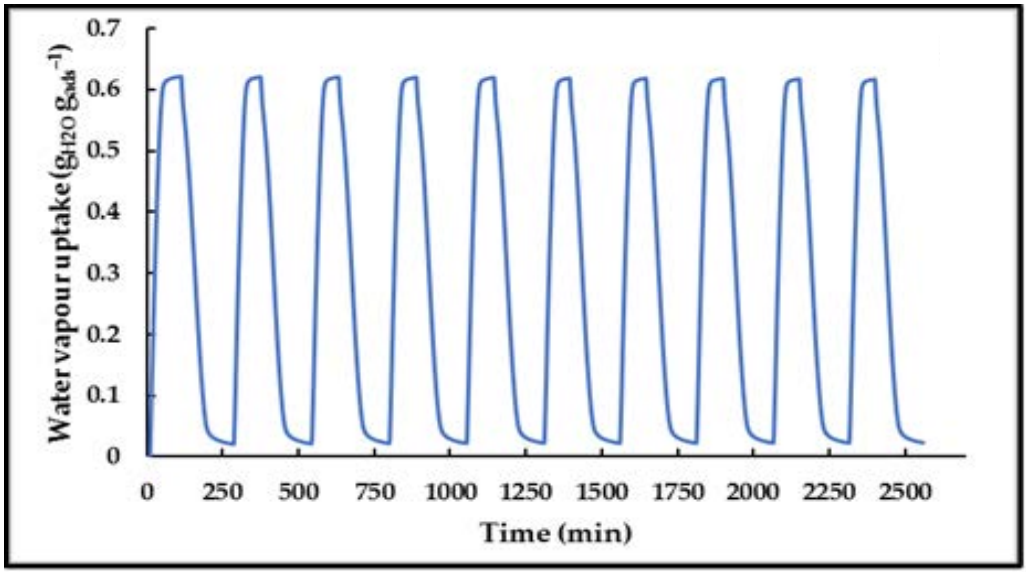

Fig. 4-39 Adsorption/desorption cycling experiments for MIL-100(Fe) at a relative pressure of 0.9.

4.4.2.8.2. Adsorption Kinetics

The rate of water adsorption was predicted through applying the LDF model (**Eq. 3-21** to **Eq. 3-24**). **Table. 4-10** gives the values of parameters E_a and k_0 for MIL-100(Fe), while **Fig. 4-40** highlights the validity of the LDF model in fitting the experimental data of MIL-100(Fe).

Table. 4-10 Values of LDF equation parameters

Adsorbent	Relative pressure range	E_a (J mol^{-1})	k_0 (s^{-1})
MIL-100(Fe)	<0.3&>0.5	21,072	8.5
	≥0.3&≤0.5	23,164	4.11

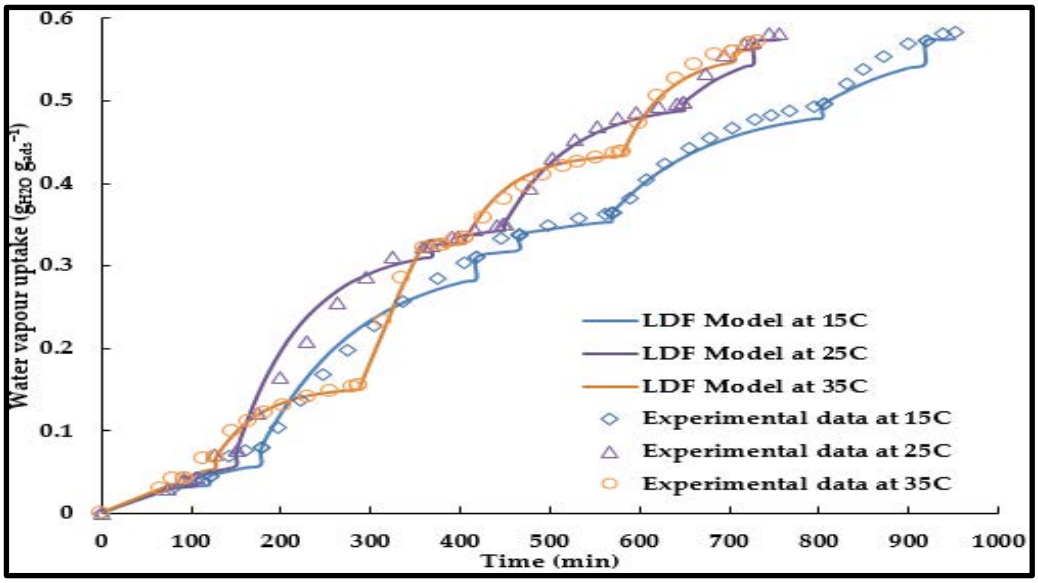

Fig. 4-40 LDF model fitting of water adsorption on MIL-100(Fe) at 15°C, 25°C and 35°C.

4.5. Aluminium fumarate

Aluminium fumarate, commercially known as MOF-A520 was synthesized and commercially produced by MOF Technologies ltd, UK.

4.5.1. Characterization

4.5.1.1. Powder XRD

Fig. 4-41 shows the powder XRD pattern of aluminium fumarate where the diffraction peak positions were in agreement with the previously reported data [151], and the very broad peaks indicate small crystallite size [221].

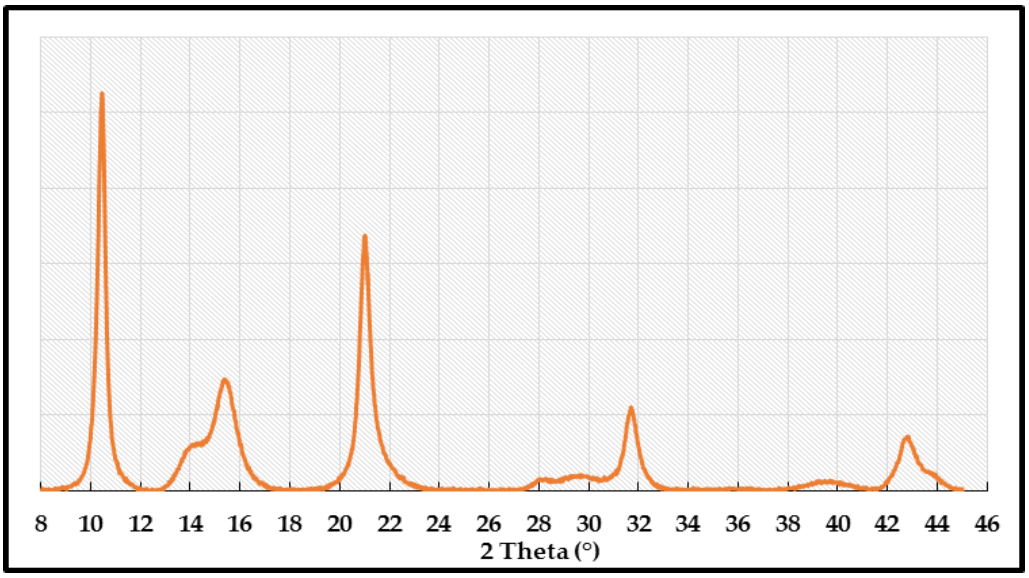

Fig. 4-41 Powder XRD patterns of aluminium fumarate [221].

4.5.1.2. Nitrogen adsorption

The surface area of aluminium fumarate was measured using the nitrogen adsorption technique at 77 K (**Fig. 4-42**); a BET surface area of 893.9 m^2 g^{-1} was recorded [221] and a pore volume of 0.48 cm^3 g^{-1} was measured [151].

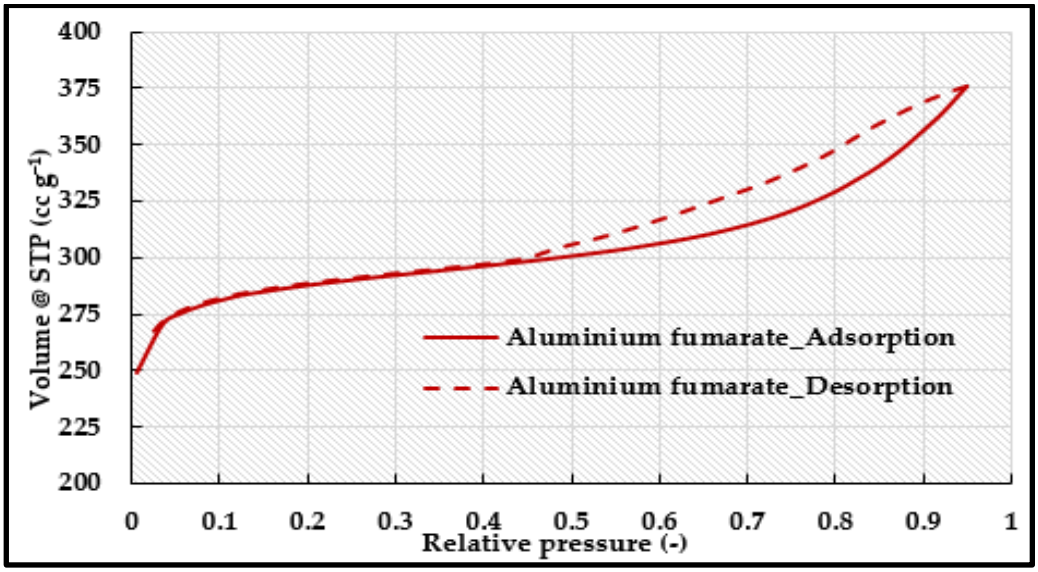

Fig. 4-42 Nitrogen adsorption isotherm of aluminium fumarate at 77 K [221].

4.5.1.3. Thermogravimetric analysis (TGA)

The thermal stability of aluminium fumarate was assessed using the thermal gravimetric technique where the change in mass was recorded as the temperature increased under a flow of nitrogen. **Fig. 4-43** shows the TGA traces of the MOF material. It can be noticed that the material lost all its physically adsorbed water at a temperature as low as 60°C which highlights the low desorption temperature required to reach its dry state. After that the material was thermally stable until a temperature of 450°C was reached. As the temperature increased, the final stage took place where the weight loss was due to the destruction of the structure and the decomposition of the organic ligand. This is in good agreement with information reported by *Karmakar et al* [267].

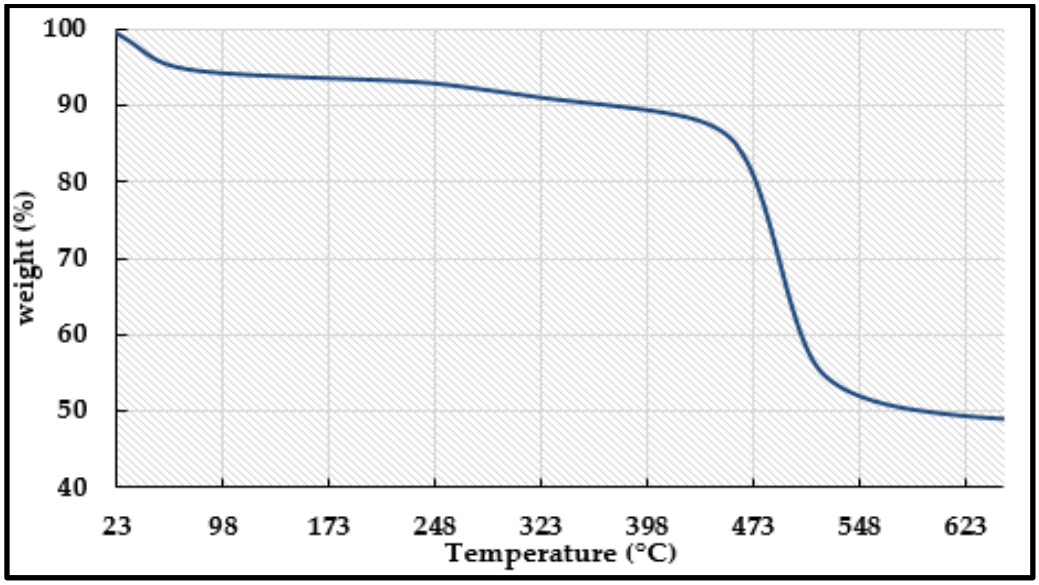

Fig. 4-43 Thermogravimetric analysis of aluminium fumarate.

4.5.1.4. Scanning Electron Microscopy (SEM)

The morphology of the aluminium fumarate crystals was investigated using SEM. **Fig. 4-44** shows SEM images of the MOF material which indicate that the material possessed a lozenge shape which synchronizes with the framework shape. Also, it can be noticed that the crystals had a rough surface. These findings are in agreement with the previously published data [267, 268].

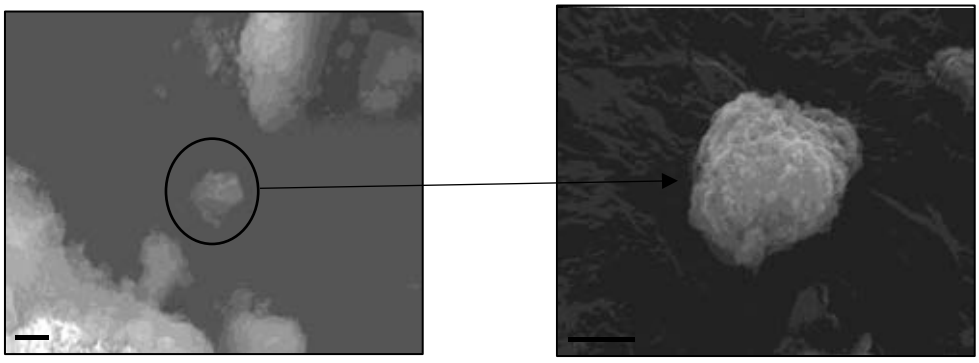

Fig. 4-44 SEM images of aluminium fumarate.

4.5.1.5. Fourier Transform Infrared Spectroscopy (FTIR)

The presence of functional groups in aluminium fumarate was examined using FTIR technique (**Fig. 4-45**). The presence of the characteristic vibrational bands of the carboxylate group (O-C-O)- at 1400 and 1620 cm^{-1} confirms the presence of the dicarboxylate group within

the framework while the absorbance of the broad peak at 3451 cm^{-1}confirms the presence of hydroxyl group and water [160, 258, 269].

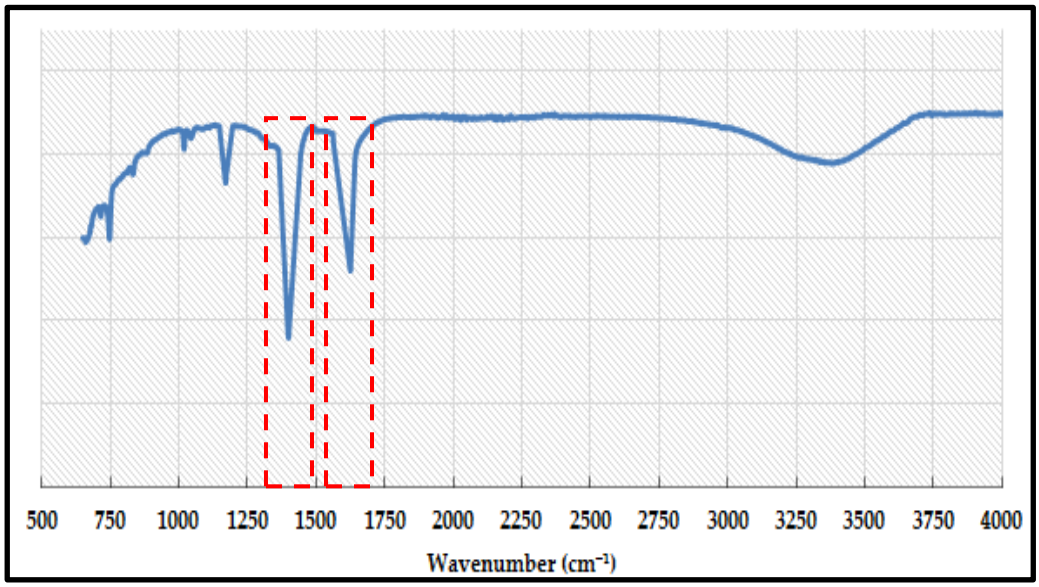

Fig. 4-45 FTIR spectrum of aluminium fumarate [151].

4.5.1.6. True density

The true density of aluminium fumarate was measured using a helium pycnometer. **Table. 4-11** shows the values of the true, bulk densities and porosity of MOF material.

Table. 4-11 True, bulk densities and porosity of aluminium fumarate

Material	True density (kg m^{-3})	Bulk density (kg m^{-3})	Porosity (–)
Aluminium fumarate	1581.3	520	0.67

4.5.1.7. Thermal conductivity

The thermal conductivity of aluminium fumarate was previously reported by *Jeremias et al.*, [151] as shown in **Fig. 4-46**. The data were fitted through the equation presented in **Table. 4-12** to predict the effective thermal conductivity at different temperatures. The measured specific heat capacity was 0.97 kJ (kg K) $^{-1}$.

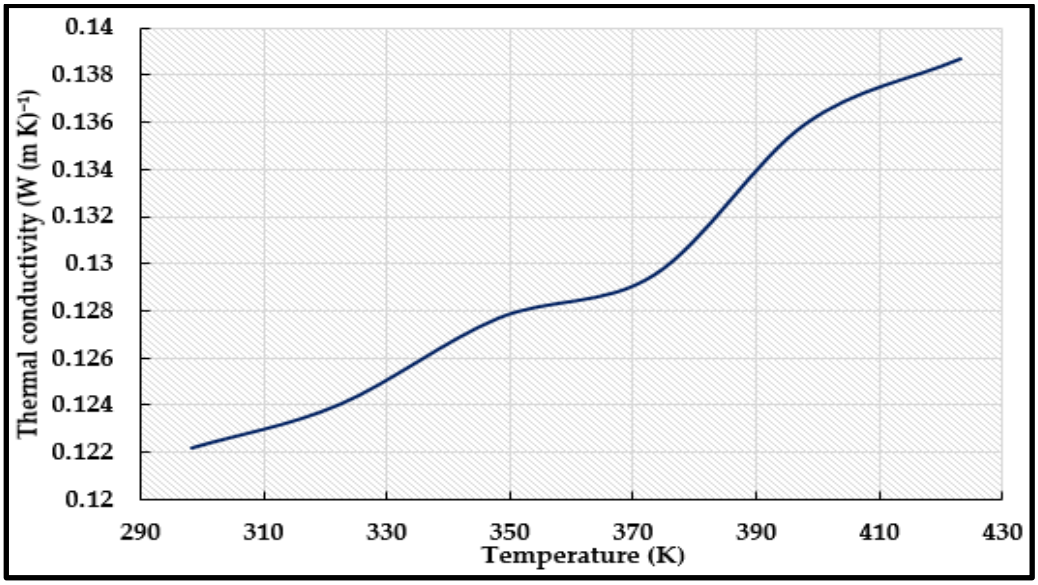

Fig. 4-46 Thermal conductivity of aluminium fumarate [151].

Table. 4-12 Effective thermal conductivity of aluminium fumarate

Material	Effective thermal conductivity (W (m K)$^{-1}$)
Aluminium fumarate	$0.08 + 1.4E-4T_{bed}$

4.5.1.8. Water adsorption characteristics

4.5.1.8.1. Adsorption isotherms

Fig. 4-47 shows the measured water adsorption/desorption isotherm of aluminium fumarate at 25°C where it is evident that the material exhibits type IV isotherm [221]. At partial pressure < 0.2, the water uptake was low but steeply increased in the relative pressure range of 0.2 to 0.3 to reach 0.35 $g_{H_2O}\ g_{ads}^{-1}$. Aluminium fumarate exhibited a maximum uptake of 0.53 $g_{H_2O}\ g_{ads}^{-1}$ at a relative pressure of 0.9. As there are no unsaturated metal sites in aluminium fumarate structure, the water molecules are uniformly accumulated in the inner pores of the material due to the hydrophilicity of the inner pore surface (**Fig. 4-48**). The low water vapour uptake at the low relative pressure range is related to the hydrophobicity of the organic linker [14, 221]. Based on the isotherm shape, it is evident that the material possesses a very low desorption temperature. Also, as the steep increase in the water vapour uptake took place at a

relative pressure of 0.2-0.3, the material is suitable for adsorption cooling applications with a working relative pressure higher than 0.3. Nevertheless, the material is expected to be more efficient in applications with high working relative pressure due to its isotherm shape [14, 221].

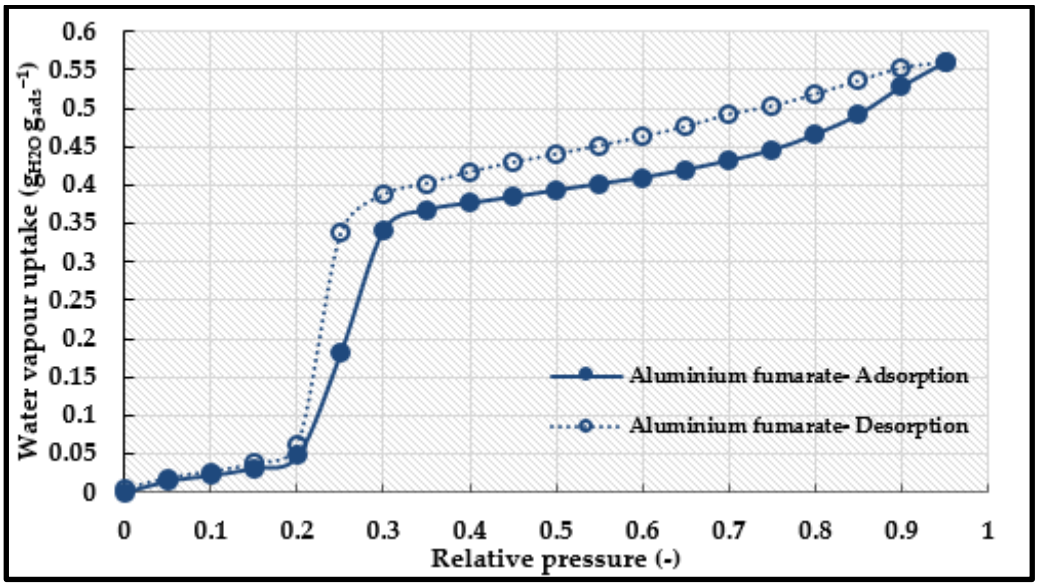

Fig. 4-47 Water adsorption isotherm of aluminium fumarate at 25°C [14, 221].

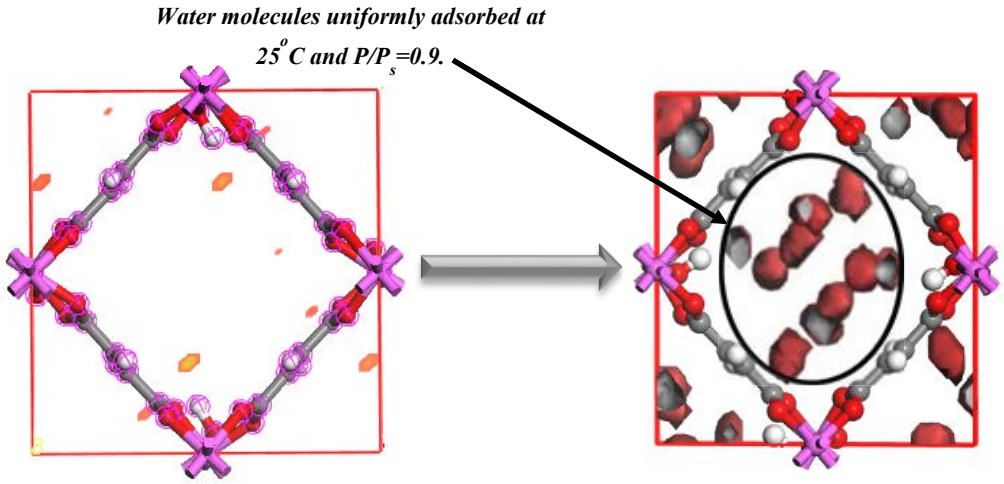

Fig. 4-48 Water adsorption sites and the adsorbed water molecules field at 25°C [14].

(Figure was developed using Materials Studio software)

The water adsorption uptake was measured at 15°C, 25°C and 35°C (**Fig. 4-49**).

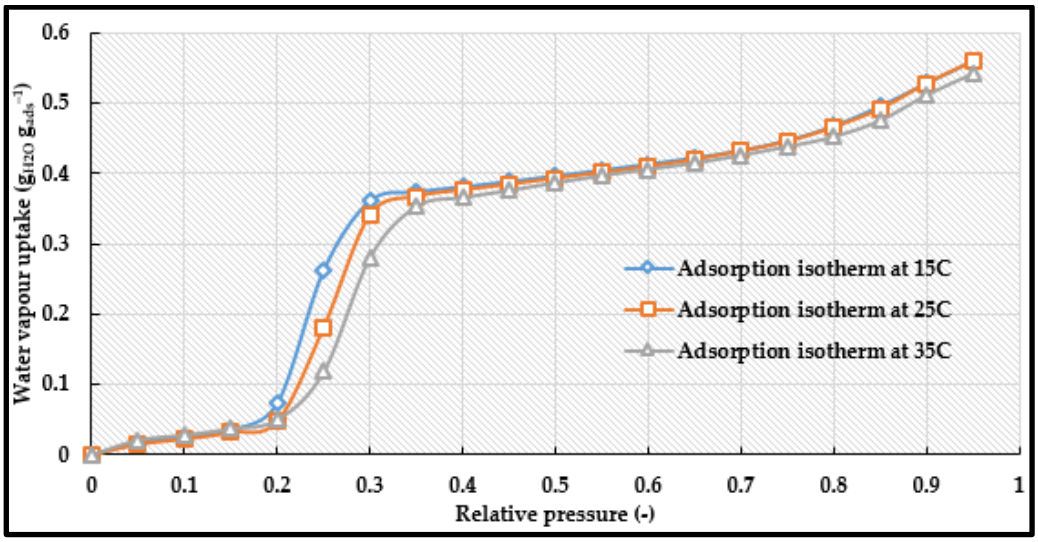

Fig. 4-49 Water adsorption isotherm of aluminium fumarate at different adsorption temperatures [14, 221].

The measured data were fitted using a series of equations in terms of adsorption potential (A) (**Eq. 4-9** to **Eq. 4-11**) **[14, 221]**. **Fig. 4-50** shows good agreement between the experimental data and the proposed model.

$$X = 0.17\exp(-3.1E-4A) \qquad \textbf{A>3700} \qquad \textbf{(4-9)}$$

$$X = 2.4-1E-03A+1.1E-07A^2 \qquad \textbf{2700} \le \textbf{A} \le \textbf{3700} \qquad \textbf{(4-10)}$$

$$X = 1.1E-14A^4-8.9E-11A^3+2.6E-7A^2-3.6E-4A+0.6 \qquad \textbf{A<2700} \qquad \textbf{(4-11)}$$

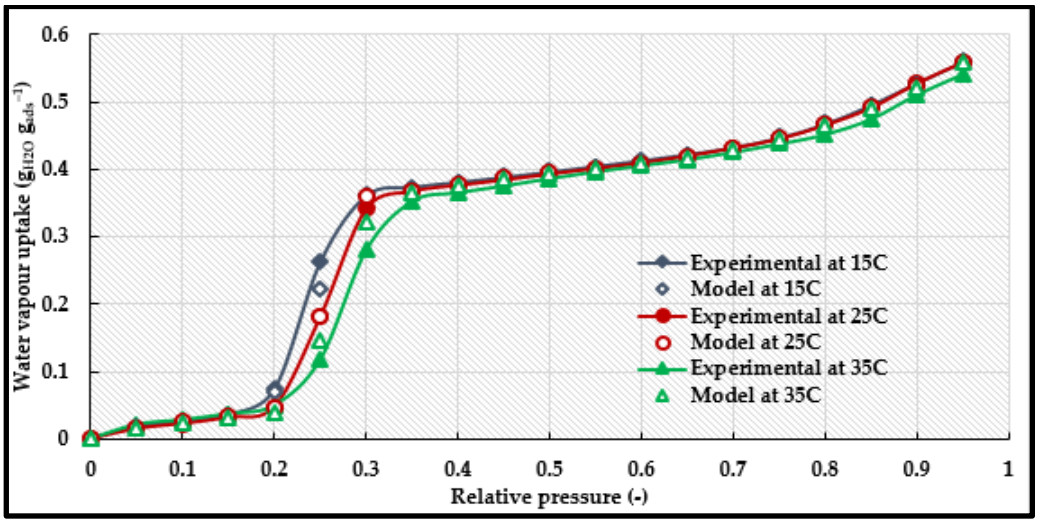

Fig. 4-50 Proposed isotherm model fitting of water adsorption on aluminium fumarate [221].

In order to evaluate aluminium fumarate performance stability, the material was subjected to ten successive adsorption/desorption cycles. **Fig. 4-51** shows that aluminium fumarate had a decreased water vapour capacity during the first four cycles and it exhibited a stable performance afterwards. This could be attributed to the breathing phenomenon observed in some MOFs like MIL-53 causing the thermodynamic water sorption equilibrium not to be completely reached within the first cycles. The material was reported to exhibit a stable performance after the first few cycles [221].

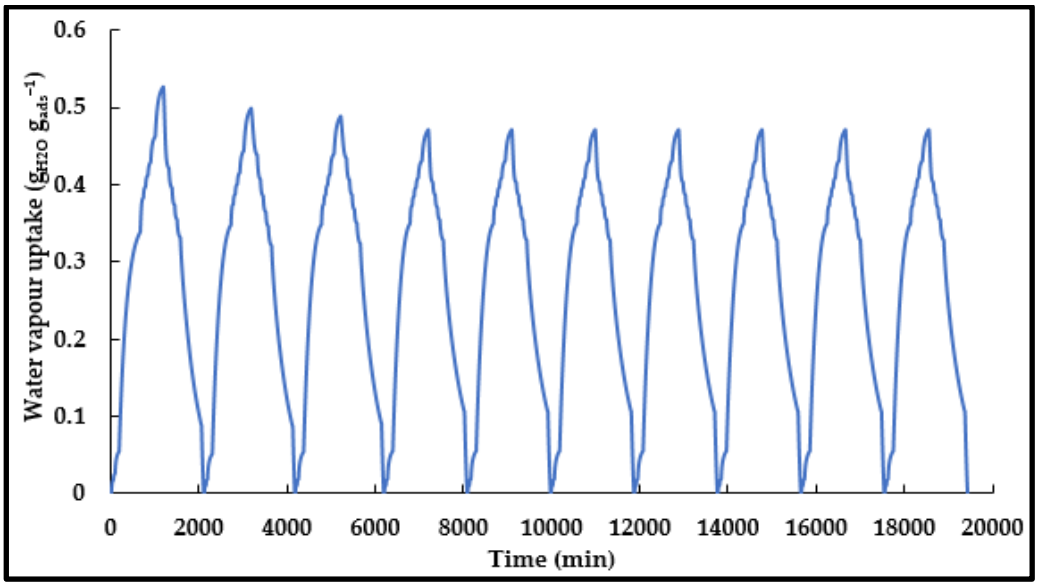

Fig. 4-51 Complete adsorption/desorption cycling experiments for aluminium fumarate [221].

4.5.1.8.2. Adsorption Kinetics

The rate of water adsorption was predicted through applying the LDF model (**Eq. 3-21** to **Eq. 3-24**). **Table. 4-13** gives the values of parameters E_a and k_0 for aluminium fumarate. **Fig. 4-52** highlights the validity of the LDF model in fitting the experimental data of the material under investigation [14, 221].

Table. 4-13 Values of LDF equation parameters

Adsorbent	Relative pressure range	E_a (J mol^{-1})	k_0 (s^{-1})
Aluminium fumarate	<0.2&>0.3	22,696	7.35
	≥0.2&≤0.3	37,763	678

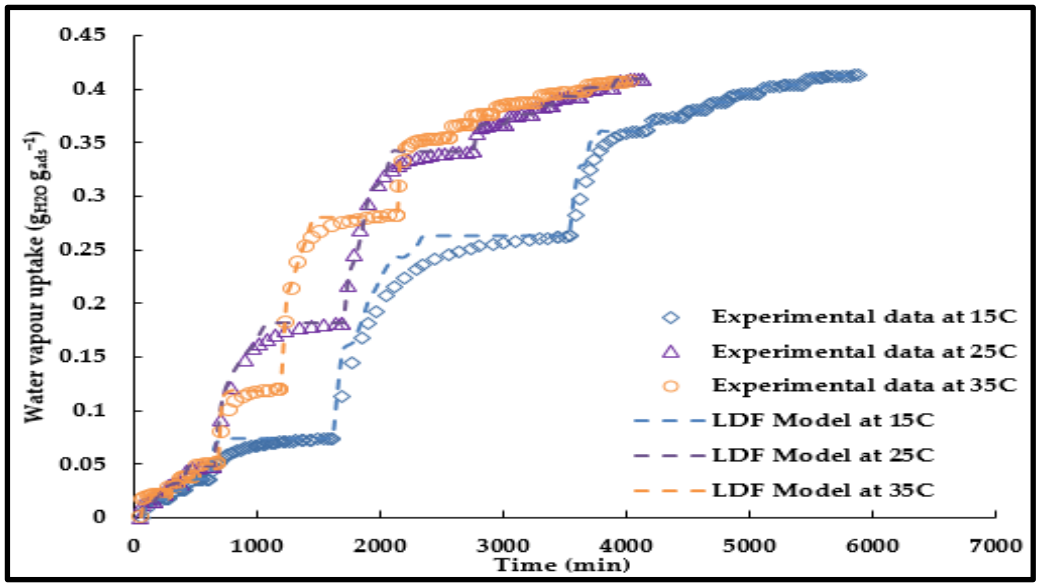

Fig. 4-52 LDF model fitting of water adsorption on aluminium fumarate at 15°C, 25°C and 35°C.

4.6. Summary

Among the different MOF materials, four MOFs were chosen to be fully characterised. Two MOFs were commercially available, aluminium fumarate and CPO-27(Ni), while the other two, MIL-101(Cr) and MIL-100(Fe), were synthesized at the University of Birmingham (UoB). The optimum operating conditions to successfully synthesize both MIL-101(Cr) and MIL-100(Fe) were investigated. The four MOFs were characterized in terms of their XRD patterns, thermal stability, SEM images, FTIR spectra, thermal conductivity and their densities.

As water is an environmentally friendly refrigerant with high heat of vaporization, all the materials were also characterized based on their water vapour uptake. It was found that MIL-101(Cr) had the highest water vapour capacity followed by MIL-100(Fe), aluminium fumarate and CPO-27(Ni). Based on the adsorption isotherm of the four materials, it can be concluded that CPO-27(Ni) is the most suitable material for adsorption cooling application or application working at low relative pressure followed by MIL-100(Fe), aluminium fumarate and MIL-101(Cr). While for applications working at high relative pressure such as adsorption desalination without cooling effect, MIL-101(Cr) should be the best candidate followed by MIL-100(Fe), aluminium fumarate and CPO-27(Ni). This shows the versatility of MOFs properties and how they can be employed in various adsorption applications proving their potential in adsorption applications.

CHAPTER 5
ENHANCING MOF PERFORMANCE

5.1. Introduction

This chapter investigates using different routes to enhance the performance of the four MOFs under investigation. The first method was MOFs composites where a number of MOF materials composites were synthesised and characterized to improve and enhance the heat and mass transfer properties of the parent MOF materials. The second technique was introducing the four MOF materials as a coated layer to the heat exchanger. The different properties of the developed coated layers were characterized.

(This chapter is based on the published paper: E. Elsayed, H. Wang, P. A. Anderson, R. Al-Dadah, S. Mahmoud, H. Navarro, Y. Ding, and J. Bowen, "Development of MIL-101 (Cr)/GrO composites for adsorption heat pump applications," Microporous and Mesoporous Materials, vol. 244, pp. 180-191, 2017).

5.2. MIL-101(Cr) composites

5.2.1. Synthesis

Even though MIL-101(Cr) possesses exceptional properties compared to other MOFs such as the high surface area, pore volume, water vapour uptake (at relative pressure > 0.5) and high-performance stability, MIL-101(Cr) suffers from low heat and mass transfer properties. As mentioned earlier in chapter 2, composites have been investigated to enhance the functionality, stability, ease of preparation and selectivity of materials [270-272]. The synthesis of two novel MIL-101(Cr) composites will be discussed in the next section.

5.2.1.1. MIL-101(Cr)/ graphene oxide [225]

Graphene oxide (GrO) is a graphene derivative which is a highly thermal conductive material. It is constructed from a one-atom-thick carbon atom planar sheets in a hexagonal crystal lattice. Graphene oxide is produced through the oxidation of graphene giving a graphene layer with functional groups such as carboxyl (-COOH), hydroxyl (-OH) and epoxide (-O-). The MIL-101(Cr)/GrO composites were synthesized to exploit the enhanced thermal properties and the hydrophilicity of graphene oxide.

The composites were synthesized using two different methods: the first method was the physical mixing of pre-synthesized MIL-101(Cr) crystals and graphene oxide to obtain the 'GrO_physical' composites. To ensure homogeneous mixing between the two components, the GrO was added to the pre-synthesized MIL-101(Cr) with a few drops of water. The mixture was sonicated, filtered and then left to dry in air. The second method was the synthesis process where graphene oxide was incorporated into MIL-101(Cr) during synthesis using the same synthesis procedures of parent MIL-101(Cr). The procedures to prepare these composites were the same as the ones used for the synthesis of neat MIL-101(Cr) in Chapter 4, while the procedures to suspense GrO was adopted from [257]. This was carried out by a thorough mixing of chromium nitrate, tetramethyl ammonium hydroxide and terephthalic acid. The GrO was added in different ratios based on the mass of produced MIL-101(Cr). The reactants suspension was sonicated for 30 min and then stirred at 40°C for another 15 min. Finally, the mixture was transferred into a Teflon-lined autoclave of 45 ml. It was left for 24 hr at 180°C and after it cooled down slowly to the ambient temperature, the product crystals were washed and filtered in the same manner as the neat MIL-101(Cr) obtaining the 'GrO_synthesis' composites [225].

5.2.1.2. MIL-101(Cr)/ $CaCl_2$

As mentioned in chapter 4, MIL-101(Cr) has a high-water uptake of up to 1.47 g_{H_2O} g_{ads}^{-1} [1]. Nevertheless, MIL-101(Cr) exhibits a type IV isotherm (S- shape isotherm) which means that the high-water uptake only takes place at high relative pressure (≥ 0.5) [14]. Such a drawback makes MIL-101(Cr) impractical for adsorption cooling applications.

Novel MIL-101(Cr)/$CaCl_2$ composites were synthesized through suspending the pre-synthesised MIL-101(Cr) powder with solutions of different $CaCl_2$ concentration with the mass ratio of one-part MIL-101(Cr) to 3, 4, 5, 6 and 8 parts $CaCl_2$ salt. The composites were assigned the names Comp_1:3, Comp_1:4, Comp_1:5, Comp_1:6 and Comp_1:8. The $CaCl_2$ salt was dissolved in water and MIL-101(Cr) powder was added. The suspension was stirred overnight, filtered, repeatedly washed with water and finally left to dry in air.

5.2.2. Characterization

5.2.2.1. Powder XRD

Fig. 5-1 shows the PXRD patterns of GrO, MIL-101(Cr) and their physical and synthesis composites. It can be noticed that when GrO was introduced to the MIL-101(Cr) through either physical mixing or synthesis process, the main peaks of the parent MIL-101(Cr) were preserved in both composites. This can be attributed to the fact that MIL-101(Cr) is the major component. This shows that the GrO presence in case of the synthesis_composites did not prohibit the MIL-101(Cr) formation. However, a significant decrease in the peaks intensity of the high GrO concentration composites was observed which may be attributed to the partial distortion of the MIL-101(Cr) structure due to the presence of GrO during the crystal growth process [273]. Also, it can be noticed that GrO is amorphous material because it has only one peak at 11° which did not appear in the patterns of any of the composites. This can be attributed to the low amount of GrO used [274] and it being well dispersed [275, 276].

Fig. 5-2 shows the diffraction patterns of the anhydrous $CaCl_2$ salt, the neat MIL-101(Cr) and the MIL-101(Cr)/$CaCl_2$ composites where a similar behaviour to the GrO composites was observed. As it can be noticed, the MIL-101(Cr) peaks were all preserved for all the composites with no traces of the diffraction peaks of the salt. This indicates that the presence of the $CaCl_2$ did not interfere or cause any significant distortion to the MIL-101(Cr) crystal structure.

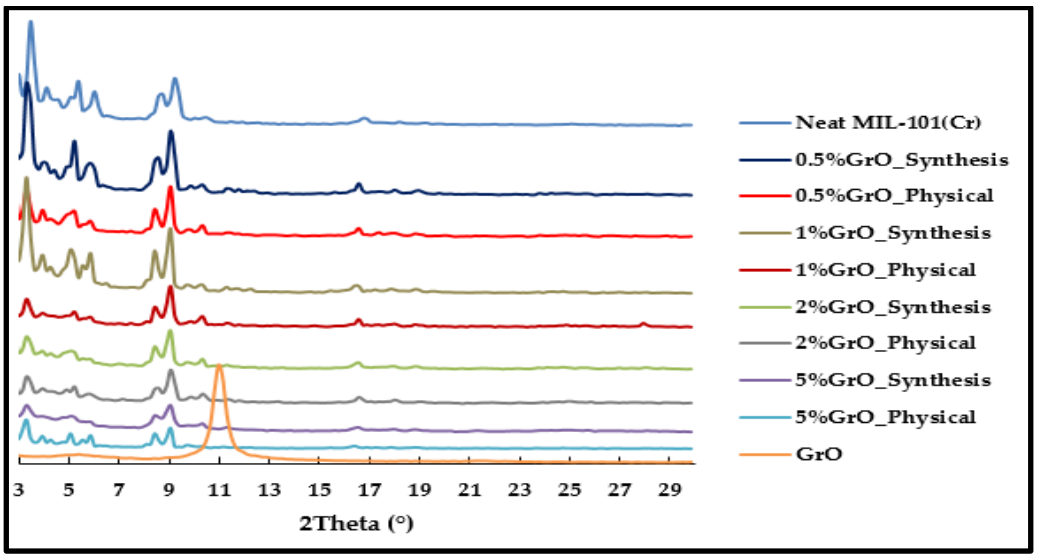

Fig. 5-1 Powder XRD patterns of MIL-101(Cr), GrO and their different composites [225].

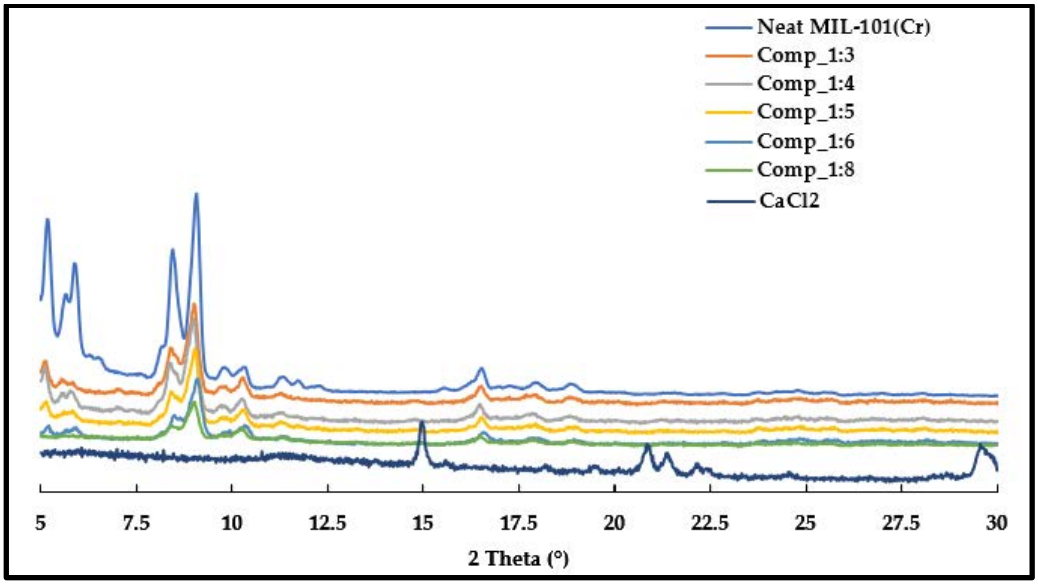

Fig. 5-2 Powder XRD patterns of MIL-101(Cr), $CaCl_2$ and their composites.

5.2.2.2. Nitrogen adsorption

Fig. 5-3 shows the nitrogen adsorption isotherms of MIL-101(Cr) and its GrO composites while the BET surface area and pore volume of the parent material and its GrO composites are listed in **Table. 5-1**. It can be noticed that the 2%GrO_synthesis composite exhibited the highest surface area which was more than 6% higher than the neat MIL-101(Cr). This suggests that the 2%GrO_synthesis composite had additional porosity compared to parent MIL-101(Cr) as its total pore volume increased from 1.75 for the neat MIL-101(Cr) to 2.14 $cm^3 g^{-1}$. The increase in the pore volume can be attributed to the increase in the meso-pores volume [225].

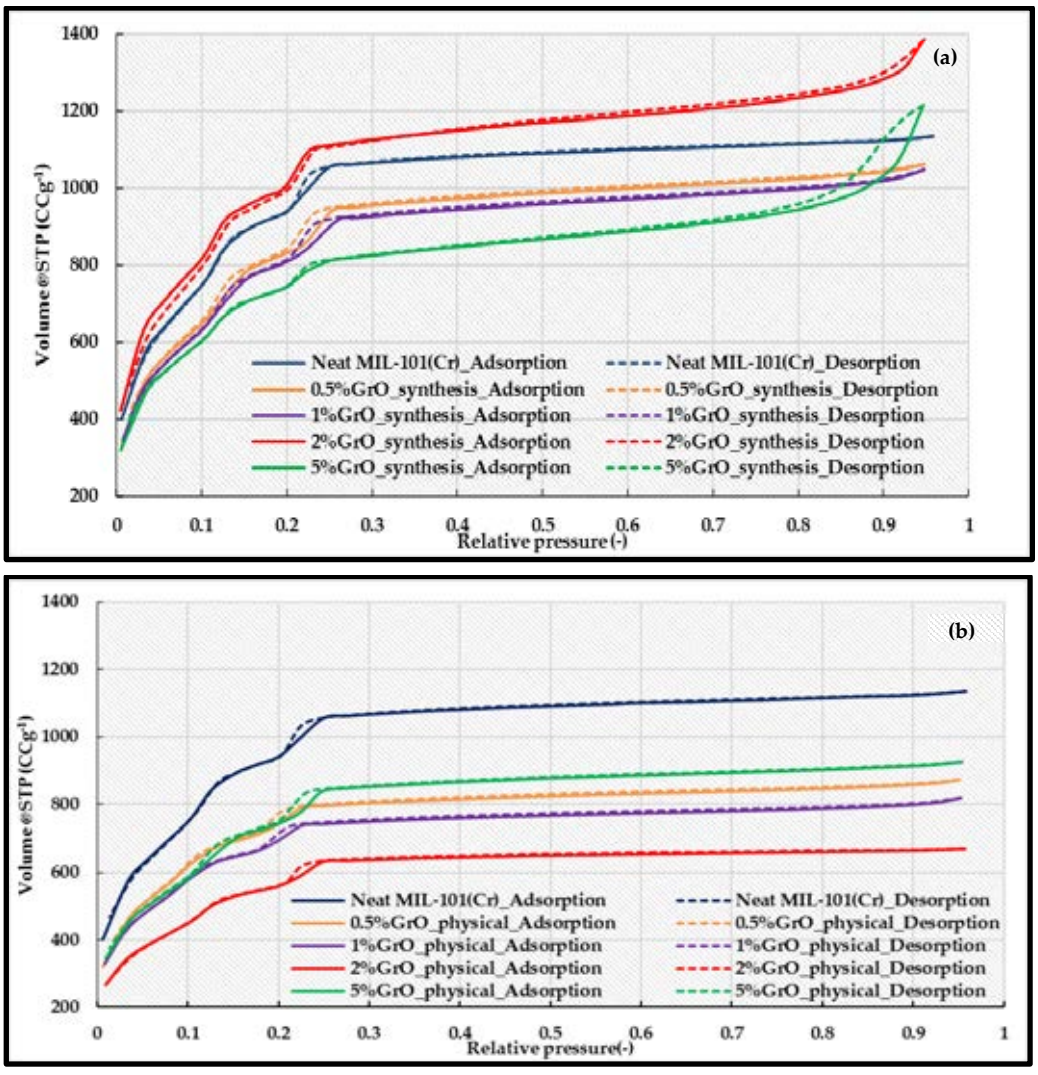

Fig. 5-3 Nitrogen adsorption isotherms of MIL-101(Cr), a. synthesis GrO composites and b. physical GrO composites at 77 K [225].

Table. 5-1 Surface area of MIL-101(Cr) and GrO composite [225]

Material	BET surface area (m^2g^{-1})	Total pore volume (cm^3g^{-1})
GrO	Nil	Nil
Neat MIL-101(Cr)	3460	1.753
0.5%GrO_synthesis	3137.8	1.641
0.5%GrO_physical	2608.5	1.346
1%GrO_synthesis	3028.1	1.619
1%GrO_physical	2425.7	1.265
2%GrO_synthesis	3674	2.14
2%GrO_physical	2077	1.035
5%GrO_synthesis	2810	1.879
5%GrO_physical	2626	1.33

Fig. 5-4 explains the increase in both the surface area and pore volume through modelling the crystal structures of both GrO and MIL-101(Cr) using Materials Studio software. Such increase may be produced by the formation of new accessible meso-pores formed due to the interaction between the MIL-101(Cr) framework and the sheets of GrO. This took place through the coordination between the GrO epoxy groups and the MIL-101(Cr) metal ions. As the GrO content increased, a lower surface area was noticed. Due to the spherical shape of MIL-101(Cr) crystal, the sheets of GrO have more than one possible orientation to coordinate to the crystal. This may not only restrain the proper GrO sheets attachment but also causes MIL-101(Cr) structure partial distortion. Increasing the GrO content may also block the MIL-101(Cr) diffusion pathways resulting in completely inaccessible volumes of the crystals causing significantly lower measured surface areas. This is consistent with the noticed surface area decrease. The BET surface area decreased from 3674 $m^2\ g^{-1}$ for the 2%GrO composite to reach only 2810 $m^2\ g^{-1}$ for the 5%GrO composite. In case of the physical composites, the surface area and pore volume were significantly reduced compared to the parent material which supports the suggestion that the GrO sheets may cause MIL-101(Cr) pores to be blocked hence resulting in a significant reduction in the accessible pore volume [225].

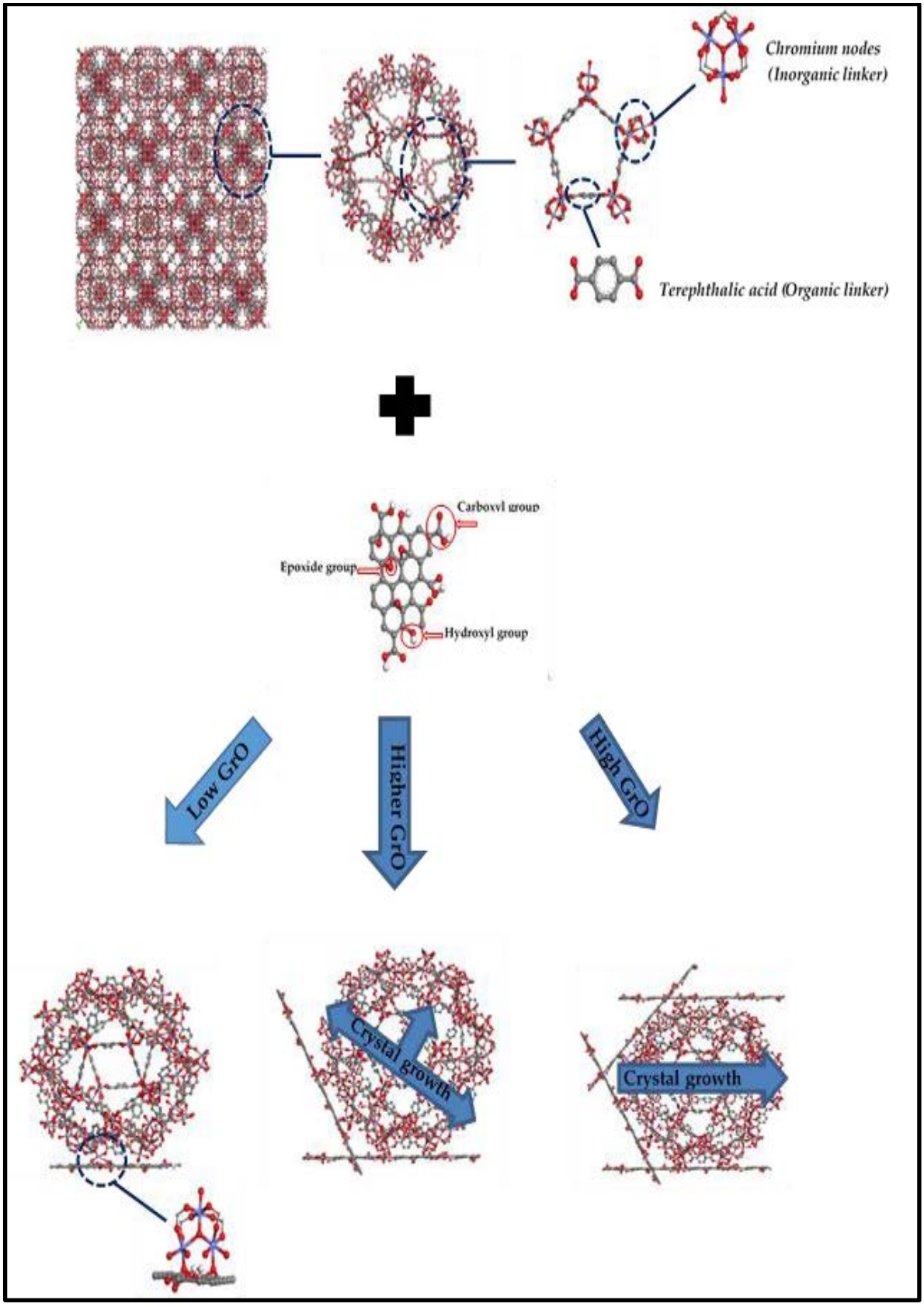

Fig. 5-4 MIL-101(Cr) cage, GrO layer and the GrO layer configuration on the MIL-101(Cr) crystal at different GrO concentrations [225].
(Figure was developed using Materials Studio software)

Fig. 5-5 shows the pore size distribution calculated using the DFT method. It can be noticed that the physical and synthesis composites maintained the same pore size distribution curves which shows that there was no change in the pore width between the composites and the MIL-101(Cr). It can be also noticed that the 2%GrO_synthesis composite had the highest pore volume. This is consistent with the measurement of the surface area and total pore volume [225].

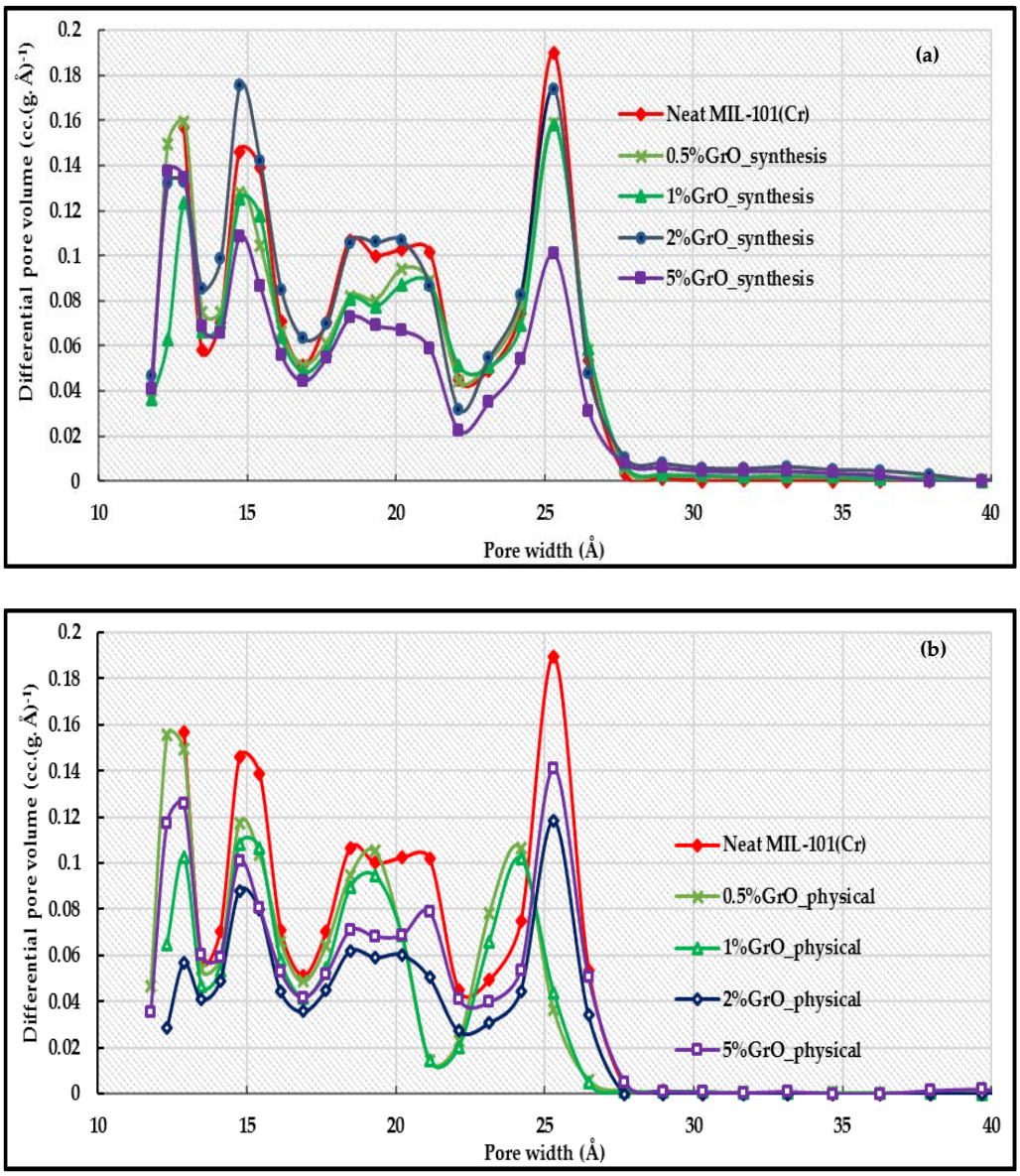

Fig. 5-5 Pore size distribution of MIL-101(Cr), a. GrO synthesis composites and b. GrO physical composites [225].

Regarding the $CaCl_2$ composites and from **Fig. 5-6**, it can be noticed that introducing $CaCl_2$ to MIL-101(Cr) in Comp_1:3, Comp_1:4 and Comp_1:5 composites slightly decreased the BET surface area and the total pore volume as illustrated in **Table. 5-2**, while for the Comp_1:6 and Comp_1:8 composites, the surface area significantly decreased to almost half that of the neat MIL-101(Cr). The decrease in the surface area and the pore volume could be attributed to either of two reasons (**Fig. 5-7**); (1) the deposition (accommodation) of the salt inside the pores of the MIL-101(Cr) which leads to blocking of the accessible pores, such mechanism was reported when $CaCl_2$ was incorporated in silica gel to produce SWS-1L [201]; or (2) an ion exchange mechanism where the ions of the salt replace the ions of the framework, a similar mechanism was observed when the $CaCl_2$ was incorporated in zeolite 13X [84]. In such mechanism, the chlorine ion is believed to substitute for the hydroxide ion which co-ordinates to the chromium cluster. In this case, the decrease in the surface area would be due to the different ion size as the size of the chloride ion is in the range of 1.81Å while the size of the hydroxide ion is only 0.958Å. Nevertheless, the pore size distribution calculated from the DFT method showed that even though the neat material has the highest pore volume, the incorporated $CaCl_2$ had almost no effect on the pore width as shown in **Fig. 5-8**.

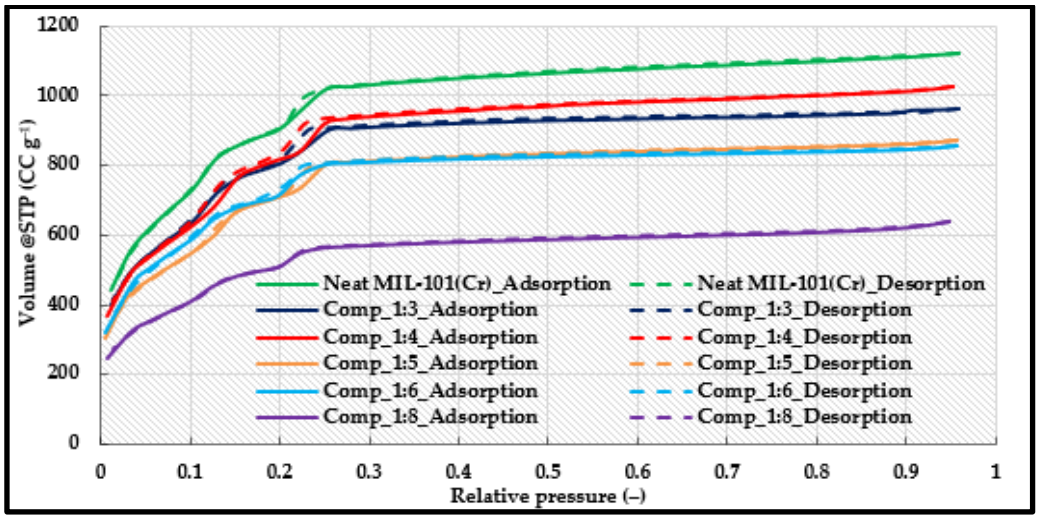

Fig. 5-6 Nitrogen adsorption isotherms of MIL-101(Cr) and its $CaCl_2$ composites at 77 K.

Table. 5-2 Surface area of MIL-101(Cr) and $CaCl_2$ composite

Material	BET surface area ($m^2\ g^{-1}$)	Total pore volume ($cm^3\ g^{-1}$)
Neat MIL-101(Cr)	3354.84	1.73
Comp_1:3	2976.77	1.49
Comp_1:4	3117.14	1.58
Comp_1:5	2675.9	1.35
Comp_1:6	2641.5	1.32
Comp_1:8	1876.01	0.99

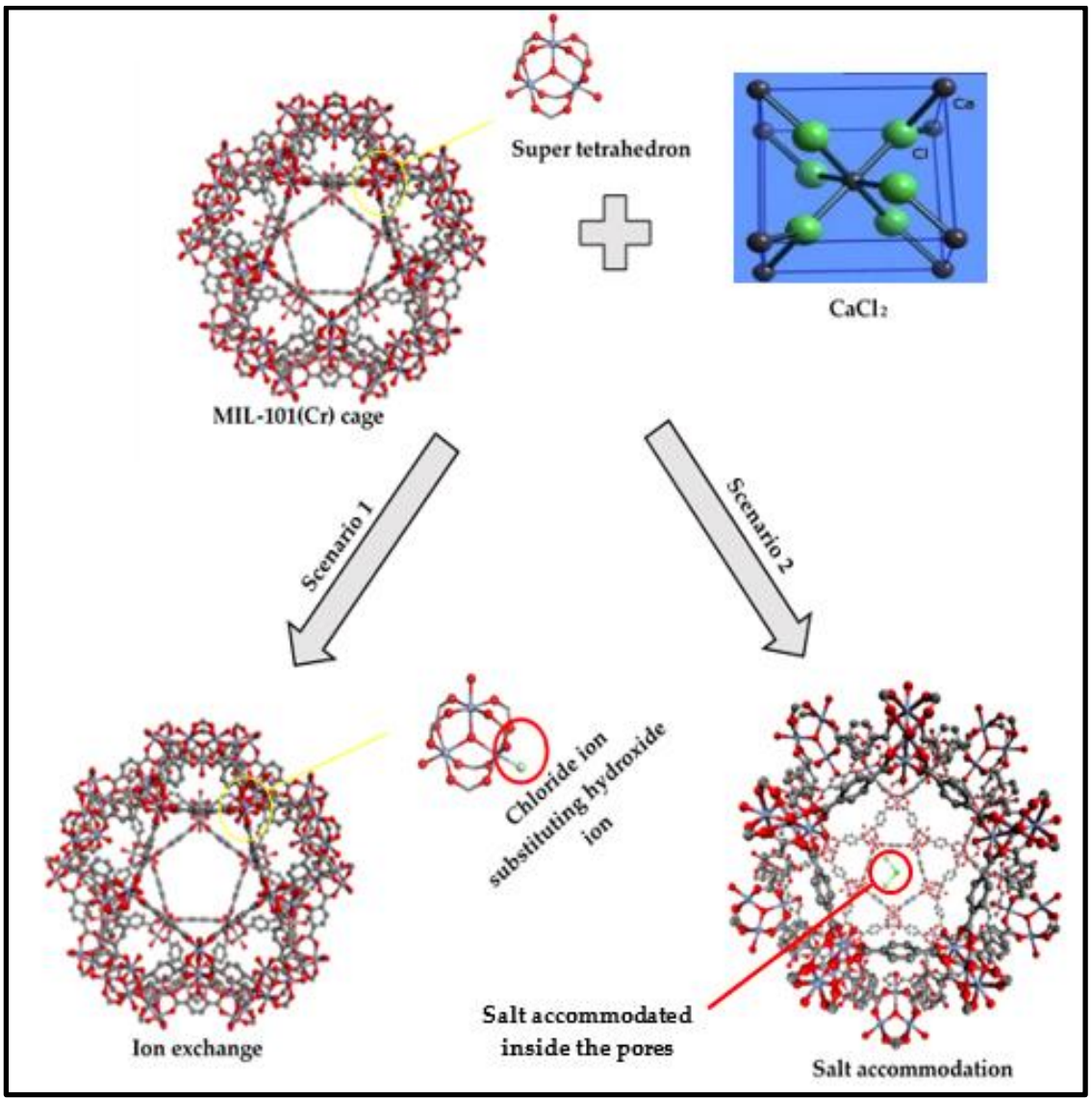

Fig. 5-7 MIL-101(Cr) cage and configuration of the $CaCl_2$ on the MIL-101(Cr)/$CaCl_2$ composites.
(Figure was developed using Materials Studio software)

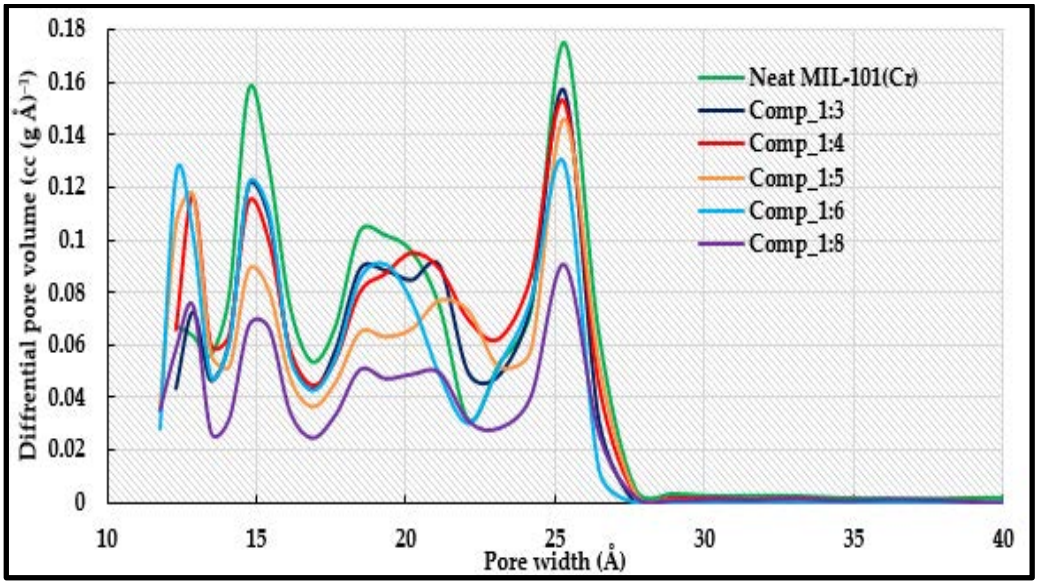

Fig. 5-8 Pore size distribution of MIL-101(Cr) and its $CaCl_2$ composites.

5.2.2.3. Thermogravimetric analysis (TGA)

Fig. 5-9 shows the change in mass as a function of temperature for the parent MIL-101(Cr), GrO and their composites. It can be noticed that there were three stages of weight loss. In the first stage, the materials lose the guest water trapped in their pores. In this stage, MIL-101(Cr) lost almost 50% of its weight till it reached a temperature of 137°C while the synthesis composites showed a lower weight loss. The physical composites showed a much lower water content than the neat material and the synthesis composites.

In the second stage, the materials lose its co-ordinated water molecules hence a lower weight loss is expected. For MIL-101(Cr), this stage took place in the temperature range of 137–337°C while it was shifted to higher temperature ranges in case of composites. This shows that the composites improved the thermal stability of the neat material. The decomposition of the structure and the combustion of the terephthalic acid caused the weight loss in the final stage [225].

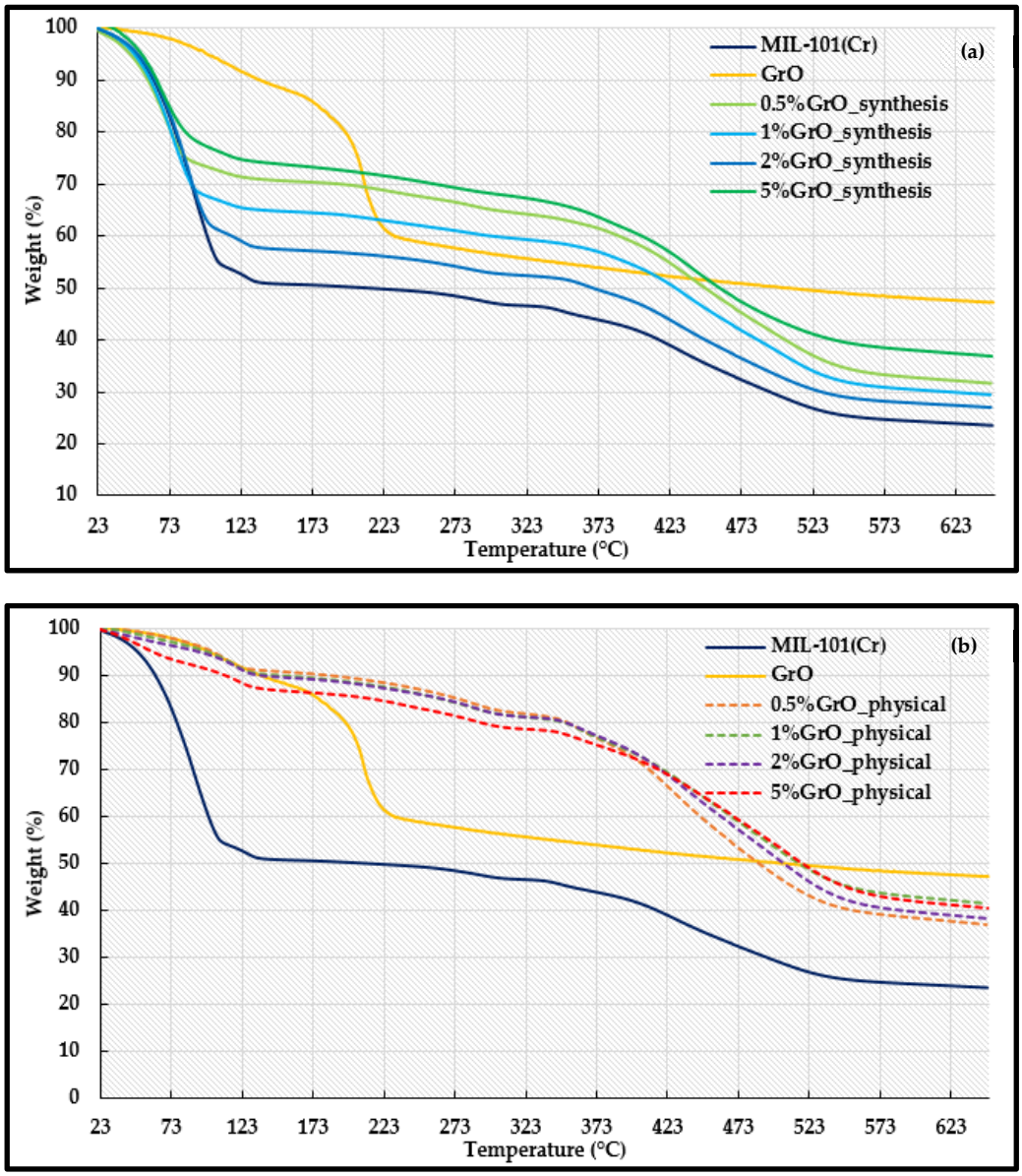

Fig. 5-9 TGA of MIL-101(Cr), GrO, a. GrO synthesis composites and b. GrO physical composites [225].

Regarding the $CaCl_2$ composites and similar to the GrO composites, as the $CaCl_2$ concentration in the composite increased, the thermal stability of the composite was increased (**Fig. 5-10**). In the first stage, all the composites showed slightly lower weight loss due to the removal of the guest water molecules except for the Comp_1:8 composite which showed a much lower weight loss.

In the second stage, it can be noticed that all the composites showed a higher thermal stability over the temperature range 123-423°C which is higher than that of MIL-101(Cr) (137–337°C). This highlights the higher thermal stability of the $CaCl_2$ composites.

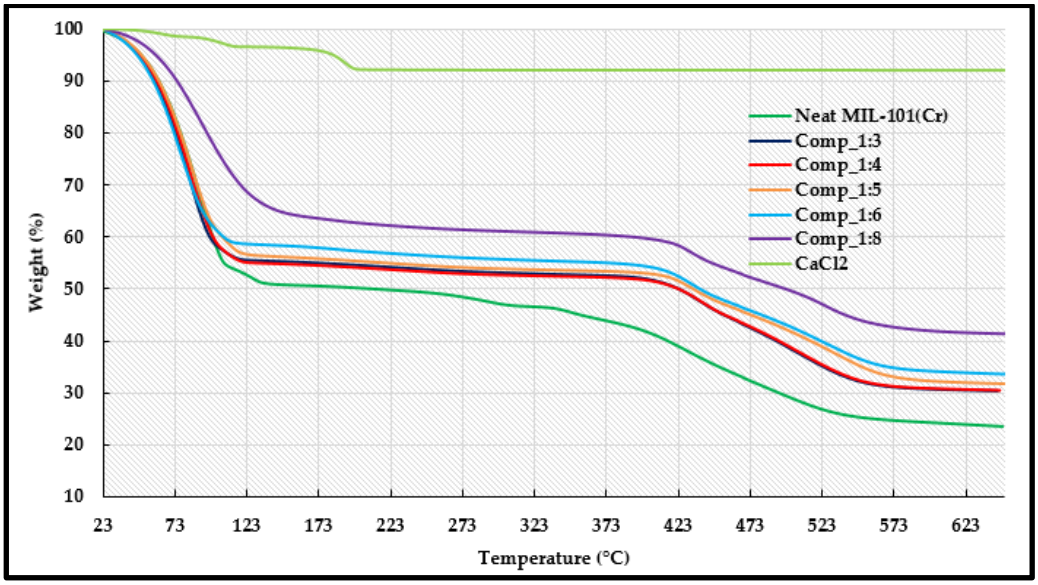

Fig. 5-10 TGA of MIL-101(Cr) and its $CaCl_2$ composites.

5.2.2.4. Scanning Electron Microscopy (SEM)

The morphology of MIL-101(Cr) and the effect of GrO and $CaCl_2$ on its crystals were investigated using SEM images. **Fig. 5-11** shows the SEM images of MIL-101(Cr), GrO and its composites. It can be noticed that, MIL-101(Cr) had well defined octahedral crystals as shown in **Fig. 5-11a** while the wrinkles on the GrO sheets (**5-11b**) are due to the presence of the functional groups (hydroxyl, carboxylate and epoxide) [277]. Regarding the synthesis composites, it can be noticed that as the GrO content increased, the formed crystals started to lose their defined octahedral shape. This supports the suggestion that as the GrO content increases, additional constraints on the crystal growth of the MIL-101(Cr) crystals are expected which causes a partial distortion in the crystal morphology (**Fig. 5-4**). Increasing the GrO concentration to 5%, the crystals completely lost its defined shape, became irregular and agglomerated into larger particles. In case of the physical composites, their surface was much rougher than that of the MIL-101(Cr) which may be attributed to that the graphene layers covering the MIL-101(Cr) crystals [225].

In the case of the $CaCl_2$ composites, **Fig. 5-12** shows that the presence of the salt might have caused the formation of agglomerates. It is also evident that all the composites preserved the defined octahedral crystal shape of the parent MIL-101(Cr). This proves that the presence of $CaCl_2$ did not cause distortion of the pre-synthesized MIL crystals.

The elemental analysis of the different $CaCl_2$ composites was performed using EDX and XRF techniques. It can be noticed that with low concentration of $CaCl_2$ salt, there was almost no traces of Ca^{2+}. This supports the suggestion that in this case the incorporation mechanism is done through ion exchange as shown in scenario 1 (**Fig. 5-7**). In this mechanism, the salt is not accommodated in the pores but rather the Cl^- replaces the OH^- on the chromium cluster. As the salt concentration increased, the concentration of the calcium increased where the 2nd scenario is expected to take place. In this mechanism both salt anions and cations are accommodated inside the pores of the MIL-101(Cr). The concentration of Cl and Cr was also measured using both techniques; good agreement was observed between the EDX and XRF results as the ratio between Cr and Cl is shown in **Table. 5-3**.

Table. 5-3 Elemental analysis of $CaCl_2$ composites using EDX and XRF

	EDX		XRF	
Material	Cr/Cl	Ca/Cl	Cr/Cl	Ca/Cl
Comp_1:3	7.18	0	7.1	0.01
Comp_1:4	5.42	0.04	5.2	0.05
Comp_1:5	2.5	0.25	2.9	0.29
Comp_1:6	3.5	0.20	3.56	0.21
Comp_1:8	0.54	0.48	0.7	0.5

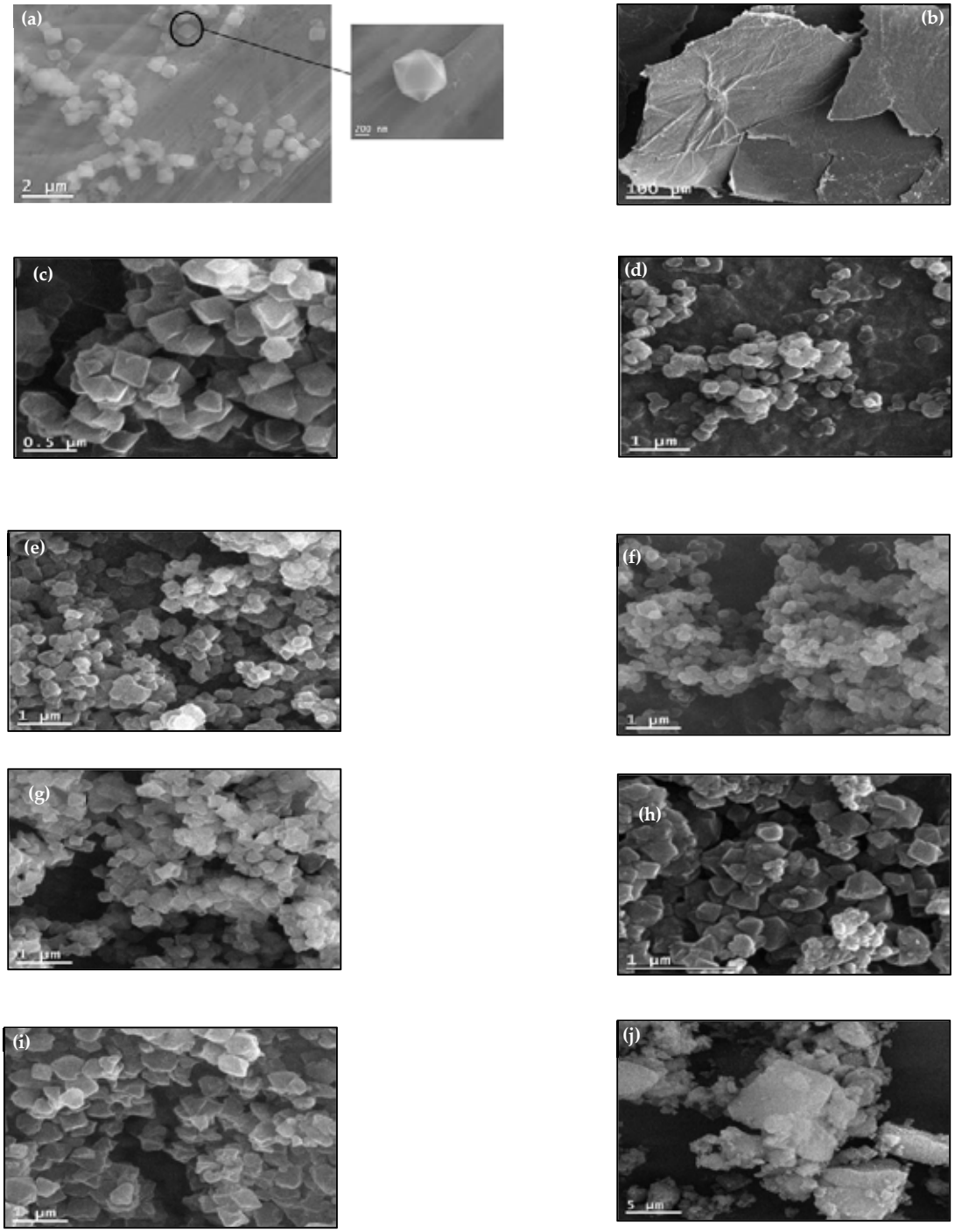

Fig. 5-11 SEM images of a. MIL-101(Cr), b. GrO, c. 0.5%GrO_synthesis, d. 0.5%GrO_physical, e. 1%GrO_synthesis, f. 1%GrO_physical, g. 2%GrO_synthesis, h. 2%GrO_physical, i. 5%GrO_synthesis and j. 5%GrO_physical [225].

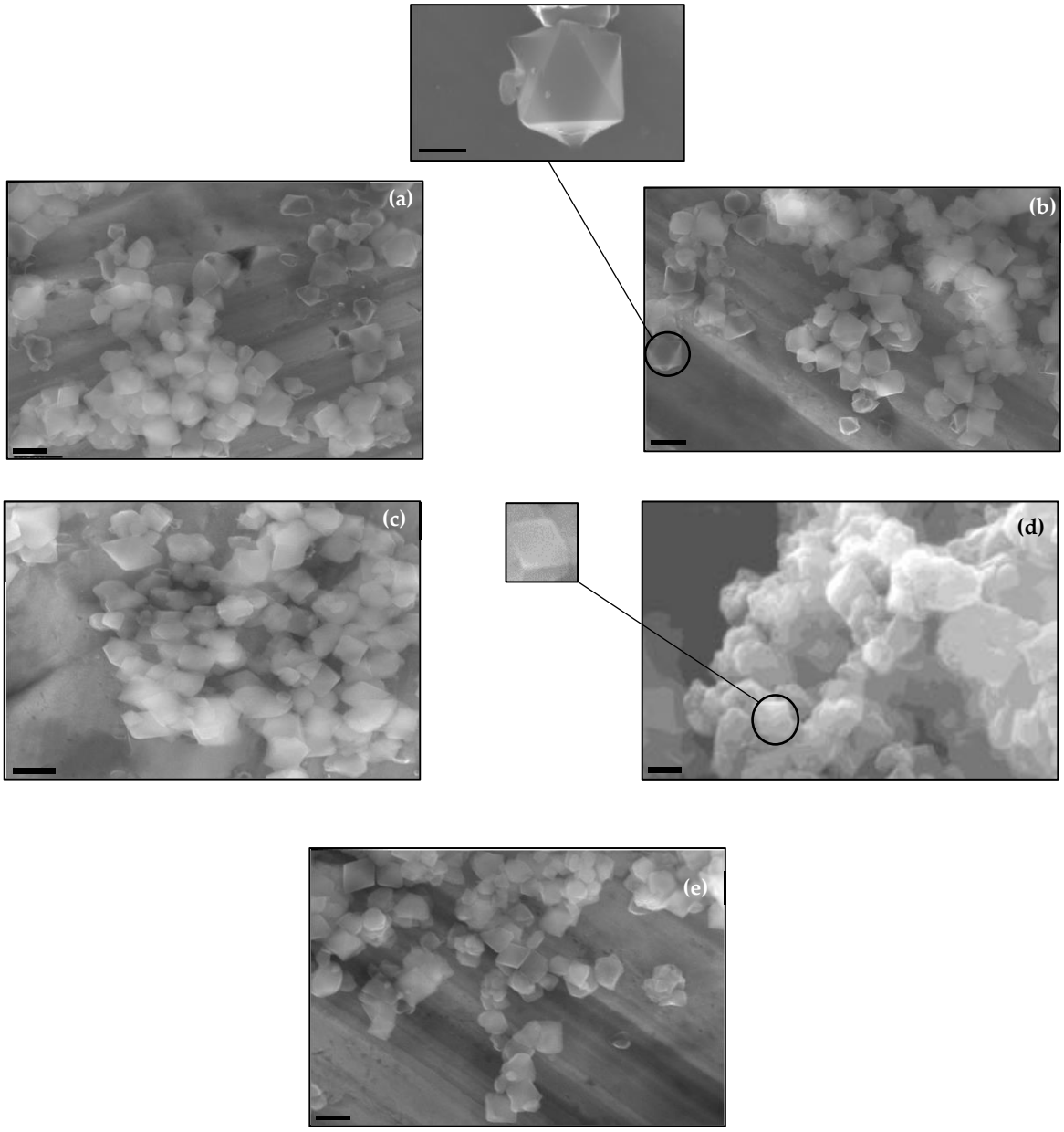

Fig. 5-12 SEM images of MIL-101(Cr)/$CaCl_2$ composites a. Comp_1:3, Comp_1:4, c. Comp_1:5, d. Comp_1:6 and e. Comp_1:8.

5.2.2.5. Fourier Transform Infrared Spectroscopy (FTIR)

Fig. 5-13 shows the FTIR spectra of MIL-101(Cr) and its GrO composites where it can be observed that all the GrO composites preserved the same spectrum. Also, as the GrO concentration increased, the intensity of the 1620 cm^{-1} band increased and became broader. This can be attributed to the functional groups in GrO being co-ordinated to the MOF metallic

sites [149]. Also, a new shoulder appeared at 1570 cm^{-1} and 1050 –1200 cm^{-1} which may be attributed to the formation of new bonds between the GrO and the MIL-101(Cr) structure.

Regarding the $CaCl_2$ composites and similar to the GrO ones, **Fig. 5-14** shows that all the $CaCl_2$ composites preserved the absorption vibrational bands of the parent MIL-101(Cr), indicating that the addition of the salt did not affect the structure of the parent material. Also, a new band appeared at 1570 cm^{-1} which may be attributed to the change of the functionality coordinated to the metal sites in the MOF framework [149].

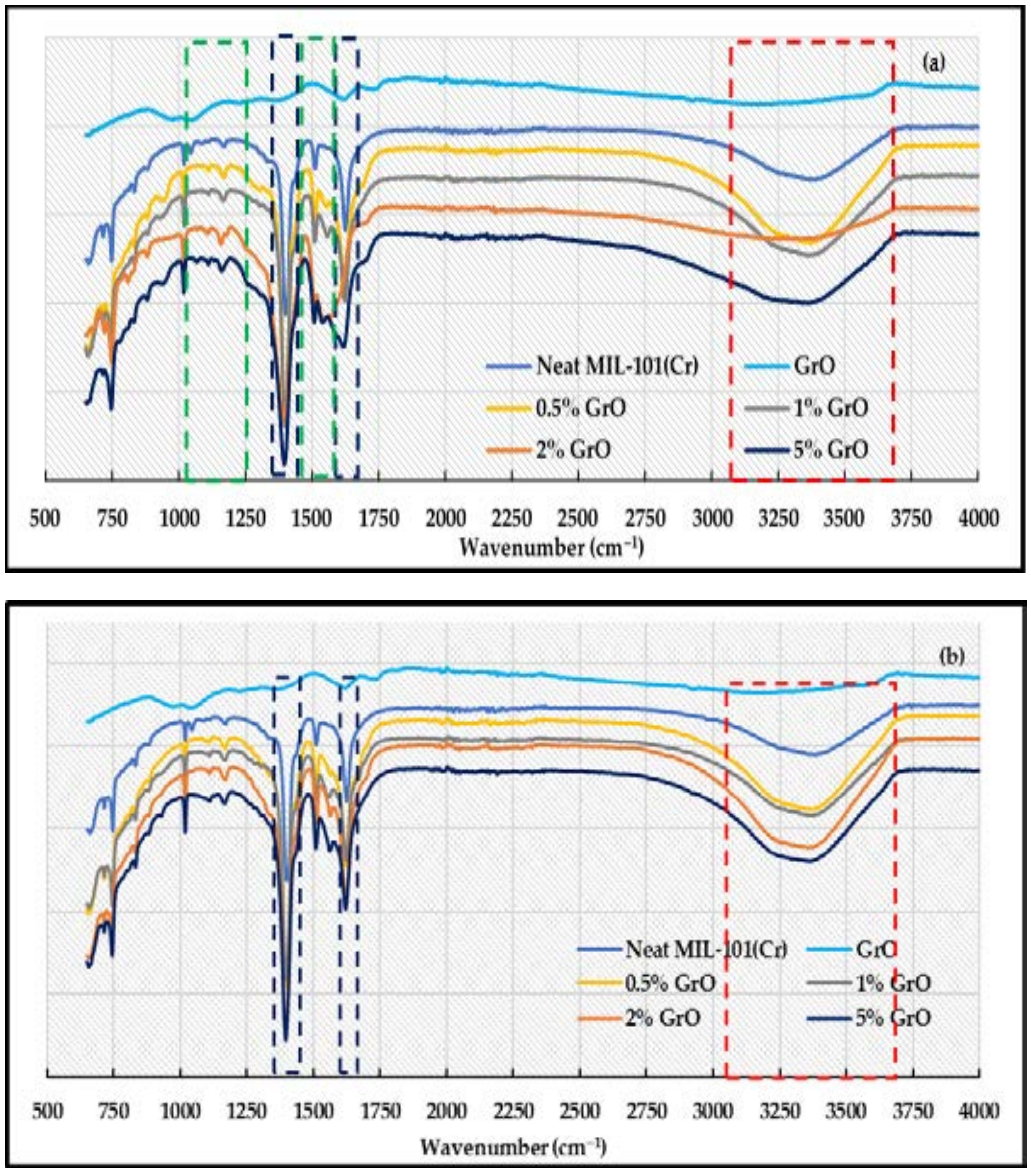

Fig. 5-13 FTIR spectra of MIL-101(Cr), GrO, a. synthesis composites and b. physical composites.

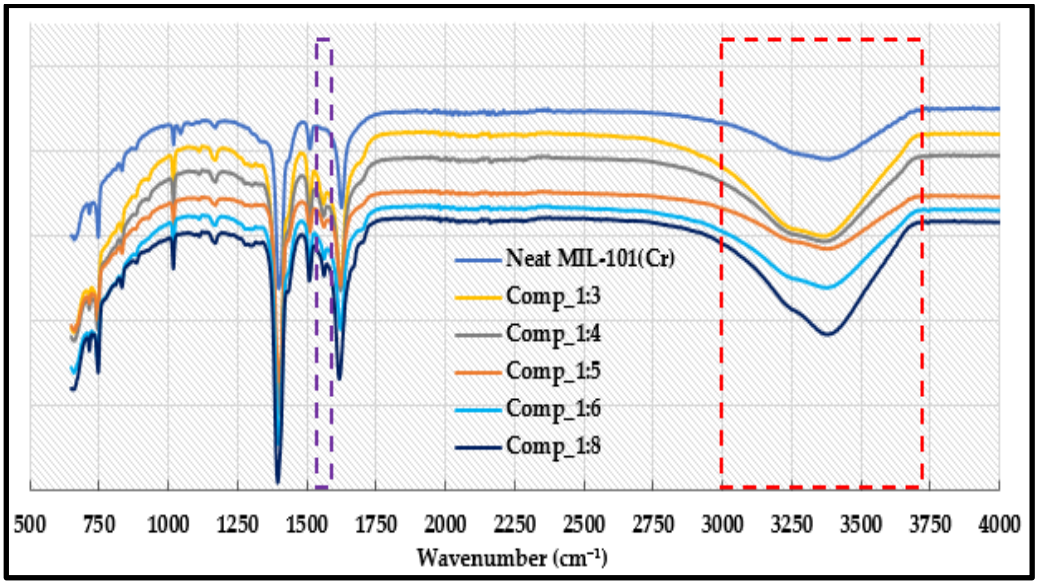

Fig. 5-14 FTIR spectra of MIL-101(Cr) and different $CaCl_2$ composites.

5.2.2.6. True density

The true density of MIL-101(Cr) composites was measured using a helium pycnometer. **Table. 5-4** shows the values of the true, bulk densities and porosity of some of compsoites that were chosen to be further investigated based on their performance namely, MIL-101(Cr), 2%GrO_synthesis and 5%GrO_physical, and $CaCl_2$ composites: Comp_1:4, Comp_1:5 and Comp_1:8.

Table. 5-4 True, bulk densities and porosities of MIL-101(Cr)/GrO and MIL-101(Cr)/$CaCl_2$ composites

Material	True density (kg m^{-3})	Bulk density (kg m^{-3})	Porosity (–)
2%GrO_synthesis	1339	150	0.88
5%GrO_physical	2467.7	157	0.93
Comp_1:4	1343.9	252.8	0.81
Comp_1:5	1311.6	318.6	0.75
Comp_1:8	1458.6	373	0.744

5.2.2.7. Thermal conductivity

MIL-101(Cr) suffers from poor thermal conductivity as a consequence of its large pore size and high free volumes [225]. The thermal conductivity of the parent material was improved through the GrO composites. **Fig. 5-15** shows the thermal conductivity of pellets of different GrO composites as a function of temperature [225].

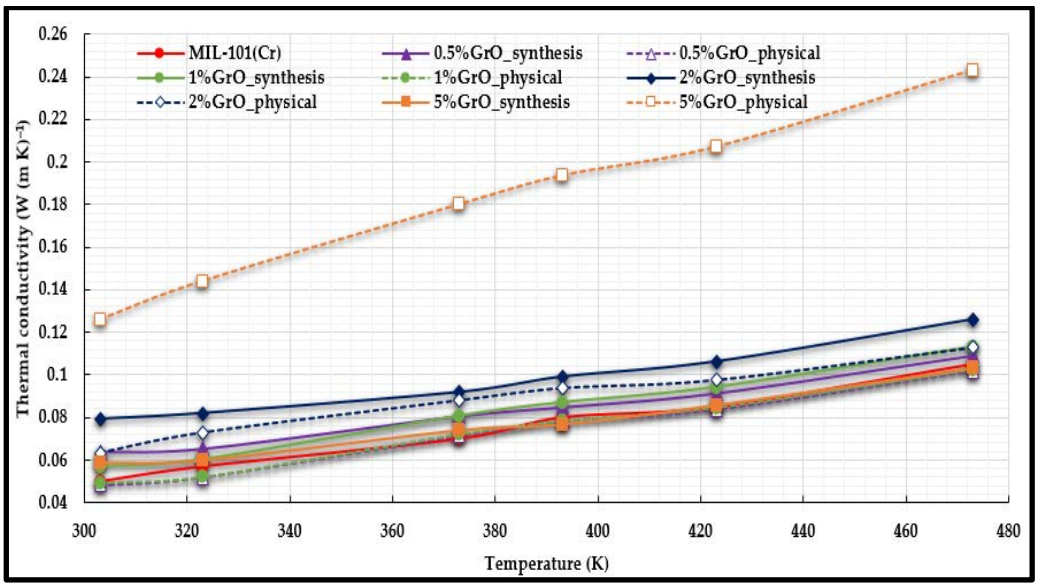

Fig. 5-15 Measured thermal conductivity of MIL-101(Cr) and MIL/GrO composites [225].

It can be noticed that the pellet thermal conductivity of neat MIL-101(Cr) was 0.05 W (m K)$^{-1}$ at 303 K (30°C) which increased linearly to reach 0.103 W (m K)$^{-1}$ at 473 K (200°C). Regarding the GrO composites, it can be noticed that the presence of GrO significantly enhanced the thermal conductivity of the parent MIL-101(Cr). This can be attributed to interactions between the oxygen atoms of the GrO and the MIL-101(Cr) framework [278]. At low GrO concentration (0.5%GrO and 1%GrO), the thermal conductivity was not improved while increasing the GrO content to 2wt%, increased the conductivity by 20–30% compared to the neat material. Further increase in the GrO content (5% in the physical composite), enhanced the thermal conductivity by a factor of 2.5 times. Nevertheless, with the same concentration in the synthesis composites, the thermal conductivity was adversely affected. This was attributed to the insufficient interface between the GrO and the MIL-101(Cr) increasing the interfacial

resistance and reducing the heat flow [277] or due to the crystal defects caused by the presence of the GrO affecting the material's physical properties [225]. As the $CaCl_2$ had no effect on the thermal conductivity, the thermal conductivity of these composites was assumed to be similar to that of parent MIL-101(Cr). **Table. 5-5** shows the empirical equations to estimate the effective thermal conductivity of the 2%GrO_synthesis and 5%GrO_physical and the $CaCl_2$ composites. The specific heat capacities were 1.11, 1.09 and 1.1 kJ $(kg\ K)^{-1}$, respectively.

Table. 5-5 Effective thermal conductivities of MIL-101(Cr)/GrO and MIL-101(Cr)/$CaCl_2$ composites

Material	Effective thermal conductivity $(W\ (m\ K)^{-1})$
2%GrO_syn composite	$-1.261E-4+1.392E-4T_{bed}$
5%GrO_phys composite	$-3.017E-2+2.842E-4T_{bed}$
Comp_1:4	$-4.7E-2+3.1E-4T_{bed}$
Comp_1:5	$-6.8E-2+4.2E-4T_{bed}$
Comp_1:8	$-7E-2+4.3E-4T_{bed}$

5.2.2.8. Water vapour adsorption

5.2.2.8.1. Adsorption isotherms

One of the important features of MIL-101(Cr) that make it a good candidate as an adsorbent in various adsorption applications is its high-water capacity.

Fig. 5-16 shows the water adsorption isotherms of MIL-101(Cr) and its GrO composites, both exhibiting type IV isotherm. At relative pressure ≤0.4, the water vapour adsorption is caused by the unsaturated metal centres (UMCs). UMCs are formed due to the removal of guest ligands from metal atoms in the framework. These sites attract water molecules especially at low realtive pressure ranges. Nevertheless, the low water vapour capacity at this range is due to the hydrophobic effect of the organic linker [225].

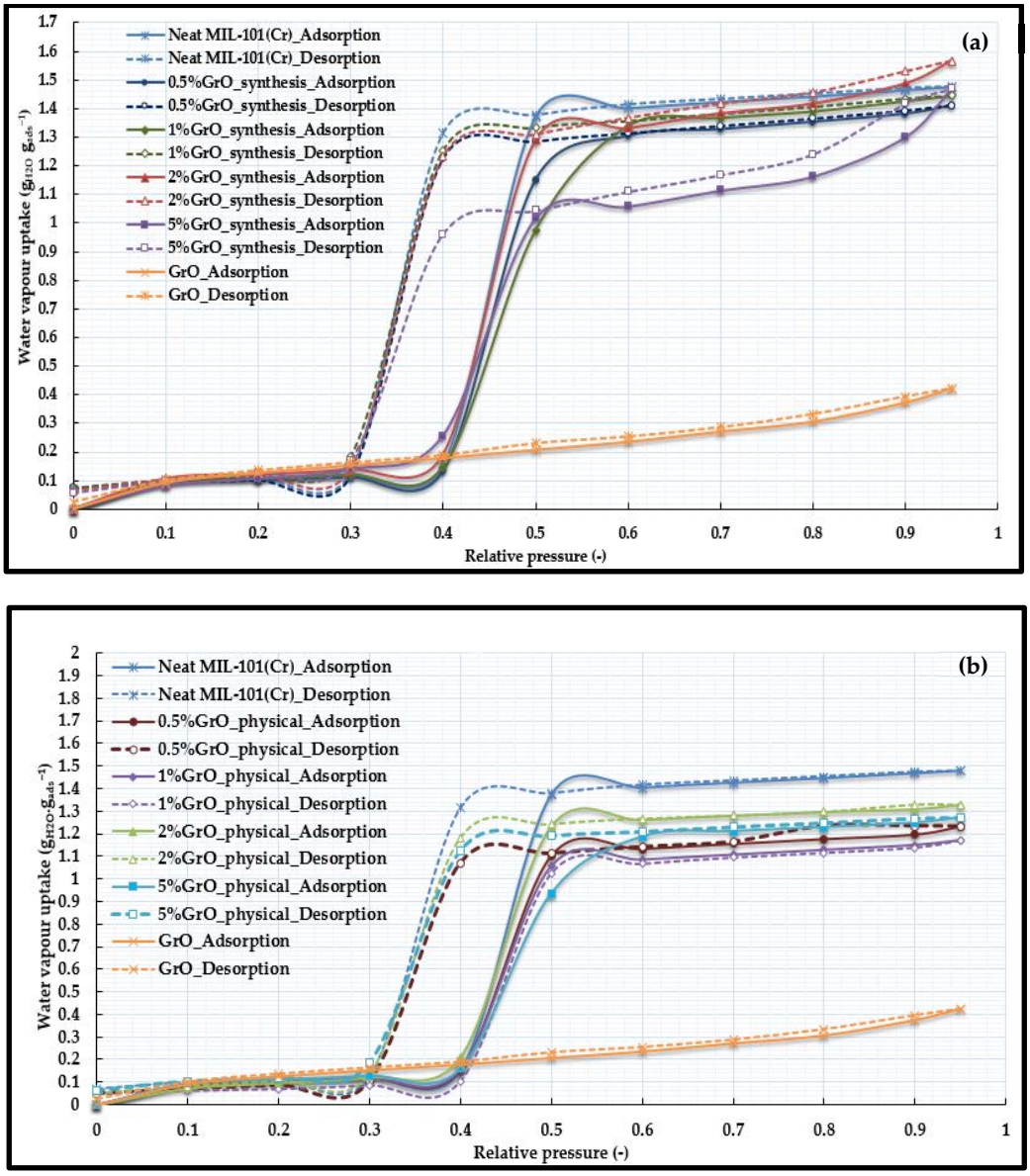

Fig. 5-16 Water adsorption isotherms of neat MIL-101(Cr), GrO and a. synthesis composites and b. physical composites at 25°C [225].

At higher relative pressure (0.4-0.5), the water vapour uptake took a steep increase as the capillary condensation phenomenon took place [18]. This phenomenon also causes the hysteresis loop between the adsorption and desorption processes [24, 259]. For a relative pressure ≥0.5, the materials exhibited a stable uptake as the pores were almost filled. All the physical mixtures exhibited a lower water vapour uptake compared to MIL-101(Cr). This may be attributed to the lower adsorption capacity of GrO, the poorer crystallinity and GrO blocking the pores. It can be noticed that the water vapour of the 2%GrO_synthesis and

5%GrO_synthesis composites increased in the high relative pressure range. This is in agreement with the suggestion that the GrO functional groups coordinated with the metallic centres of MIL-101(Cr) structure creating new meso-pores. The 2%GrO and 5%GrO synthesis composites exhibited a water uptake of 1.56 and 1.5 g_{H_2O} g_{ads}^{-1}, respectively. For the synthesis composites, a concentration of 2wt% GrO is considered as an optimum concentration as decreasing or increasing GrO content would adversely affect the water uptake. This is due to that GrO is a non-porous material and it may block the MIL-101(Cr) pores decreasing the accessible surface area and pore volume of the composites. Hence, the water vapour uptake cannot be improved any further [149, 225]. Also, MIL-101(Cr) spherical shape crystal structure **(Fig. 5-4)** where high amount GrO may create additional constraints on the crystal growth preventing the proper building of the MIL-101(Cr) structure and its cages [274]. For very low GrO concentration (1%GrO and 0.5%GrO) composites, the probability of GrO preventing the proper crystal formation is reduced but at the same time, the GrO concentration is not sufficient to coordinate with the MIL structure and creates new pores, hence no improvement in the water adsorption capacity was observed. Very high GrO concentrations may cause structure partial distortion and may narrow the pore size of parent MIL-101(Cr) [225, 279].

In physical composites, GrO was found to adversely affect the MIL-101(Cr) water vapour capacity as some of the pores are blocked by GrO decreasing its water vapour capacity. It can be concluded that due to the shape of the MIL-101(Cr) adsorption isotherm and its GrO composites, these materials are suitable for adsorption application working at high relative pressures, which may include heat storage, desalination without cooling effect and high temperature cooling [225].

Due to the superior water vapour capacity of the 2%GrO_synthesis composite, and the enhanced thermal conductivity of the 5%GrO_physical, the two composites were chosen to be investigated further.

After measuring the adsorption isotherms at 15°C, 25°C and 35°C, the 2%GrO_synthesis adsorption isotherms were fitted using **Eq. 5-1** to **Eq. 5-3** [260]

$$X = 7.8A^{-0.5} \qquad A > 2100 \qquad \textbf{(5-1)}$$

$$X = 177.276 - 0.54A + 6.4E-4A^2 - 3.73E-7A^3 + 1.06E-10A^4 - 1.17E-14A^5 \qquad 1100 \le A \le 2100 \qquad \textbf{(5-2)}$$

$$X = 1.533 - 8E-5A \qquad A < 1100 \qquad \textbf{(5-3)}$$

Measured adsorption isotherms of the 5%GrO_physical composite at 15°C, 25°C and 35°C were fitted using **Eq. 5-4** to **Eq. 5-6** [260]

$$X = 13.036A^{-0.574} \qquad A \ge 2100 \qquad \textbf{(5-4)}$$

$$X = -477.607 + 0.967A - 7.252E-4A^2 + 2.389E-7A^3 - 2.926027E-11A^4 \qquad 1600 \le A < 2100 \qquad \textbf{(5-5)}$$

$$X = -6.395E-5A + 1.28 \qquad A < 1600 \qquad \textbf{(5-6)}$$

Fig. 5-17 and **Fig. 5-18** show the good agreement between the proposed adsorption isotherm models and the experimental data for both the 2%GrO_synthesis and the 5%GrO_physical.

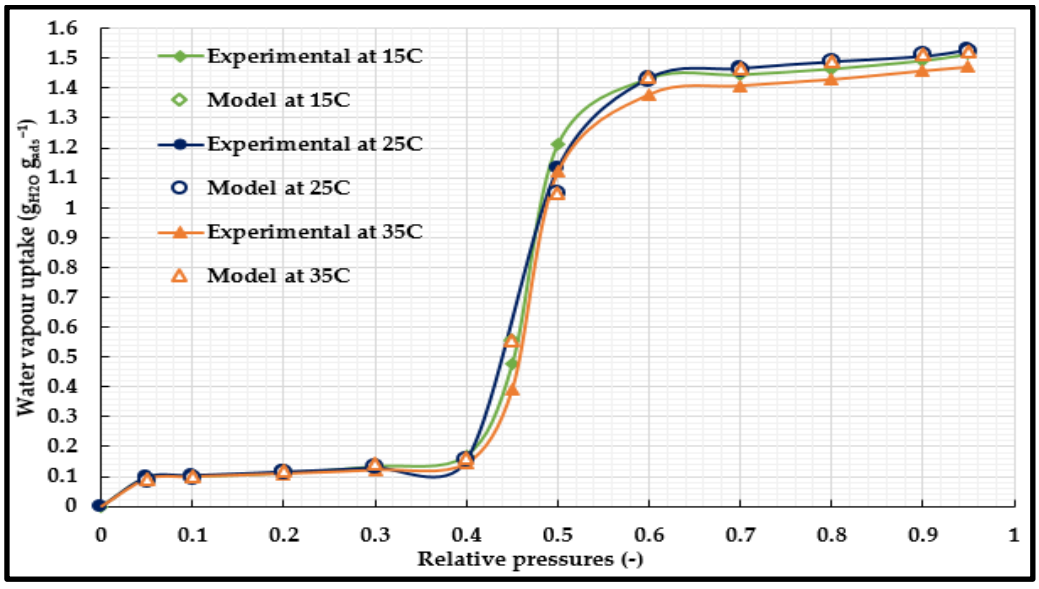

Fig. 5-17 Proposed isotherm model fitting of water adsorption on 2%GrO_synthesis at different adsorption temperatures.

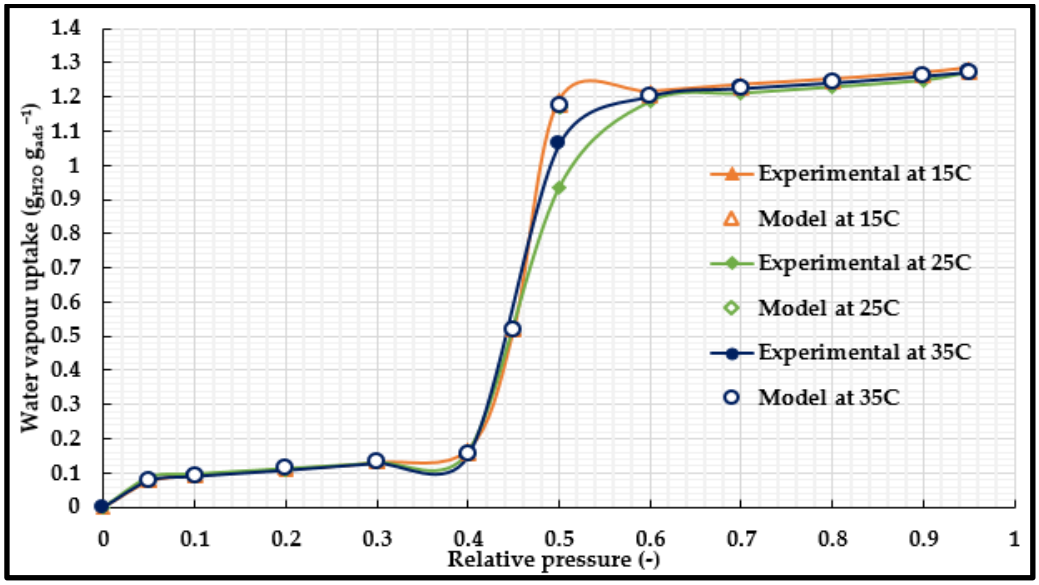

Fig. 5-18 Proposed isotherm model fitting of water adsorption on 5%GrO_physical at different adsorption temperatures.

The performance stability of the two MIL-101(Cr)/GrO composites was investigated through subjecting the materials to ten successive adsorption/desorption cycles (**Fig. 5-19**) highlighting the performance stability of the two composites.

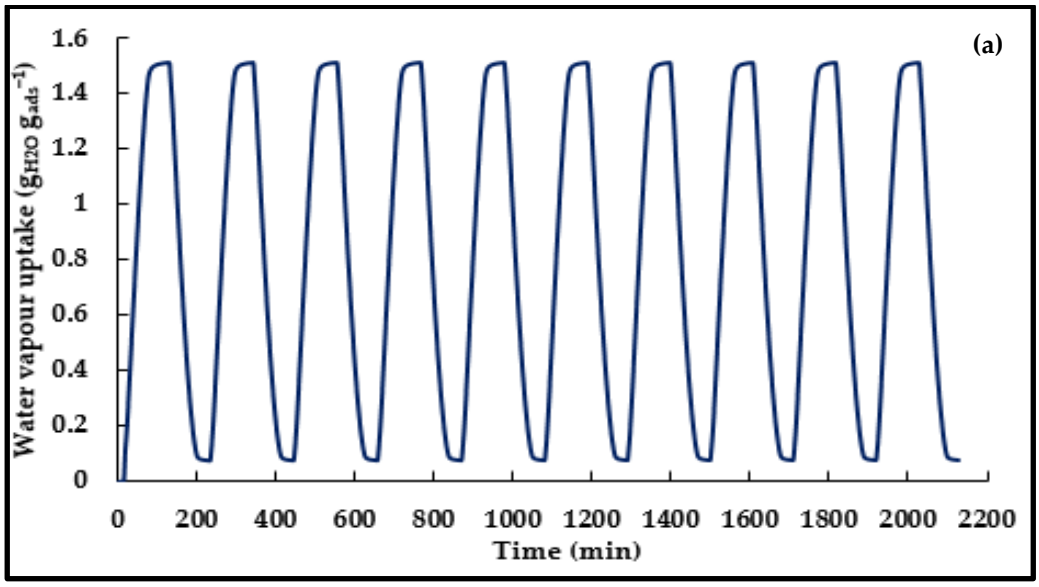

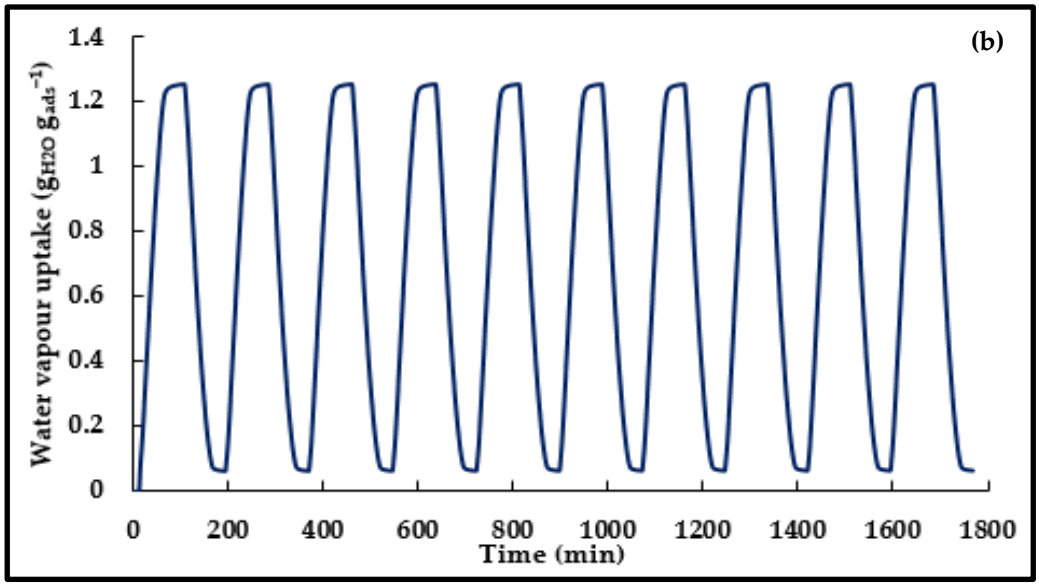

Fig. 5-19 Cyclic analysis (10 adsorption/desorption cycles) of MIL-101(Cr)/GrO composites: a. 2%GrO_synthesis and b. 5%GrO_physical at 25°C and a relative pressure of 0.9.

As previously highlighted, MIL-101(Cr) and its GrO composites are only suitable for applications working at high relative pressure or high evaporation temperatures. This means that these materials are impractical for adsorption cooling applications due to the limited uptake in the low relative pressure range. This problem was addressed through synthesizing MIL-101(Cr)/$CaCl_2$ composites. **Fig. 5-20** shows the water adsorption isotherms of the neat material, Comp_1:3, Comp_1:4 and Comp_1:5 composites that also exhibited type IV isotherms. Nevertheless, it can be noticed that introducing the $CaCl_2$ significantly enhanced the water vapour uptake especially for the Comp_1:5 $CaCl_2$ composite. This is attributed to the presence of the hydrophilicity and hygroscopic nature of $CaCl_2$ which outweighs the hydrophobic effect of the organic ligand. At a relative pressure higher than 0.5, it can be noticed that all the composites have lower water vapour capacity. This can be attributed to the pores being partially filled with the salt and hence the accessible pores and surface area for the water molecules decreased causing the water vapour uptake to decrease. At higher relative pressure (≥0.5), the pores are almost filled exhibiting a stable uptake.

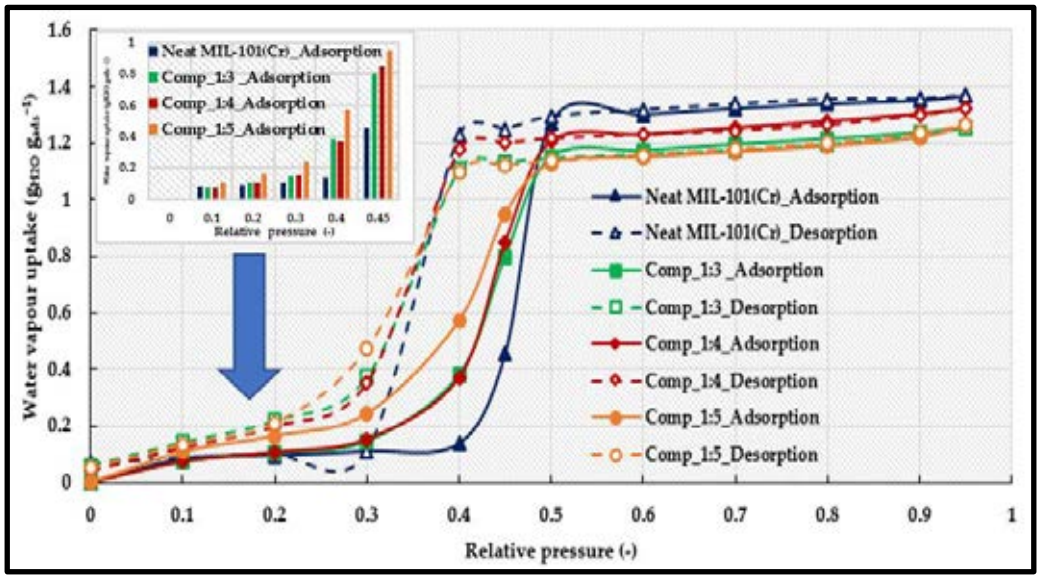

Fig. 5-20 Water adsorption isotherms of neat MIL-101(Cr) and $CaCl_2$ composites: Comp_1:3, Comp_1:4 and Comp_1:5 at 25°C.

Fig. 5-21 shows the water adsorption isotherm of the Comp_1:6 and Comp_1:8 composites. It can be noticed, that the Comp_1:6 maintained the type IV isotherm, while increasing the concentration of the $CaCl_2$ further changed the isotherm to a type II in the Comp_1:8 composite. This may be attributed to increasing salt concentration changing the impregnation mechanism from ion exchange to salt accommodation. Such adsorption isotherm was observed in the case of SWS-1L. At a relative pressure lower than 0.3, the anhydrous salt accommodated in the pores of the structure started forming a low hydration degree of the salt; this may be similar in composition to the bulk phase of ($CaCl_2.0.33H_2O$). A plateau was observed in the range (0.3-0.5), where the water content may correspond to two water molecules per calcium ion as in the solid stable crystalline hydrate $CaCl_2.2H_2O$. As the relative pressure increased, the water vapour capacity increased and a higher degree of hydration comparable to that in ($CaCl_2.4H_2O$) was formed [201, 202]. This shows that introducing the $CaCl_2$ significantly enhanced the water adsorption characteristics at the low relative pressure range.

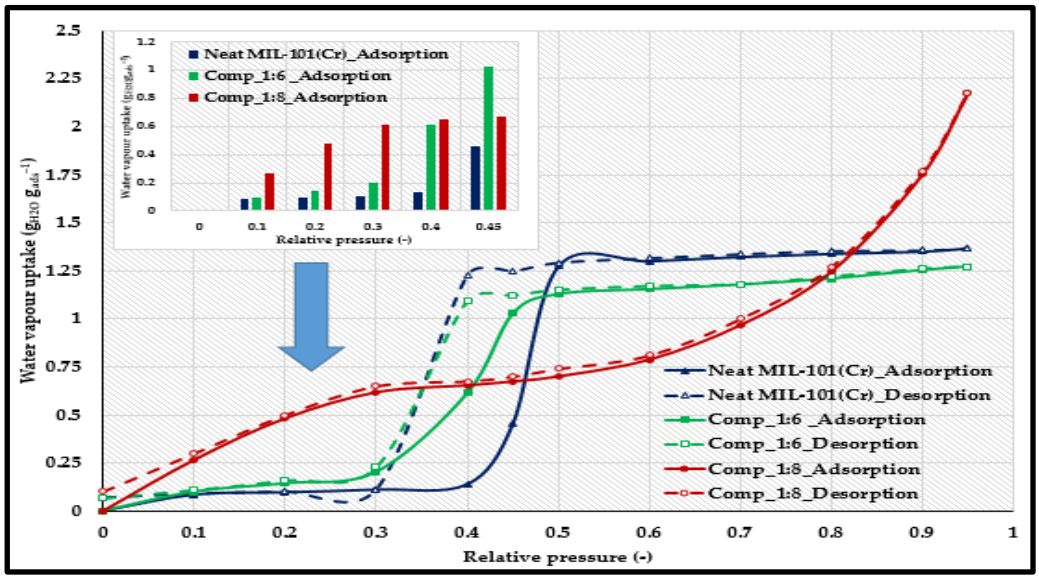

Fig. 5-21 Water adsorption isotherms of neat MIL-101(Cr) and $CaCl_2$ composites: Comp_1:6 and Comp_1:8 at 25°C.

As Comp_1:4, Comp_1:5 and Comp_1:8 had the highest water vapour uptake, they were investigated further.

The adsorption isotherms of Comp_1:4 composite were measured at 15°C, 25°C and 35°C and fitted using **Eq. 5-7** to **Eq. 5-9**.

$$X = 210.3A^{-0.92} \qquad A \geq 3700 \qquad \textbf{(5-7)}$$

$$X = 24.2 - 2.9E - 3A + 1.2E - 5A^2 - 2.5E - 9A^3 + 1.8E - 13A^4 \qquad 1840 \leq A < 3700 \qquad \textbf{(5-8)}$$

$$X = 1.27 + 4.7E - 4A - 1.5E - 6A^2 + 1.4E - 9A^3 - 4.2E - 13A^4 \qquad A < 1840 \qquad \textbf{(5-9)}$$

Fig. 5-22 shows good agreement between the proposed isotherm model and the experimental data in case of Comp_1:4 composite.

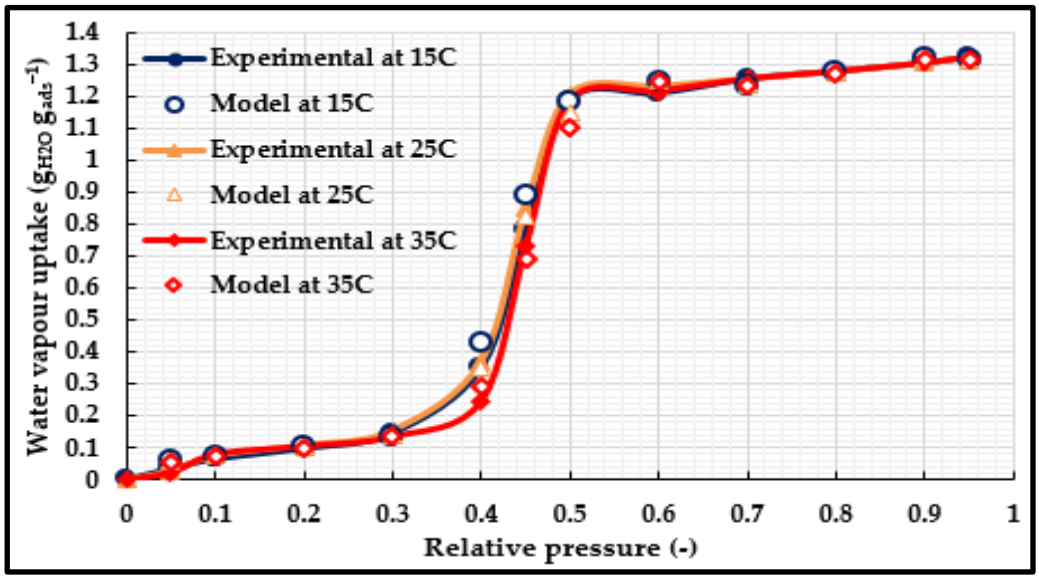

Fig. 5-22 Proposed isotherm model fitting of water adsorption of Comp_1:4 at different adsorption temperatures.

The Comp_1:5 composite adsorption isotherms were measured at 15°C, 25°C and 35°C and fitted using **Eq. 5-10** to **Eq. 5-12**.

$$X = 0.64\exp(-3E - 4A) \qquad A > 3700 \qquad \textbf{(5-10)}$$

$$X = 16.6 - 1.8E - 2A + 7.8E - 6A^2 - 1.5E - 9A^3 + 1E - 13A^4 \qquad 1840 < A \leq 3700 \qquad \textbf{(5-11)}$$

$$X = 1.34 - 6.5E - 4A + 7.5E - 7A^2 - 2.7E - 10A^3 \qquad A \leq 1840 \qquad \textbf{(5-12)}$$

Fig. 5-23 shows the good agreement between the proposed isotherm model and the experimental data in case of Comp_1:5 composite.

The Comp_1:8 composite adsorption isotherms were measured at 15°C, 25°C and 35°C and fitted using **Eq. 5-13** to **Eq. 5-15**.

$$X = 1.65\exp(-3.2E - 4A) \qquad A > 2700 \qquad \textbf{(5-13)}$$

$$X = 1.1 - 3.3E - 4A + 5.6E - 8A^2 \qquad 1200 \leq A \leq 2700 \qquad \textbf{(5-14)}$$

$$X = 2.45 - 2.8E - 3A + 1.2E - 6A^2 \qquad 1200 > A \qquad \textbf{(5-15)}$$

Fig. 5-24 shows the good agreement between the proposed isotherm model and the experimental data in case of Comp_1:8 composite.

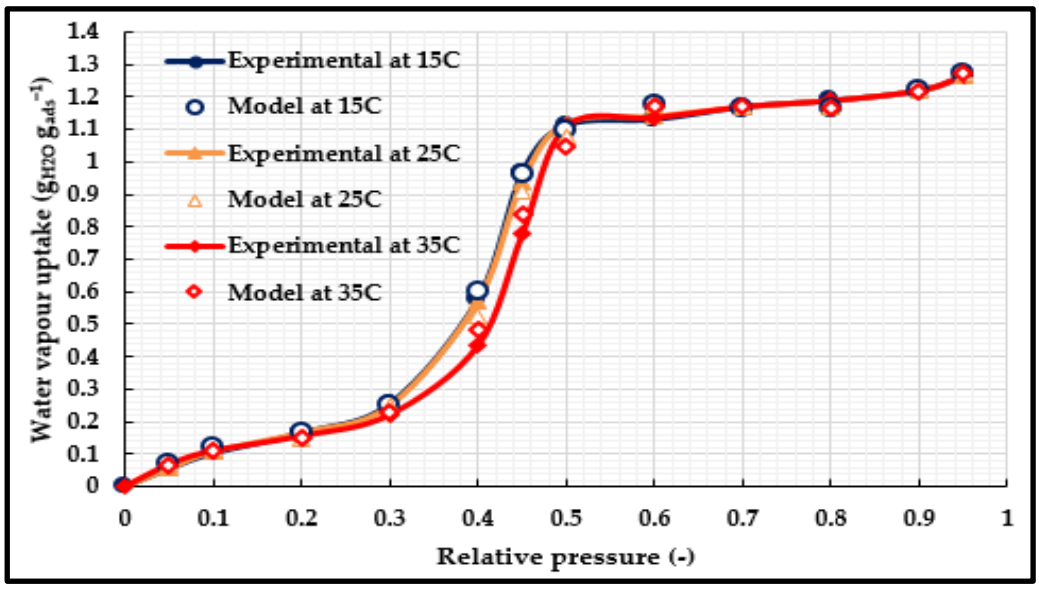

Fig. 5-23 Proposed isotherm model fitting of water adsorption of Comp_1:5 at different adsorption temperatures.

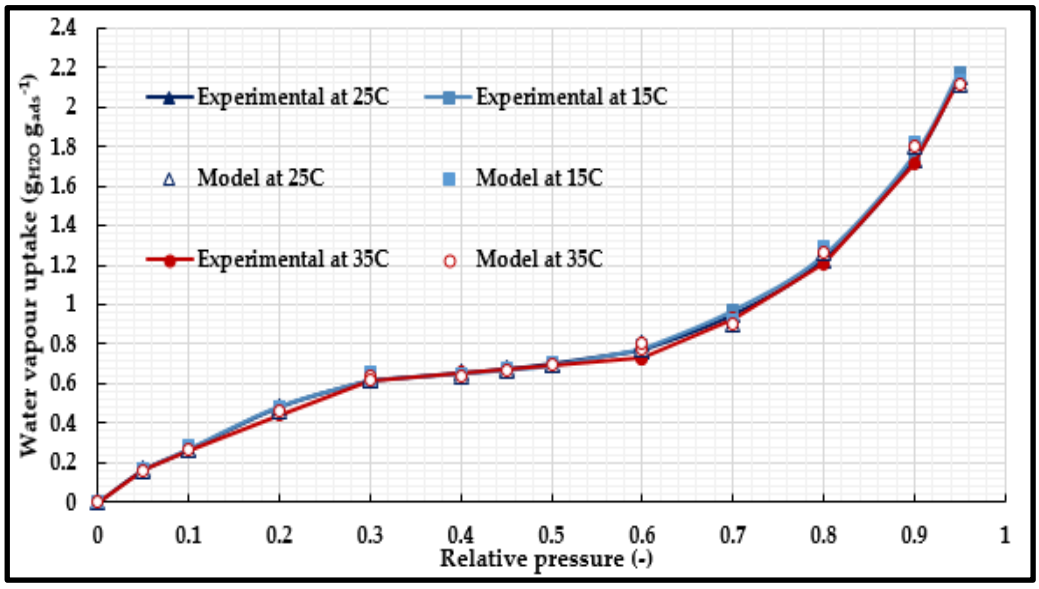

Fig. 5-24 Proposed isotherm model fitting of water adsorption of Comp_1:8 at different adsorption temperatures.

The performance stability of the $CaCl_2$ composites was investigated through subjecting the materials to ten successive adsorption/desorption cycles; the materials showed excellent performance stability. As the main improvement in the water uptake took place below a relative pressure of 0.5, the cyclic analysis was investigated for 10 successive cycles in the range 0-

0.45. As shown in **Fig. 5-25**, the composites had a steady performance over the tested cycles and the high uptake was not affected by the successive adsorption/desorption processes.

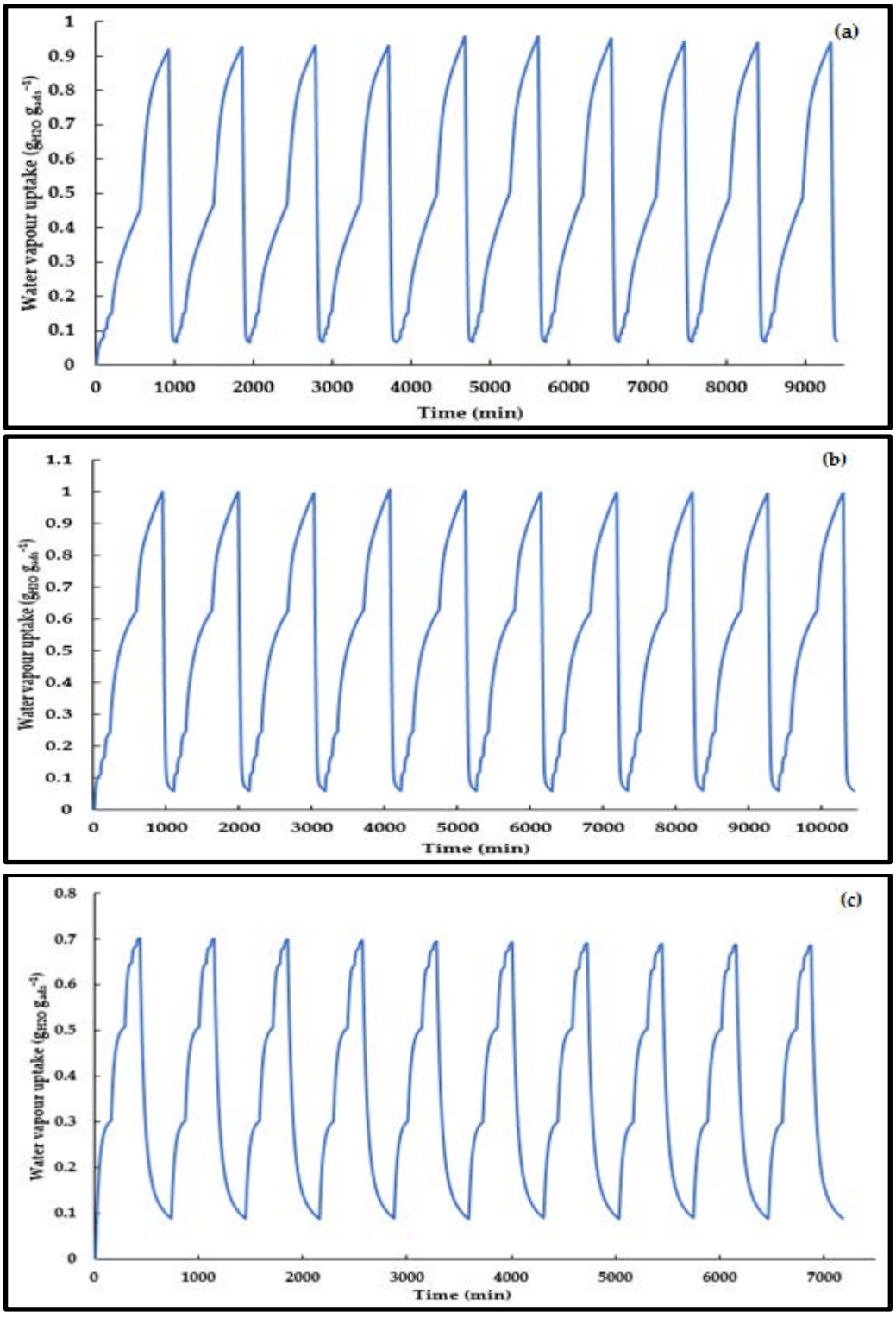

Fig. 5-25 Cyclic analysis (10 adsorption/desorption cycles) of $CaCl_2$ composites: a. Comp_1:4, b. Comp_1:5 and c. Comp_1:8 at 25°C.

5.2.2.8.2. Adsorption Kinetics

The rate of water adsorption was predicted through applying the linear driving force (LDF) (**Eq. 3-21** to **Eq. 3-24). Table. 5-6** gives the values of parameters E_a and k_0 for the different MIL-101(Cr) composites, while **Fig. 5-26** to **Fig. 5-30** highlight the validity of the LDF model in fitting the experimental data of the materials under investigation.

Table. 5-6 Values of LDF equation parameters

Material	Relative pressure range	E_a (J mol^{-1})	k_0 (s^{-1})
2% GrO_synthesis	>0.4&≤0.5	30,872	1.5E3
	≤0.4&>0.5	31,148	42.4
5% GrO_physical	≤0.4&>0.5	30,872	718
	≤0.4&>0.5	31,148	42.4
Comp_1:4	<0.4&>0.5	24,997	31.87
	≥0.4&≤0.5	27,266	10.87
Comp_1:5	<0.4&>0.5	24,868	4.01
	≥0.4&≤0.5	27,266	10.87
Comp_1:8	≤0.2	30,193	84
	>0.2	30,193	204

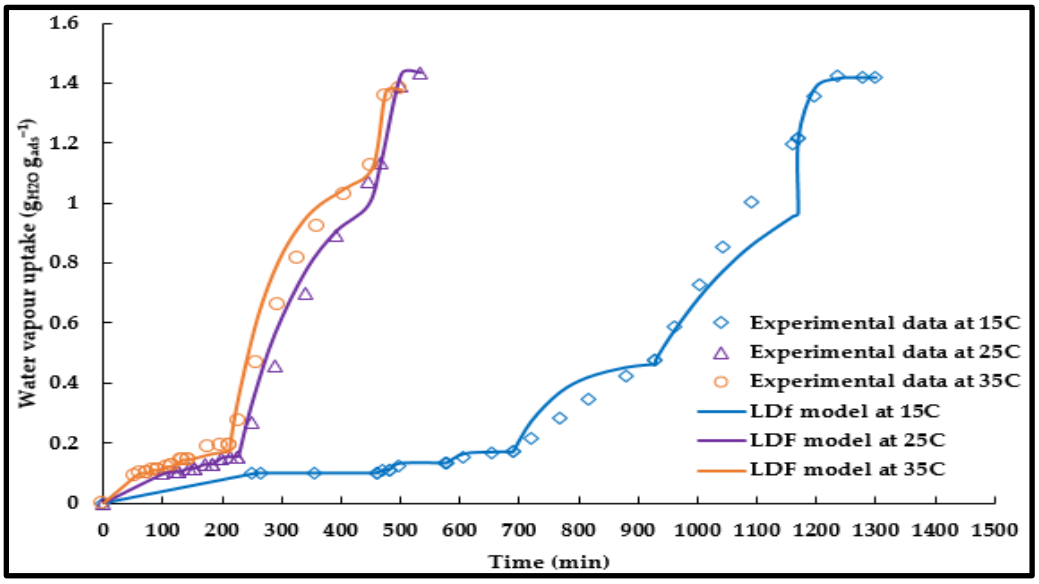

Fig. 5-26 LDF model fitting of water adsorption of 2%GrO_syn composite at 15°C, 25°C and 35°C.

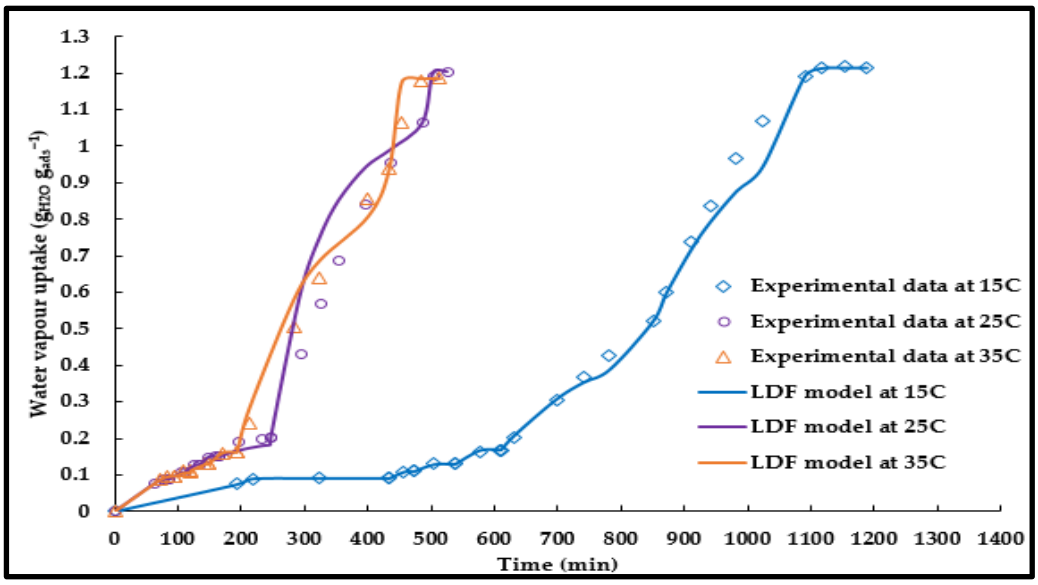

Fig. 5-27 LDF model fitting of water adsorption of 5%GrO_phys composite at 15°C, 25°C and 35°C.

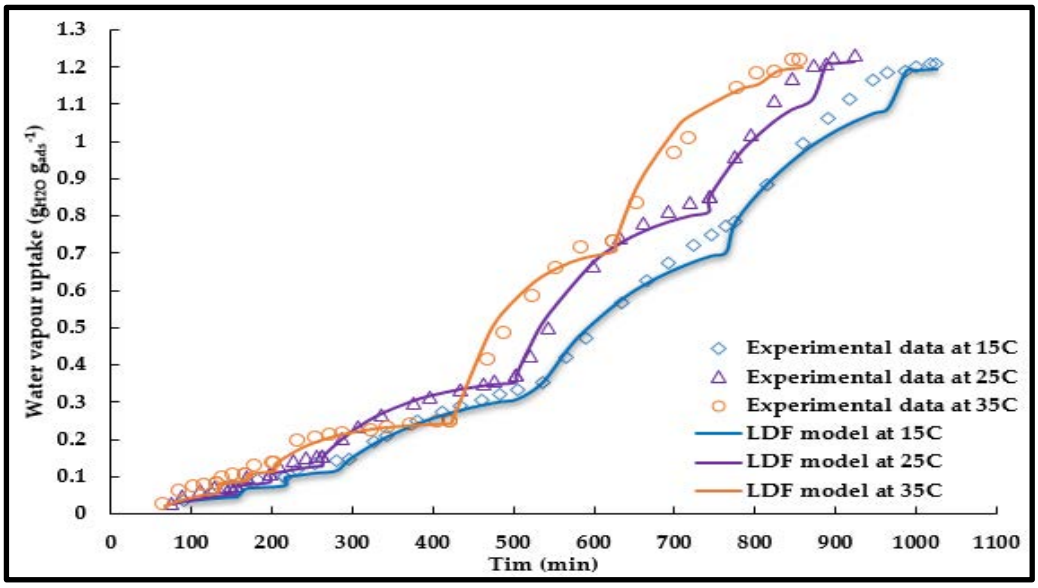

Fig. 5-28 LDF model fitting of water adsorption of Comp_1:4 at 15°C, 25°C and 35°C.

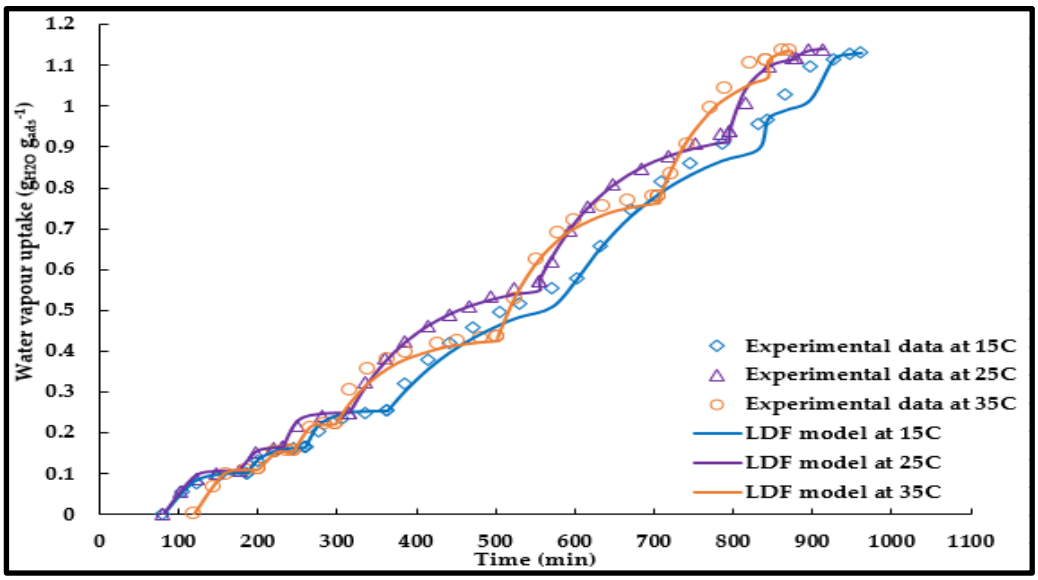

Fig. 5-29 LDF model fitting of water adsorption of Comp_1:5 at 15°C, 25°C and 35°C.

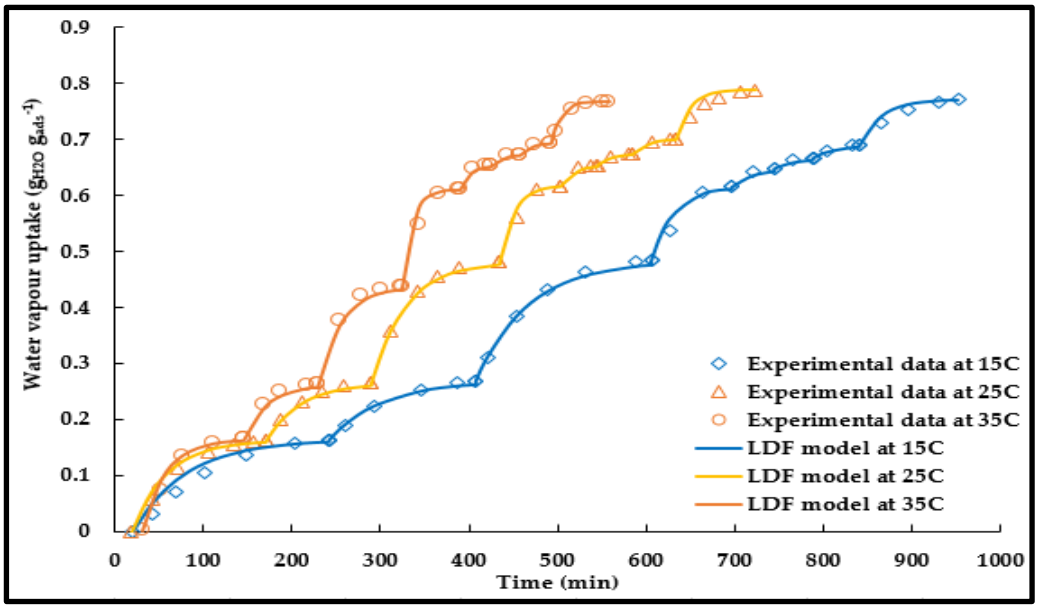

Fig. 5-30 LDF model fitting of water adsorption of Comp_1:8 at 15°C, 25°C and 35°C.

5.3. MIL-100(Fe) composites

5.3.1. Synthesis

MIL-100(Fe) is a mesoporous material with two types of cages. The high performance of the material was further improved through the synthesis of novel composites with other MOFs, namely MIL-101(Cr) and CPO-27(Ni) to exploit the unique water adsorption characteristic of the two MOFs at the high and low relative pressure range, respectively.

5.3.1.1. MIL-101(Cr)/MIL-100(Fe) composites

A hybrid MIL-101(Cr)/MIL-100(Fe) composite was synthesized through using MIL-101(Cr) as the seeding crystals. The pre-synthesised MIL-101(Cr) powder was added to the reaction solution of MIL-100(Fe), consisting of 1.0 Fe^0: 0.67 1,3,5-BTC (1, 3, 5-BTC = 1,3,5-benzenetricarboxylic acid or trimesic acid): 0.6 HNO_3: 277 H_2O. The reactant mixture was loaded in a 100ml round-bottomed flask, and the flask was heated up to the reaction temperature and kept at 90-95^oC for 16 hr with furtherly investigating the effect of MIL-101(Cr) %weight. The light orange solid product was recovered by centrifugation, and the separated solids were further purified by a two-step process using an equal volume of water and ethanol. The purification was performed at 80^oC for 1 hr each time. After centrifugation for the last time, the solids were finally dried overnight in air.

5.3.1.2. CPO-27(Ni)/MIL-100(Fe) composites

Another hybrid composite was synthesized through using CPO-27(Ni) as the seeding crystals. The CPO-27(Ni) powder was added to the reaction solution of MIL-100(Fe), consisting of 1.0 Fe^0: 0.67 1,3,5-BTC (1,3,5-BTC = 1,3,5-benzenetricarboxylic acid or trimesic acid): 0.6 HNO_3: 277 H_2O. The reactant mixture was loaded in a 100ml round-bottomed flask, and the flask was heated up to the reaction temperature and kept at 90-95^oC for 16 hr. The effect of CPO-27(Ni) %weight was further investigated. The light greenish solid product was recovered by centrifugation, and the separated solids were further purified by a two-step process

using an equal volume of water and ethanol. The purification was performed at 80°C for 1 hr each time. After the last centrifugation, the solids were finally dried overnight in air.

5.3.2. Characterization

5.3.2.1. Powder XRD

Two types of composites were synthesized through introducing MIL-101(Cr) and CPO-27(Ni) in different amounts based on the mass of MIL-100(Fe). **Fig. 5-31** shows the XRD patterns of MIL-100(Fe), MIL-101(Cr) and the synthesized MIL-101(Cr)/MIL-100(Fe) composites. It can be noticed that the diffraction peaks of the MIL-100(Fe) were preserved in all the composites which means that the presence of the pre-synthesized MIL-101(Cr) did not interfere with the formation of the MIL-100 crystals. It can also be noticed that as the concentration of MIL-101(Cr) increased, the diffraction peaks of MIL-101(Cr) became more evident. This confirms the co-presence of both MOFs in the synthesized composite. A similar behaviour was also noticed regarding the CPO-27(Ni)/MIL-100(Fe) composites (**Fig. 5-32**). The presence of CPO-27(Ni) did not prevent the formation of MIL-100(Fe) crystals. Also, all the composites had the characteristic diffraction peaks of both CPO-27(Ni) and MIL-100(Fe).

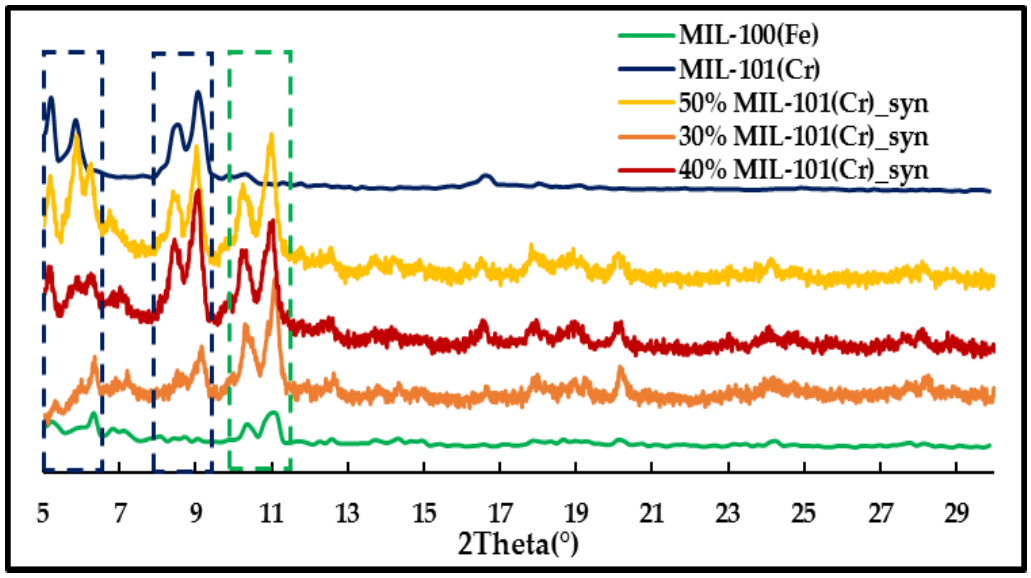

Fig. 5-31 Powder XRD patterns of synthesized MIL-100(Fe), MIL-101(Cr) and MIL-101(Cr)/MIL-100(Fe) composites.

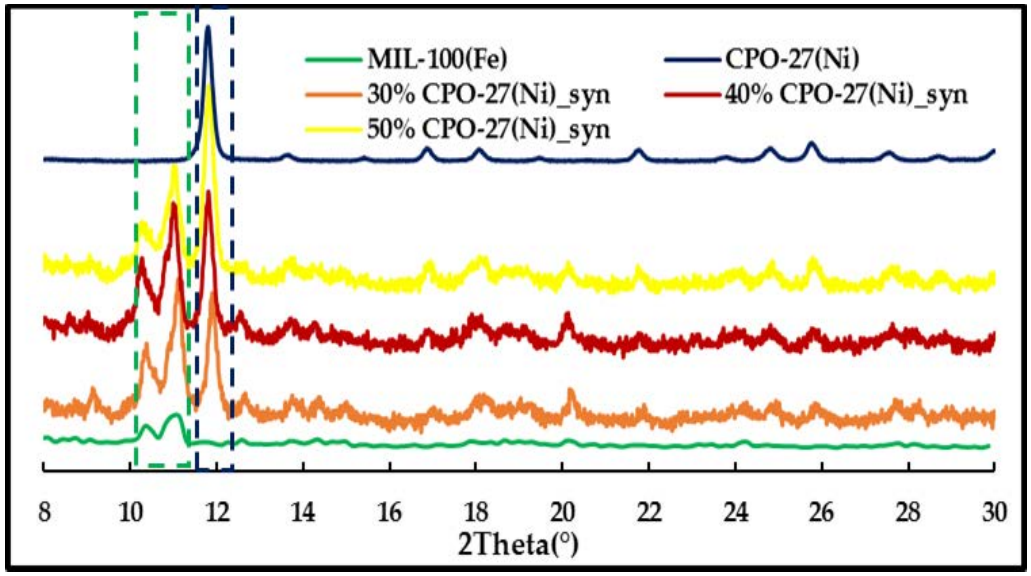

Fig. 5-32 Powder XRD patterns of synthesized MIL-100(Fe), CPO-27(Ni) and CPO-27(Ni)/MIL-100(Fe) composites.

5.3.2.2. Nitrogen adsorption

Fig. 5-33 shows the adsorption isotherms of MIL-100(Fe), MIL-101(Cr) and their composites; while those of MIL-100(Fe), CPO-27(Ni) and their composites are shown in **Fig. 5-34**. The measured BET surface areas and their pore volumes for the two types of composites and their neat materials are listed in **Table. 5-7** .

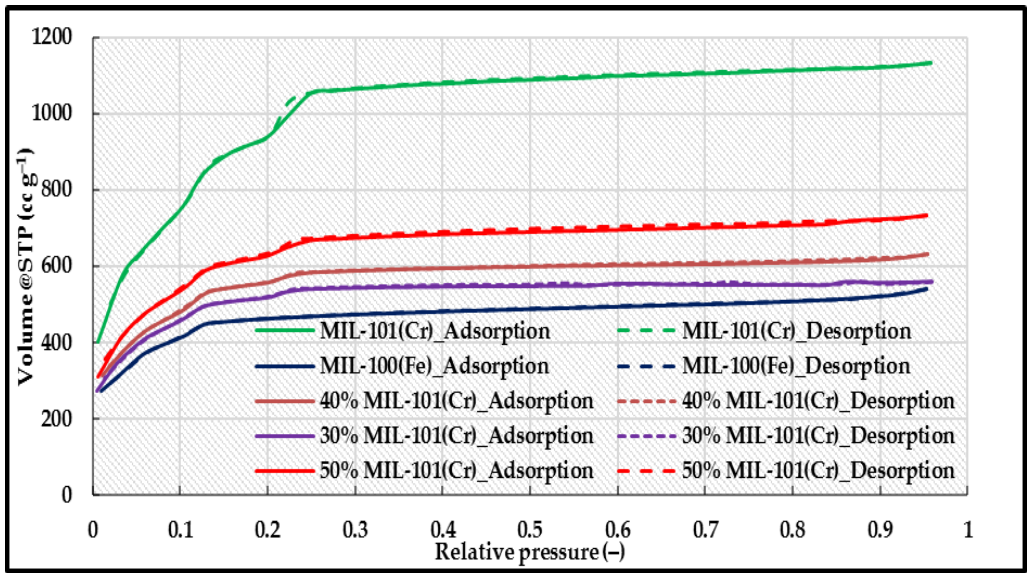

Fig. 5-33 Nitrogen adsorption isotherms of MIL-101(Cr), MIL-100(Fe) and MIL-101(Cr)/MIL-100(Fe) composites at 77 K.

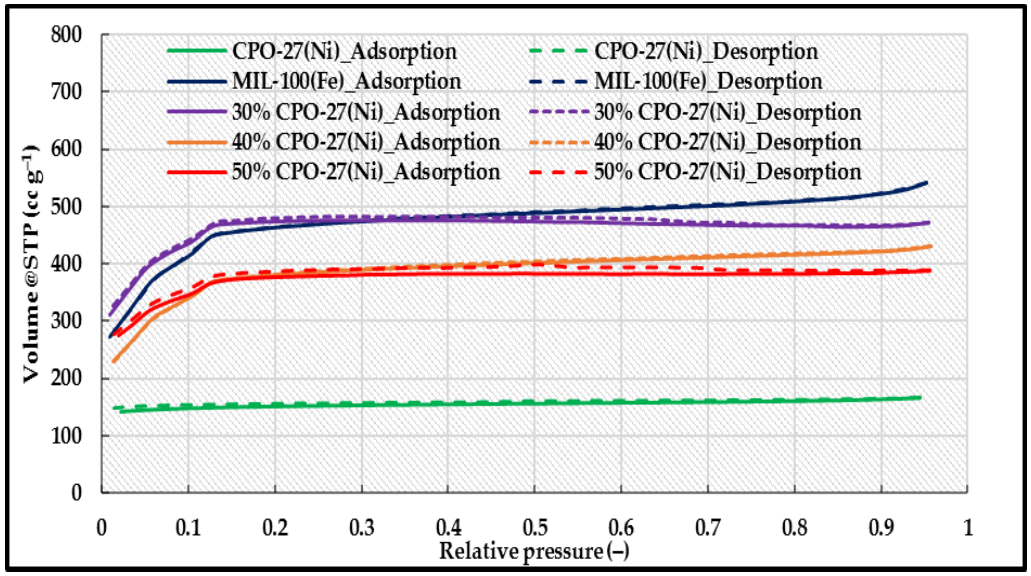

Fig. 5-34 Nitrogen adsorption isotherms of CPO-27(Ni), MIL-100(Fe) and CPO-27(Ni)/MIL-100(Fe) composites at 77 K.

Table. 5-7 surface area of MIL-100(Fe), MIL-101(Cr), CPO-27(Ni) and their composites

Material	BET surface area (m^2g^{-1})	Total pore volume (cm^3g^{-1})
MIL-100(Fe)	1481.6	0.83
MIL-101(Cr)	3460	1.75
30% MIL-101(Cr)	1725.1	0.86
40% MIL-101(Cr)	1872.0	0.98
50% MIL-101(Cr)	2159.5	1.13
CPO-27(Ni)	469.7	0.26
30% CPO-27(Ni)	1470.7	0.73
40% CPO-27(Ni)	1213.1	0.66
50% CPO-27(Ni)	1178.8	0.6

Regarding the MIL-101(Cr)/MIL-100(Fe) composites (**Fig. 5-33** and **Table. 5-7**), it can be noticed that the MIL-101(Cr) had the highest surface area while the MIL-100(Fe) had the lowest one. As the amount of the MIL-101(Cr) in the composite increased, the surface area surpassed that of MIL-100(Fe). This can be attributed to the increased active mass of the high surface area MIL-101(Cr) in the composite and hence the total surface area of the composite was increased. This was also shown in the pore size distribution curve (**Fig. 5-35**) where it is evident that the composites are adopting the pore size of both materials as they have the same crystal structure

with comparable pore sizes. It is also evident that the MIL-101(Cr) had the highest pore volume while the MIL-100(Fe) had the lowest and the composites were lying in between.

For the CPO-27(Ni)/MIL-100(Fe) (**Fig. 5-34** and **Table. 5-7**), the opposite trend was observed as the MIL-100(Fe) had the highest surface area while the CPO-27(Ni) had the lowest. In these composites, as the amount of the CPO-27(Ni) in the composite increased, the surface area diminished. This can be attributed to the low surface area of CPO-27(Ni) compared to that of MIL-100(Fe). This was also shown in the pore size distribution curve (**Fig. 5-36**) where it is evident that pore size distribution was more dominated by that of MIL-100(Fe) as the two materials have completely different crystal structures with different pore sizes. It is also evident that the MIL-100(Fe) had the highest pore volume while the CPO-27(Ni) had the lowest and the composites were in between.

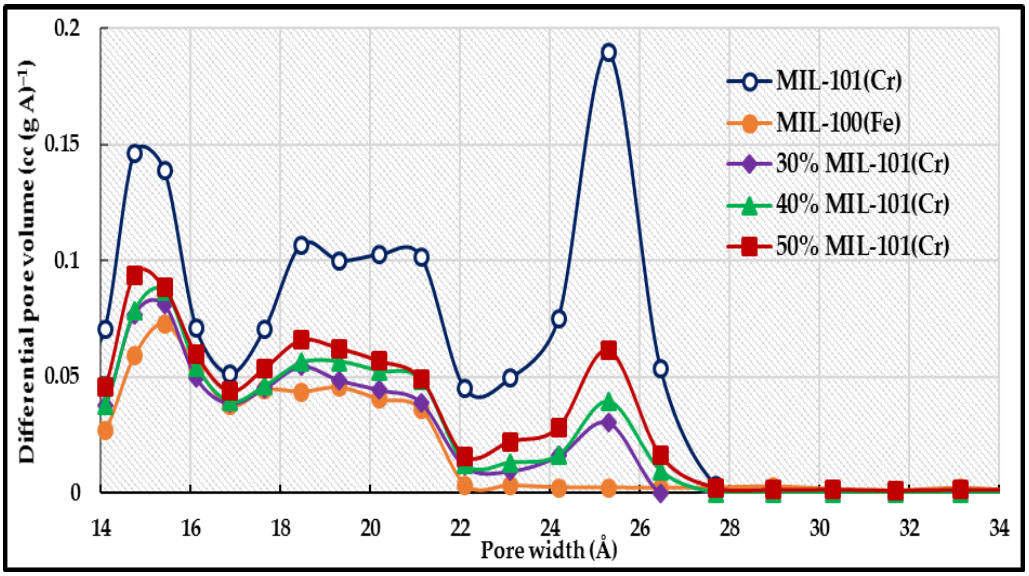

Fig. 5-35 Pore size distribution of MIL-100(Fe), MIL-101(Cr) and MIL-101(Cr)/MIL-100(Fe) composites.

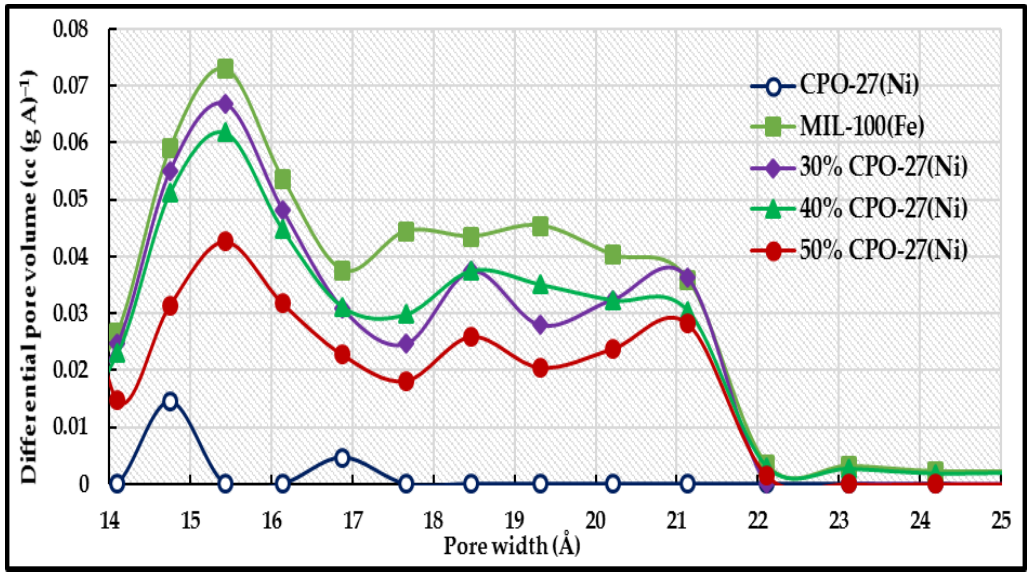

Fig. 5-36 Pore size distribution of MIL-100(Fe), CPO-27(Ni) and CPO-27(Ni)/MIL-100(Fe) composites.

5.3.2.3. Thermogravimetric analysis (TGA)

The thermal stability of MIL-100(Fe), MIL-101(Cr), CPO-27(Ni) and their composites was assessed using the thermal gravimetric technique where the change in mass with temperature under a flow of nitrogen was recorded. **Fig. 5-37** shows the TGA traces of MIL-100(Fe), MIL-101(Cr) and their composites. There were three stages of weight loss for all the materials. The first stage where the material lost its guest or free water trapped in the pores, amounting to 20% of initial weight at 73°C for MIL-100(Fe) and 50% at 137°C for MIL-101(Cr). As the amount of MIL-101(Cr) in the composite increased, the weight loss became more comparable to the neat MIL-101(Cr). The second stage was due to the departure of the co-ordinated water molecules where a relatively low weight loss took place in the temperature range of 73°C – 400°C. This is a higher temperature range than that of neat MIL-101 (137-337°C) and similar to MIL-100(Fe). This means that the synthesized composites have a higher thermal stability than the parent MIL-101(Cr). As the temperature increased, the final stage took place where the weight loss was due to the destruction of the structure and the decomposition of the terephthalic and trimesic acids.

The thermal analyses of MIL-100(Fe), CPO-27(Ni) and their composites are shown in **Fig. 5-38**. Once again, there were three stages of weight loss for all the materials. The first stage where the material lost its guest or free water trapped in the pores amounting to 20-30% of its weight. It can be noticed that as the amount of CPO-27(Ni) in the composite increased, the amount of the adsorbed water increased and temperature at which it is desorbed decreased. This is an indication of the higher water vapour capacity of the synthesized composites compared to MIL-100(Fe) and also their lower desorption temperature compared to CPO-27(Ni). The second stage was due to the departure of the coordinated water molecules where a relatively low weight loss took place in the temperature range of 123–423°C for the three composites. This is a higher temperature range compared to that of CPO-27(Ni), which means that the synthesized composites had a higher thermal stability than the parent CPO-27(Ni). As the temperature increased, the final stage took place where the weight loss was due to the destruction of the structure and the decomposition of both the dihydroxyterephthalic and trimesic acids.

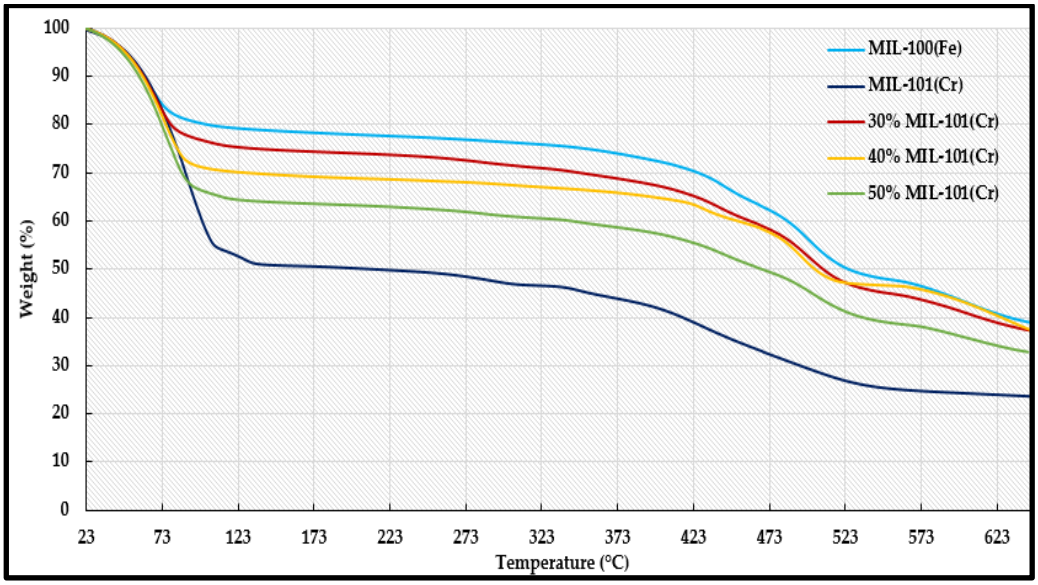

Fig. 5-37 Thermogravimetric analysis of MIL-100(Fe), MIL-101(Cr) and MIL-101(Cr)/MIL-100(Fe) composites.

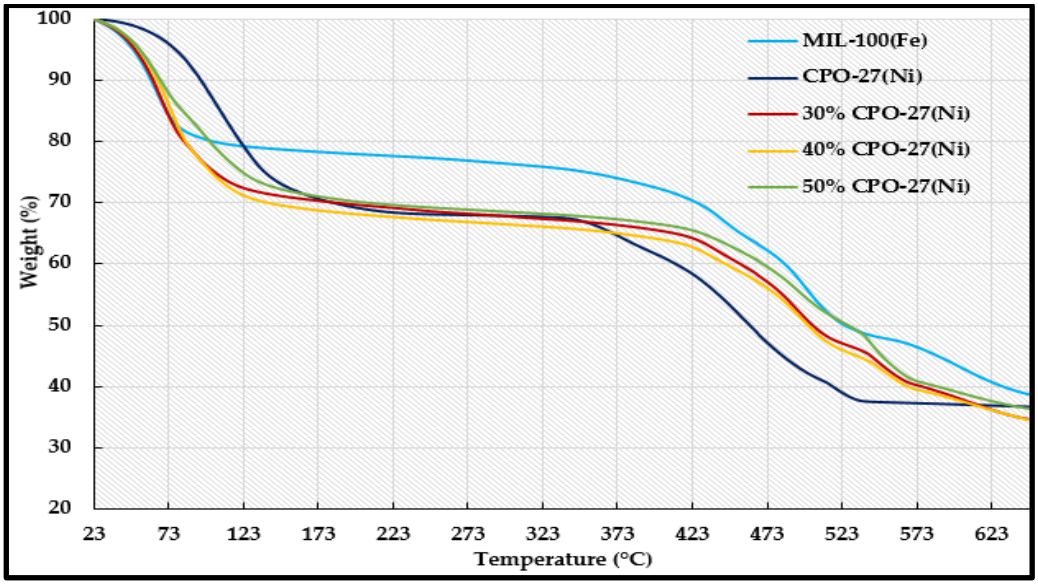

Fig. 5-38 Thermogravimetric analysis of MIL-100(Fe), CPO-27(Ni) and CPO-27(Ni)/MIL-100(Fe) composites.

5.3.2.4. Transmission Electron Microscopy (TEM) and Scanning Electron Microscopy (SEM)

The morphology of MIL-100(Fe), MIL-101(Cr) and CPO-27(Ni) was investigated using SEM while the morphology of the synthesized composites was investigated through the TEM technique to prove their core-shell structures (**Fig. 5-39**). Two composites, 50% MIL-101(Cr) and 50% CPO-27(Ni), were chosen to represent the other composites. **Fig. 5-40** shows TEM images of the 50% CPO-27(Ni) and SEM images of parent MOF materials. It can be noticed that the MIL-100(Fe) crystals grew on an agglomerate of CPO-27(Ni). A similar behaviour was observed when MIL-100(Fe) grew on Au nanoparticles [280] or on Fe_3O_4 [281].

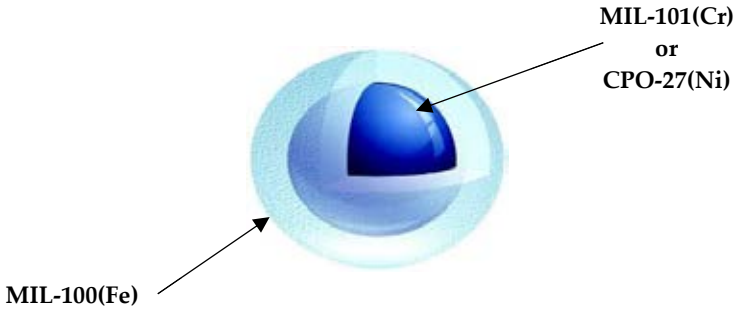

Fig. 5-39 Proposed core-shell structure.

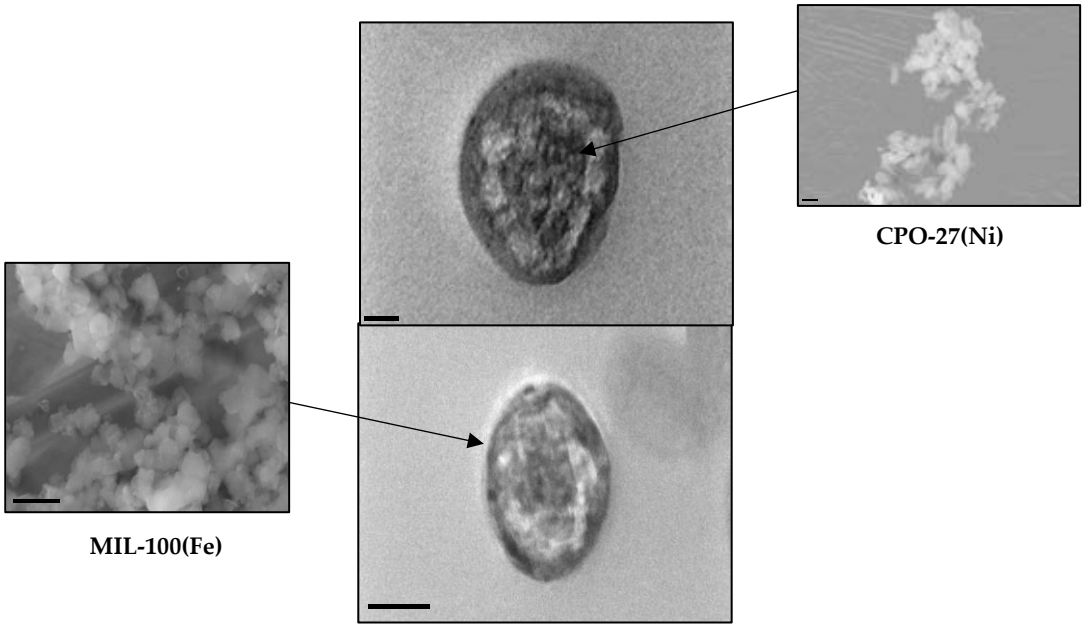

Fig. 5-40 SEM images of CPO-27(Ni), MIL-100(Fe) and TEM images of 50% CPO-27(Ni) composite.

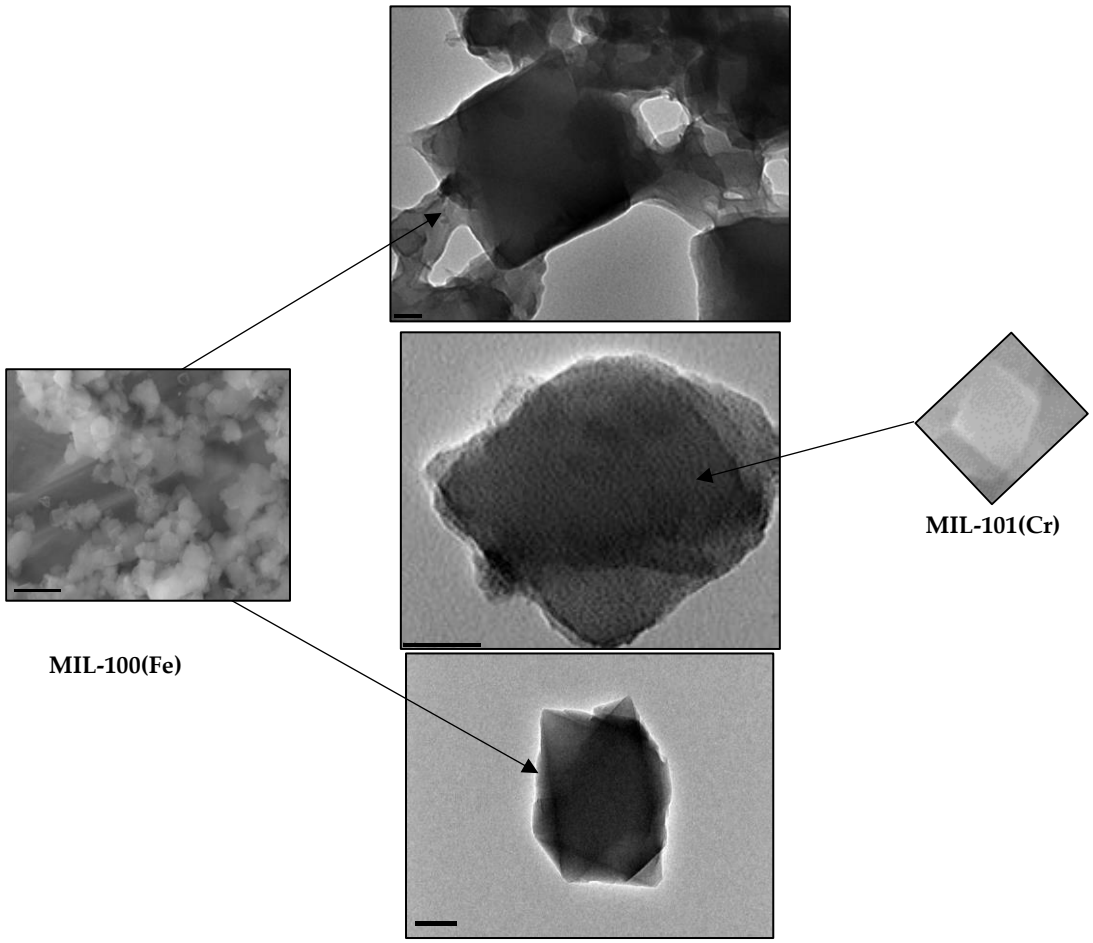

Fig. 5-41 SEM images of MIL-101(Cr), MIL-100(Fe) and TEM images of 50% MIL-101(Cr) composite.

The TEM images of the 50% MIL-101(Cr) and SEM images of MIL-100(Fe) and MIL-101(Cr) are shown in **Fig. 5-41**. It can be noticed that once again the MIL-100(Fe) grew on the crystals of MIL-101(Cr). These figures prove the successful core-shell synthesis of both CPO-27(Ni)/MIL-100(Fe) and MIL-101(Cr)/MIL-100(Fe) composites.

5.3.2.5. Fourier Transform Infrared Spectroscopy (FTIR)

The presence of functional groups in MIL-100(Fe), CPO-27(Ni) and their composites was examined using the FTIR technique (**Fig. 5-42**). It can be noticed that all the composites preserved the characteristic bands of both MIL-100(Fe) and CPO-27(Ni). For MIL-100(Fe), the vibration at 1628 cm^{-1} is attributed to the interaction between the craboxylate and the Fe^{3+} ion in the structure while the band at 1385 cm^{-1} is due to carboxylate group stretching. The characteristic bands of CPO-27(Ni) at 1560 and 1244 cm^{-1} are also present in all the composites. The presence of those bands in the spectra of the composites proves the co-existence of the two structures and growth of MIL-100(Fe) crystals on the surface of CPO-27(Ni) crystals.

The same observation was noticed for MIL-100(Fe)/MIL-101(Cr) composites (**Fig. 5-43**). It can be seen that all the composites preserved the bands of both MIL-101(Cr) and MIL-100(Fe) which indicates that the MIL-100(Fe) was successfully grown on the crystals of MIL-101(Cr).

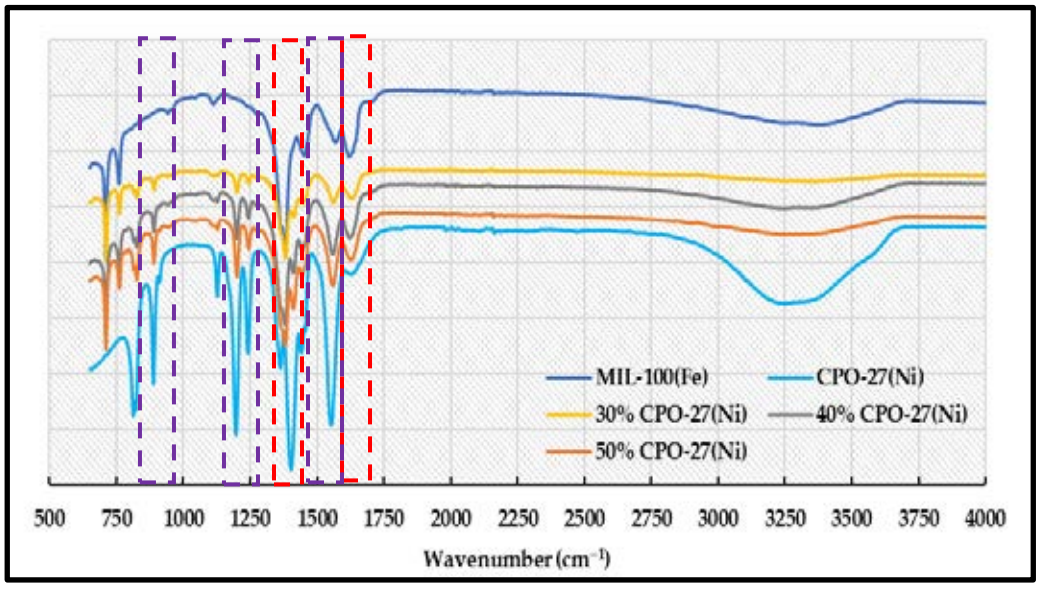

Fig. 5-42 FTIR spectra of MIL-100(Fe), CPO-27(Ni) and their composites.

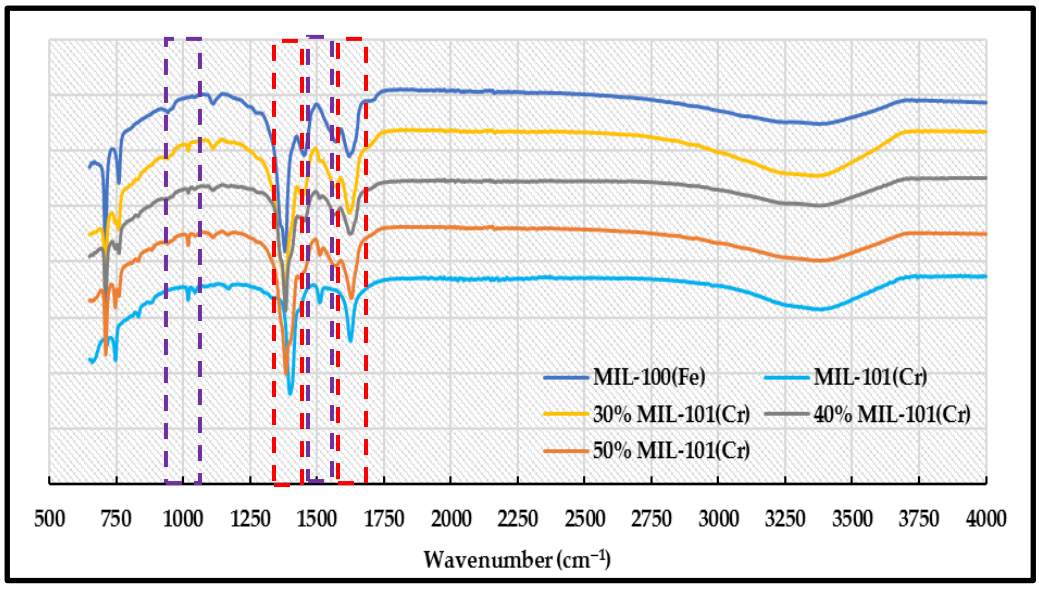

Fig. 5-43 FTIR spectra of MIL-100(Fe), MIL-101(Cr) and their composites.

5.3.2.6. True density

The true and bulk densities of MIL-100(Fe), MIL-101(Cr), CPO-27(Ni) and their 50% composites were measured. The 50% composites were chosen to represent other concentrations. **Table. 5-8** shows the values of the true, bulk densities and porosities of the 50% MOF composites.

Table. 5-8 True, bulk densities and porosities of the 50% CPO-27(Ni)/MIL-100(Fe) and 50% MIL-101(Cr)/MIL-100(Fe) composites

Material	True density (kg m^{-3})	Bulk density (kg m^{-3})	Porosity (–)
50% CPO-27(Ni)	1704.9	359	0.79
50% MIL-101(Cr)	1587.1	240	0.85

5.3.2.7. Thermal conductivity

The thermal conductivities of MIL-100(Fe), MIL-101(Cr), CPO-27(Ni) and their 50% composites are shown in **Fig. 5-44**. It can be noticed that among the parent materials, the CPO-27(Ni) had the highest thermal conductivity followed by MIL-100(Fe), while MIL-101(Cr) had the lowest value. This is attributed to the high free volume in case of MIL-101(Cr) as highlighted before. The measured thermal conductivity and the calculated porosity were used

to develop empirical equations to predict the effective thermal conductivity at different temperatures as shown in **Table. 5-9**. The specific heat capacity of the 50% MIL-101(Cr)/MIL-100(Fe) composite was 1.05 kJ (kg K)$^{-1}$ while it was 1.03 kJ (kg K)$^{-1}$ in case of the 50% CPO-27(Ni)/MIL-100(Fe).

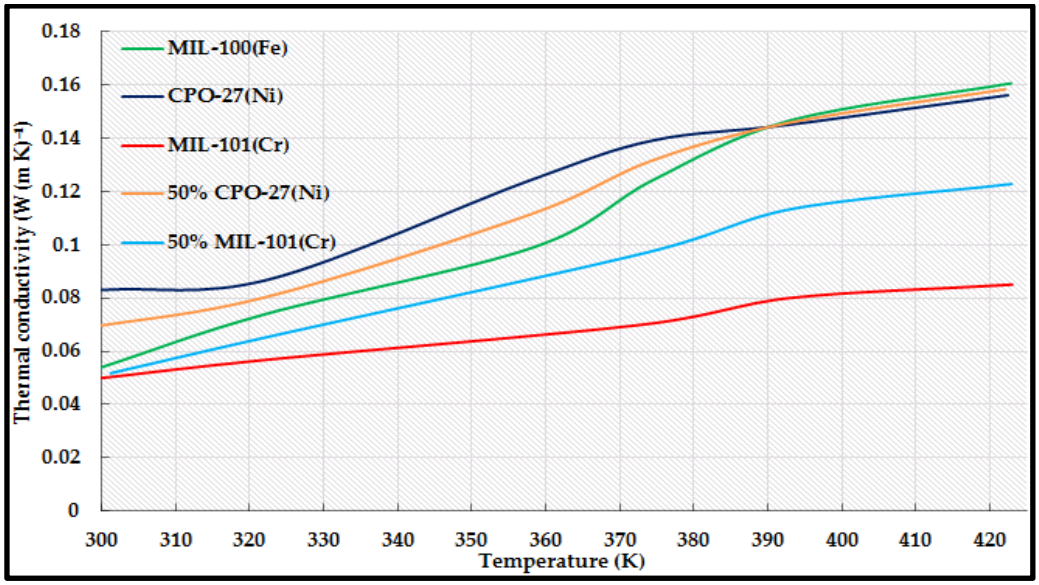

Fig. 5-44 Thermal conductivity of MIL-100(Fe), MIL-101(Cr), CPO-27(Ni) and their composites.

Table. 5-9 Effective thermal conductivities of 50% CPO-27(Ni)/MIL-100(Fe) and 50% MIL-101(Cr)/MIL-100(Fe) composites

Material	Effective thermal conductivity (W (m K)$^{-1}$)
50% MIL-101(Cr)	$3.7E-4T_{bed}-0.076$
50% CPO-27(Ni)	$5.4E-4T_{bed}-0.115$

5.3.2.8. Water adsorption characteristics

5.3.2.8.1. Adsorption isotherms

Fig. 5-45 shows the measured water adsorption/desorption isotherms of MIL-100(Fe), MIL-101(Cr) and their composites at 25°C. It can be noticed that all the composites exhibited a type IV isotherm in common with their parent MOF materials and preserved the two-step shape of MIL-100(Fe). Also, it can be noticed that at low partial pressure, there was no

improvement observed in the water uptake. This may be attributed to the fact that both MOF materials had the same isotherm type which is characterized by its low uptake at low relative pressure range as highlighted earlier. Once the water molecules are introduced to the composite structure, it starts to fill the smaller pores first and then the larger ones [143]. That is why at the low relative pressure range, the material adopts the MIL-100(Fe) two step isotherm shape as it has smaller pore size compared to that of MIL-101(Cr). Nevertheless, a significant enhancement in the high relative pressure range was observed as the amount of MIL-101(Cr) increased. This can be attributed to the higher active mass of the high capacity mesoporous MIL-101(Cr). Once the small pores are filled, the water molecules start to fill the larger pores of MIL-101(Cr) and hence a higher uptake is expected compared to the neat MIL-100(Fe). As the improvement was observed in the high relative pressure range, the MIL-100(Fe) and its composites with MIL-101(Cr) are adequate for applications like adsorption desalination or heat storage where high evaporation temperature can be applied (high working relative pressure).

Fig. 5-46 shows the adsorption isotherms of MIL-100(Fe), CPO-27(Ni) and their composites. It can be noticed that a significant improvement was observed as the composites adopted the CPO-27(Ni) isotherm shape in the low relative pressure range. As highlighted above, the water molecules initially start to fill the smaller pores of the microporous CPO-27(Ni). Due to the UMCs and the hydrophilicity of the hydroxyl group in the dihydroxyterephthalate in the CPO-27(Ni) and its composites, the material is expected to almost adsorb half of its capacity at the low relative pressure range. Once the CPO-27(Ni) pores were filled, the water molecules started to fill the pores of the larger mesoporous MIL-100(Fe). As the amount of CPO-27(Ni) increased in the synthesized composites, a reduction in the equilibrium uptake was expected. This is due to the reduction in the accessible mesopores in the total mass of the composites. This shows that the CPO-27(Ni) and its MIL-100(Fe) composites can be more suitable for applications

working at low relative pressures applications such as adsorption cooling or adsorption desalination with cooling effect.

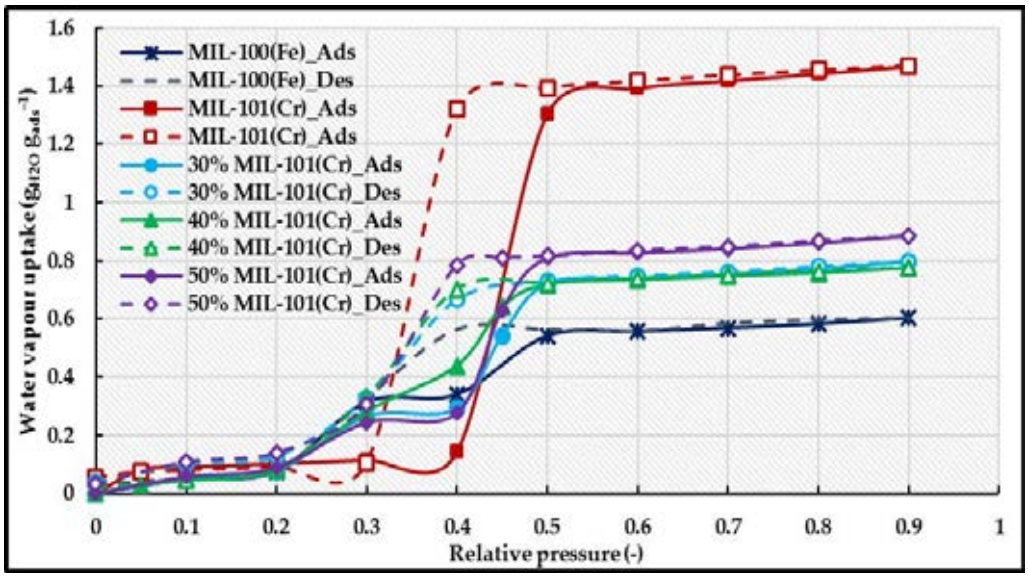

Fig. 5-45 Water adsorption isotherm of MIL-100(Fe), MIL-101(Cr) and their synthesized composites at 25°C.

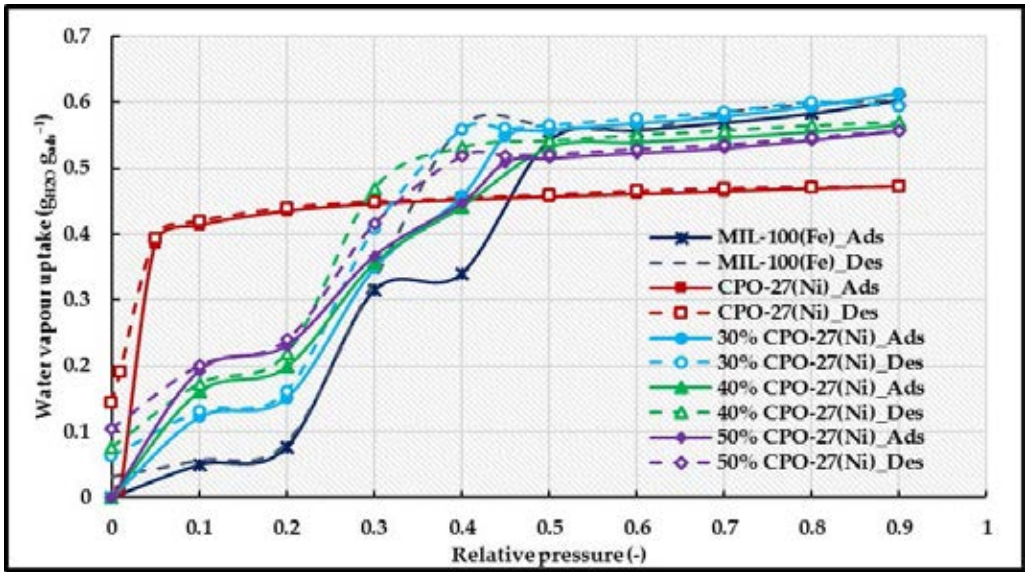

Fig. 5-46 Water adsorption isotherm of MIL-100(Fe), CPO-27(Ni) and their synthesized composites at 25°C.

The 50% composites were chosen to be further investigated as models for the CPO-27(Ni)/MIL-100(Fe) and MIL-101(Cr)/MIL-100(Fe). The water adsorption uptake of the neat MIL-100(Fe) and its composites was measured at 15°C, 25°C and 35°C (**Fig. 5-47**).

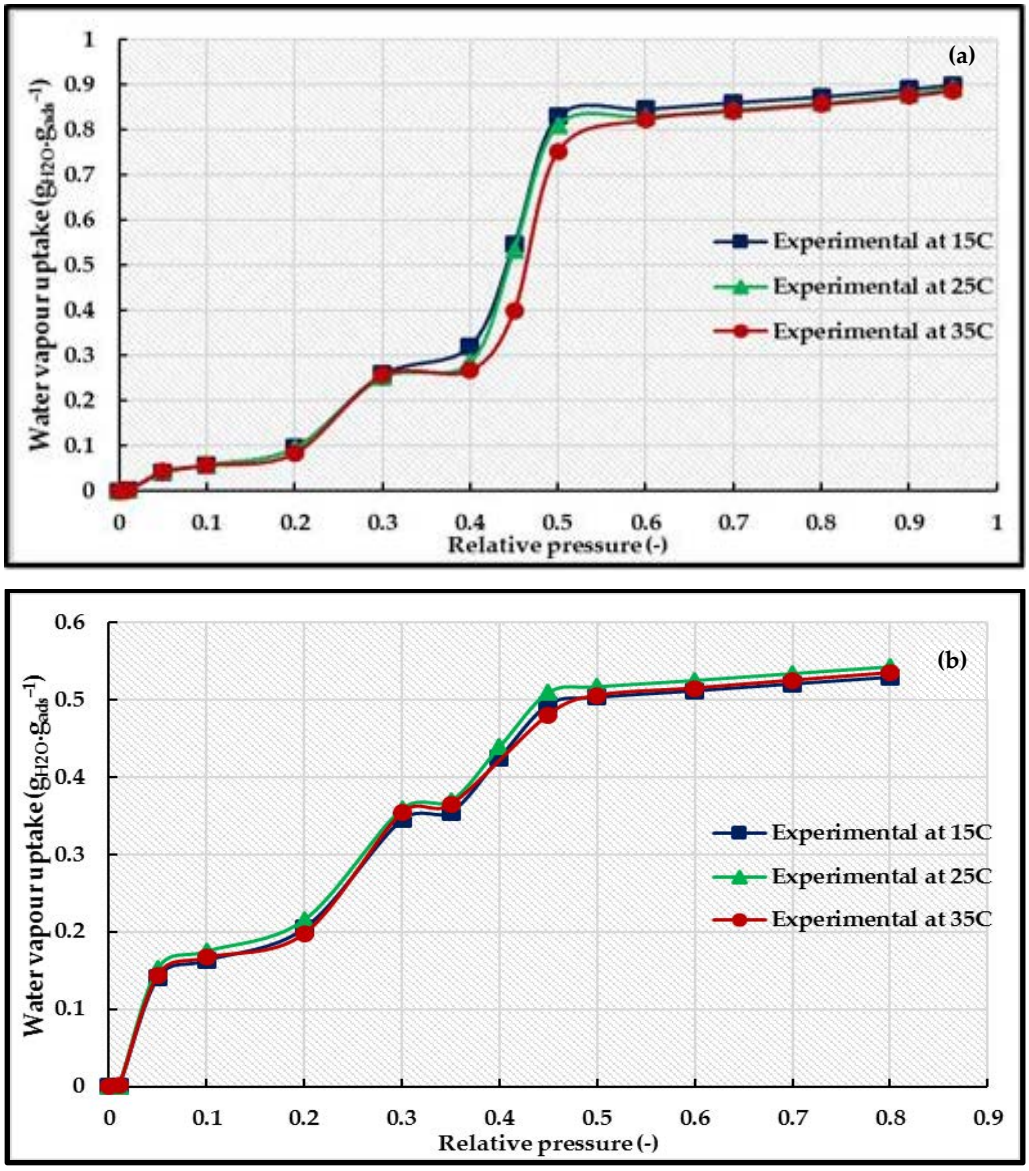

Fig. 5-47 Water adsorption isotherm of a. 50%MIL-101(Cr) and b. 50%CPO-27(Ni) composites at different adsorption temperatures.

The previously shown measured data were fitted using a series of equations in terms of adsorption potential (A) (**Eq. 5-16** to **Eq. 5-18**) for the 50% MIL-101(Cr) composite and **Eq. 5-19** to **Eq. 5-20** in case of 50% CPO-27(Ni) composite**.**

50% MIL-101(Cr) composite

$$X = 57.64\exp(-9.7E-4A) \qquad \textbf{A}\geq\textbf{6900} \qquad \textbf{(5-16)}$$

$$X = 1.82-9.2E-4A+1.6E-7A^2-8.9E-12A^3 \qquad \textbf{2700} \leq \textbf{A<6900} \qquad \textbf{(5-17)}$$

$$X = 0.72 + 0.2E-2A - 6.6E-6A^2 + 9.1E-9A^3 - 5.83E-12A^4 + 1.69E-15A^5 - 1.81E-19\,\mathrm{A}^6$$ **2700 > A** **(5-18)**

50% CPO-27(Ni) composite

$$X = 0.2\exp\left[-\left(\frac{A}{9026.35}\right)^{5.4}\right]$$ **A≥3700** **(5-19)**

$$X = 0.56 - 9.1E-5A + 1.1E-7A^2 - 6E-11A^3 + 8.13E-15A^4$$ **A<3700** **(5-20)**

Fig. 5-48 shows the good agreement between the experimental data and the proposed models for the neat MIL-100(Fe) and its composites.

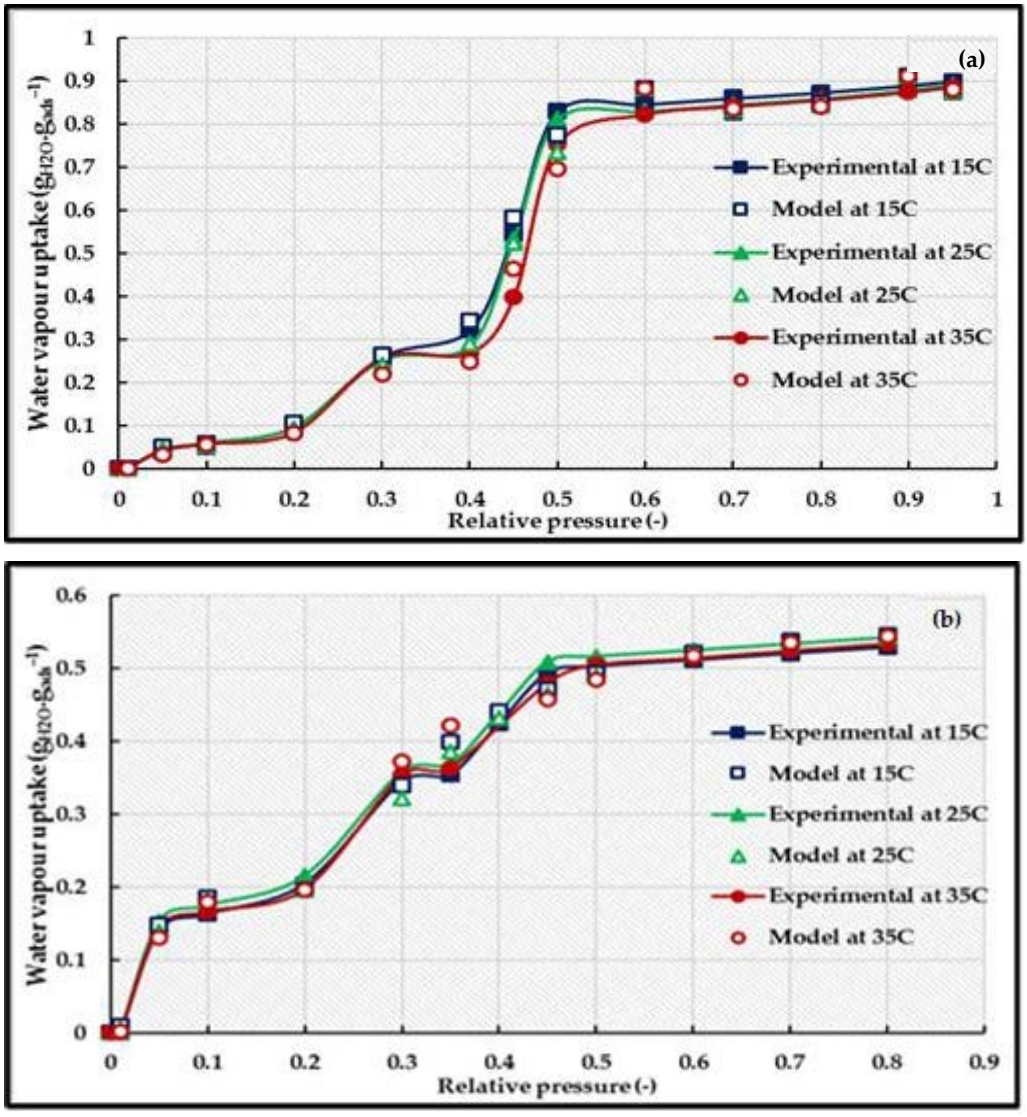

Fig. 5-48 Proposed isotherm model fitting of water adsorption of a. 50%MIL-101(Cr) and b. 50%CPO-27(Ni) at different adsorption temperatures.

In order to evaluate the performance stability, MIL-100(Fe) composites were subjected to ten successive adsorption/desorption cycles in the respective regions of improvement (**Fig. 5-49**). The test was held in the relative pressure range of 0 to 0.9 in case of MIL-101(Cr)/MIL-100(Fe) composite while it was held in the range of 0 to 0.45 in case of MIL-100(Fe)/CPO-27(Ni) composite.

Both composites showed a steady performance over the investigated range which emphasize the stability of the parent MIL-100(Fe) and the robustness of its composites.

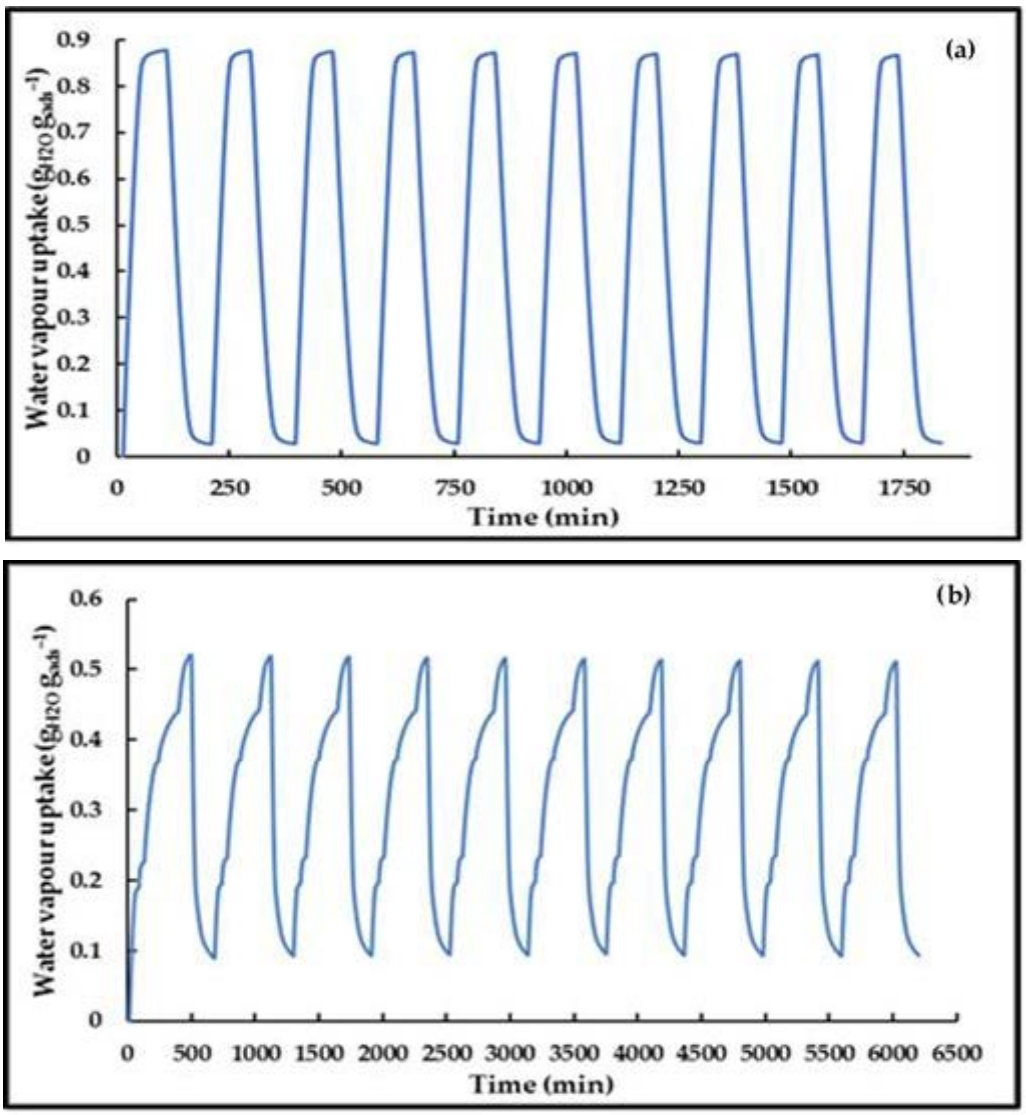

Fig. 5-49 Adsorption/desorption cycling experiments for a. 50%MIL-101(Cr) (0 to 0.9) and b. 50%CPO-27(Ni) (0 to 0.45).

5.3.2.8.2. Adsorption kinetics

The rate of water adsorption was predicted through applying the LDF model (**Eq. 3-21** to **Eq. 3-24**). **Table. 5-10** gives the values of parameters E_a and k_0 for MIL-100(Fe) composites. **Fig. 5-50** and **Fig. 5-51** highlight the validity of the LDF model in fitting the experimental data of the materials under investigation.

Table. 5-10 Values of LDF equation parameters

Adsorbent	Relative pressure range	E_a (J mol^{-1})	k_0 (s^{-1})
50% MIL-101(Cr)	<0.3&>0.5	21,072	6.5
	≥0.3&≤0.5	23,164	4.11
50% CPO-27(Ni)	<0.3&>0.5	21,072	6.5
	≥0.3&≤0.5	23,164	4.11

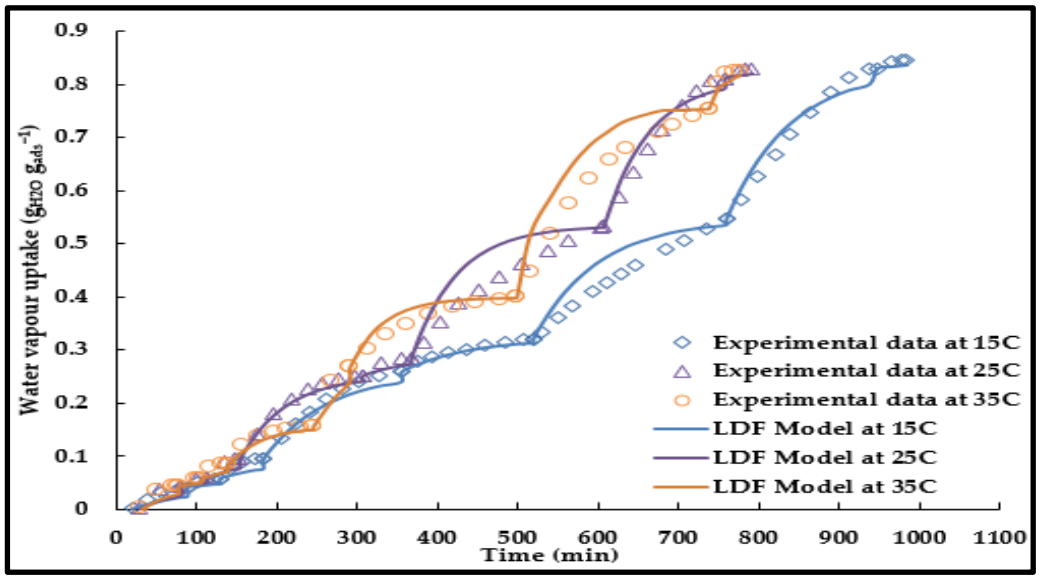

Fig. 5-50 LDF model fitting of water adsorption of 50% MIL-101(Cr)/MIL-100(Fe) at 15°C, 25°C and 35°C.

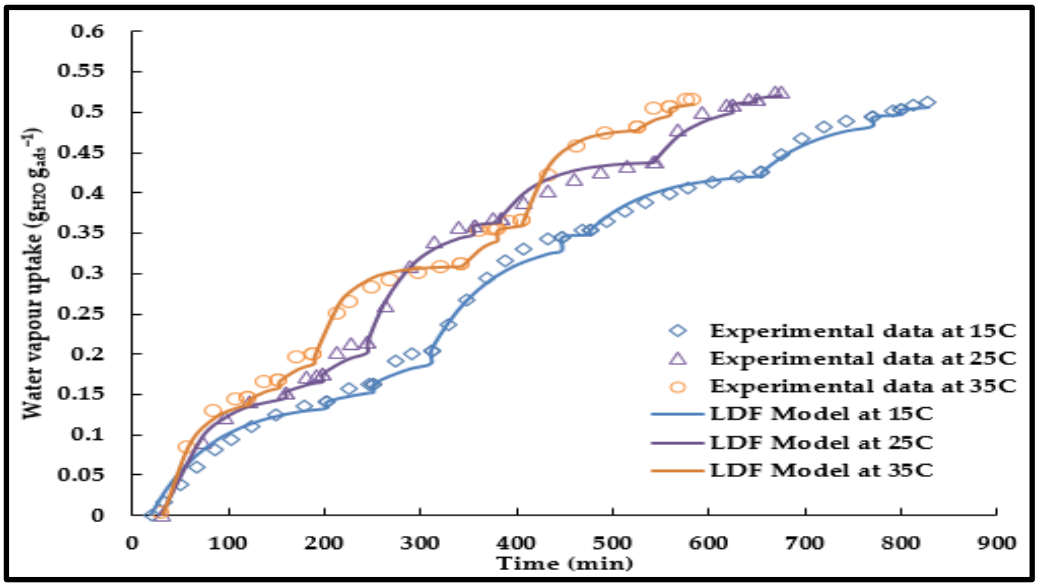

Fig. 5-51 LDF model fitting of water adsorption of 50% CPO-27(Ni)/MIL-100(Fe) at 15°C, 25°C and 35°C.

5.4. Metal-organic framework coating

As it was highlighted earlier, integrating adsorbents as a coating layer can offer many advantages over the granules form. The four MOF materials were coated on aluminium substrates following the procedures mentioned in section 5.4.1. The effect of binder concentration on the mechanical properties and water adsorption characteristics was investigated through testing different MOFs samples with concentrations of 10 and 15wt%. The effect of the coating thickness was also investigated through measuring the change in water adsorption uptake for different thicknesses.

The prepared coatings were characterized based on their water vapour adsorption capacity, thermal conductivity and their mechanical strength.

5.4.1. Synthesis

Prior to coating, the aluminium substrates were cleaned by dipping each substrate in 2N NaOH solution for 2 min, washing with water and finally rinsing in acetone. A new coating preparation method was employed using a binder solution which was prepared through dissolving Hydroxyethyl Cellulose (HEC) in water in the mass ratio of 1:50. The binder solution was added to the dried MOF powder and shortly stirred to produce suspensions with different binder concentrations (10 and 15%). The substrate was dipped in the suspension and then placed in the oven at 75°C for 10 min. A second layer was added through dipping the substrate in the suspension and then leaving it to dry in the oven at 75°C for another 10 min. The process was repeated several times till the desired thickness was produced. Such technique reduces the stress on the coating layer and hence prevent the cracking of the coating layer. After the final layer, the substrate was left in the oven at 75°C for 24 hr. A mild drying temperature of 75°C was chosen as the aluminium substrate and the coating layer have different thermal expansion, hence higher drying temperatures may cause fast drying and cracked coating layer.

5.4.2. Characterization

5.4.2.1. Water adsorption isotherms

5.4.2.1.1. MIL-101(Cr)

The aluminium substrate was coated through the dip coating technique which was achieved through immersing an aluminium piece that represent the aluminium fin in a heat exchanger (**Fig. 5-52**) into the prepared MOF/binder solution. The thickness of the MOF coating was controlled through the number of layers grown on the metal piece.

Fig. 5-52 Metal substrate before and after coating with MIL-101(Cr).

The effect of the binder percentage on the water uptake is shown in **Fig. 5-53** where it can be noticed that increasing the amount of binder from 10 to 15wt%, decreased the water vapor uptake of the coating layer which can be attributed to the decrease in the effective mass of the adsorbent material. **Fig. 5-54** shows the effect of the coating thickness on the adsorption rate and the equilibrium uptake. It can be noticed that for a binder concentration of 10wt% increasing the thickness from 0.3 to 0.5 mm had no effect on the equilibrium uptake as it remained relatively constant but decreased the mass transfer rate as adsorption kinetics are significantly slower. This can be attributed to that as the thickness increased, it became harder for the water vapour to diffuse through the layer due to increased interparticle resistance.

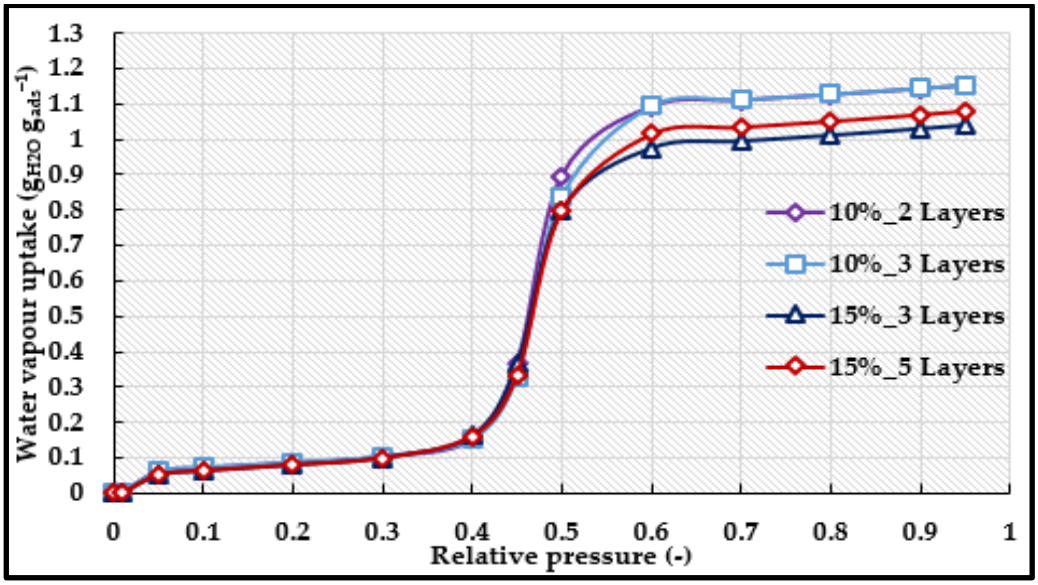

Fig. 5-53 Effect of binder percentage on the water uptake of MIL-101(Cr) coating at 25°C.

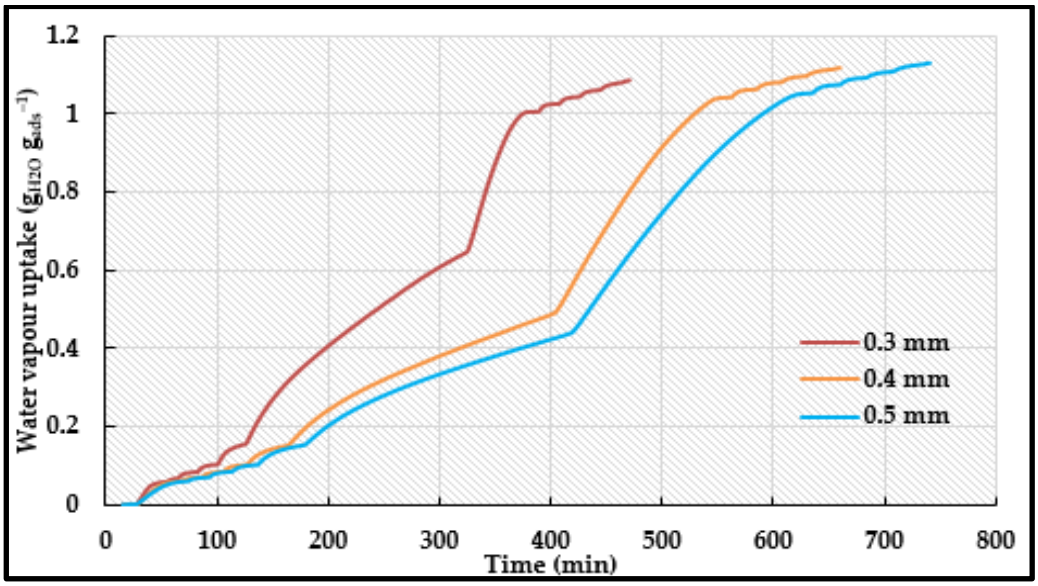

Fig. 5-54 Effect of coating thickness on the water vapour uptake of 10wt% binder at 25°C.

5.4.2.1.2. CPO-27(Ni)

The effect of the binder percentage on the water uptake of CPO-27(Ni) is shown in **Fig. 5-55**. The effect of the coating thickness was investigated through increasing it from 0.3 to 0.5 mm (**Fig. 5-56)** where similar to MIL-101(Cr), increasing the thickness decreased the mass transfer rate but kept the equilibrium uptake constant.

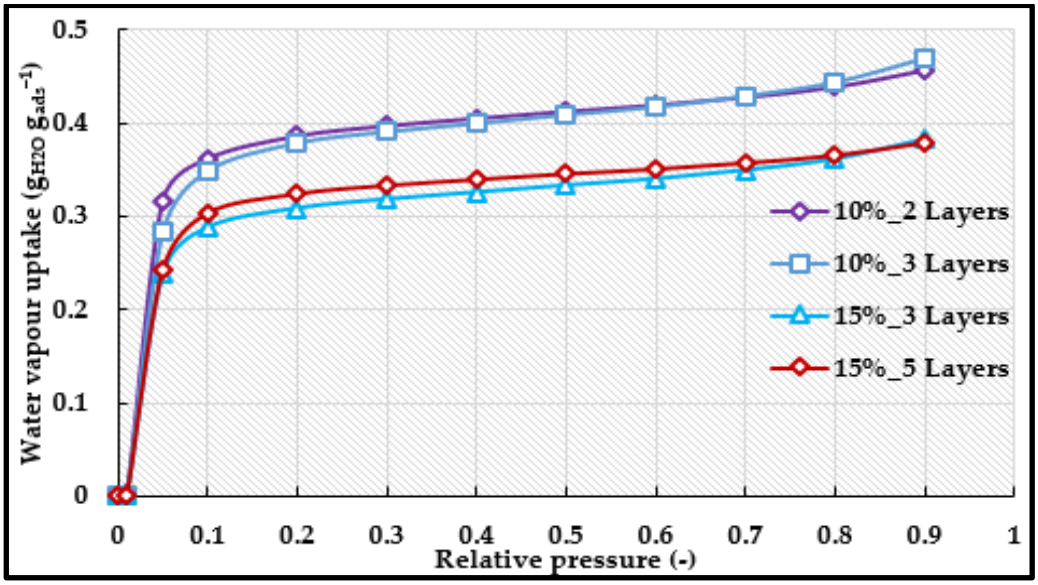

Fig. 5-55 Effect of binder percentage on the water uptake of CPO-27(Ni) coating at 25°C.

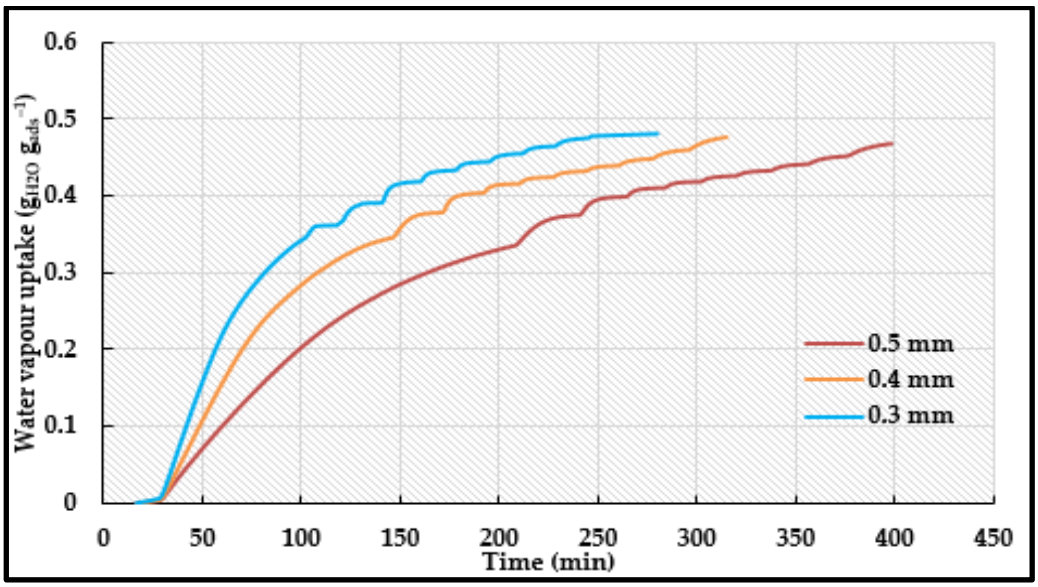

Fig. 5-56 Effect of coating thickness on the water vapour uptake of 10wt% binder at 25°C.

5.4.2.1.3. MIL-100(Fe)

The effect of the binder percentage on the water uptake of MIL-100(Fe) is shown in **Fig. 5-57**. The effect of the coating thickness was investigated through increasing it from 0.3 to 0.5 mm (**Fig. 5-58)** where it is evident that increasing the thickness decreased the mass transfer rate but kept the equilibrium uptake constant.

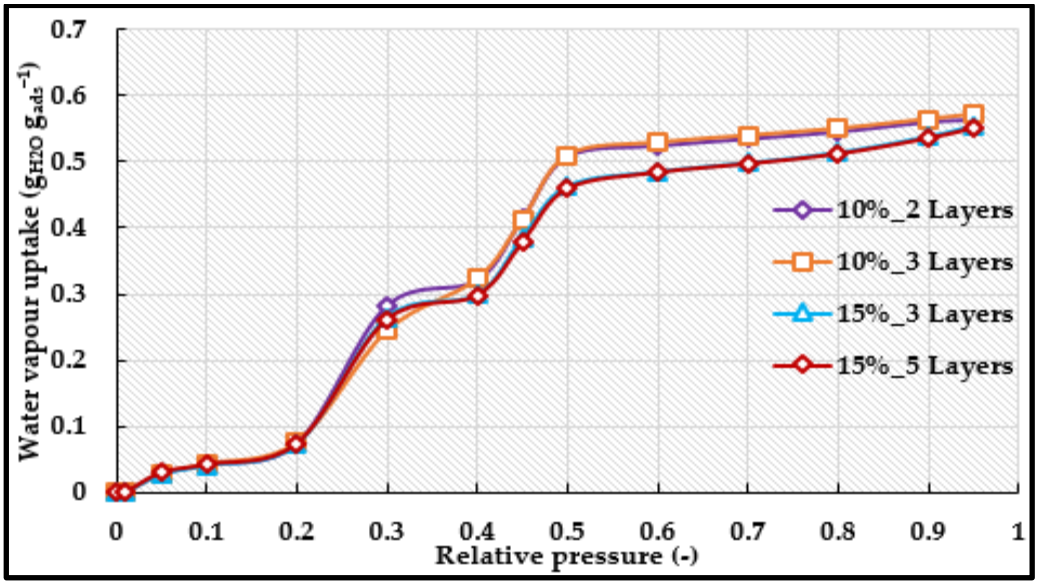

Fig. 5-57 Effect of binder percentage on the water uptake of MIL-100(Fe) coating at 25°C.

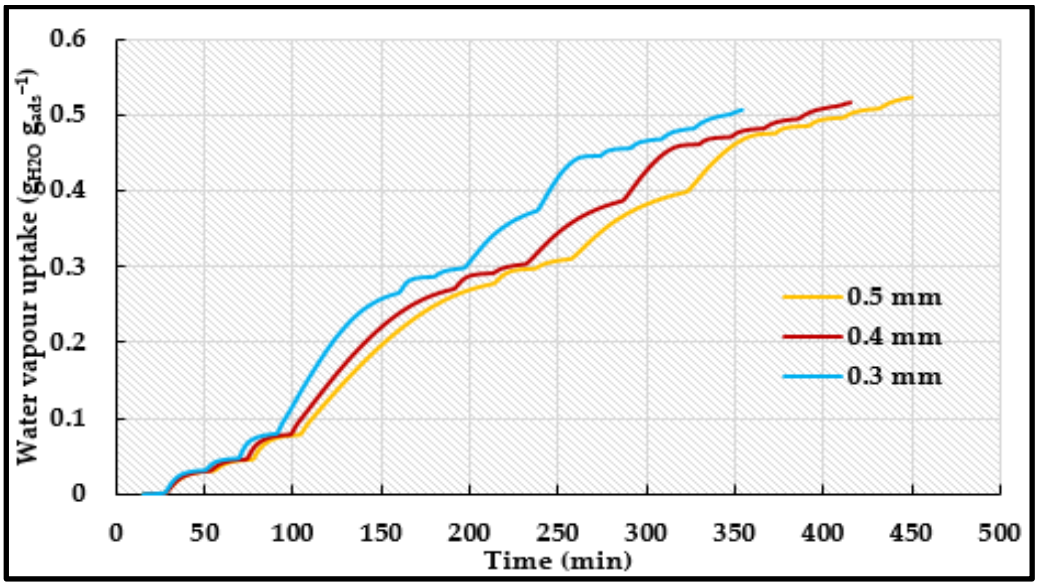

Fig. 5-58 Effect of coating thickness on the water vapour uptake of 10wt% binder of MIL-100(Fe) at 25°C.

5.4.2.1.4. Aluminium fumarate

The effect of the binder percentage on the water uptake of aluminium fumarate is shown in **Fig. 5-59**. The effect of the coating thickness was investigated through increasing it from 0.3 to 0.5 mm (**Fig. 5-60)** where it is evident that increasing the thickness decreased the mass transfer rate but kept the equilibrium uptake constant.

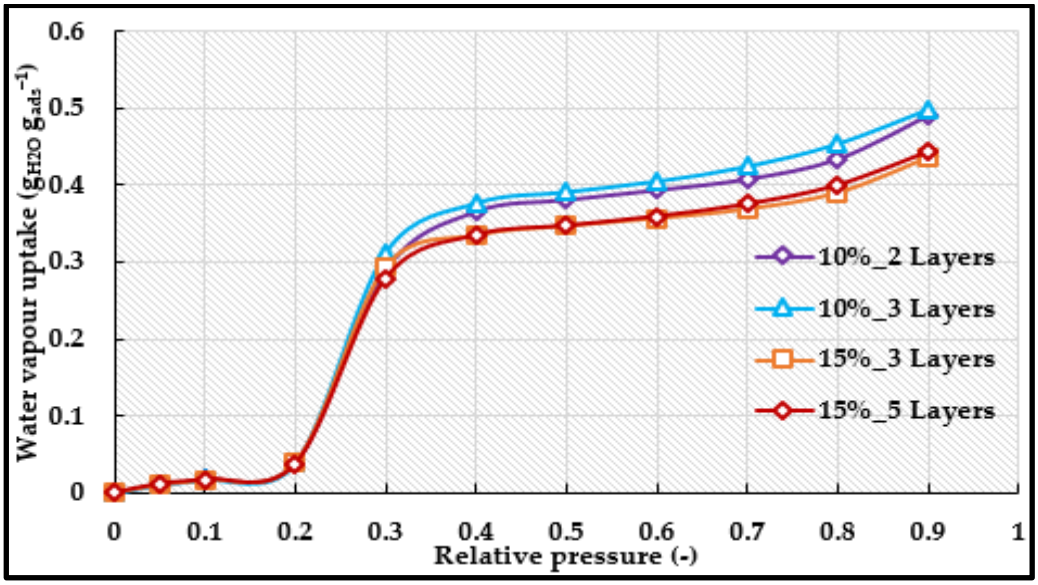

Fig. 5-59 Effect of binder percentage on the water uptake of aluminium fumarate coating at 25°C.

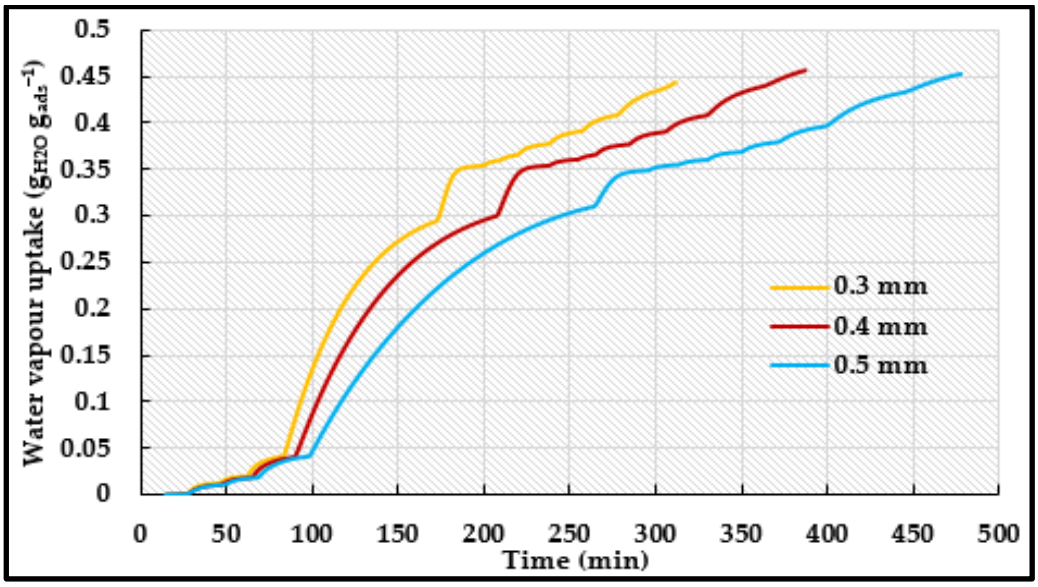

Fig. 5-60 Effect of coating thickness on the water vapour uptake of aluminium fumarate at 25°C.

5.4.2.2. Thermal conductivity and contact resistance

As it was highlighted in chapter 2, one of the main advantages of integrating the adsorbent material as a coated layer instead of granules is that it can offer an improved heat transfer rate as it removes the contact thermal resistance and provides high contact area between the adsorbent layer and the metal surface. The thermal conductivity and the thermal contact

resistance were measured for all the MOF materials. A circular aluminium substrate was coated with MOF material, plated with graphite and then placed in the furnace for measurement as it is shown in **Fig. 5-61**.

Fig. 5-61 Substrate, aluminium fumarate coated sample and graphite plated sample in furnace for thermal conductivity measurement.

Fig. 5-62 shows the thermal conductivity of the MOF coated samples. It can be noticed from comparing the thermal conductivity of the coated samples and that of the pressed pellet (**Figs. 4-9, 4-19, 4-35 and 4-46**) that there is a significant improvement in the thermal conductivity when the adsorbent material is integrated as a coated layer. A similar behaviour was previously observed which was attributed to the enhanced heat transport between the coated layer and the metal substrate [151] due to the elimination of the contact resistance at the interface. **Fig. 5- 63** shows the thermal contact resistances of the four MOF materials which highlight the negligible value of the contact resistance and the independency of the resistance on the adsorbent material. A similar behaviour was noticed for silica gel and zeolite granules [282].

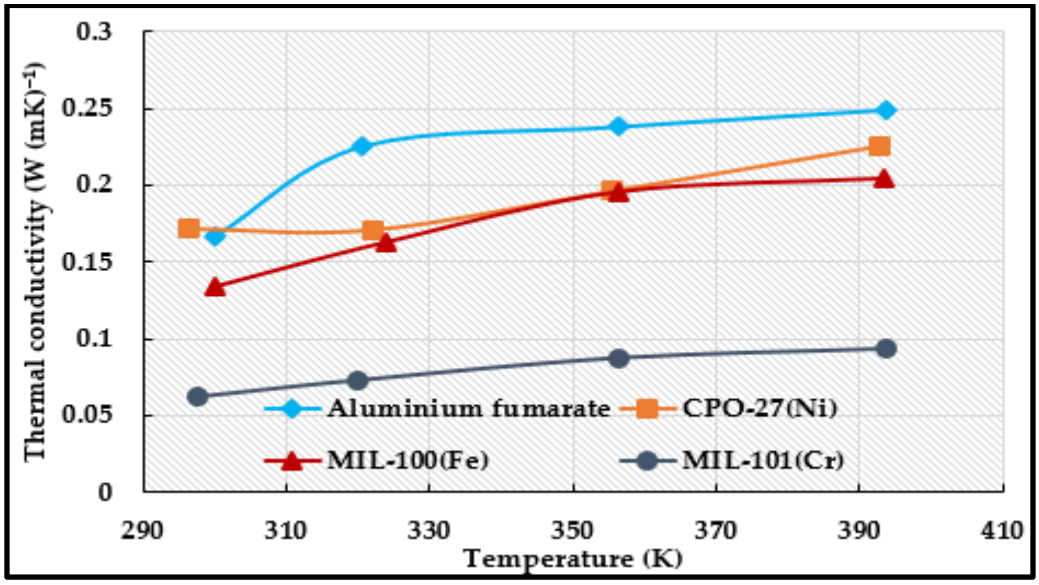

Fig. 5-62 Thermal conductivities of MOF coated samples.

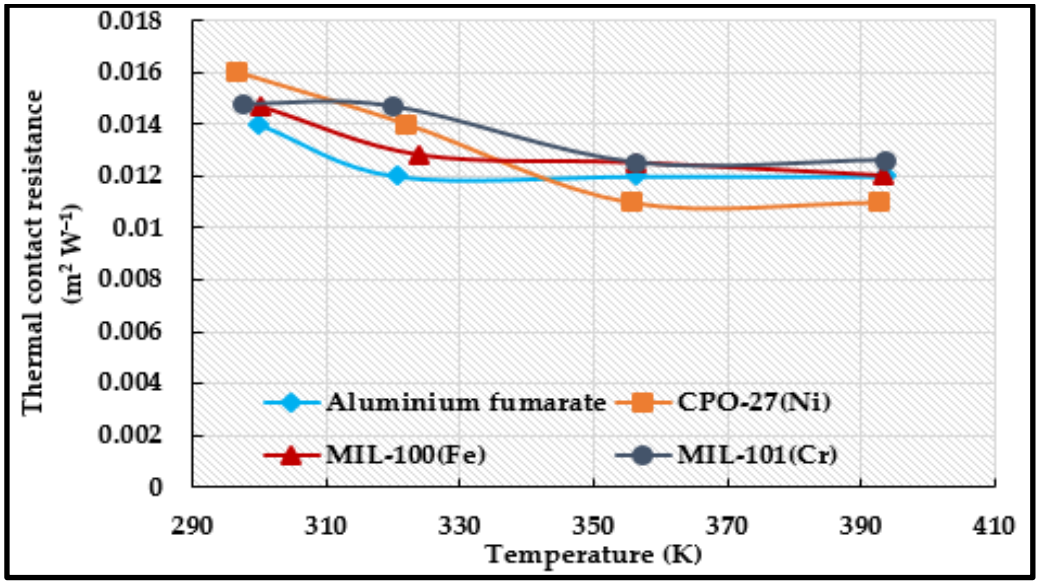

Fig. 5-63 Thermal contact resistances of MOF coated samples.

5.4.2.3. Mechanical strength

The durability of the coating layer and its adhesion to the aluminium substrate was examined through applying three tests on the coated substrate; compression, bending and micro-hardness tests. Aluminium fumarate coating was chosen as an example to represent the other MOFs coating.

5.4.2.3.1. Micro-hardness test

Two samples with binder concentration of 10 and 15wt%, (**Fig. 5-64**) were tested. The coated samples were placed in a cylindrical sample holder, a resin mixture (epoxy resin, epoxy hardener and flat edge filler) was added and left to dry. After complete dryness, the samples (**Fig. 5-65**) were polished to remove the excess resin till the interface between the aluminium substrate and the coating layer is visible. The polished samples were placed in the Beuhler MMT-7 micro-hardness tester (**Fig. 5-66**). Vickers indenter with 100g load at 15 s was applied. **Table. 5-11** shows the results obtained for the 10wt% and 15wt% samples. The obtained hardness values highlight the high strength and durability of the developed coating layers.

Fig. 5-64 Aluminium fumarate coated samples with 10wt% and 15wt% binder for microhardness test.

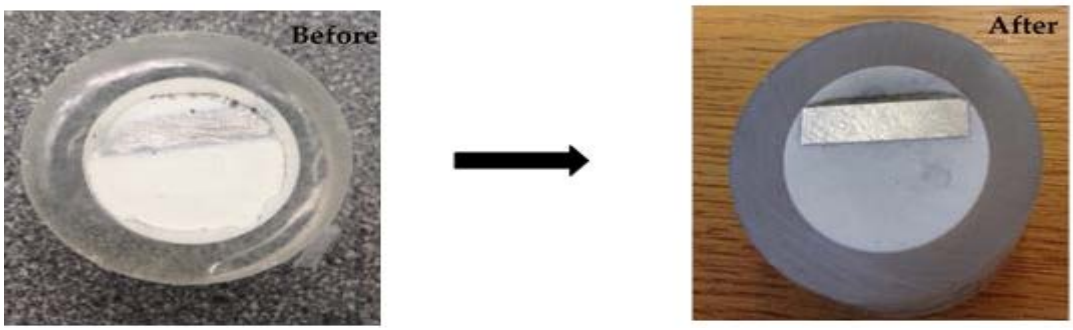

Fig. 5-65 Aluminium fumarate sample before and after polishing.

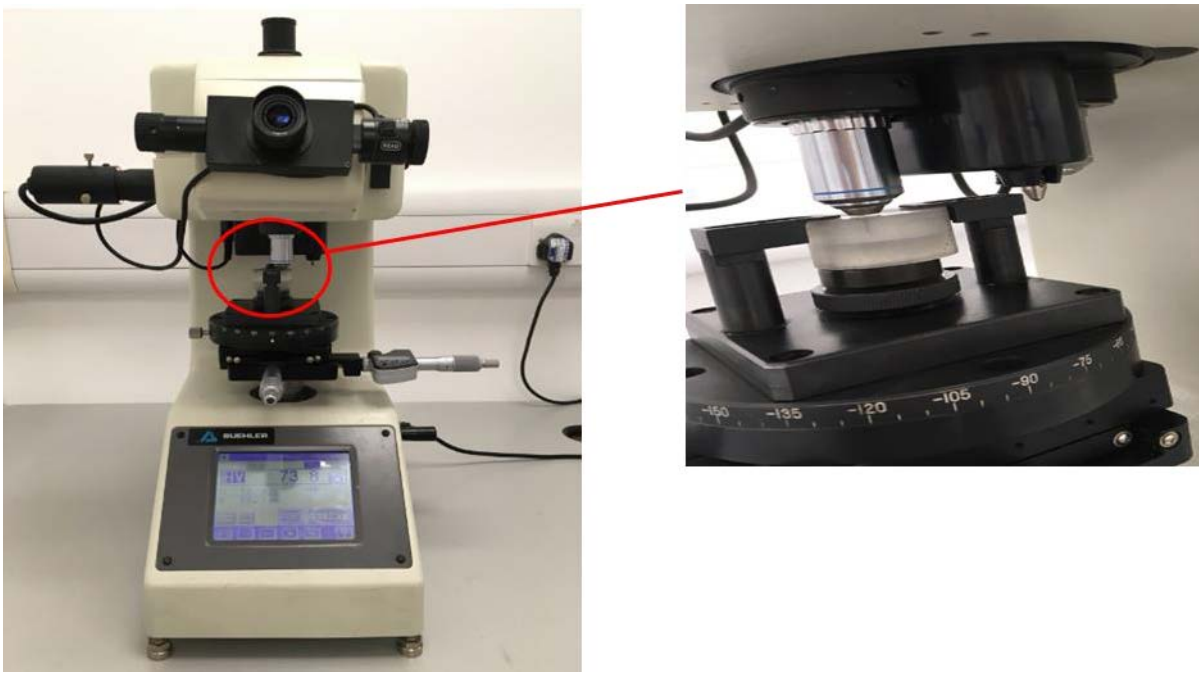

Fig. 5-66 Aluminium fumarate sample on the micro-hardness tester.

Table. 5-11 Vickers hardness of aluminium fumarate samples

Sample	Average hardness (HV)
Aluminium fumarate coating (10% binder)	40
Aluminium fumarate coating (15% binder)	52

5.4.2.3.2. Compression test

A compression test using a 2kN load was performed to investigate the behaviour of coating layer under crushing loads. As the applied exertion (stress) is inversely proportional to the surface area, the area of the aluminium substrate was changed through changing the dimensions of the substrate as shown in **Fig. 5-67**. As the applied force was kept constant at 2kN and the surface area changed, the applied exertion changed accordingly.

Fig. 5-68 shows the change in the extension with applied load (force) for the 10wt% samples. It can be noticed that as the load increased to reach the max value of the 2kN, the thickness of the coating layer decreased as a result of the applied force. It can also be noticed that at the

same load and as the area of the sample decreased (from sample 1 to sample 3), the extension increased. This is attributed to that the applied force is distributed on a lower area and hence a higher exertion is produced. Images of the three samples and the aluminium substrate were taken after the test using Alicona infinite focus facility (**Fig. 5-69**). The coated samples were coloured with a red colour dye to improve the light absorbance and hence clearer images were obtained. It can be noticed that the image shows that there was no cracks or damage observed for sample 1 while for sample 2 and 3, the coating on the edges of the metal substrate was fractured. This can be attributed to higher exertion applied for the two samples. Due to the compression and as the width of the two samples is small to handle the increase in the coating layer width due being flatter after compression, the coating breaks on the edges. Nevertheless, no cracks or detachment of the coating were observed on the middle of the three samples after the compression test which highlight the robustness of the coated samples.

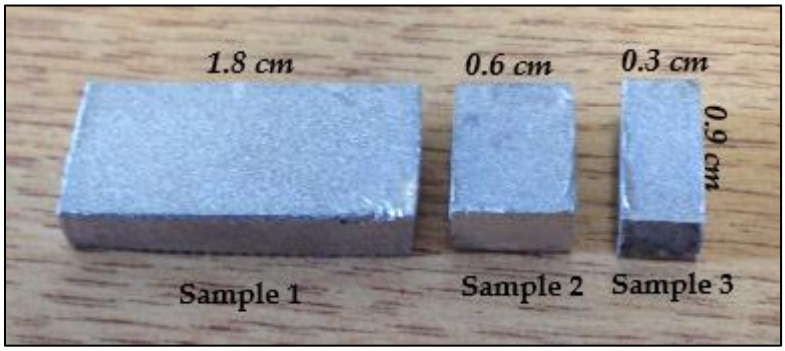

Fig. 5-67 Samples used in the compression test.

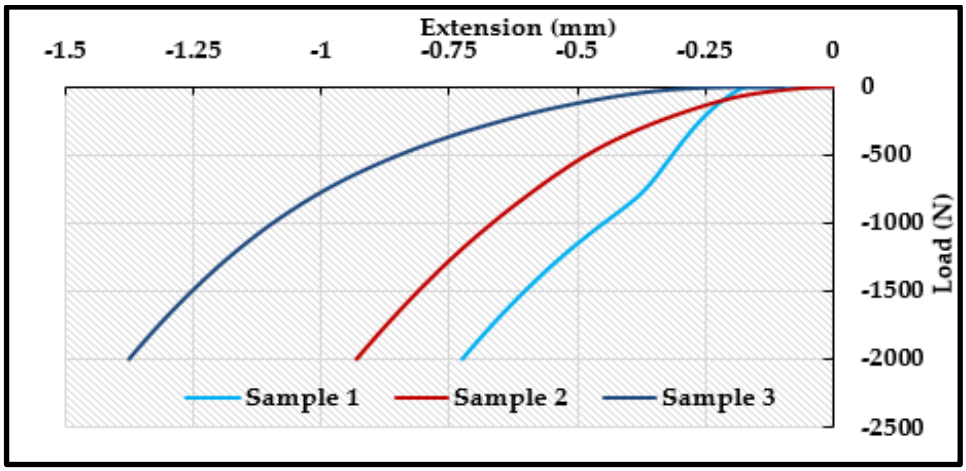

Fig. 5-68 Effect of the compression load on the extension for the 10% sample.

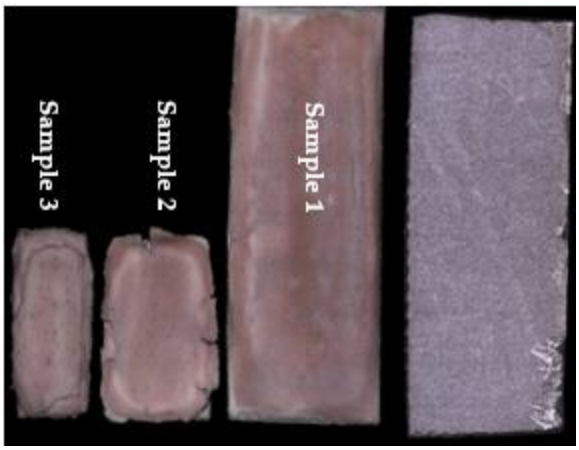

Fig. 5-69 Optical images of the 10wt% sample after compression test.

Fig. 5-70 shows the change in the extension with applied load (force) for the 15wt% samples. It can be noticed that increasing the binder percentage from 10wt% to 15wt% had an evident effect on the results of the compression test. Once again as the load increased, the thickness of the coating layer decreased.

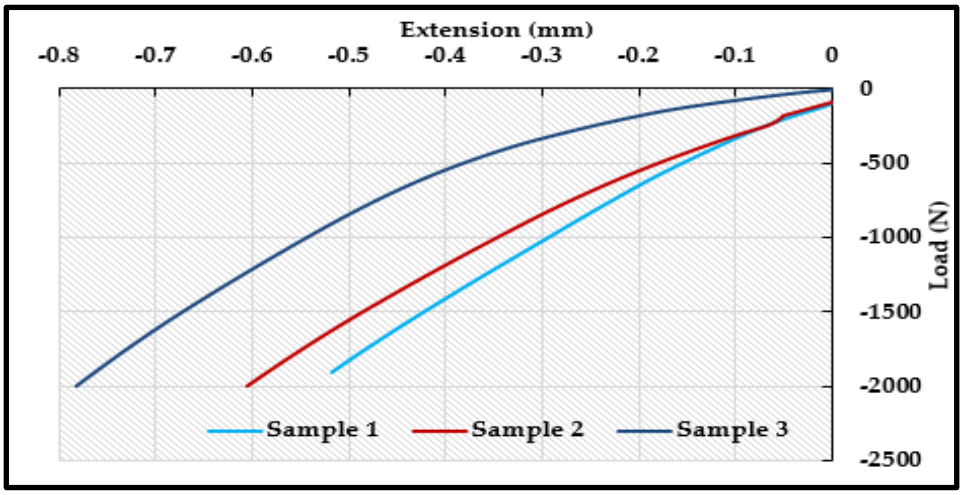

Fig. 5-70 Effect of the compression load on the extension for the 15wt% sample.

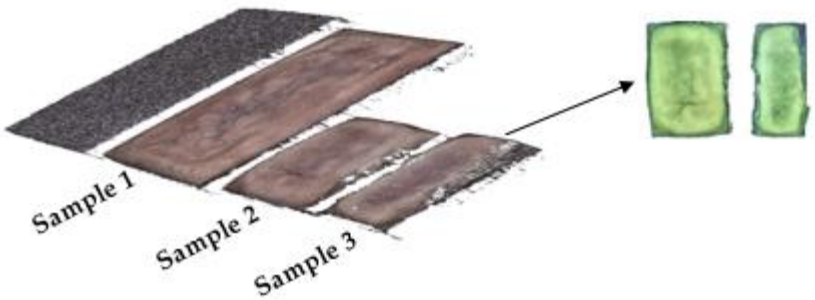

Fig. 5-71 Optical images of the 15wt% sample after compression test.

Comparing **Fig. 5-68** and **Fig. 5-70**, it can be noticed that increasing the binder percentage from 10 to 15wt% caused the coating layer to show lower thickness (extension) decrease. For instance, the thickness of sample 3 decreased by 1.38 mm when the binder percentage was 10wt% while it decreased by only 0.78 mm when the binder amount was increased to 15wt%. This is attributed to that increasing the binder content, increased the strength of the coating layer and hence it showed a higher resistance for the compression effect. **Fig. 5-71** shows an image of the three samples after the test. The image shows that in case of sample 1, there was no cracks or destruction observed on the coating layer. In case of samples 2 and 3, it was observed that small pieces on the edges of the samples started to fall down. This is attributed to the higher exertion applied. Other than that, there was no cracks or destruction observed on the main coating layer and it maintained its attachment to the metal substrate which highlight the robustness of the coating sample.

5.4.2.3.3. Bending test

The three points bending test was performed using a 2kN load as shown in **Fig. 5-72**. **Fig. 5-73** shows the coated samples before and after the test. It can be noticed that as the substrate bended, the coating layer broke at the bending point and started to detach from one side but without peeling off and leaving the substrate. Increasing the binder amount to 15wt% showed a higher strength as the coating layer cracked only at the bending point without leaving the substrate (**Fig. 5-74**) and maintained its attachment to the metal. The test again highlights the robustness of the coating layer and being well attached to the aluminium substrate.

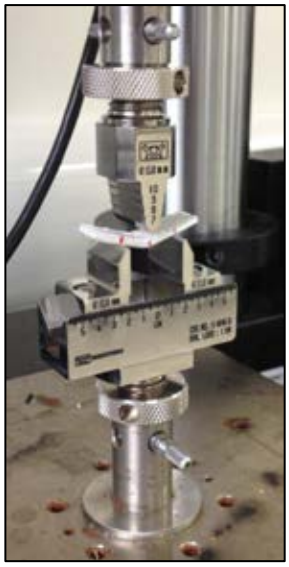

Fig.5-72 Three points bending test facility.

Thickness= 0.2 cm

Fig. 5-73 Images of substrate, 10wt% binder sample before and after three points bending test.

Thickness= 0.2 cm

Fig. 5-74 Images of substrate, 15wt% binder sample before and after three points bending test.

5.5. Summary

This chapter investigated the synthesis of novel composites of MIL-101(Cr) where the crystals of the MOF materials was incorporated with $CaCl_2$ or GrO. It was found that the GrO composites significantly improved the thermal conductivity while the $CaCl_2$ notably improved the water uptake in the low relative pressure range making the material more suitable for cooling applications.

Also, novel MIL-100(Fe) composites were synthesized through developing core-shell structure of MIL-101(Cr)/MIL-100(Fe) and CPO-27(Ni)/MIL-100(Fe) composites. The MIL-100(Fe) composites were found to offer a great advantage which is being hard enough to be ground into different sizes without the need of any external binder as shown in **Fig. 5-75**. In case of physical mixing of the two MOFs, a binder must be used to shape the powder into granules.

Fig. 5-75 MIL-100(Fe) composite: a. synthesized CPO-27(Ni)/MIL-100(Fe), b. synthesized MIL-101(Cr)/MIL-100(Fe) and c. physical mixture of CPO-27(Ni)/MIL-100(Fe) and MIL-101(Cr)/MIL-100(Fe).

The shape of the isotherm and the adsorption capacity was significantly improved through means of composites. This can be used to manipulate the performance of the MOF material and

make it suitable for a wider range of applications. Also, integrating the MOF material as a coated layer instead of the granular form showed a high durability and improved heat transfer properties which highlight the potential of coated heat exchangers as an alternative for conventional packed adsorption beds.

CHAPTER 6
MODELLING AND OPTIMISATION

6.1. Introduction

Mathematical modelling is an effective technique to evaluate and improve the performance of systems. In adsorption systems in particular, modelling has been efficiently used to improve the design and hence the overall system performance [185, 244, 283].

In this study, Materials Studio software which is a complete modelling and simulation environment was used to simulate the crystal structure of MOF materials and their composites. Even though the software is complicated, it helped to predict, understand and justify the relationship between the MOFs molecular structures and their properties and behaviour. Even though, the software library is limited to conventional porous materials such as zeolites, the crystal structures of the parent MOFs and their composites were successfully modelled.

The performance of different MOF materials in a two-bed adsorption system was also evaluated using a lumped-parameter simulation through SIMULINK/MATLAB (**Fig. 6-1)**, where differential equations representing the adsorption isotherms, kinetic equations, heat and mass transfer at various operating parameters, such as temperature, pressure and cycle time were fed in. Through the modelling, the potential and suitability of each adsorbent in different adsorption applications can be assessed. This simulation model is based on a two-bed adsorption system which includes two adsorption beds, an evaporator and a condenser as shown in **Fig. 6-2**.

(a)

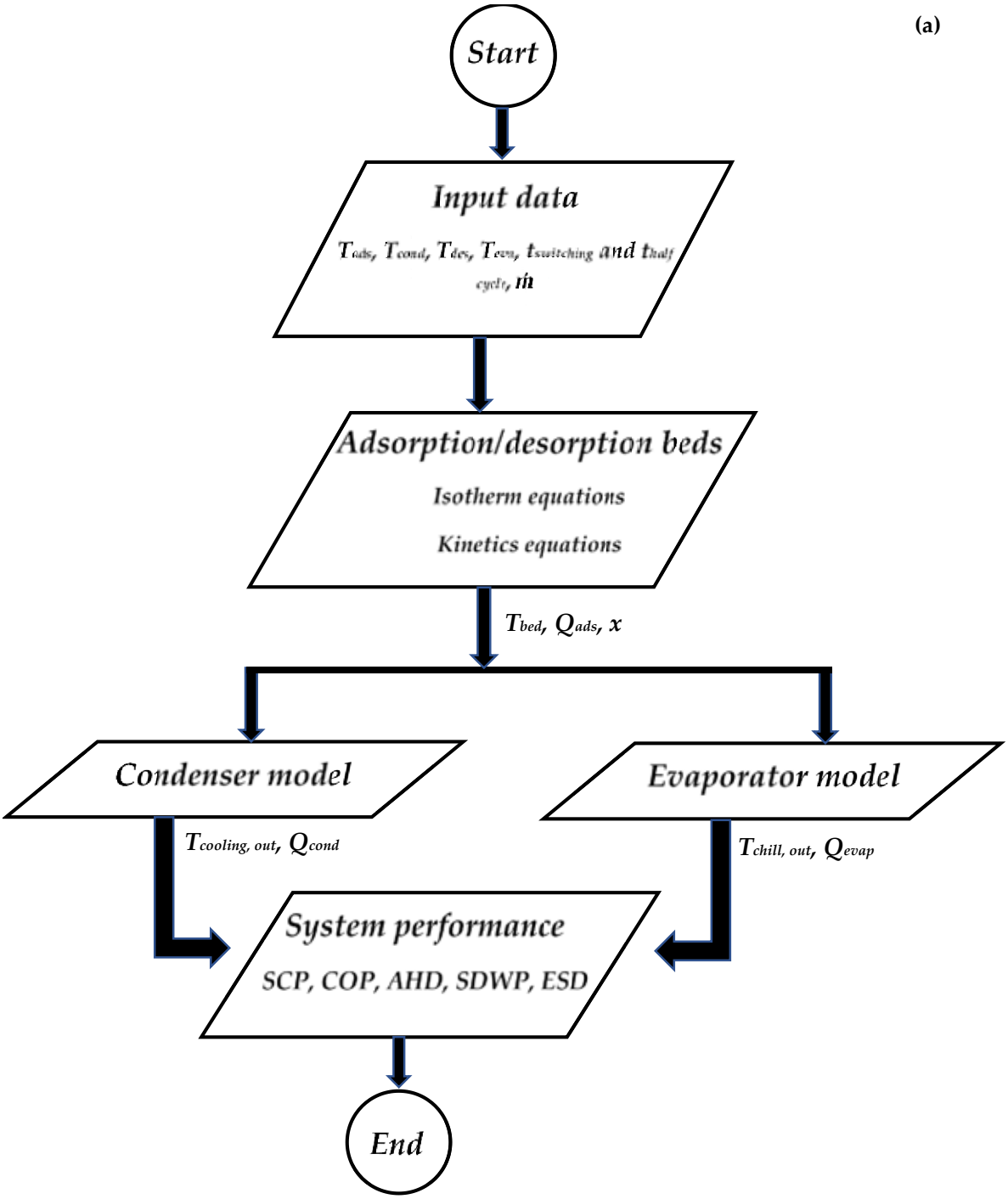
Start
Input data
T_{ads}, T_{cond}, T_{des}, T_{evp}, $t_{switching}$ and $t_{half\ cycle}$, $\dot{m}$
Adsorption/desorption beds
Isotherm equations
Kinetics equations
T_{bed}, Q_{ads}, x
Condenser model
Evaporator model
$T_{cooling,\ out}$, Q_{cond}
$T_{chill,\ out}$, Q_{evap}
System performance
SCP, COP, AHD, SDWP, ESD
End

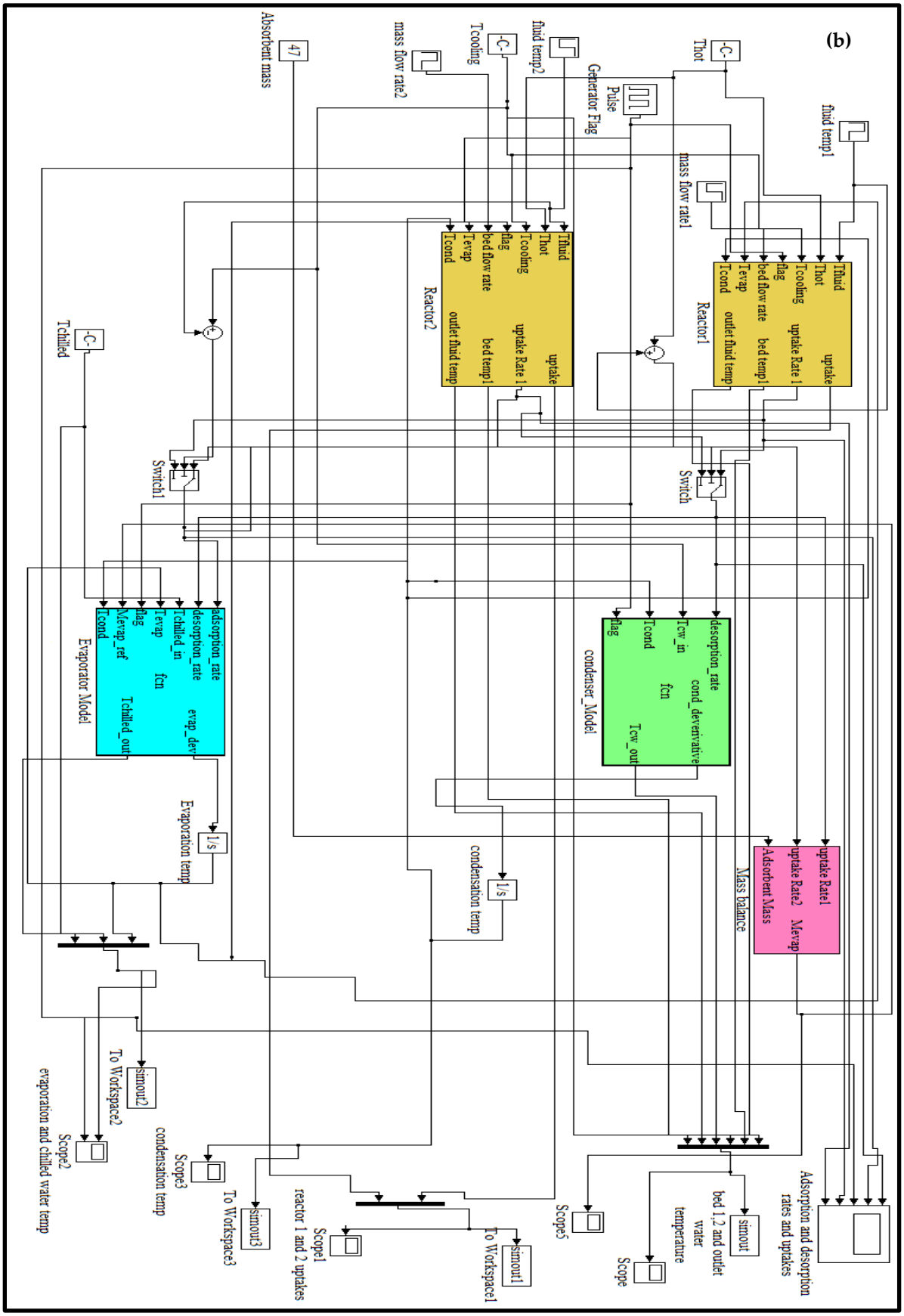

Fig. 6-1 a. Flowchart of the numerical model, b. two beds adsorption system SIMULINK simulation interface.

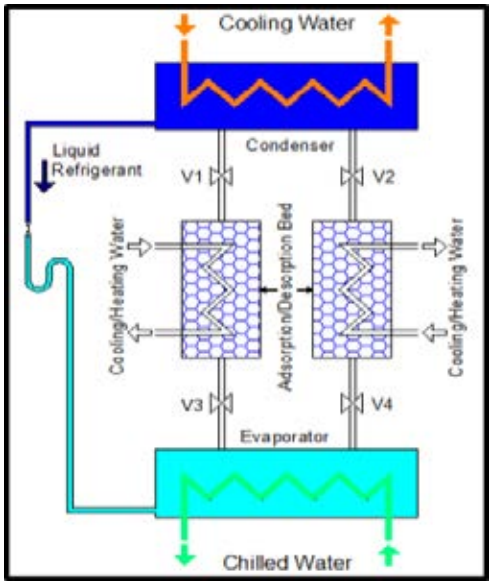

Fig. 6-2 Two bed adsorption system [102].

6.2. Governing equations

In this section, the governing equations of energy and mass balance for the adsorption/desorption beds, the evaporator and the condenser of each application are discussed.

Adsorption heat pump/cooling [284]

In this application and as explained in chapter 2, the adsorption bed is connected to the evaporator where the water (refrigerant) is evaporated, taking its evaporation heat from the surroundings and thereby producing useful cold (when used in cooling applications). Then the vapour is adsorbed into the porous adsorbent material, generating the heat of adsorption. This heat is either released to the environment in the cooling application or used as useful heat in the heating application. During the desorption process, the bed is dried by applying heat from external high temperature heat sources and the desorbed water vapour is condensed at the condenser releasing the heat of condensation, which is useful in the heating application or can be released to the environment in cooling application.

The overall mass balance recirculated in the system:

$$\frac{dM_{w,evap}}{dt} = -M_a \frac{dx_{des}}{dt} - M_a \frac{dx_{ads}}{dt} \qquad \textbf{(6-1)}$$

The adsorption/desorption bed energy balance:

$$\left(M_a(C_{p_a}+xC_{p_{w,v}})+M_{Cu,ads}C_{p_{Cu,ads}}+M_{Al,ads}C_{p_{Al,ads}}\right)\frac{dT_{ads}}{dt} = M_aQ_{st}\frac{dx}{dt}+m_w^{\bullet}C_{p_w}(T_{w,in}-T_{w,out}) \quad \textbf{(6-2)}$$

The isosteric heat of adsorption:

$$Q_{st} = -R_{water}\frac{\partial \ln(P)}{\partial(\frac{1}{T})} \quad \textbf{(6-3)}$$

Evaporator energy balance:

$$\left(M_{w,evap}C_{p_{w,l}}+M_{cu,evap}C_{p_{cu,evap}}\right)\frac{dT_{evap}}{dt} = -\left(M_a\frac{dx_a}{dt}\right)h_{fg}-M_aC_{p_{w,l}}T_{cond}\frac{dx_{des}}{dt} +m_{chill}^{\bullet}C_{p_w}(T_{chill,in}-T_{chill,out}) \quad \textbf{(6-4)}$$

The chilled water outlet temperature:

$$T_{chill,out} = T_{evap}+\left(T_{chill,in}-T_{evap}\right)\exp(-\frac{U_{evap}A_{evap}}{m_{chill}^{\bullet}C_{p_w}}) \quad \textbf{(6-5)}$$

The condenser energy balance:

$$\left(M_{cu,cond}C_{p_{cu,cond}}\right)\frac{dT_{cond}}{dt} = -\left(M_a\frac{dx_{des}}{dt}\right)h_{fg}+M_aC_{p_{w,l}}T_{cond}\frac{dx_{des}}{dt} +m_{cooling}^{\bullet}C_{p_w}(T_{cooling,in}-T_{cooling,out}) \quad \textbf{(6-6)}$$

The cooling water outlet temperature:

$$T_{cooling,out} = T_{cond}+\left(T_{cooling,in}-T_{cond}\right)\exp(-\frac{U_{cond}A_{cond}}{m_{cooling}^{\bullet}C_{p_w}}) \quad \textbf{(6-7)}$$

The adsorption heat:

$$Q_{ads} = \frac{m_w^{\bullet}C_{p_w}\int_0^{t_{cycle}}\left(T_{w,in}-T_{w,out}\right)dt}{t_{cycle}} \quad \textbf{(6-8)}$$

The heating density:

$$AHD = \frac{\dot{m}_w C_{p_w} \int_0^{t_{cycle}} \left(T_{w,in} - T_{w,out}\right) dt}{M_a} \quad \textbf{(6-9)}$$

The condensation heat:

$$Q_{cond} = \frac{\dot{m}_{cooling} C_{p_w} \int_0^{t_{cycle}} \left(T_{cooling,in} - T_{cooling,out}\right) dt}{t_{cycle}} \quad \textbf{(6-10)}$$

The evaporation heat:

$$Q_{evap} = \frac{\dot{m}_{chill} C_{p_w} \int_0^{t_{cycle}} \left(T_{chill,in} - T_{chill,out}\right) dt}{t_{cycle}} \quad \textbf{(6-11)}$$

The specific cooling power:

$$SCP = \int_0^{t_{cycle}} \frac{Q_{evap}}{M_a} dt \quad \textbf{(6-12)}$$

The desorption heat:

$$Q_{des} = \frac{\dot{m}_{hot} C_{p_w} \int_0^{t_{cycle}} \left(T_{hot,in} - T_{hot,out}\right) dt}{t_{cycle}} \quad \textbf{(6-13)}$$

The heating coefficient of performance

$$COP_h = \int_0^{t_{cycle}} \frac{Q_{ads} + Q_{cond}}{Q_{des}} \quad \textbf{(6-14)}$$

The cooling coefficient of performance

$$COP_{ref} = \int_0^{t_{cycle}} \frac{Q_{evap}}{Q_{des}} dt \quad \textbf{(6-15)}$$

The calculation of the thermal resistances, heat transfer coefficient U and conductance UA of the evaporator, condenser and adsorption/desorption beds were calculated according to [73].

6.2.1. Adsorption desalination [14]

In this application and as explained in chapter 2, the first bed is in the evaporation–adsorption mode where the seawater is evaporated due to the affinity of the adsorbent resulting in the cooling effect from the evaporator. Heat of adsorption is released to cooling water in the adsorption bed. During the desorption–condensation mode, heat is supplied to the desorption bed to remove the adsorbed water vapour. As the desorption bed and condenser are connected, the water vapour migrates to the condenser where the vapour is condensed, and the desalinated water is collected. This means that the condensed water is not returned to the evaporator unlike what happens in the heat pump application.

Evaporator energy balance:

$$[M_{sw,evap}C_{p_{sw}} + M_{Cu,evap}C_{p_{Cu,evap}}]\frac{dT_{evap}}{dt} = -h_{fg}M_a\frac{dx_{ads}}{dt} + \dot{m}_{chill}C_{p_w}(T_{chill,in} - T_{chill,out}) \quad \textbf{(6-16)}$$

Condenser energy balance:

$$M_{Cu,cond}C_{p_{Cu,cond}}\frac{dT_{cond}}{dt} = h_{fg}M_a\frac{dx_{des}}{dt} + \dot{m}_{cooling}c_{p_w}(T_{cooling,in} - T_{cooling,out}) \quad \textbf{(6-17)}$$

Adsorption/Desorption bed energy balance can be calculated using **Eq. 6-2**.

For assessment of cycle performance, the specific daily water production (SDWP), specific cooling power (SCP) (**Eq. 6-12**) and coefficient of performance (COP) (**Eq. 6-15**) are calculated.

$$SDWP = \int_0^{t_{cycle}} \frac{Q_{cond}\tau}{h_{fg}M_a}dt \quad \textbf{(6-18)}$$

$$\tau = \frac{24\times 60\times 60}{t_{cycle}} \quad \textbf{(6-19)}$$

6.2.2. Adsorption energy storage [285]

The operating of mode of the adsorption energy storage is similar to that of the heat pump application. The mass and heat balance of the evaporator, the heat balance of the condenser and finally the heat balance equation for the adsorption/desorption beds can be calculated from **Eq. 6-1** to **Eq. 6-10** [285].

The heat released and can be stored

$$Q_{\mathrm{Re}leased} = Q_{ads} + Q_{cond} \quad \textbf{(6-20)}$$

The specific energy storage density (ESD) can be calculated through **Eq. 6-21**:

$$ESD = \frac{Q_{\mathrm{Re}leased}\, t_{cycle}}{M_a \times 3600} \quad \textbf{(6-21)}$$

6.3. Simulink model validation

A Simulink model was developed for a two-bed adsorption system with the specifications listed in **Table. 6-1**. The mathematical model is based on the following assumptions:

1. The adsorbed phase and the refrigerant vapour are considered to be liquid and ideal gas, respectively.
2. Fully developed turbulent fluid is assumed, and the convection coefficient between the tube and fluid is calculated using the Dittus-Boelter equation.
3. All adsorbent particles are uniform in size, shape and porosity, and are distributed uniformly throughout the bed.
4. Local thermal equilibrium between the adsorbed and vapour phases is assumed.
5. Heat losses through the chamber walls are neglected.

The model was validated with the experimental data generated at the operating conditions shown in **Table. 6-2**. Experimental data were generated through testing adsorption beds packed with aluminium fumarate. **Fig. 6-3** compares the temperature profile predicted by the model to

those experimentally measured showing the good agreement between both. The deviation between experimental data and simulation model during the switching time can be attributed to the heat losses that were neglected in the numerical model.

The validity of the SIMULINK model was also highlighted through comparing the system outputs (**Fig. 6-4**), SCP in case of cooling and SDWP in case of desalination, where once again good agreement between experimental and model data was observed.

Table. 6-1 Specifications of the heat exchangers used in the Simulink two-bed adsorption system

Parameter	Units	Value
Length	m	350×10^{-3}
Fin width	m	173×10^{-3}
Fin height	m	30×10^{-3}
Fin pitch	m	1.0×10^{-3}
Fin thickness	m	0.1×10^{-3}
Tube outer diameter	m	15.87×10^{-3}
Tube thickness	m	0.8×10^{-3}
Number of fins in one heat exchanger	—	354
Adsorbent/heat exchanger	kg	0.375

Table. 6-2 Experimental and modelling operating conditions

Parameter	Units	Value
Chilled water inlet temperature	°C	10
Adsorption bed cooling water inlet temperature	°C	30
Condenser cooling water inlet temperature	°C	30
Desorption bed heating water inlet temperature	°C	90
Half cycle time	s	700
Switching time	s	70

Adsorption bed cooling water flowrate	L min^{-1}	16
Adsorption bed heating water flowrate	L min^{-1}	20
Chilled water flowrate	L min^{-1}	3.25
Condenser cooling water flowrate	L min^{-1}	3.5
Adsorbent/heat exchanger	kg	0.375
No of heat exchangers/bed	—	2

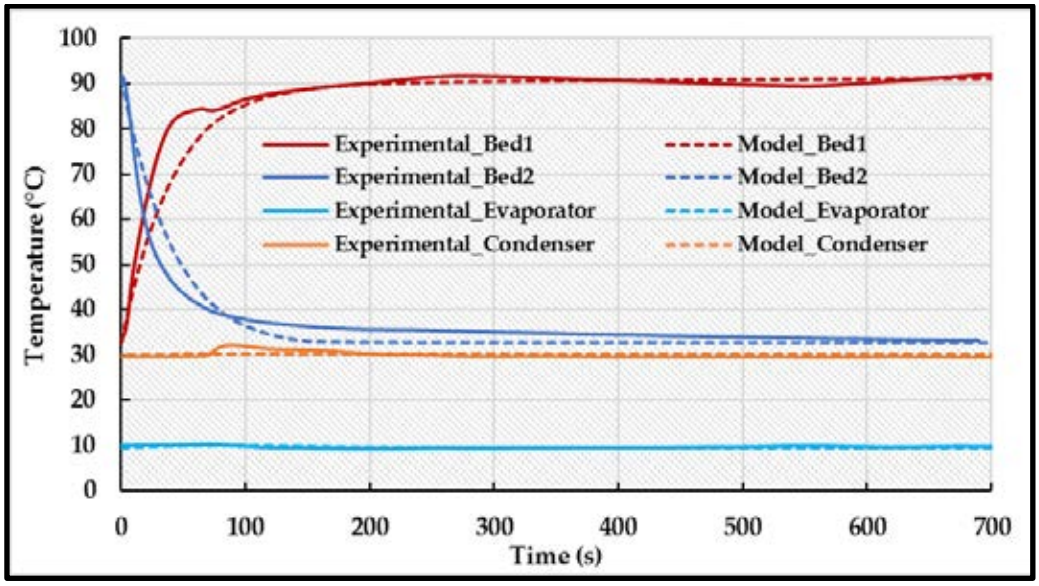

Fig. 6-3 Experimental and numerical temperature profiles of adsorption system components.

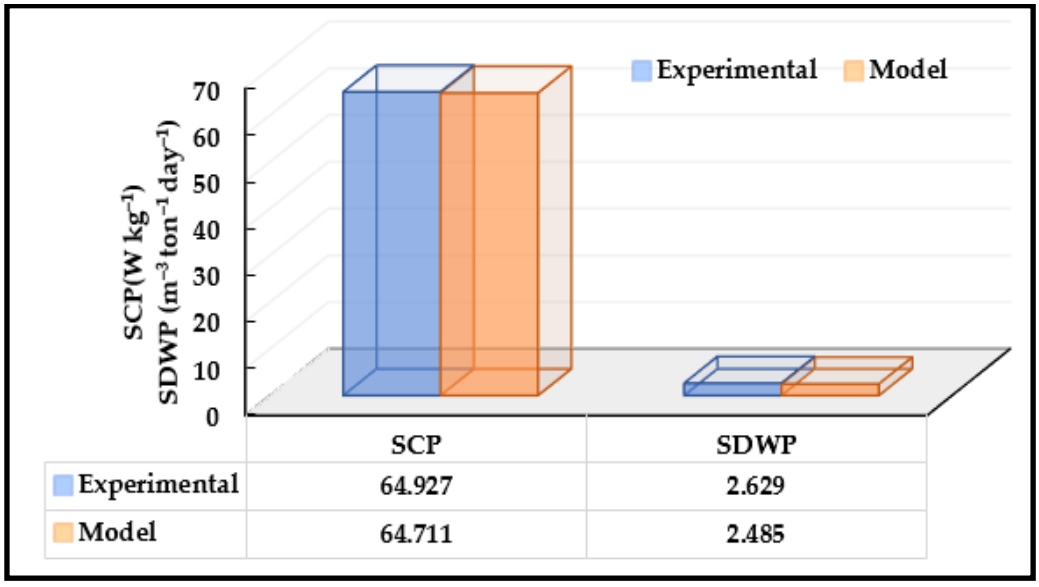

Fig. 6-4 Experimental and numerical SCP and SCP comparison.

Using the validated model, the performance of the MOF materials described in chapter 4 and 5 will be investigated in the next section at standard operating conditions for each application.

6.4. Adsorption air conditioning

The performance of MOF materials and their composites was investigated for air conditioning/refrigeration application using standard operating conditions adopted from *Saha et al.,* [286] and *Tamainot-Telto et al.,* [80] where an adsorption bed and condenser cooling water inlet temperatures of 30°C were used while a chilled water inlet temperature of 10°C was assumed. For moderate cooling (cooling at higher temperature), a chilled water inlet temperature of 20°C was also investigated [35]. A desorption bed heating water inlet temperature of 90°C was assumed as it can easily be supplied either by industrial waste heat or renewable energy resources such as solar energy. The cycle time in a finned tube heat exchanger using silica gel/water as working pair varies from 15 min [286] to 34 min [230], hence an average cycle time of 23 min (1400 s) was chosen.

Fig. 6-5 shows the SCP of each material at evaporation temperatures of 10°C and 20°C. It can be noticed that the performance of all materials except CPO-27(Ni) was significantly improved with increasing the evaporation temperature. This is attributed to the fact that all the investigated materials exhibit a type IV isotherm (**Fig. 6-6**) where the uptake increases significantly with increasing the operating relative pressure (chilled water inlet temperature). In case of CPO-27(Ni), increasing the chilled water inlet temperature was found to have a very limited effect as the material exhibits a type I water adsorption isotherm (**Fig. 6-6**) reaching 81% of its capacity at a very low relative pressure and hence less dependent on the evaporation temperature [221].

It can also be noticed that at a chilled water inlet temperature of 10°C, CPO-27(Ni) outperformed all other neat MOFs as it produced an SCP of 146 W kg^{-1}. It was followed by MIL-100(Fe) with an SCP of 97 W kg^{-1}, MIL-101(Cr) with 76 W kg^{-1} and finally aluminium

fumarate with 65 W kg^{-1} compared to 160 W kg^{-1} for silica gel. MOFs are expected to outperform silica gel at longer cycle times as it was previously concluded [285] or at higher desorption temperatures. Nevertheless, the MOFs composites, specially the $CaCl_2$ composites: Comp_1:8 and Comp_1:5, showed an exceptional performance as they outperformed silica gel and all the studied MOF materials giving 246 and 147 W kg^{-1}. The two composites were followed by another composite which was the 50% CPO-27(Ni) giving 115 W kg^{-1}. The improvement of such composites compared to their parent MIL-100(Fe) and MIL-101(Cr) is attributed to the improvement in the isotherm shape and the mass transfer properties (**Fig. 6-6**). The performance of all the MOFs and their composites is expected to significantly improve with increasing the desorption temperatures, specially CPO-27(Ni) and its composite with MIL-100(Fe) as both exhibit type I isotherm where a desorption temperature higher than 100°C is needed as it was previously concluded [221]

Regarding the performance of the system at a chilled water inlet temperature of 20°C, the Comp_1:8 composite had the highest SCP of 366 W kg^{-1}, the MIL-100(Fe) and its composites showed SCP higher than 200 W kg^{-1} and was followed by the 50% $CaCl_2$ and aluminium fumarate giving a cooling effect of 217 and 211 W kg^{-1}.

In case of MIL-101(Cr) and its GrO composites, it was found that the three materials required longer cycle times to reach their maximum capacities. The 2% GrO_synthesis composite outperformed the parent MIL-101(Cr) while in a previous study a significant decrease in the desorption temperature was observed in case of the 5%GrO_physical composite due to the enhancement in the thermal conductivity [260].

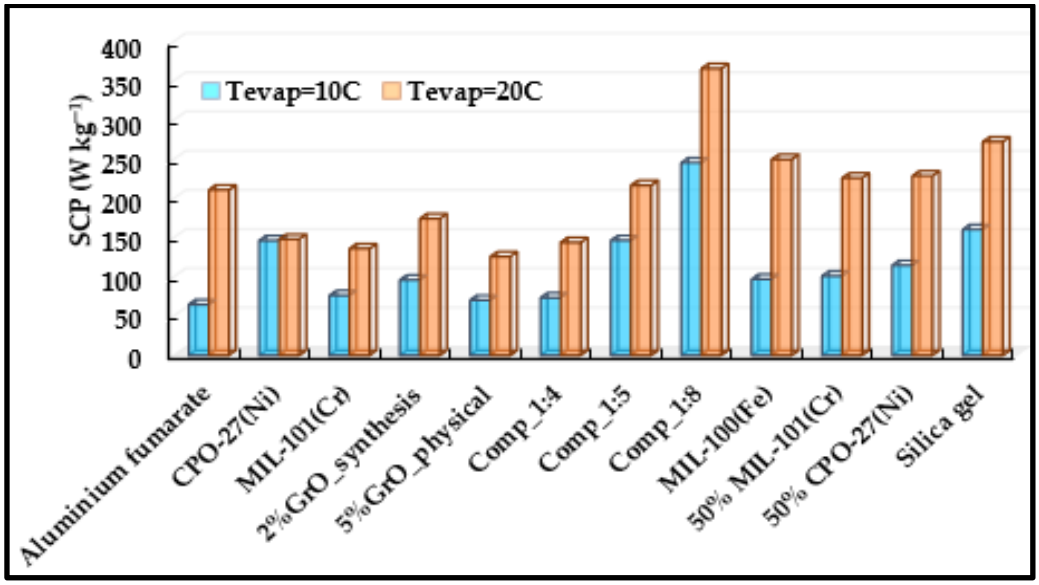

Fig. 6-5 Specific cooling power of different MOFs and their composites in air conditioning application.
(T_{ads}=30°C, T_{cond}=30°C, T_{des}=90°C, half cycle time=700 s and $t_{switching}$=70 s)

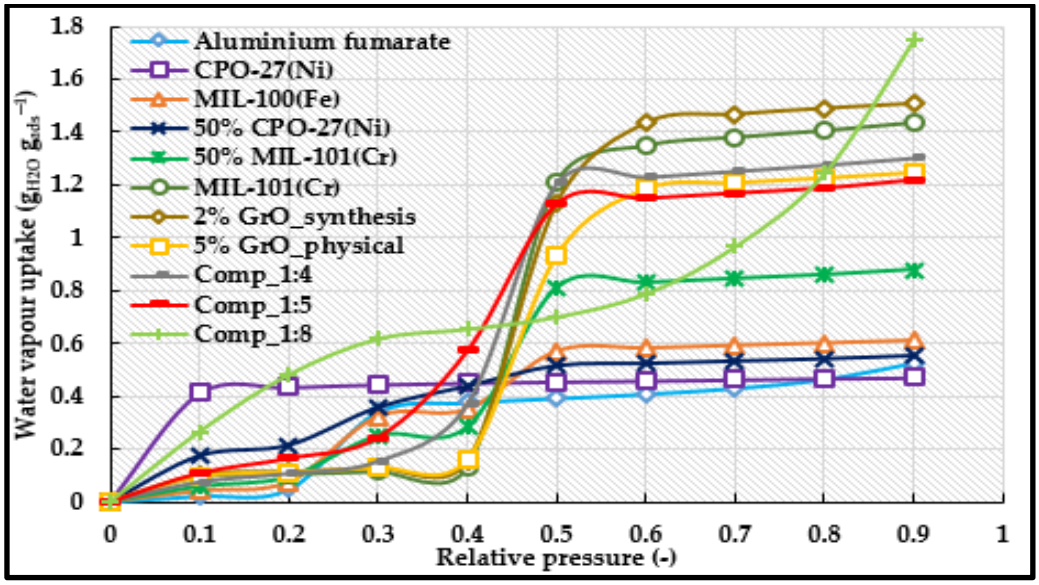

Fig. 6-6 Water vapour uptake of different MOF materials.

6.5. Adsorption heat pumping

One of the most commonly used applications of adsorption systems is the adsorption heat pump for heating purposes. In this application the heat of adsorption generated during the adsorption phase and the heat of condensation generated during the desorption phase are recovered to be used for heating purposes instead of wasting it to the ambient.

In this modelling work, the operating conditions of a standard heat pump cycle was adopted from *Tamainot-Telto et al.,* [80] where the adsorption bed cooling water and condenser cooling water inlet temperatures were 40°C, the chilled water inlet temperature was 5°C and the desorption bed heating water inlet temperature was 90°C. A half cycle time of 700 s and a switching time of 70 s were used. Another cycle was adopted from *Núñez et al.*, [75] where a lower condenser cooling water and a higher chilled water inlet temperatures both of 15°C were also used. The rate of heat recovered and the heating density of the two cycles are shown in **Fig. 6-7** and **6-8**.

For the first cycle and between the main four MOF materials, CPO-27(Ni) showed the highest performance with a heating rate of 1.15 kW and heating density of 1079 kJ kg^{-1}. It was followed by MIL-100(Fe), MIL-101(Cr) and aluminium fumarate giving a heating density of 1038, 1011 and 960 kJ kg^{-1}, respectively. The composites showed an improved performance compared to their parent materials including silica gel specially the $CaCl_2$ composite (Comp_1:8) which gave a heating density of 1185 kJ kg^{-1}.

Regarding the second cycle, it is evident that the performance of the materials including silica gel significantly improved. This is attributed to both the higher chilled water and lower adsorption temperatures employed which means a higher working relative pressure and a higher adsorbed water. Also, the second cycle utilized a significantly lower condensation temperature which means an efficient drying and facilitating the water vapour flow from the bed to the condenser. These conditions increased the heating density of CPO-27(Ni) to 2297 kJ kg^{-1}

followed by MIL-100(Fe), MIL-101(Cr) and aluminium fumarate giving a heating density of 1400, 1394 and 1288 kJ kg^{-1}, respectively. The composites showed an improved performance compared to their parent materials specially the $CaCl_2$ composites which gave a heating density up to 2133 kJ kg^{-1}. The comparison between the two cycles highlights that the performance of adsorbents in general highly depends on the operating conditions.

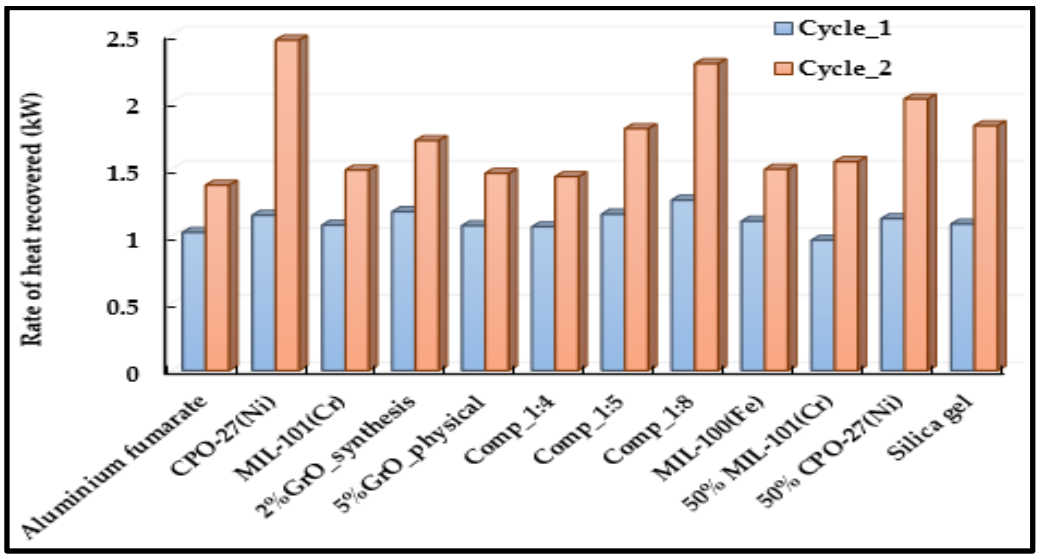

Fig. 6-7 Rate of heat recovered for different MOFs and their composites in heat pump application.
(Cycle 1: T_{eva}=5°C, T_{ads}=40°C, T_{cond}=40°C, T_{des}=90°C, half cycle time=700 s and $t_{switching}$=70 s).
(Cycle 2: T_{eva}=15°C, T_{ads}=35°C, T_{cond}=15°C, T_{des}=90°C, half cycle time=700 s and $t_{switching}$=70 s).

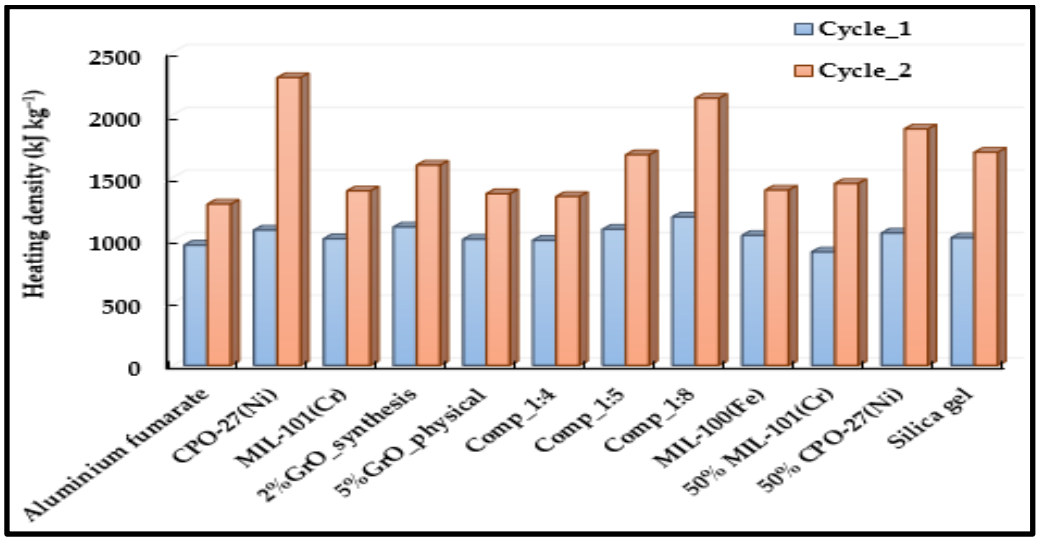

Fig. 6-8 Heating density for different MOFs and their composites in heat pump application.
(Cycle 1: T_{eva}=5°C, T_{ads}=40°C, T_{cond}=40°C, T_{des}=90°C, half cycle time=700 s and $t_{switching}$=70 s).
(Cycle 2: T_{eva}=15°C, T_{ads}=35°C, T_{cond}=15°C, T_{des}=90°C, half cycle time=700 s and $t_{switching}$=70 s).

6.6. Adsorption desalination

Adsorption desalination is a relatively new application that have gained a considerable amount of research as the problem of water scarcity is becoming more serious around the world. The operating conditions for an adsorption desalination cycle were adopted from *Thu* [209] where an adsorption bed cooling water inlet temperature of 30°C, a condenser cooling water inlet temperature of 30°C and a desorption bed heating water inlet temperature of 90°C were used. The half cycle time was 700 s and the switching time was 70 s. The chilled water inlet temperature varied between 10°C and 20°C for adsorption desalination with cooling to 29°C for adsorption desalination without cooling. **Fig. 6-9** shows that all the investigated materials produced an SDWP varying with the chilled water inlet temperature except CPO-27(Ni) that produced 5.6 m^3 ton^{-1} day^{-1} regardless of the temperature used. The MIL-100(Fe) and its 50% CPO-27(Ni) and 50%MIL-101(Cr) composites produced 3.7, 4.4, 3.8 m^3 ton^{-1} day^{-1} at a chilled water inlet temperature of 10°C and significantly higher values of 14.7, 14.0 and 13.7 m^3 ton^{-1} day^{-1} at an evaporation temperature of 29°C.

In case of composites, the Comp_1:8 $CaCl_2$ composite outperformed all other materials giving 9.4, 14 and 19 m^3 ton^{-1} day^{-1} at the investigated chilled water temperatures. The SDWP produced from the MOF materials and their composites is expected to increase significantly through increasing the desorption temperature or decreasing the condensation temperature. The SCP produced from the desalination system can be extracted from the data presented in **Fig. 6-5** where it is evident that the Comp_1:8 composite outperformed all the investigated materials at both temperatures.

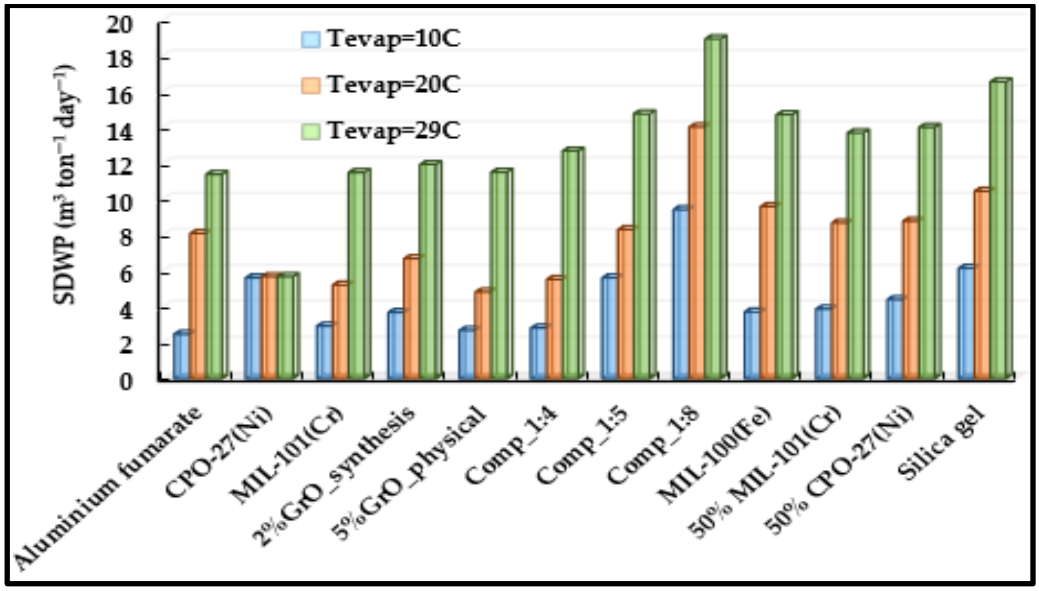

Fig. 6-9 Specific daily water production for different MOFs and their composites in adsorption desalination application.
(T_{ads}=30°C, T_{cond}=30°C, T_{des}=90°C, half cycle time=700 s and $t_{switching}$=70 s)

6.7. Adsorption energy storage

Thermal energy storage (TES) has proved to be a potential solution for the high-energy consumption problem. Such systems can reduce the power consumption as it can reduce the electric power demands in buildings through utilizing waste heat recovery and renewable energy [47]. Also, energy storage can balance the demand on the power grid through storing cheap electricity at off peak hours to be re-used at peak times. Adsorption heat storage technology is a thermal energy storage that can offer numerous advantages such as being a green technology, high energy storage density, negligible heat loss, long-term heat storage capability and flexible working mode [54, 55] as highlighted in chapter 2.

The potential of the various MOF materials in adsorption energy storage application was numerically investigated. **Fig. 6-10** shows the energy storage densities of MOFs under investigation and their composites compared to silica gel in adsorption thermal energy storage application. The operating conditions were adopted from *Elsayed et al.*, [285] where an adsorption cooling water inlet temperature of 30°C, a chilled water inlet temperature of 15°C,

a condenser cooling water inlet temperature of 30°C and a desorption bed heating water inlet temperature 90°C were used with a half cycle time of 3600 s. It can be noticed that at the specified operating conditions and among the four main MOF materials, MIL-100(Fe) showed the highest performance storing 821 W h kg^{-1} followed by aluminium fumarate storing 802 W h kg^{-1}, CPO-27(Ni) storing 711 W h kg^{-1} and MIL-101(Cr) giving 454 W h kg^{-1} compared to 611 W h kg^{-1}. The poor performance of MIL-101(Cr) is attributed to the low working relative pressure while in case of CPO-27(Ni) is due to the low desorption temperature. Also, it can be observed that the synthesized composites significantly enhanced the performance of the parent MOF materials. The highest energy density was marked for the Comp_1:8 $CaCl_2$ composite with a density of 1192 W h kg^{-1} followed by the 50% CPO-27(Ni)/MIL-100(Fe) giving 813 W h kg^{-1} which is expected to store higher energy using a higher desorption temperature. The two composites of MIL-101(Cr) with MIL-100(Fe) and Comp_1:5 gave a comparable performance of 764 and 724 W h kg^{-1}. Even though the two GrO composites showed an enhanced performance compared to the neat MIL-101(Cr), similar to MIL-101(Cr) the two composites require high relative pressure range to work at.

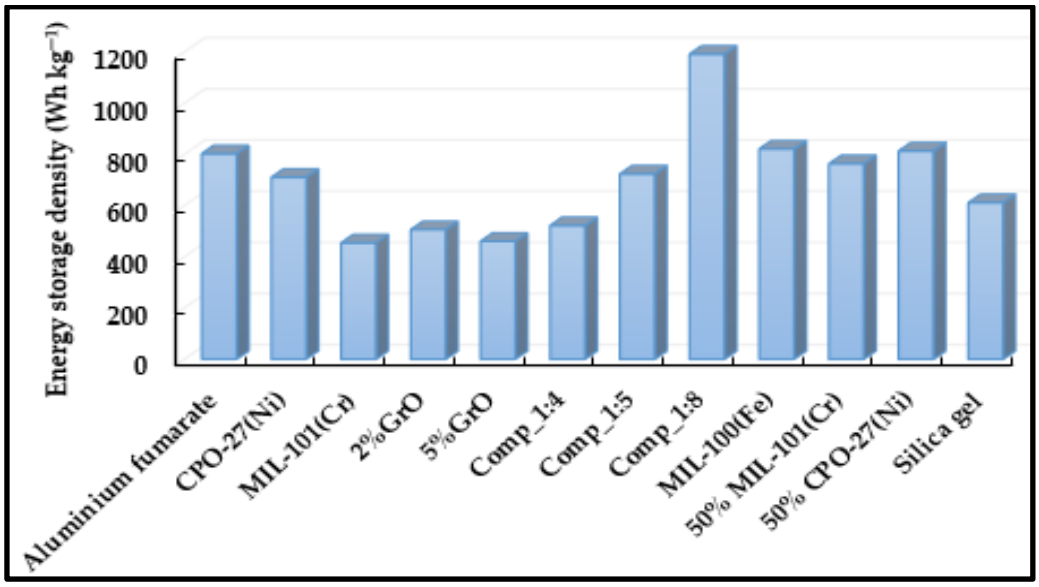

Fig. 6-10 Energy storage densities of different MOFs and their composites in adsorption thermal energy storage application.
(T_{ads}=30°C, T_{eva}=15°C, T_{cond}=30°C, T_{des}=90°C, half cycle time=3600 s and $t_{switching}$=70 s)

6.8. Summary

A SIMULINK model for a two-bed adsorption system was developed and validated with experimental data generated using aluminium fumarate/water as working pair. The validated numerical model was utilized to investigate the potential of different MOFs and their composites in different adsorption applications. It was found that:

1- The performance of all the adsorbent materials significantly depends on the operating conditions of the system.

2- Adsorbents exhibiting type I adsorption isotherms (such as CPO-27(Ni)) require high desorption temperatures, nevertheless such adsorbents outperform other adsorbents at application working at low chilled water inlet temperatures such as adsorption cooling or adsorption desalination with cooling effect.

3- MIL-100(Fe) and aluminium fumarate showed good performance at the different adsorption applications and under various operating conditions.

4- MIL-101(Cr) requires long cycle times and is only suitable for applications working at high relative pressure ranges.

5- Synthesising composites has proven to be an efficient technique to significantly improve the system performance, MIL-101(Cr)/$CaCl_2$ composites have outperformed all other adsorbent at the different operating conditions.

6- Despite their remarkable performance, there is still a problem facing MIL-101(Cr) and its composites as it can be only available at lab scale without any mean for mass production till now. Such problem hinders building and commercialization of an adsorption system employing these adsorbents.

7- Despite the remarkable performance of CPO-27(Ni) at low chilled water inlet temperatures and its availability in large amounts, the material can only be used in

applications employing high temperature energy sources which limit its use in certain applications.

8- Due to the mass production of aluminium fumarate and the development of a method to scale up the synthesis of MIL-100(Fe) as it was shown in chapter 4 and that both materials can work at a wide range of operating conditions, the two materials were chosen to be experimentally tested in a two-bed adsorption system as it will be shown in chapter 7.

CHAPTER 7
EXPERIMENTAL TEST FACILITY

7.1. Introduction

In this chapter, the components and testing of a double bed adsorption system are described. Based on the conclusions of chapter 4 and 6, MIL-100(Fe) and aluminium fumarate were chosen to be experimentally tested. The adsorption system was tested at different operating conditions through varying the half cycle time, the child water, adsorption bed cooling water, condenser cooling water and desorption bed heating water temperatures to determine the optimum operating conditions for different adsorption applications.

7.2. Test facility description

Fig. 7-1 shows a schematic diagram and a pictorial presentation of the experimental test facility**.** As it can be noticed, the main components of the system are two identical adsorption beds, an evaporator and a condenser. Each bed is fitted with two fin and tube heat exchangers packed with 0.375 kg each in case of aluminium fumarate or with one fin and tube heat exchanger packed with 0.23 kg in case of MIL-100(Fe).

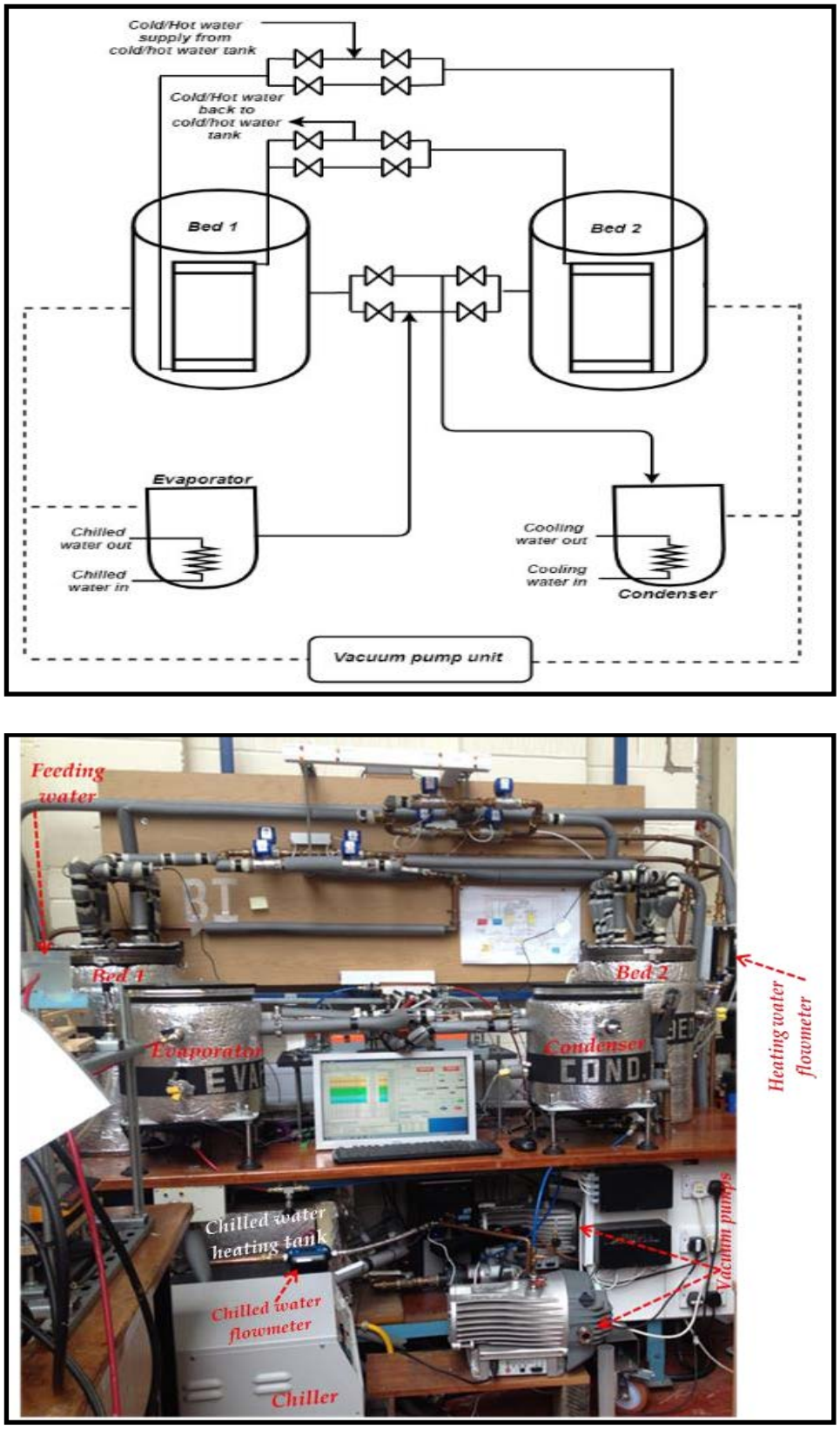

Fig. 7-1 Schematic diagram and pictorial presentation of the 2-bed system test facility.

7.2.1. Adsorption bed

The adsorption/desorption bed is the main component in any adsorption system. During the adsorption phase, the bed is connected to the evaporator to adsorb the water vapour while during the desorption phase, the bed is connected to the condenser to desorb the vapour. Each bed consists of a cylindrical steel vessel where pressure transducers and thermocouples are fitted. In case of aluminium fumarate, each vessel contained two heat exchangers with six copper tubes that are connected to hot/cold water supply header and the return water pipe (**Fig. 7-2a**) with the dimensions shown in **Table. 7-1**. While in case of MIL-100(Fe) and due to the smaller amount of the adsorbent material, there was only one heat exchanger in each bed with 4 copper tubes (**Fig. 7-2b**) and the dimensions shown in **Table. 7-1**.

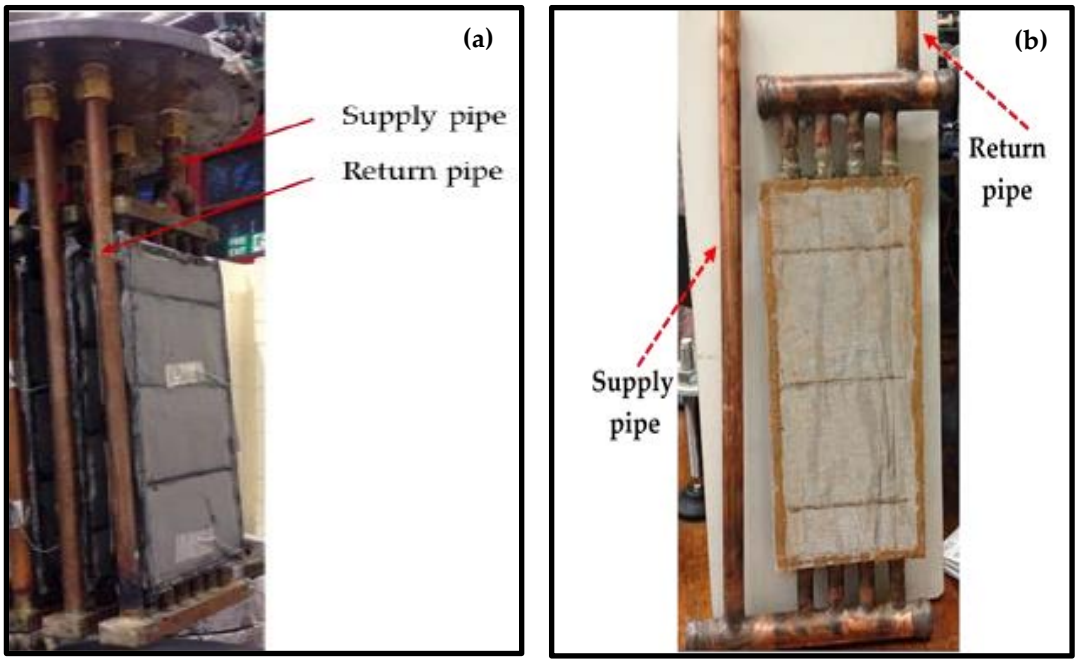

Fig. 7-2 Fin and tube heat exchanger of a. aluminium fumarate and b. MIL-100(Fe).

Table. 7-1 Dimensions of aluminium fumarate and MIL-100(Fe) heat exchangers

		Aluminium fumarate	MIL-100(Fe)
Parameter	**Units**	**Value**	
Length	m	350E–3	275E–3
Fin width	m	173E–3	115E–3
Fin height	m	30E–3	
Fin pitch	m	1.0E–3	
Fin thickness	m	0.1E–3	
Tube outer diameter	m	15.87E–3	
Tube thickness	m	0.8E–3	
Number of fins in one heat exchanger	—	354	270
Adorbent/heat exchanger	kg	0.375	0.232
No of heat exchangers/bed	—	2	1

7.2.2. Evaporator

Another essential part of the adsorption system is the evaporator where the evaporation of water (seawater in case of adsorption desalination application) takes place. The Evaporator used in this study consists of stainless-steel vacuum chamber with a two-level helical coil formed using 10 m of 8 mm outer diameter copper tube working as the chilled water circuit (**Fig. 7-3**). The water (refrigerant) was introduced to the evaporator using a nozzle to enhance the contact between the coil surface and the water droplets (**Fig. 7-4**).

Fig. 7-3 Top and side views of the copper coil in evaporator.

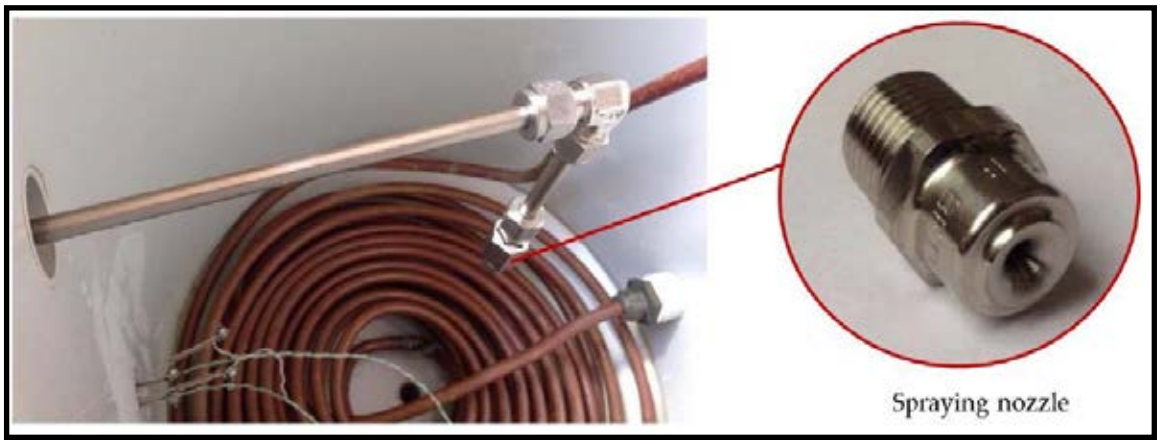

Fig. 7-4 Spraying nozzle.

7.2.3. Condenser

The condenser is where the desorbed water vapour is condensed to produce distilled water in case of desalination or sent back to the evaporator in case of other applications. It consists of a stainless-steel shell and a helical copper coil. The stainless-steel shell is identical to the one used in the evaporator with the copper coil consists of two spiral coils, one inside the other formed from a 10 m of 8 mm outer diameter copper tube as shown in **Fig. 7-5**.

Fig. 7-5 Top and side views of the copper coil in condenser.

7.2.4. Pumps

Three circulating pumps were used to circulate water through the system while two vacuum pumps were used to place the system under vacuum. The first circulating pump is the chilled water pump which was SS-9R-MD pump from March May Ltd (**Fig. 7-6**) with a maximum mass flow rate of 60 L min^{-1} and maximum operating pressure of 6 bar.

Fig. 7-6 Chilled water pump.

Two identical horizontal multi-stage circulating pumps were used in the system as cold and hot water pump to feed the system with cooling/heating water during adsorption/desorption processes (**Fig. 7-7**). The Calpeda pump has a maximum flow rate of 70 L min^{-1} and a maximum operating temperature of 110°C.

Fig. 7-7 Heating and cooling water pump.

The two vacuum pumps were Edwards nXDS15i dry (oil free) pumps (**Fig. 7-8**) that can reach a pressure as low as 0.5 Pa. The two vacuum pumps were connected to the adsorption/desorption beds, the evaporator and the condenser.

Fig. 7-8 nXDS15i dry vacuum pump.

7.2.5. Measuring devices

The measuring devices in the test facility includes pressure transducers, thermocouples and flowmeters.

7.2.5.1. Pressure transducers

Five pressure transducers were fitted in the system. Two were fitted on the adsorption beds, one at the evaporator, one at the condenser and one at the collection tank where the distilled water was collected. The pressure transducers were OMEGA-PXM319-0.35AI (**Fig. 7-9**) with an accuracy of ±0.8 mbar and a measuring range of 0-350 mbar. The transducer output

is a signal of 4 to 20 mA which is converted to a voltage signal through a 100Ω resistance connected to the data logger to give the final value of the pressure.

Fig. 7-9 Pressure transducer.

7.2.5.2. Thermocouples

Two types of thermocouples are used in the system to measure the temperature, namely 'K' and 'RTD' thermocouples (**Fig. 7-10**). The 'K' type was used in the i) adsorption bed to measure the temperature of the adsorbent material at different positions; ii) evaporator to measure the temperature of vapour and liquid and iii) condenser to measure the vapour and liquid temperatures. These K type thermocouples were fitted using feed through connections capable of maintaining vacuum conditions. The resistance temperature detectors (RTD) probes were used to measure the inlet and outlet temperatures of the flowing water at the adsorption beds, evaporator and condenser. The RTD probes sheath is 100 mm in length and 6 mm outer diameter fitted such that the sensing element is positioned at the centre of the flow.

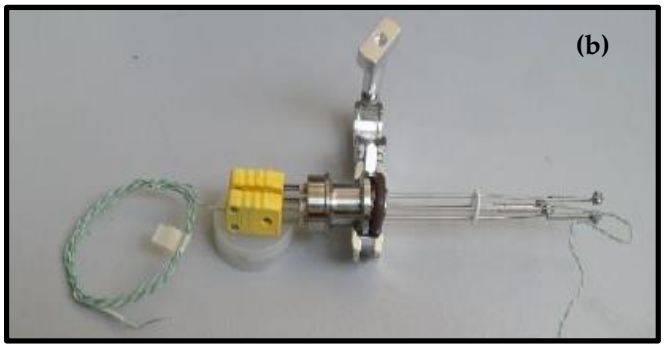

Fig. 7-10 a. RTD and b. K thermocouples.

Detailed information on the calibration of the thermocouples and pressure transducers can be found in [287, 288]. It was found that the average absolute uncertainty was ±0.377°C for the type K thermocouples, ±0.246°C for the type RTD thermocouples and ±0.8 mbar for the pressure transducers [288].

7.2.5.3. Flowmeters

Four float-type flowmeters were used to measure the flowrates of the adsorption bed cooling water, heating water, the evaporator chilled water and the condenser cooling water. The flowmeter of the heating water was a Platon-A24S.S.Mk2 with a maximum flowrate of 40 L min^{-1} and accuracy of ±1 L min^{-1} while that of the evaporator was a Platon-A12S.S.Mk2 with a maximum flowrate of 10 L min^{-1} and accuracy of ±0.25 L min^{-1}. The adsorption bed cooling water line was fitted with a Brooks-2500 series with a maximum flowrate of 36 L min^{-1} and accuracy of ±2 L min^{-1} while the condenser cooling water flowrate was measured using a Parker- LOFLOW flowmeter with a maximum flowrate of 9 L min^{-1}.

7.2.6. Testing procedures

1. The data logging system is turned on and connected to all the components to measure their temperature and pressure.
2. The heating, cooling and chilled water tanks are filled, and their temperatures are set at the desired temperature. The temperature of the cooling water fed to condenser is also adjusted.

3. The vacuum pumps are switched on and the system (adsorption beds, evaporator, condenser and collecting tank) is vacuumed to ensure the complete removal of air.
4. After the vacuum pumps are switched off, the feed water is introduced to the evaporator and the pump is turned on till the liquid temperature inside the evaporator reaches the desired temperature. The cooling and heating water pumps are turned on as the system is now ready for adsorption/desorption cycles.
5. The system is controlled through LabVIEW software.
6. To start the adsorption/desorption process, the switching time starts through closing the valves between the beds, the condenser and the evaporator. The temperature and pressure of bed 1 are increased through using hot water (pre-heating) while the temperature and pressure of bed 2 are decreased through using the cold water (pre-cooling).
7. After the switching time is finished, the valve between bed 1 and the condenser is opened to allow the desorption of the water vapour while the valve between bed 2 and the evaporator is opened to allow the evaporation and adsorption of the water vapour. The process is continued for a half cycle time.
8. After the end of the half cycle time, the valves between the beds, the condenser and the evaporator are closed. The mode is reversed as the temperature and pressure of bed 1 are decreased using cold water (pre-cooling) while the temperature and pressure of bed 2 are increased through flowing hot water (pre-heating).
9. After the switching time is finished, the valve between bed 1 and the evaporator is opened to allow the evaporation and adsorption of the water vapour while the valve between bed 2 and the condenser is opened to allow the desorption and condensation of the water vapour. The process is continued for a half cycle time.
10. The process is repeated for a number of cycles.

11. After the end of the cycles, water is collected from the collection tank in case of desalination application, specific cooling power (SCP) and specific daily water production (SDWP) are calculated using **Eq. 6-12** and **Eq. 6-18**, respectively.

The absolute uncertainties of SCP and SDWP of both aluminium fumarate and MIL-100(Fe) are calculated in **Appendix I**. The low uncertainty values prove the precision and reliability of the measured data for both materials.

7.3. Aluminium fumarate experimental results

The suitability of aluminium fumarate for different adsorption applications such as heating, cooling, desalination and heat storage was assessed through investigating the effect of different parameters on the performance of a two-bed system. The parameters included half cycle time, chilled water, condenser cooling water, adsorption bed cooling water and desorption bed heating water temperatures. The operating conditions used in this study are shown in **Table. 7-2.**

Table. 7-2 Aluminium fumarate operating conditions

Parameter	Units	Value
Chilled water inlet temperature	°C	10, 15, 20 and 30
Adsorption bed cooling water inlet temperature	°C	24, 30, 40 and 50
Condenser cooling water inlet temperature	°C	20, 30, 40 and 50
Desorption bed heating water inlet temperature	°C	70, 80 and 90
Half cycle time	s	500, 700, 900 and 1100
Switching time	s	70
Adsorption bed cooling water flowrate	L min^{-1}	17
Adsorption bed heating water flowrate	L min^{-1}	20
Chilled water flowrate	L min^{-1}	3.25
Condenser cooling water flowrate	L min^{-1}	3.5
Adsorbent/heat exchanger	kg	0.375
No of heat exchangers/bed	—	2

7.3.1. Repeatability test

To ensure the consistency of the adsorption system operation, two tests were performed at the same operating conditions as depicted in **Table. 7-3**. The adsorption system temperature profile shown in **Fig. 7-11** shows the temperature variation of the adsorption beds, the chilled water outlet temperature and the cooling water (from the condenser) outlet temperature. The system produced a specific cooling power (SCP) of 188.6 W kg^{-1} in the first test and 191.2 W kg^{-1} in the second; giving a deviation of 1.37% between the two tests.

Table. 7-3 Aluminium fumarate repeatability test operating conditions

Parameter	Units	Value
Chilled water inlet temperature	°C	20
Adsorption bed cooling water inlet temperature	°C	30
Condenser cooling water inlet temperature	°C	30
Desorption bed heating water inlet temperature	°C	90
Half cycle time	S	700
Switching time	S	70
Adsorption bed cooling water flowrate	L min^{-1}	17
Adsorption bed heating water flowrate	L min^{-1}	20
Chilled water flowrate	L min^{-1}	3.25
Condenser cooling water flowrate	L min^{-1}	3.5
Adsorbent/heat exchanger	Kg	0.375
No of heat exchangers/bed	—	2

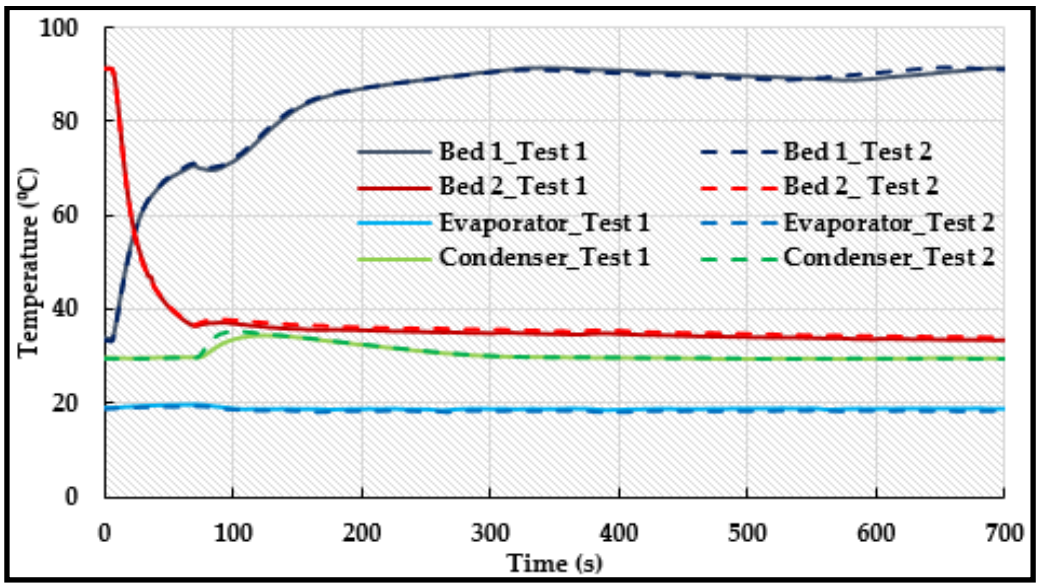

Fig. 7-11 Temperature profile the two adsorption beds, the chilled water outlet and the condenser water outlet.

7.3.2. Effect of chilled water inlet temperature

Fig. 7-12 shows the effect of the chilled water inlet temperature on the performance of aluminium fumarate through assessing the specific cooling power (SCP) using **Eq. 6-12** and specific daily water production (SDWP) using **Eq. 6-18**. It can be noticed that increasing the chilled water inlet temperature significantly improved the performance as the SCP increased from only 65 W kg^{-1} at 10°C to 191 W kg^{-1} at 20°C and the SDWP increased from 2.6 to 6.8 m^3 ton^{-1} day^{-1} at the same temperatures. For adsorption desalination application without cooling effect, the material showed it can produce up to 12 m^3 ton^{-1} day^{-1} working at a chilled water inlet temperature of 29°C.

This can be explained by the material adsorption isotherm shape (**Fig. 4-47**) showing that the material possesses a type IV isotherm where the material uptake increases significantly with increasing the chilled water inlet temperature or the working relative pressure [14].

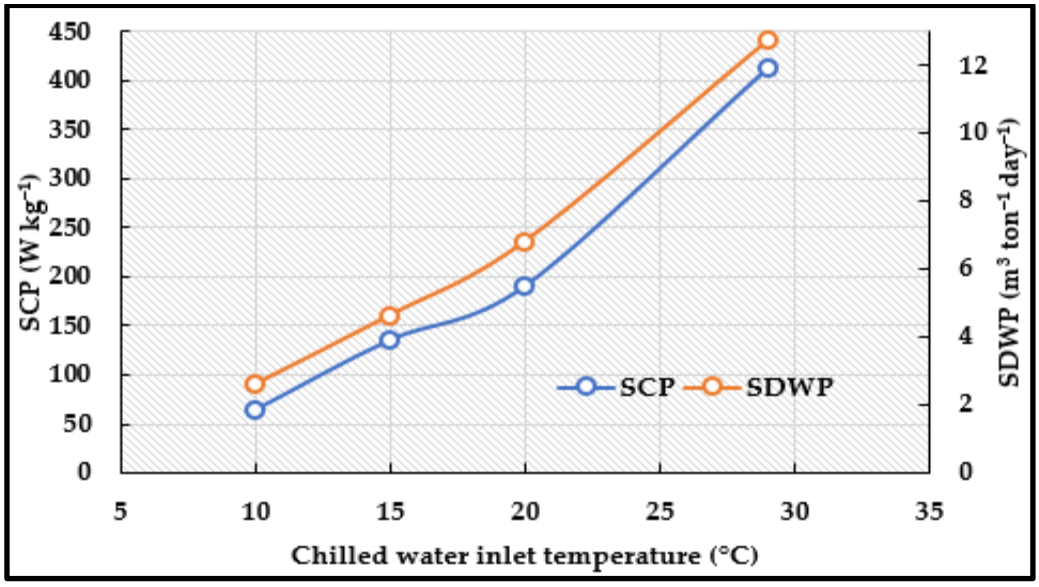

Fig. 7-12 Effect of chilled water inlet temperature on the performance of aluminium fumarate.
(T_{ads}=30°C, T_{cond}=30°C, T_{des}=90°C, half cycle time=700 s and $t_{switching}$=70 s).

7.3.3. Effect of half cycle time

Optimum half cycle time is a crucial parameter that significantly affects the adsorption system performance. Short cycle time results in poor performance as the adsorbent material does not have sufficient time to adsorb/desorb the water vapour while prolonged cycle time is accompanied with a decrease in the performance due to that the increase in the adsorbed water vapour does not compensate for the increase in cycle time. This is evident in **Fig. 7-13** where at short half cycle times, both the SDWP and SCP are low, but they increase to reach their maximum values at optimum half cycle time of 900 s. At such time, the material achieved an SCP of 245 W kg^{-1} and SDWP of 8.5 m^3 ton^{-1} day^{-1}. At longer half cycle time, both SDWP and SCP start to decrease. Based on these results, an optimum half cycle time of 900 s was chosen to be further investigated.

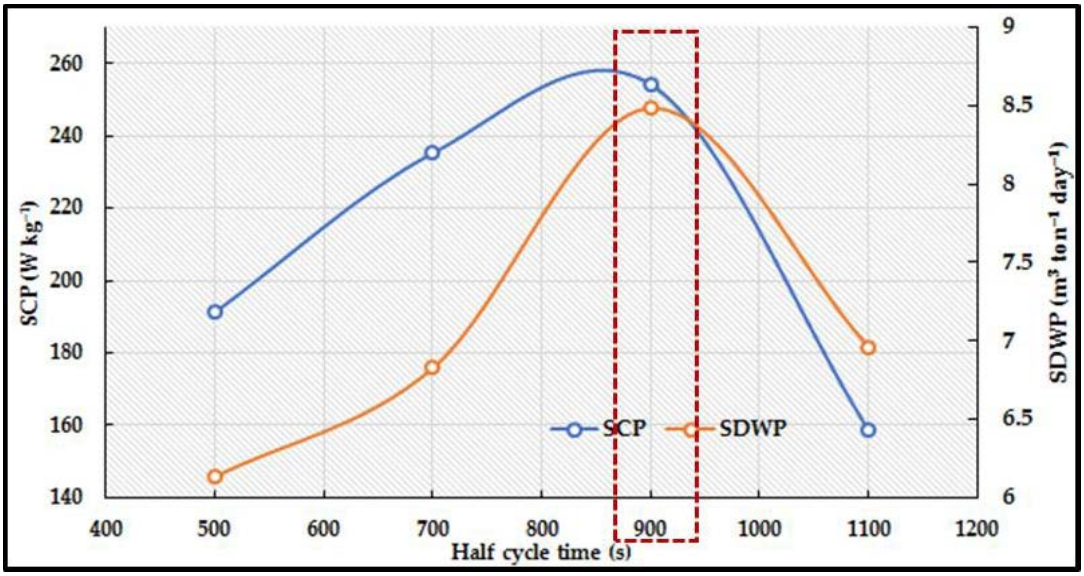

Fig. 7-13 Effect of half cycle time on the performance of aluminium fumarate. (T_{ads}=30°C, T_{cond}=30°C, T_{des}=90°C, T_{eva}=20°C and $t_{switching}$=70 s).

7.3.4. Effect of adsorption bed cooling water inlet temperature

Another important parameter is the adsorption temperature. **Fig. 7-14** depicts the effect of the adsorption bed cooling water inlet temperature on the performance of the system. It can be noticed that as the temperature increased from 24 to 50°C the SCP decreased from 318 to 20.5 W kg^{-1} while the SDWP decreased from 9.7 to only 1.2 m^3 ton^{-1} day^{-1}. This shows that increasing the adsorption bed cooling water inlet temperature adversely affects the performance of the system. Increasing the adsorption bed cooling water temperature means decreasing the working relative pressure and as highlighted earlier (**Fig. 4-47**), the performance of aluminium fumarate depends significantly on the working relative pressure.

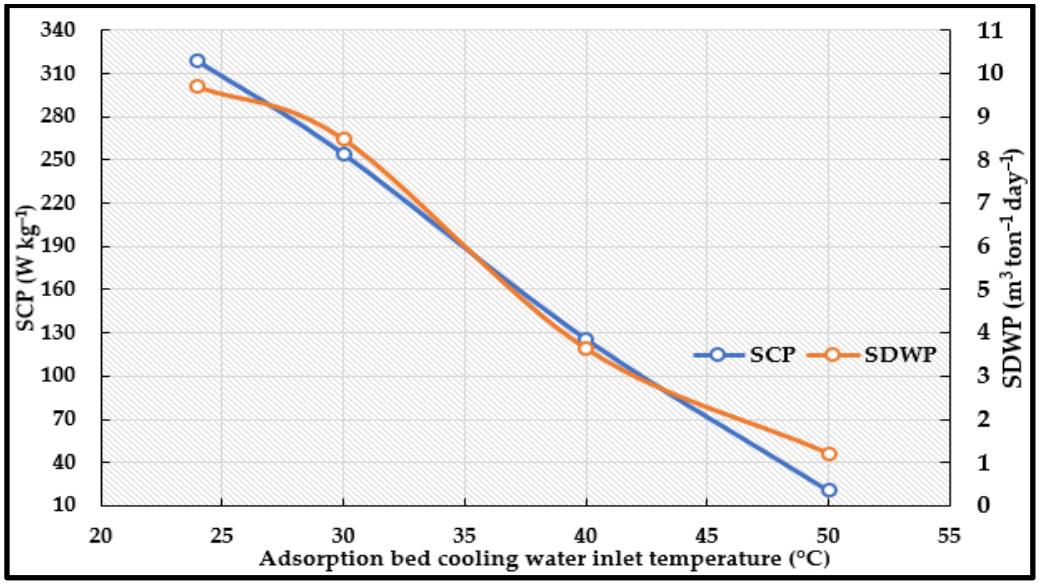

Fig. 7-14 Effect of adsorption bed cooling water inlet temperature on the performance of aluminium fumarate.
(T_{cond}=30°C, T_{des}=90°C, T_{eva}=20°C, half cycle time=900 s and $t_{switching}$=70 s).

7.3.5. Effect of condenser cooling water inlet temperature

The effect of the condensation temperature is shown in **Fig. 7-15** where it can be seen that increasing the condenser cooling water inlet temperature adversely affects both SCP and SDWP. Increasing the condenser cooling water inlet temperature from 20 to 50°C decreased the SCP from 265 to 141 W kg^{-1} while the SDWP decreased from 9 to 4 m^3 ton^{-1} day^{-1}. This is attributed to that as the condenser cooling water inlet temperature increases, the condenser pressure increases retarding the water vapour flow from the bed to the condenser and hence result in an incomplete desorption. The incomplete desorption may lead to that the material does not reach its capacity during the next adsorption phase.

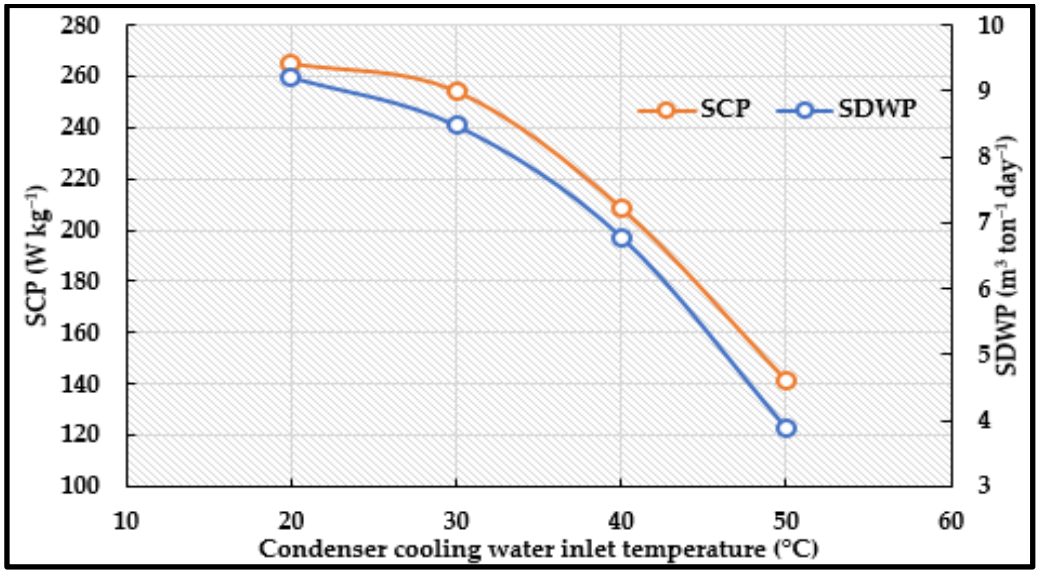

Fig. 7-15 Effect of condenser cooling water inlet temperature on the performance of aluminium fumarate.
(T_{ads}=30°C, T_{des}=90°C, T_{eva}=20°C, half cycle time=900 s and $t_{switching}$=70 s).

7.3.6. Effect of desorption bed heating water inlet temperature

The low desorption temperature required to regenerate aluminium fumarate is highlighted through **Fig. 7-16**. It can be noticed that increasing the desorption bed hot water inlet temperature from 70°C to 90°C slightly increased the SCP from 246 to 254 W kg^{-1} while the SDWP increased from 8.2 to 8.5 m^3 ton^{-1} day^{-1}. This highlights the potential of this material in adsorption application working at low temperature heat sources.

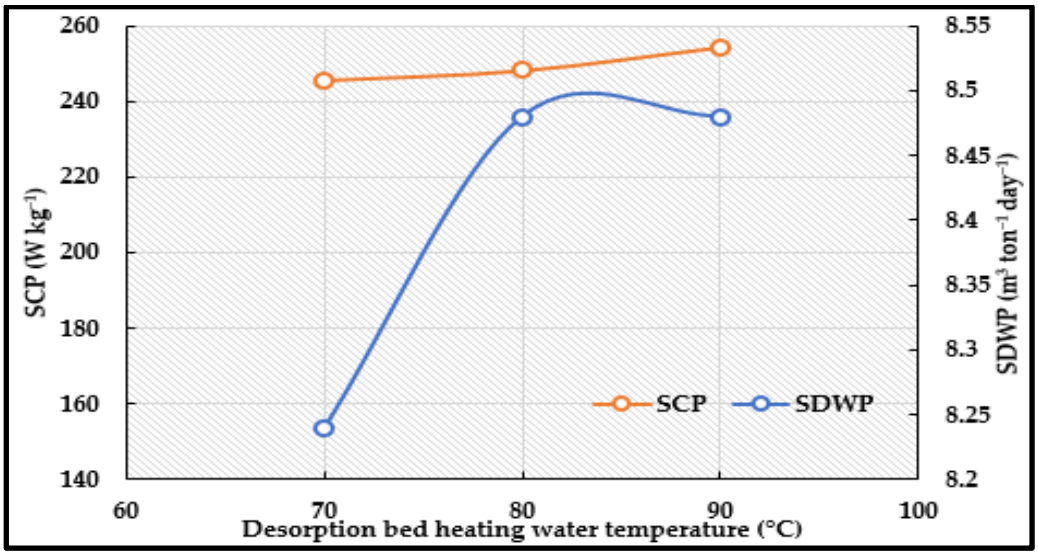

Fig. 7-16 Effect of desorption bed heating water inlet temperature on the performance of aluminium fumarate.
(T_{ads}=30°C, T_{cond}=30°C, T_{eva}=20°C, half cycle time=900 s and $t_{switching}$=70 s).

7.4. MIL-100(Fe) experimental results

MIL-100(Fe) was synthesized at UoB through the developed technique mentioned in Chapter 4. As the amount of the material is smaller than aluminium fumarate, one smaller heat exchanger per bed is used. Before packing the bed, the synthesized MIL-100(Fe) was manually crushed and screened twice using stainless steel screens with screen aperture size ranging from 90 to 740µm. The beds were packed with particle with a size ranging between 125 - 400 µm. The suitability of MIL-100(Fe) for different adsorption applications was assessed through investigating the effect of different parameters on the performance of a two-bed system. The parameters include half cycle time, chilled water, condenser cooling water, adsorption bed cooling water and desorption bed heating water inlet temperatures. When MIL-100(Fe) was used at the same operating condition of the repeatability cycle, the system gave an SCP of only 91 W kg^{-1}. This poor performance can be justified through the isotherm shape of MIL-100(Fe) (**Fig. 4-36**), where a higher temperature is required to fully desorb the material thus a desorption temperature of 95°C and a condensation temperature of 20°C were used. The operating conditions used for MIL-100(Fe) testing in this study are shown in **Table. 7-4.**

Table. 7-4 MIL-100(Fe) operating conditions

Parameter	Units	Value
Chilled water inlet temperature	°C	10, 15, 20 and 30
Adsorption bed cooling water inlet temperature	°C	22, 30, 40 and 50
Condenser cooling water inlet temperature	°C	20, 30, 40 and 50
Desorption bed heating water inlet temperature	°C	70, 80 and 95
Half cycle time	s	500, 700, 900 and 1100
Switching time	s	70
Adsorption bed cooling water flowrate	L	17
Adsorption bed heating water flowrate	L	20
Chilled water flowrate	L	3.25
Condenser cooling water flowrate	L	3.5
Adsorbent/heat exchanger	kg	0.232
No of heat exchangers/bed	—	1

7.4.1. Effect of chilled water inlet temperature

Fig. 7-17 depicts the effect of the chilled water inlet on both the SCP and SDWP in the MIL-100(Fe) adsorption system. It can be noticed that similar to aluminium fumarate, increasing the chilled water inlet temperature significantly improves the performance as the SCP increased from only 89 W kg^{-1} at 10°C to 337 W kg^{-1} at 20°C and the SDWP increased from 4 to 14 m^3 ton^{-1} day^{-1} at the same temperatures. Similar to aluminium fumarate, the material possesses a two-step type IV isotherm where the material uptake increases significantly with increasing the chilled water inlet temperature or the working relative pressure [14]. For adsorption desalination without cooling application, the material showed it can produce up to 19 m^3 ton^{-1} day^{-1} working at a chilled water inlet temperature of 29°C.

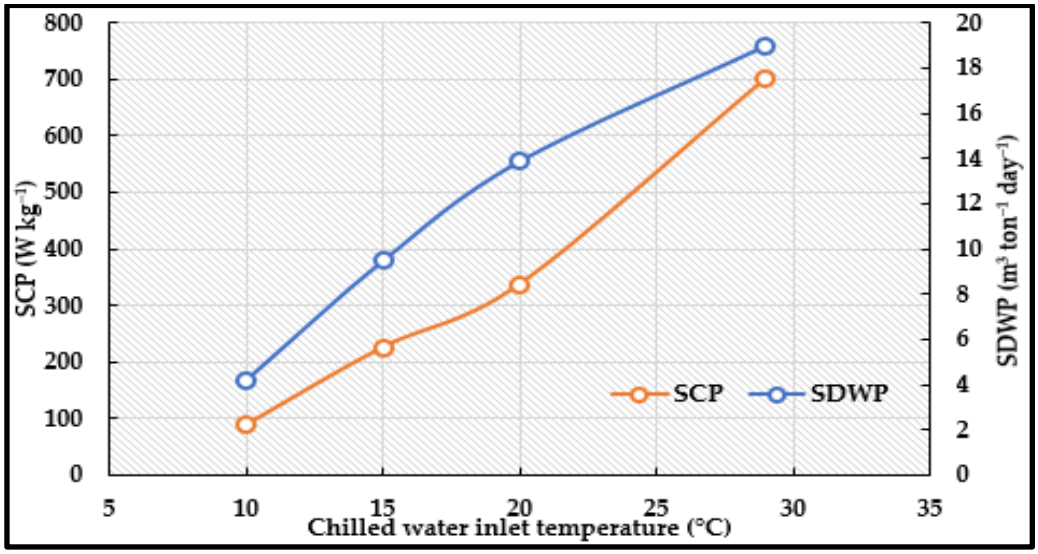

Fig. 7-17 Effect of chilled water inlet temperature on the performance of MIL-100(Fe). (T_{ads}=30°C, T_{cond}=20°C, T_{des}=95°C, half cycle time=700 s and $t_{switching}$=70 s).

7.4.2. Effect of half cycle time

Fig. 7-18 shows that increasing the half cycle increased both SDWP and SCP which reached their maximum values of 14 m^3 ton^{-1} day^{-1} and 337 W kg^{-1}, respectively at a half cycle time of 700 s. At longer half cycle times, both SDWP and SCP start to decrease. Based on these result, an optimum half cycle time of 700 was selected in the following investigations.

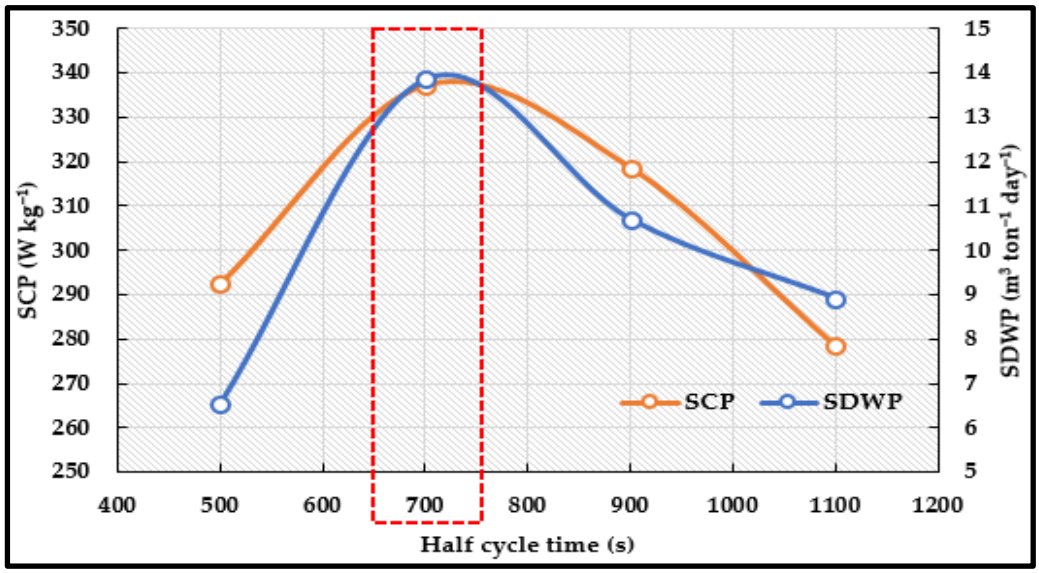

Fig. 7-18 Effect of half cycle time on the performance of MIL-100(Fe). (T_{ads}=30°C, T_{cond}=20°C, T_{des}=95°C, T_{eva}=20°C and $t_{switching}$=70 s).

7.4.3. Effect of adsorption bed cooling water inlet temperature

Fig. 7-19 depicts the effect of the adsorption bed cooling water inlet temperature on the performance of the system. It can be noticed that as the temperature increased from 22 to 50°C the SCP decreased from 516 to 42 W kg^{-1} while the SDWP decreased from 16 to only 2 m^3 ton^{-1} day^{-1}. This shows that increasing the adsorption temperature adversely affects the performance of the system.

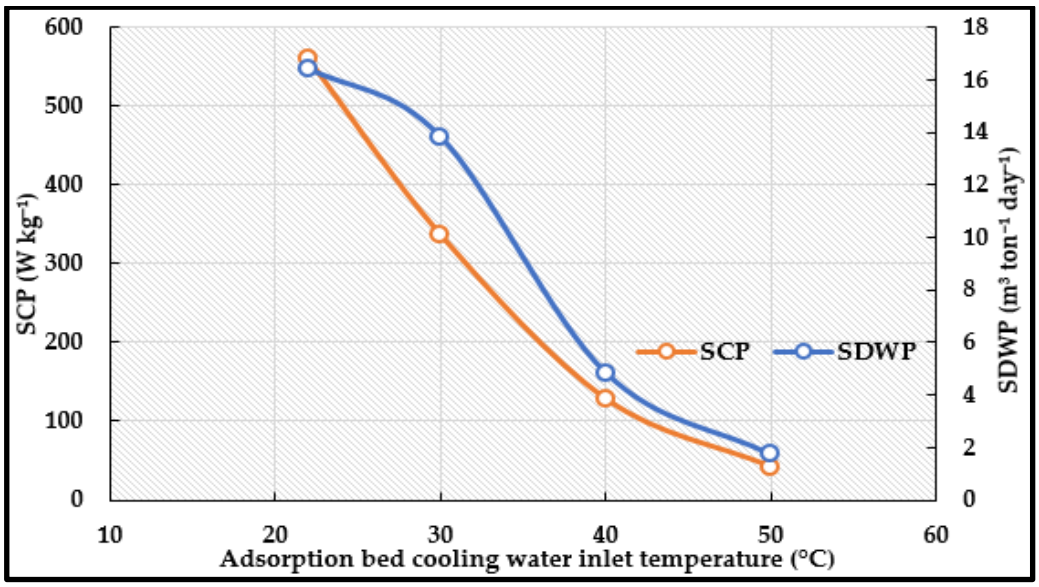

Fig. 7-19 Effect of adsorption bed cooling water inlet temperature on the performance of MIL-100(Fe).
(T_{cond}=20°C, T_{des}=95°C, T_{eva}=20°C, half cycle time=700 s and $t_{switching}$=70 s).

7.4.4. Effect of condenser cooling water inlet temperature

The effect of condenser cooling water inlet temperature is shown in **Fig. 7-20** where it can be noticed that increasing the condenser inlet temperature adversely affects both SCP and SDWP. Increasing the condenser cooling water inlet temperature from 20 to 50°C decreased the SCP from 337 to 139 W kg^{-1} while the SDWP decreased from 14 to 2 m^3 ton^{-1} day^{-1}. These results highlight the high dependency of MIL-100(Fe) performance on the condenser cooling water inlet temperature.

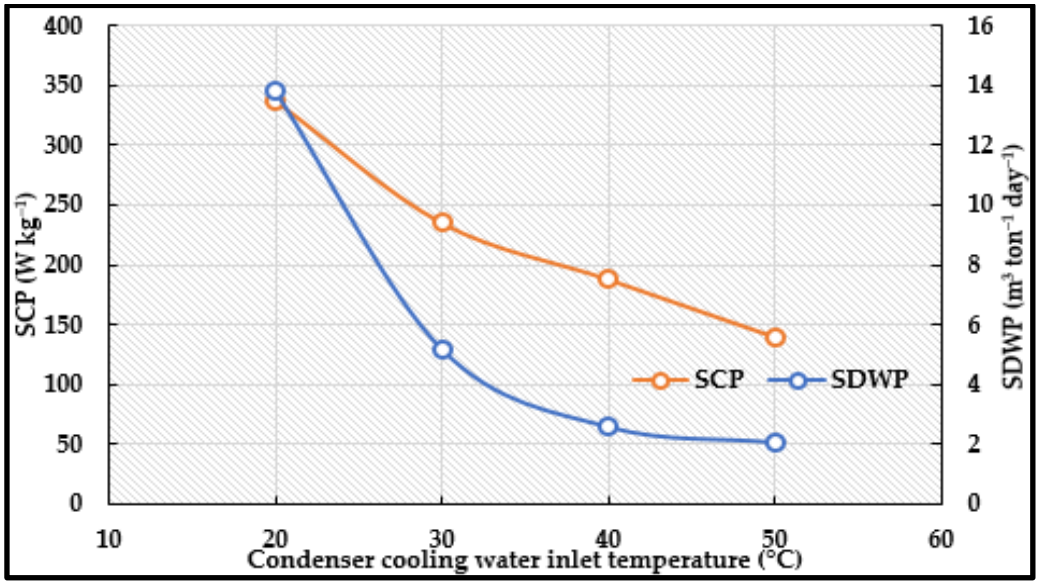

Fig. 7-20 Effect of condenser cooling water inlet temperature on the performance of MIL-100(Fe).
(T_{ads}=30°C, T_{des}=95°C, T_{eva}=20°C, half cycle time=700 s and $t_{switching}$=70 s).

7.4.5. Effect of desorption bed heating water inlet temperature

The dependency of the MIL-100(Fe) on the desorption bed heating water inlet temperature is highlighted through **Fig. 7-21**. It can be noticed that increasing the desorption bed heating water inlet temperature from 70 to 95°C significantly increased the SCP from 242 to 337 W kg^{-1} and increased the SDWP from 8 to 14 m^3 ton^{-1} day^{-1}.

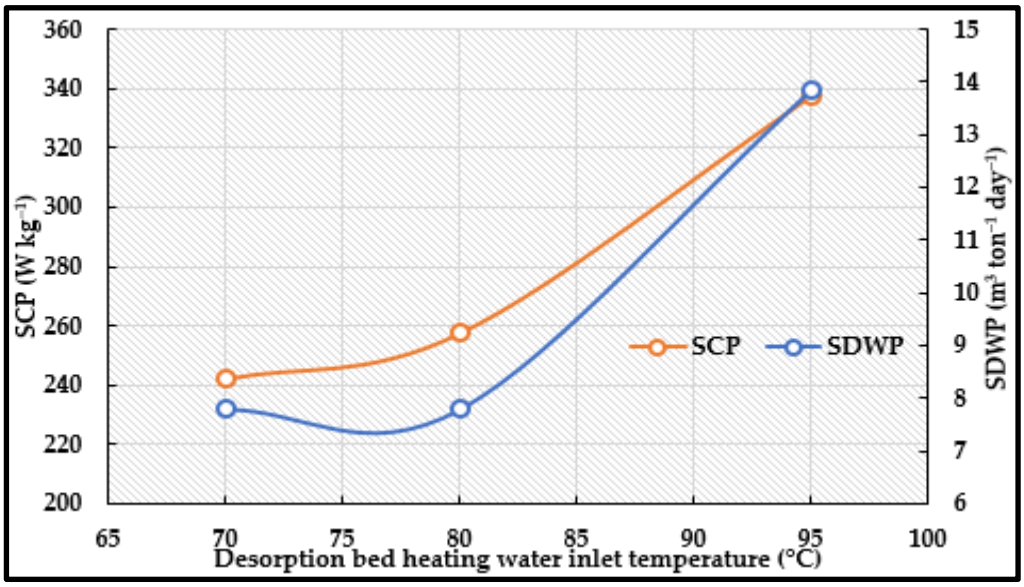

Fig. 7-21 Effect of desorption bed heating water inlet temperature on the performance of MIL-100(Fe).
(T_{ads}=30°C, T_{cond}=20°C, T_{eva}=20°C, half cycle time=700 s and $t_{switching}$=70 s).

7.5. Aluminium fumarate and MIL-100(Fe) in different adsorption applications

The suitability of aluminium fumarate and MIL-100(Fe) for different adsorption applications was assessed at the investigated temperature ranges summarized in **Table. 7-5**.

Table. 7-5 Aluminium fumarate and MIL-100(Fe) in different adsorption applications

				Application				
Eva. Temp.	**Ads. Temp.**	**Cond. Temp.**	**Des. Temp**	**Cooling**	**Heating**	**Desalination with cooling**	**Desalination without cooling**	**Heat storage**
10	30	20-30	90-95	√	√	√	×	√
15	30	20-30	90-95	√	√	√	×	√
20	30	20-30	90-95	√	√	√	×	√
30	30	20-30	90-95	×	×	×	√	×
20	22-24	20-30	90-95	×	×	×	√	×
20	30	20-30	90-95	√	√	√	×	√
20	40	20-30	90-95	√	√	√	×	√
20	50	20-30	90-95	√	√	√	×	√
20	30	20	90-95	√	√	√	×	√
20	30	30	90-95	√	√	√	×	√
20	30	40	90-95	√	√	√	×	√
20	30	50	90-95	√	√	√	×	√

7.5.1. Adsorption desalination

Adsorption systems can be used for water desalination to produce potable water only or to produce both potable water and cooling effect. Based on the data extracted from **Fig. 7-12** and **Fig. 7-17, Fig. 7-22** shows a. distilled water produced (SDWP), b. cooling effect (SCP) and c. coefficient of performance (COP) of the two adsorbent materials. It can be noticed that MIL-100(Fe) outperformed aluminium fumarate at all the investigated chilled water inlet temperatures. For chilled water inlet temperatures used in cooling (10 and 15°C), aluminium fumarate produced SDWP of 2.6 and 4.6 m^3 ton^{-1} day^{-1} and a cooling effect of 65 and 136 W kg^{-1}, respectively. At the same temperatures, MIL-100(Fe) produced SDWP of 4 and 9 m^3 ton^{-1} day^{-1} and a cooling effect of 89 and 226 W kg^{-1}. However, it can be noticed that the COP of the aluminium fumarate is higher than that of MIL-100(Fe) which may be attributed to the different adsorbent to metal mass ratios [289]. For a moderate cooling effect (20°C), aluminium fumarate produced 7 m^3 ton^{-1} day^{-1} and 191 W kg^{-1}, while MIL-100(Fe) produced 14 m^3 ton^{-1} day^{-1} and 337 W kg^{-1}. Regarding the desalination without cooling effect, **Fig. 7-23** shows that at high evaporation temperatures, MIL-100(Fe) produced 19 m^3 ton^{-1} day^{-1} while aluminium fumarate produced 13 m^3 ton^{-1} day^{-1}.

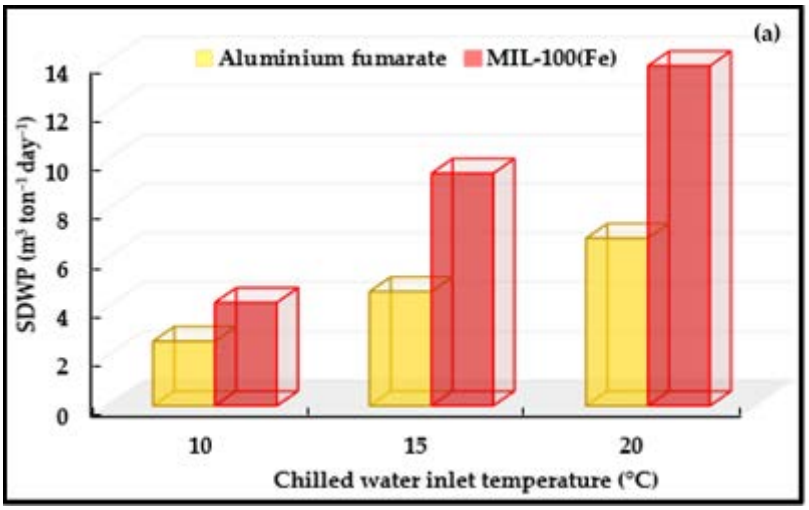

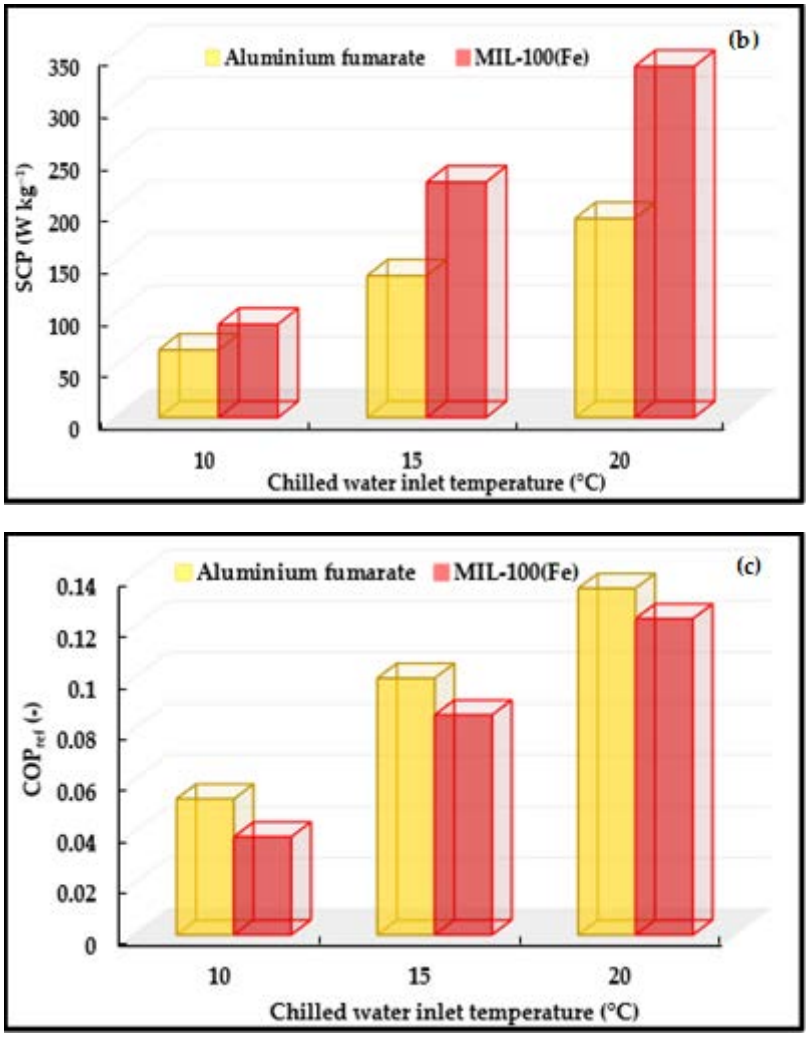

Fig. 7-22 Adsorption desalination with cooling effect. (T_{ads}=30°C, half cycle time=700 s, $t_{switching}$=70 s) (Aluminium fumarate: T_{cond}=30°C, T_{des}=90°C and MIL-100(Fe): T_{cond}=20°C, T_{des}=95°C).

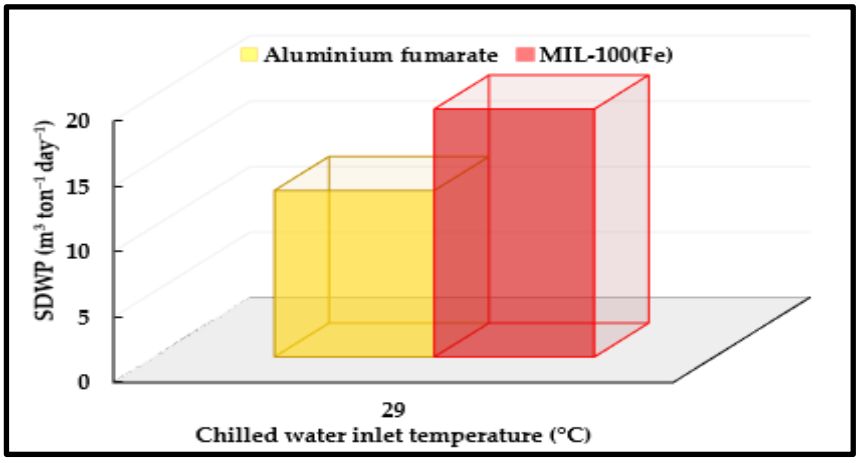

Fig. 7-23 Adsorption desalination without cooling effect. (T_{ads}=30°C, half cycle time=700 s, $t_{switching}$=70 s) (Aluminium fumarate: T_{cond}=30°C, T_{des}=90°C and MIL-100(Fe): T_{cond}=20°C, T_{des}=95°C).

Salty water was prepared to simulate the seawater. The elemental analysis of the salt used to prepare the salty water can be found in a previous study [288].The quality of water produced from both aluminium fumarate and MIL-100(Fe) systems was assessed through measuring the total dissolved solids (TDS) and water conductivity. The measured values were then compared to those of filtered water, tap water and the World Health Organization (WHO) potable water specification for 2017.

Results in **Table. 7-6** shows that the aluminium fumarate and the MIL-100(Fe) desalination systems produced high quality water. For aluminium fumarate, the TDS decreased from 23,000 ppm for the feed salty water to only 17.5 ppm while the conductivity decreased from 39,000 µS cm^{-1} to 28 µS cm^{-1}. In case of MIL-100(Fe), the TDS decreased from 23,000 ppm for the feed salty water to only 10 ppm while the conductivity decreased from 38,000 µS cm^{-1} to 15 µS cm^{-1}.

According to the WHO standards and based on the measurement shown below, the adsorption system under investigation has proven its ability to be used for drinking water production.

Table. 7-6 Quality analysis of water produced from aluminium fumarate and MIL-100(Fe) systems

Sample	TDS (mg L^{-1})	Conductivity (µS cm^{-1})
Tap water (UoB)	94	157.1
Filtered water (UoB)	1.24	2.1
Potable water (WHO)[290, 291]	<600	2500
Feed water to aluminium fumarate desalination system	23.3E3	39.1E3
Water produced from aluminium fumarate desalination system	17.5	28
Feed water to MIL-100(Fe) desalination system	22.9E3	37.9E3
Water produced from MIL-100(Fe) desalination system	10	15.5

7.5.2. Adsorption heating/cooling

Adsorption heat pump is the most commonly used application for adsorption systems. The suitability of the two materials for cooling or heating effects can also be studied using the data extracted from **Fig. 7-14** and **Fig. 7-19**. **Fig. 7-24** shows the cooling effect generated when the ambient temperature (adsorption temperature in cooling application) is in the range of 40-50°C. Using a chilled water inlet temperature of 20°C, MIL-100(Fe) gave an SCP of 128-42 W kg^{-1} and COP_{ref} of 0.06-0.02. At the same temperatures, aluminium fumarate gave an SCP of 126-20 W kg^{-1} and COP_{ref} of 0.14-0.03.

Fig. 7-25 shows heating density and the COP of heating effect when the ambient temperature (chilled water inlet temperature in the heating application) is 20°C.

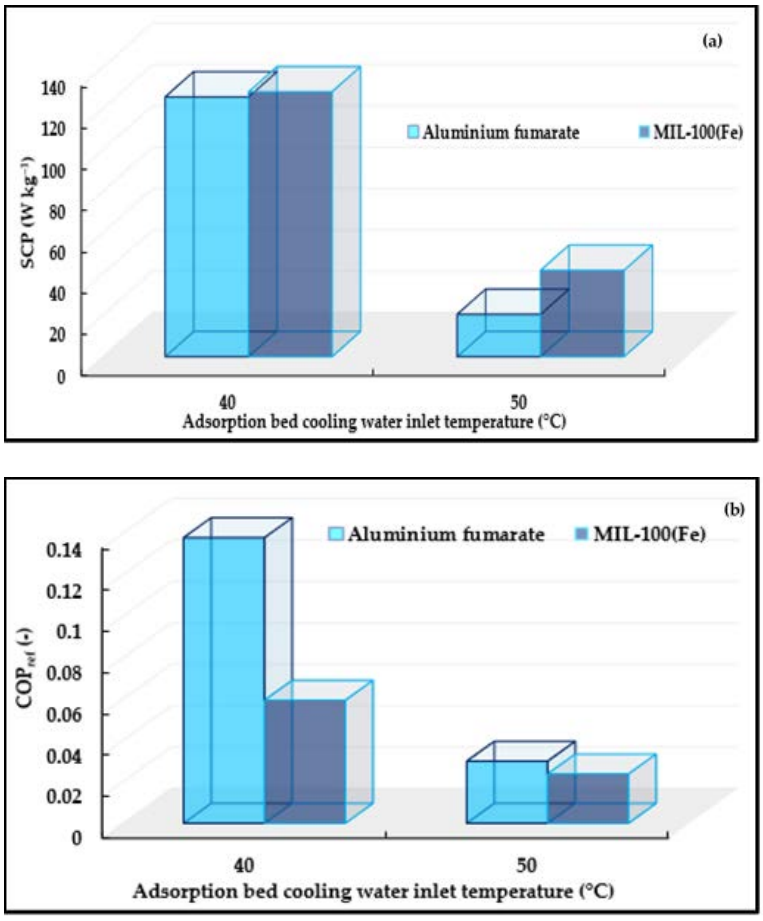

Fig. 7-24 Adsorption cooling application (a. SCP and b. COP_{ref}). (T_{eva}= 20°C, $t_{switching}$=70 s, Aluminium fumarate: T_{cond}=30°C, T_{des}=90°C, half cycle time=900 s, MIL-100(Fe): T_{cond}=20°C, T_{des}=95°C, half cycle time=700 s).

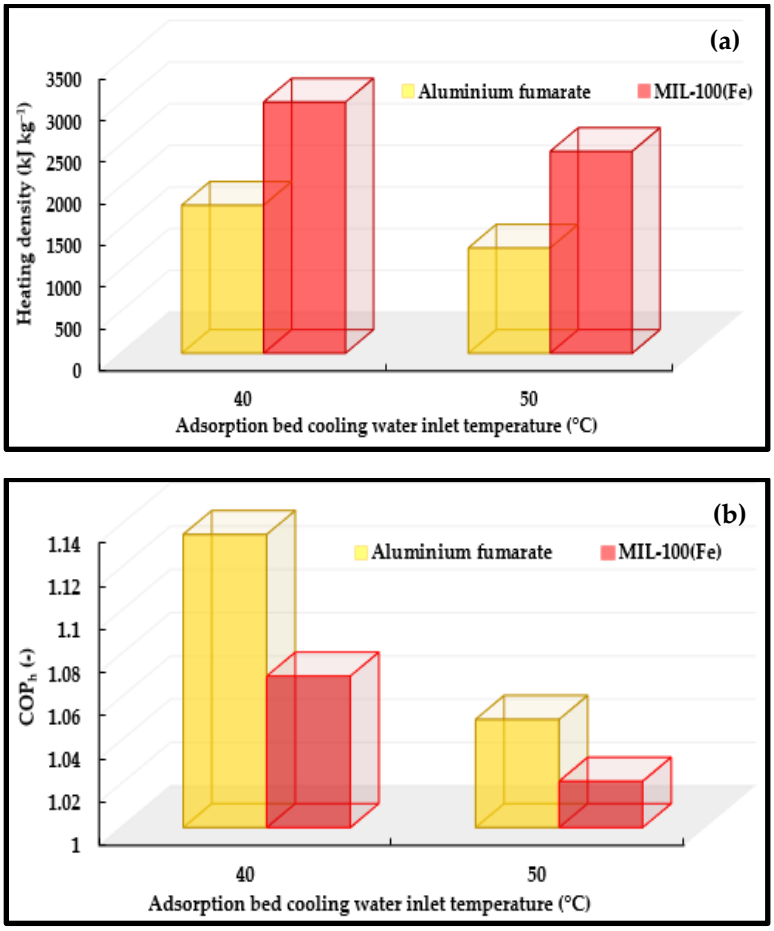

Fig. 7-25 Adsorption heating application (a. heating density and b. COP_h). (T_{eva}= 20°C, $t_{switching}$=70 s, Aluminium fumarate: T_{cond}=30°C, T_{des}=90°C, half cycle time=900 s, MIL-100(Fe): T_{cond}=20°C, T_{des}=95°C, half cycle time=700 s).

7.5.3. Adsorption energy storage

Adsorption energy storage application is another important application in which the heat of adsorption and condensation is recovered whenever needed. The performance of the two materials was compared in terms of their specific energy density (**Eq. 6-21**) at two different cycle times, 900 and 2700 s. **Fig. 7-26** shows that at a chilled water inlet temperature of 20°C and an adsorption bed cooling water inlet temperature of 40°C, MIL-100(Fe) stored 948 W h kg^{-1} at half cycle time of 900 s (15 minutes) while aluminium fumarate stored 517 W h kg^{-1}. Increasing the half cycle time to 2700 s (45 minutes), the energy stored was increased to 870 W h kg^{-1} in case of aluminium fumarate while it increased to reach 1200 W h kg^{-1} in case of MIL-100(Fe).

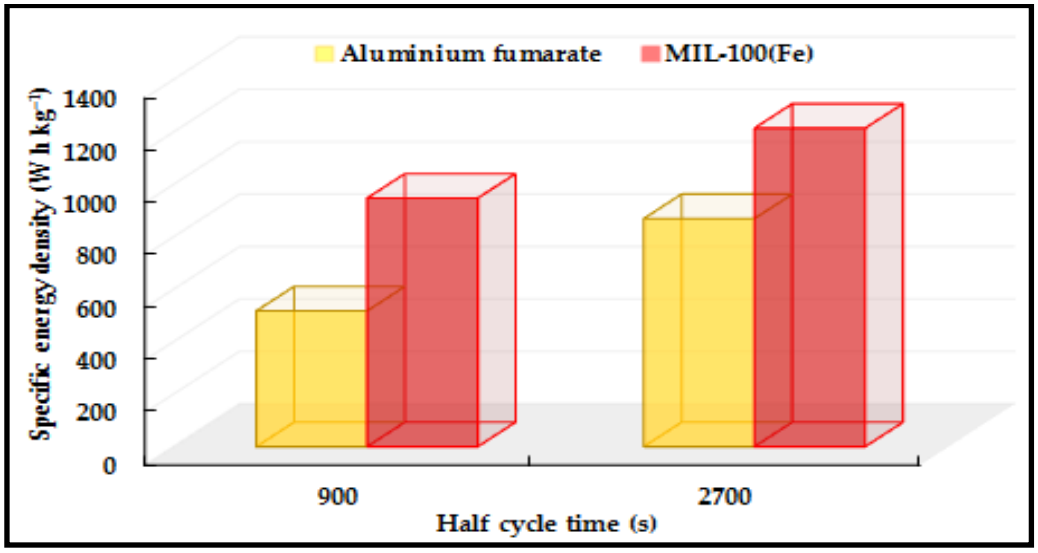

Fig. 7-26 Specific energy density of aluminium fumarate and MIL-100(Fe). (T_{eva}= 20°C, T_{ads}= 40°C and $t_{switching}$=70 s) (Aluminium fumarate: T_{cond}=30°C, T_{des}=90°C, MIL-100(Fe): T_{cond}=20°C, T_{des}=95°C).

7.6. Summary

In this chapter the potential of two MOF materials, aluminium fumarate and MIL-100(Fe), in different adsorption applications was experimentally investigated using a two-bed adsorption system. The effect of different operating conditions such as chilled water, condenser cooling water, adsorption bed cooling water and desorption bed heating water inlet temperatures were investigated to set optimum operating conditions for each adsorption application. It was found that both materials performance significantly improved with increasing the chilled water inlet temperature and decreasing the adsorption bed cooling water inlet temperature. Aluminium fumarate was found to be independent of the desorption temperature which was the opposite for MIL-100(Fe) as its performance significantly depends on the desorption bed heating water and condenser cooling water temperatures. It was also found that MIL-100(Fe) outperformed aluminium fumarate at different operating conditions. Analysing the water produced from the adsorption desalination system using both aluminium fumarate and MIL-100(Fe) showed that the water produced from both systems was a high grade distilled water which highlights the potential of using MOFs in adsorption desalination systems to produce potable water.

CHAPTER 8

CONCLUSIONS AND FUTURE WORK

8.1. Introduction

Currently, the world faces problems such as water scarcity, global warming due to the excessive use of fossil fuels and GHG emissions and the ozone layer depletion due to the CFC and HCFC refrigerants leakage. To overcome these problems, new technologies and new energy resources should be used. Adsorption is considered to be as an efficient alternative to conventional technologies used in cooling, heating, desalination and energy storage as it can be operated using renewable energy resources or waste heat having zero CO_2 emissions.

8.2. Conclusions

This study aimed to investigate the potential of using metal-organic framework materials in adsorption applications such as heating/cooling, desalination and energy storage. **Fig. 8-1** highlights the main problems of current adsorption systems and how they were addressed in this study. Four MOFs were chosen to be fully characterised, two of them are commercially available (aluminium fumarate and CPO-27(Ni)) in addition to two synthesized MOFs, MIL-101(Cr) and MIL-100(Fe). The optimum reaction conditions to successfully synthesize both MIL-101(Cr) and MIL-100(Fe) were investigated. The performance of MIL-101(Cr) and MIL-100(Fe) was further improved through synthesizing novel composites of MIL-101(Cr)/ $CaCl_2$ or GrO or two MOFs together as in case of MIL-101(Cr)/MIL-100(Fe) and CPO-27(Ni)/MIL-100(Fe).

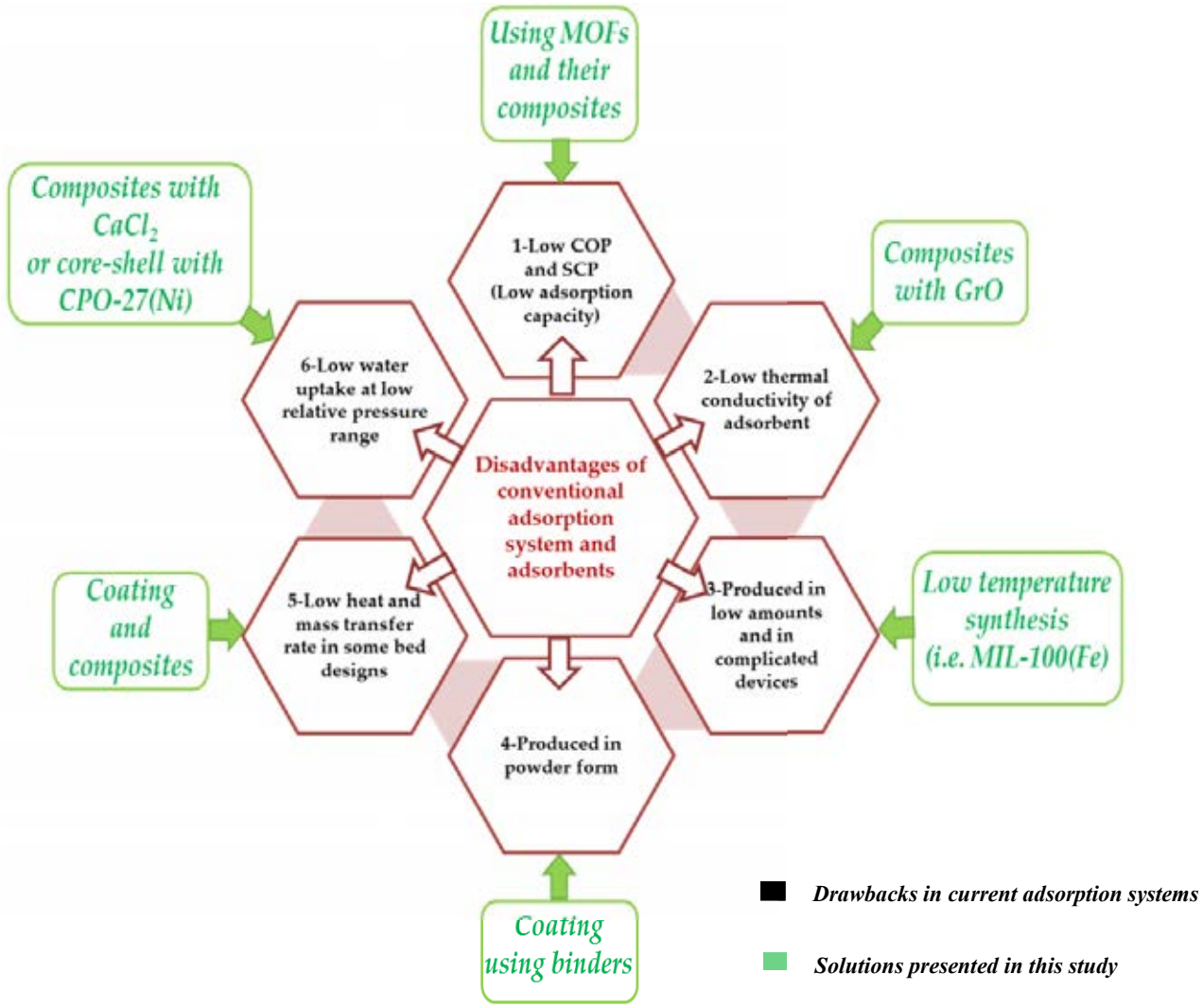

Fig. 8-1 Main drawbacks in current adsorption systems shaping the research gap of knowledge and how they were solved through this study.

The different MOF materials and their composites were characterized using various techniques such as X-ray diffraction, FTIR, SEM, thermal conductivity and water vapour adsorption properties. According to the nitrogen adsorption characteristics, MIL-101(Cr) had the highest surface area and pore volume while CPO-27(Ni) had the lowest. The free accessible surface area affected the thermal conductivity of the different MOF materials that is why MIL-101(Cr) had the lowest thermal conductivity while CPO-27(Ni) had the highest. Also, the water adsorption capacity of MIL-101(Cr) was the highest with an IV isotherm shape making it suitable for applications working at high relative pressure ranges (>0.5), aluminium fumarate had also an IV isotherm shape while MIL-100(Fe) had a two-step IV isotherm. The performance

of these materials was found to be profoundly dependant on the working relative pressure. CPO-27(Ni) was found to have a type I isotherm where it can work at low relative pressure ranges but requires high desorption temperatures.

The performance of MIL-101(Cr) and MIL-100(Fe) was further improved through synthesizing composites. The water vapour capacity at the low relative pressure range was significantly improved through synthesizing MIL-101(Cr)/$CaCl_2$ while its thermal conductivity was enhanced through incorporating it with GrO. The exceptionally high-water vapour capacities of MIL-101(Cr) at the high relative pressure range and of CPO-27(Ni) at the low range were adopted through synthesizing two MIL-100(Fe) composites. The MIL-101(Cr)/MIL-100(Fe) and CPO-27(Ni)/MIL-100(Fe) showed an enhanced performance compared to the parent MIL-100(Fe). Also, integrating the MOF as a coated layer instead of the granular form was investigated and tested using different techniques to examine the durability and mechanical strength of the developed coatings.

A two-adsorption bed SIMULINK model was developed and validated with experimental data generated using aluminium fumarate/water as a working pair. The validated numerical model was utilized to investigate the potential of different MOFs and their composites in different adsorption applications.

It was found that:

1. The performance of all the adsorbent materials significantly depends on the operating conditions of the system.
2. Adsorbents exhibiting type I adsorption isotherms (such as CPO-27(Ni)) require high desorption temperatures, nevertheless such adsorbents outperform other adsorbents at applications working at low chilled water temperatures such as adsorption cooling or adsorption desalination with cooling effect.

3. MIL-100(Fe) and aluminium fumarate showed good performance at the different adsorption applications and under various operating conditions. For cooling applications and with a chilled water inlet temperature of 10°C, MIL-100(Fe) produced 97 W kg^{-1} while aluminium fumarate produced 64 W kg^{-1}. For desalination without cooling, MIL-100(Fe) produced 15 m^3 $ton^{-1}day^{-1}$ while aluminium fumarate produced 11 m^3 $ton^{-1}day^{-1}$.

4. MIL-101(Cr) requires long cycle times and is only suitable for applications working at high relative pressure ranges.

5. Synthesising composites has proven to be an efficient technique to significantly improve the system performance, MIL-101(Cr)/$CaCl_2$ composites have outperformed all other adsorbents at the different operating conditions.

6. Despite their remarkable performance, there is still a problem facing MIL-101(Cr) and its composites as it can be only available at lab scale without any mean for mass production until now. Such problem hinders building and commercialization of an adsorption system employing these adsorbents.

7. Despite the remarkable performance of CPO-27(Ni) at low evaporation temperatures and its availability in large amounts, the material can only be used in applications employing high temperature energy sources, which limit its use in certain applications.

Due to the mass production of aluminium fumarate, the successful development of a method to scale up the synthesis of MIL-100(Fe) and that both materials can work at a wide range of operating conditions, the two materials were chosen to be experimentally tested in a two-bed adsorption system.

The effect of different operating conditions such as the temperatures of chilled water, condenser cooling water, adsorption and desorption beds on the performance of aluminium fumarate and MIL-100(Fe) was experimentally investigated to determine optimum operating conditions for various adsorption applications. It was found that both materials performance significantly

improved with increasing the chilled water inlet temperature and decreasing the adsorption bed cooling water temperature. Aluminium fumarate was found to be independent of the desorption bed heating water temperature which was the opposite for MIL-100(Fe) as its performance significantly depends on the desorption bed heating water and condenser cooling water temperatures. It was also found that MIL-100(Fe) outperformed aluminium fumarate at different operating conditions giving a maximum water production 19 m^3 $ton^{-1}day^{-1}$ while aluminium fumarate gave 13 m^3 $ton^{-1}day^{-1}$. For cooling applications with a chilled water inlet temperature of 15°C, MIL-100(Fe) produced a cooling effect of 226 W kg^{-1} while aluminium fumarate produced 136 W kg^{-1}.

Finally, the distilled water produced from the adsorption desalination system using both aluminium fumarate and MIL-100(Fe) was analysed based on its total dissolved solids and conductivity. Analysing the water showed that water produced from both systems was of high-grade distilled water as TDS for water from the system when employing MIL-100(Fe) was 10 mg L^{-1} while it was 17.5 mg L^{-1} for aluminium fumarate. This highlights the potential of using MOFs adsorption desalination for potable water production.

8.3. Future work

The presented work discussed the potential of using advanced MOF materials in various adsorption applications such as cooling/heating, desalination and energy storage. The performance was further improved through synthesizing a number of composites. The following can be considered for future work:

1. Composite of MIL-101(Cr)/calcium chloride has shown a significant performance improvement therefore using calcium chloride such with other MOFs to make new types of composites should be considered. The new composites can be characterized with the used techniques in addition to combining techniques together such as TGA with XRD, SEM and FTIR to identify phase transition or change for the parent materials.

2. A MIL-100(Fe) production process was developed where no pressure or elevated temperature was required; such technique offers a potential gate for further scaling up processes. Hence a continuous system to produce MIL-100(Fe) should be developed.

3. Integrating the adsorbent material as a coated layer instead of packed granules showed an enhancement of the thermal conductivity due to the elimination of the contact resistance. As the MOFs coated layers showed high mechanical strength, further work should be carried out to investigate the optimum MOFs coating thickness achieving the highest performance and experimentally investigate the performance of fully coated heat exchangers.

REFERENCES

[1] J. Henley, "World set to use more energy for cooling than heating," *The Guardian,* vol. 26, 2015.

[2] Q. C. Local, "National Climatic Data Center," 2001.

[3] "International Institute of Refrigeration (IIR), 29th. Informatory

Note on Refrigeration Technologies - The Role of Refrigeration in the Global

Economy/November 2015: Paris – France, November 2015."

[4] "The economist, Air conditioning: No sweat 2013."

[5] "Air conditioning: No sweat," *The economist,* 2013.

[6] L. Gordeeva, and Y. I. Aristov, "Composites 'salt inside porous matrix'for adsorption heat transformation: a current state-of-the-art and new trends," *International Journal of Low-Carbon Technologies,* vol. 7, no. 4, pp. 288-302, 2012.

[7] "European Commission, Taking stock of the Europe 2020 strategy for smart, sustainable and inclusive growth, COM(2014) 130 final, Brussels, 2014."

[8] K. Wang, "flsorpiio," 2011.

[9] A. Khutia, H. U. Rammelberg, T. Schmidt, S. Henninger, and C. Janiak, "Water sorption cycle measurements on functionalized MIL-101Cr for heat transformation application," *Chemistry of Materials,* vol. 25, no. 5, pp. 790-798, 2013.

[10] S. M. Salman, "United Nations General Assembly Resolution: International Decade for Action, Water for Life, 2005–2015: A Water Forum Contribution," *Water international,* vol. 30, no. 3, pp. 415-418, 2005.

[11] U. Water, "The United Nations world water development report 2014: water and energy," *United Nations, Paris,* 2014.

[12] U. Water, “The United Nations World Water Development Report 3–Water in a Changing World,” *United Nations Educational Scientific and Cultural Organization, Paris*, 2009.

[13] A. Subramani, and J. G. Jacangelo, “Emerging desalination technologies for water treatment: a critical review,” *Water research*, vol. 75, pp. 164-187, 2015.

[14] E. Elsayed, A.-D. Raya, S. Mahmoud, P. A. Anderson, A. Elsayed, and P. G. Youssef, “CPO-27 (Ni), aluminium fumarate and MIL-101 (Cr) MOF materials for adsorption water desalination,” *Desalination*, vol. 406, pp. 25-36, 2017.

[15] A. El-Ghonemy, "RETRACTED: Future sustainable water desalination technologies for the Saudi Arabia: A review," Elsevier, 2012.

[16] H. Schreiber, F. Lanzerath, C. Reinert, C. Grüntgens, and A. Bardow, “Heat lost or stored: Experimental analysis of adsorption thermal energy storage,” *Applied Thermal Engineering*, vol. 106, pp. 981-991, 2016.

[17] N. P. Stadie, “Synthesis and thermodynamic studies of physisorptive energy storage materials,” California Institute of Technology, 2013.

[18] J. Rouquerol, F. Rouquerol, P. Llewellyn, G. Maurin, and K. S. Sing, *Adsorption by powders and porous solids: principles, methodology and applications*: Academic press, 2013.

[19] A. Dąbrowski, “Adsorption—from theory to practice,” *Advances in colloid and interface science*, vol. 93, no. 1, pp. 135-224, 2001.

[20] C. Scheele, “Chemische Abhandlung von der Luft und dem Feuer (“Chemical Treatise of Air and Fire”), 1777,” *Upsala und Leipzig, Verlegt von Magn. Swederus, Buchhändler*.

[21] F. Fontana, “Encyclopedia of surface and colloid science,” *Memorie Mat. Soc. Ital. Sci*, vol. 679, 1777.

[22] T. de Saussure, *Observations sur l'absorption des gaz par différens corps*, 1814.

[23] M. De Lange, "Metal-Organic Frameworks For Adsorption Driven Energy Transformation: From Fundamentals To Applications," 2015.

[24] J. Canivet, A. Fateeva, Y. Guo, B. Coasne, and D. Farrusseng, "Water adsorption in MOFs: fundamentals and applications," *Chemical Society Reviews,* vol. 43, no. 16, pp. 5594-5617, 2014.

[25] M. Donohue, and G. Aranovich, "Classification of Gibbs adsorption isotherms," *Advances in colloid and interface science,* vol. 76, pp. 137-152, 1998.

[26] P. P. IUPAC, D. Everett, R. Haul, L. Moscou, R. Pierotti, J. Rouquerol, and T. Siemieniewska, "Pure Appl," *Chem,* vol. 57, pp. 603, 1985.

[27] E. Elsayed, H. Wang, P. A. Anderson, R. Al-Dadah, S. Mahmoud, H. Navarro, Y. Ding, and J. Bowen, "Development of MIL-101 (Cr)/GrO composites for adsorption heat pump applications," *Microporous and Mesoporous Materials,* vol. 244, pp. 180-191, 2017.

[28] H. Demir, M. Mobedi, and S. Ülkü, "A review on adsorption heat pump: Problems and solutions," *Renewable and Sustainable Energy Reviews,* vol. 12, no. 9, pp. 2381-2403, 2008.

[29] G. Eckstein, R. K. Paisley, S. Burchi, M. Curlier, and R. M. Stephan, "The Greening of Water Law: Managing Freshwater Resources for People and the Environment," 2010.

[30] K. Alhamad, M. Alardhi, and A. Almazrouee, "Preventive maintenance scheduling for multicogeneration plants with production constraints using genetic algorithms," *Advances in Operations Research,* vol. 2015, 2015.

[31] T. Mezher, H. Fath, Z. Abbas, and A. Khaled, "Techno-economic assessment and environmental impacts of desalination technologies," *Desalination,* vol. 266, no. 1, pp. 263-273, 2011.

[32] T. Humplik, J. Lee, S. O'hern, B. Fellman, M. Baig, S. Hassan, M. Atieh, F. Rahman, T. Laoui, and R. Karnik, "Nanostructured materials for water desalination," *Nanotechnology,* vol. 22, no. 29, pp. 292001, 2011.

[33] V. G. Gude, "Desalination and sustainability–an appraisal and current perspective," *Water research,* vol. 89, pp. 87-106, 2016.

[34] K. C. Ng, K. Thu, Y. Kim, A. Chakraborty, and G. Amy, "Adsorption desalination: an emerging low-cost thermal desalination method," *Desalination,* vol. 308, pp. 161-179, 2013.

[35] A. S. Alsaman, A. A. Askalany, K. Harby, and M. S. Ahmed, "A state of the art of hybrid adsorption desalination–cooling systems," *Renewable and Sustainable Energy Reviews,* vol. 58, pp. 692-703, 2016.

[36] K. C. Ng, X. WANG, L. Gao, A. Chakraborty, B. B. Saha, S. Koyama, A. Akisawa, and T. Kashiwagi, "Apparatus and method for desalination," Google Patents, 2006.

[37] Y.-D. Kim, K. Thu, M. E. Masry, and K. C. Ng, "Water quality assessment of solar-assisted adsorption desalination cycle," *Desalination,* vol. 344, pp. 144-151, 2014.

[38] P. G. Youssef, S. M. Mahmoud, and R. K. Al-Dadah, "Effect of evaporator temperature on the performance of water desalination/refrigeration adsorption system using AQSOA-ZO2," *World Academy of Science, Engineering and Technology, International Journal of Environmental, Chemical, Ecological, Geological and Geophysical Engineering,* vol. 9, no. 6, pp. 701-705, 2015.

[39] M. W. Shahzad, K. C. Ng, K. Thu, B. B. Saha, and W. G. Chun, "Multi effect desalination and adsorption desalination (MEDAD): A hybrid desalination method," *Applied Thermal Engineering,* vol. 72, no. 2, pp. 289-297, 2014.

[40] K. C. Ng, K. Thu, A. Chakraborty, B. B. Saha, and W. G. Chun, "Solar-assisted dual-effect adsorption cycle for the production of cooling effect and potable water," *International Journal of Low-Carbon Technologies,* vol. 4, no. 2, pp. 61-67, 2009.

[41] K. Thu, K. C. Ng, B. B. Saha, A. Chakraborty, and S. Koyama, "Operational strategy of adsorption desalination systems," *International Journal of Heat and Mass Transfer,* vol. 52, no. 7, pp. 1811-1816, 2009.

[42] K. C. Ng, K. Thu, B. B. Saha, and A. Chakraborty, "Study on a waste heat-driven adsorption cooling cum desalination cycle," *International Journal of refrigeration,* vol. 35, no. 3, pp. 685-693, 2012.

[43] S. Mitra, K. Srinivasan, P. Kumar, S. Murthy, and P. Dutta, "Solar driven adsorption desalination system," *Energy Procedia,* vol. 49, pp. 2261-2269, 2014.

[44] K. Thu, H. Yanagi, B. B. Saha, and K. C. Ng, "Performance analysis of a low-temperature waste heat-driven adsorption desalination prototype," *International Journal of Heat and Mass Transfer,* vol. 65, pp. 662-669, 2013.

[45] K. Thu, A. Chakraborty, Y.-D. Kim, A. Myat, B. B. Saha, and K. C. Ng, "Numerical simulation and performance investigation of an advanced adsorption desalination cycle," *Desalination,* vol. 308, pp. 209-218, 2013.

[46] P. G. Youssef, S. M. Mahmoud, and R. K. Al-Dadah, "Performance analysis of four bed adsorption water desalination/refrigeration system, comparison of AQSOA-Z02 to silica-gel," *Desalination,* vol. 375, pp. 100-107, 2015.

[47] G. Li, S. Qian, H. Lee, Y. Hwang, and R. Radermacher, "Experimental investigation of energy and exergy performance of short term adsorption heat storage for residential application," *Energy,* vol. 65, pp. 675-691, 2014.

[48] D. Dicaire, and F. H. Tezel, "Use of adsorbents for thermal energy storage of solar or excess heat: improvement of energy density," *International Journal of Energy Research,* vol. 37, no. 9, pp. 1059-1068, 2013.

[49] A. Elsayed, E. Elsayed, R. Al-Dadah, S. Mahmoud, A. Elshaer, and W. Kaialy, "Thermal energy storage using metal-organic framework materials," *Applied Energy,* vol. 186, pp. 509-519, Jan, 2017.

[50] Y. Ding, and S. Riffat, "Thermochemical energy storage technologies for building applications: a state-of-the-art review," *International Journal of Low-Carbon Technologies,* vol. 8, no. 2, pp. 106-116, 2012.

[51] M. Esen, A. Durmus, and A. Durmus, "Geometric design of solar-aided latent heat store depending on various parameters and phase change materials," *Solar Energy,* vol. 62, no. 1, pp. 19-28, Jan, 1998.

[52] Q. J. Mao, "Recent developments in geometrical configurations of thermal energy storage for concentrating solar power plant," *Renewable & Sustainable Energy Reviews,* vol. 59, pp. 320-327, Jun, 2016.

[53] L. Jiang, F. Q. Zhu, L. W. Wang, C. Z. Liu, and R. Z. Wang, "Experimental investigation on a MnCl2-CaCl2-NH3 thermal energy storage system," *Renewable Energy,* vol. 91, pp. 130-136, Jun, 2016.

[54] D. Aydin, S. P. Casey, and S. Riffat, "The latest advancements on thermochemical heat storage systems," *Renewable and Sustainable Energy Reviews,* vol. 41, pp. 356-367, 2015.

[55] S. Narayanan, X. Li, S. Yang, H. Kim, A. Umans, I. S. McKay, and E. N. Wang, "Thermal battery for portable climate control," *Applied Energy,* vol. 149, pp. 104-116, 2015.

[56] I. Sarbu, and C. Sebarchievici, “General review of solar-powered closed sorption refrigeration systems,” *Energy Conversion and Management,* vol. 105, pp. 403-422, Nov, 2015.

[57] S. Pal, M. R. Hajj, W. P. Wong, and I. K. Puri, “Thermal energy storage in porous materials with adsorption and desorption of moisture,” *International Journal of Heat and Mass Transfer,* vol. 69, pp. 285-292, 2014.

[58] K. E. N'Tsoukpoe, G. Restuccia, T. Schmidt, and X. Py, “The size of sorbents in low pressure sorption or thermochemical energy storage processes,” *Energy,* vol. 77, pp. 983-998, 2014.

[59] K. Lim, J. Che, and J. Lee, “Experimental study on adsorption characteristics of a water and silica-gel based thermal energy storage (TES) system,” *Applied Thermal Engineering,* vol. 110, pp. 80-88, 2017.

[60] S. Narayanan, S. Yang, H. Kim, and E. N. Wang, “Optimization of adsorption processes for climate control and thermal energy storage,” *International Journal of Heat and Mass Transfer,* vol. 77, pp. 288-300, 2014.

[61] A. Frazzica, and A. Freni, “Adsorbent working pairs for solar thermal energy storage in buildings,” *Renewable Energy,* vol. 110, pp. 87-94, 2017.

[62] G. Li, Y. Hwang, and R. Radermacher, “Experimental investigation on energy and exergy performance of adsorption cold storage for space cooling application,” *International journal of refrigeration,* vol. 44, pp. 23-35, 2014.

[63] J. Jänchen, and H. Stach, “Adsorption properties of porous materials for solar thermal energy storage and heat pump applications,” *Energy Procedia,* vol. 30, pp. 289-293, 2012.

[64] J. Jänchen, and H. Stach, "Shaping adsorption properties of nano-porous molecular sieves for solar thermal energy storage and heat pump applications," *Solar Energy,* vol. 104, pp. 16-18, 2014.

[65] U. Stritih, and A. Bombač, "Description and analysis of adsorption heat storage device," *Strojniški vestnik-Journal of Mechanical Engineering,* vol. 60, no. 10, pp. 619-628, 2014.

[66] H. Deshmukh, M. Maiya, and S. S. Murthy, "Study of sorption based energy storage system with silica gel for heating application," *Applied Thermal Engineering,* vol. 111, pp. 1640-1646, 2017.

[67] H. Wu, S. Wang, and D. Zhu, "Effects of impregnating variables on dynamic sorption characteristics and storage properties of composite sorbent for solar heat storage," *Solar energy,* vol. 81, no. 7, pp. 864-871, 2007.

[68] C. Finck, E. Henquet, C. van Soest, H. Oversloot, A.-J. de Jong, R. Cuypers, and H. van't Spijker, "Experimental Results of a 3 kWh thermochemical heat storage module for space heating application," *Energy Procedia,* vol. 48, pp. 320-326, 2014.

[69] H. Wu, S. Wang, D. Zhu, and Y. Ding, "Numerical analysis and evaluation of an open-type thermal storage system using composite sorbents," *International Journal of Heat and Mass Transfer,* vol. 52, no. 21, pp. 5262-5265, 2009.

[70] P. Aprea, B. de Gennaro, N. Gargiulo, A. Peluso, B. Liguori, F. Iucolano, and D. Caputo, "Sr-, Zn-and Cd-exchanged zeolitic materials as water vapor adsorbents for thermal energy storage applications," *Applied Thermal Engineering,* vol. 106, pp. 1217-1224, 2016.

[71] M. Duquesne, J. Toutain, A. Sempey, S. Ginestet, and E. P. del Barrio, "Modeling of a nonlinear thermochemical energy storage by adsorption on zeolites," *Applied Thermal Engineering,* vol. 71, no. 1, pp. 469-480, 2014.

[72] S. Ülkü, "Adsorption heat pumps," *Journal of heat recovery systems,* vol. 6, no. 4, pp. 277-284, 1986.

[73] A. R. M. Rezk, "Theoretical and experimental investigation of silica gel/water adsorption refrigeration systems," University of Birmingham, 2012.

[74] H. Demir, M. Mobedi, and S. Ülkü, "Effects of porosity on heat and mass transfer in a granular adsorbent bed," *International Communications in Heat and Mass Transfer,* vol. 36, no. 4, pp. 372-377, 2009.

[75] T. Núñez, W. Mittelbach, and H. M. Henning, "Development of a Small-Capacity Adsorption System for Heating and Cooling Applications," *HVAC&R Research,* vol. 12, no. S2, pp. 749-765, 2006.

[76] Z. Lu, R. Wang, Z. Xia, and L. Gong, "Experimental investigation adsorption chillers using micro-porous silica gel–water and compound adsorbent-methanol," *Energy conversion and management,* vol. 65, pp. 430-437, 2013.

[77] S. Mande, P. Ghosh, V. Kishore, K. Oertel, and U. Sprengel, "Development of an advanced solar–hybrid adsorption cooling system for decentralized storage of agricultural products in India," *Tata Energy Research Institute. India., Deutsche Forschungsanstalt für Luft-und Raumfahrt eV Germany,* 2000.

[78] Y. Watabe, and M. Yanadori, "Cooling Characteristics of Adsorption Refrigeration Apparatus Using Silica Gel/Ethanol System," *Kagaku Kogaku Ronbunshu,* vol. 20, pp. 589-589, 1994.

[79] D. Alda, and D. Ciarlo, *Refrigeration Systems, Design Technologies and Developments*: Nova Science Publishers, Incorporated, 2013.

[80] Z. Tamainot-Telto, S. J. Metcalf, R. E. Critoph, Y. Zhong, and R. Thorpe, "Carbon–ammonia pairs for adsorption refrigeration applications: ice making, air conditioning

and heat pumping," *international journal of refrigeration*, vol. 32, no. 6, pp. 1212-1229, 2009.

[81] I. I. El-Sharkawy, B. B. Saha, S. Koyama, and K. C. Ng, "A study on the kinetics of ethanol-activated carbon fiber: theory and experiments," *International journal of heat and mass transfer*, vol. 49, no. 17, pp. 3104-3110, 2006.

[82] Y. Hamamoto, K. Alam, B. Saha, S. Koyama, A. Akisawa, and T. Kashiwagi, "Study on adsorption refrigeration cycle utilizing activated carbon fibers. Part 2. Cycle performance evaluation," *International journal of refrigeration*, vol. 29, no. 2, pp. 315-327, 2006.

[83] S. Jribi, I. El-Sharkawy, S. Koyama, and B. Saha, "Study on activated carbon-CO2 pair: adsorption characteristics and cycle performance."

[84] K. C. Chan, C. Y. Chao, G. Sze-To, and K. S. Hui, "Performance predictions for a new zeolite 13X/CaCl 2 composite adsorbent for adsorption cooling systems," *International Journal of Heat and Mass Transfer*, vol. 55, no. 11, pp. 3214-3224, 2012.

[85] S. Waszkiewicz, H. Saidani-Scott, and M. Tierney, "Analysis of adsorption refrigeration system using zeolite and methanol."

[86] S. Izmailova, E. Vasiljeva, I. Karetina, N. Feoktistova, and S. Khvoshchev, "Adsorption of methanol, ammonia and water on the zeolite-like aluminophosphates AlPO4-5, AlPO4-17, and AlPO4-18," *Journal of colloid and interface science*, vol. 179, no. 2, pp. 374-379, 1996.

[87] F. Akhtar, L. Andersson, S. Ogunwumi, N. Hedin, and L. Bergström, "Structuring adsorbents and catalysts by processing of porous powders," *Journal of the European Ceramic Society*, vol. 34, no. 7, pp. 1643-1666, 2014.

[88] N. Yu, R. Wang, T. Li, and L. Wang, "Progress in Sorption Thermal Energy Storage," *Energy Solutions to Combat Global Warming*, pp. 541-572: Springer, 2017.

[89] I. S. Girnik, and Y. I. Aristov, “Dynamics of water vapour adsorption by a monolayer of loose AQSOA™-FAM-Z02 grains: Indication of inseparably coupled heat and mass transfer,” *Energy,* vol. 114, pp. 767-773, 2016.

[90] X. R. Zhang, and I. Dincer, *Energy Solutions to Combat Global Warming*: Springer International Publishing, 2016.

[91] Y. Hamamoto, K. A. Alam, A. Akisawa, and T. Kashiwagi, “Performance evaluation of a two-stage adsorption refrigeration cycle with different mass ratio,” *International journal of refrigeration,* vol. 28, no. 3, pp. 344-352, 2005.

[92] M. Khan, K. Alam, B. Saha, Y. Hamamoto, A. Akisawa, and T. Kashiwagi, “Parametric study of a two-stage adsorption chiller using re-heat—The effect of overall thermal conductance and adsorbent mass on system performance,” *International journal of thermal sciences,* vol. 45, no. 5, pp. 511-519, 2006.

[93] R. J. Grisel, S. F. Smeding, and R. De Boer, “Waste heat driven silica gel/water adsorption cooling in trigeneration,” *Applied Thermal Engineering,* vol. 30, no. 8, pp. 1039-1046, 2010.

[94] K. Sumathy, "An energy efficient solar ice-maker."

[95] J. Wu, R. Wang, and Y. Xu, “Dynamic analysis of heat recovery process for a continuous heat recovery adsorption heat pump,” *Energy conversion and management,* vol. 43, no. 16, pp. 2201-2211, 2002.

[96] R. E. Critoph, S. J. Metcalf, and Z. Tamainot-Telto, “Proof of concept car adsorption air-conditioning system using a compact sorption reactor,” *Heat Transfer Engineering,* vol. 31, no. 11, pp. 950-956, 2010.

[97] A. Sharafian, S. M. N. Mehr, W. Huttema, and M. Bahrami, “Effects of different adsorber bed designs on in-situ water uptake rate measurements of AQSOA FAM-Z02

for vehicle air conditioning applications," *Applied Thermal Engineering,* vol. 98, pp. 568-574, 2016.

[98] F. Poyelle, J.-J. Guilleminot, and F. Meunier, "Experimental tests and predictive model of an adsorptive air conditioning unit," *Industrial & engineering chemistry research,* vol. 38, no. 1, pp. 298-309, 1999.

[99] M. Gross, and B. Dawoud, "Experimental investigation of and adsorptive heat storage."

[100] A. Rezk, R. Al-Dadah, S. Mahmoud, and A. Elsayed, "Effects of contact resistance and metal additives in finned-tube adsorbent beds on the performance of silica gel/water adsorption chiller," *Applied Thermal Engineering,* vol. 53, no. 2, pp. 278-284, 2013.

[101] A. Rezk, R. Al-Dadah, S. Mahmoud, and A. Elsayed, "Experimental investigation of metal organic frameworks characteristics for water adsorption chillers," *Proceedings of the Institution of Mechanical Engineers, Part C: Journal of Mechanical Engineering Science,* vol. 227, no. 5, pp. 992-1005, 2013.

[102] B. Shi, "Development of an MOF based adsorption air conditioning system for automotive application," University of Birmingham, 2015.

[103] H. Kummer, G. Füldner, and S. K. Henninger, "Versatile siloxane based adsorbent coatings for fast water adsorption processes in thermally driven chillers and heat pumps," *Applied Thermal Engineering,* vol. 85, pp. 1-8, 2015.

[104] O. Cheung, and N. Hedin, "Zeolites and related sorbents with narrow pores for CO 2 separation from flue gas," *Rsc Advances,* vol. 4, no. 28, pp. 14480-14494, 2014.

[105] N. U. Qadir, S. A. Said, R. B. Mansour, K. Mezghani, and A. Ul-Hamid, "Synthesis, characterization, and water adsorption properties of a novel multi-walled carbon nanotube/MIL-100 (Fe) composite," *Dalton Transactions,* vol. 45, no. 39, pp. 15621-15633, 2016.

[106] A. Rezk, R. Al-Dadah, S. Mahmoud, and A. Elsayed, "Characterisation of metal organic frameworks for adsorption cooling," *International journal of heat and mass transfer,* vol. 55, no. 25, pp. 7366-7374, 2012.

[107] B. B. Saha, A. Chakraborty, and K. C. Ng, *Innovative Materials for Processes in Energy Systems-For Fuel Cells, Heat Pumps and Sorption Systems*: Research Publishing Service, 2011.

[108] X. Zhang, and I. Dincer, *Energy Solutions to Combat Global Warming*: Springer, 2017.

[109] S. Graf, F. Lanzerath, A. Sapienza, A. Frazzica, A. Freni, and A. Bardow, "Prediction of scp and cop for adsorption heat pumps and chillers by combining the large-temperature-jump method and dynamic modeling," *Applied Thermal Engineering,* vol. 98, pp. 900-909, 2016.

[110] H. Furukawa, K. E. Cordova, M. O'Keeffe, and O. M. Yaghi, "The chemistry and applications of metal-organic frameworks," *Science,* vol. 341, no. 6149, pp. 1230444, 2013.

[111] H. Li, M. Eddaoudi, M. O'Keeffe, and O. M. Yaghi, "Design and synthesis of an exceptionally stable and highly porous metal-organic framework," *nature,* vol. 402, no. 6759, pp. 276, 1999.

[112] A. S. Abd-El-Aziz, C. E. Carraher, C. U. Pittman, and M. Zeldin, *Macromolecules Containing Metal and Metal-Like Elements, Metal-Coordination Polymers*: John Wiley & Sons, 2005.

[113] P. W. Dunne, E. Lester, and R. I. Walton, "Towards scalable and controlled synthesis of metal–organic framework materials using continuous flow reactors," *Reaction Chemistry & Engineering,* vol. 1, no. 4, pp. 352-360, 2016.

[114] M. O'Keeffe, "Design of MOFs and intellectual content in reticular chemistry: a personal view," *Chemical Society Reviews,* vol. 38, no. 5, pp. 1215-1217, 2009.

[115] O. M. Yaghi, H. Li, C. Davis, D. Richardson, and T. L. Groy, "Synthetic strategies, structure patterns, and emerging properties in the chemistry of modular porous solids," *Accounts of Chemical Research,* vol. 31, no. 8, pp. 474-484, 1998.

[116] P. Brunton, R. Davies, J. Burke, A. Smith, A. Aggeli, S. Brookes, and J. Kirkham, "Treatment of early caries lesions using biomimetic self-assembling peptides–a clinical safety trial," *British dental journal,* vol. 215, no. 4, pp. E6-E6, 2013.

[117] J. Kim, B. L. Chen, T. M. Reineke, H. L. Li, M. Eddaoudi, D. B. Moler, M. O'Keeffe, and O. M. Yaghi, "Assembly of metal-organic frameworks from large organic and inorganic secondary building units: New examples and simplifying principles for complex structures," *Journal of the American Chemical Society,* vol. 123, no. 34, pp. 8239-8247, Aug, 2001.

[118] J. Kim, B. Chen, T. M. Reineke, H. Li, M. Eddaoudi, D. B. Moler, M. O'Keeffe, and O. M. Yaghi, "Assembly of Metal− Organic Frameworks from Large Organic and Inorganic Secondary Building Units: New Examples and Simplifying Principles for Complex Structures ▵ ," *Journal of the American Chemical Society,* vol. 123, no. 34, pp. 8239-8247, 2001.

[119] A. Burrows, C. Lamberti, E. Pidko, I. L. Minguez, D. de Vos, J. T. Hupp, J. Juan-Alcaniz, H. García, R. Palkovits, and F. Kapteijn, *Metal organic frameworks as heterogeneous catalysts*: Royal Society of Chemistry, 2013.

[120] N. Stock, and S. Biswas, "Synthesis of metal-organic frameworks (MOFs): routes to various MOF topologies, morphologies, and composites," *Chemical reviews,* vol. 112, no. 2, pp. 933-969, 2011.

[121] C. McKinstry, E. J. Cussen, A. J. Fletcher, S. V. Patwardhan, and J. Sefcik, "Effect of synthesis conditions on formation pathways of metal organic framework (MOF-5) crystals," *Crystal Growth & Design,* vol. 13, no. 12, pp. 5481-5486, 2013.

[122] M. Eddaoudi, J. Kim, N. Rosi, D. Vodak, J. Wachter, M. O'keeffe, and O. M. Yaghi, "Systematic design of pore size and functionality in isoreticular MOFs and their application in methane storage," *Science,* vol. 295, no. 5554, pp. 469-472, 2002.

[123] O. M. Yaghi, M. O'keeffe, N. W. Ockwig, and H. K. Chae, "Reticular synthesis and the design of new materials," *Nature,* vol. 423, no. 6941, pp. 705, 2003.

[124] C. Dey, T. Kundu, B. P. Biswal, A. Mallick, and R. Banerjee, "Crystalline metal-organic frameworks (MOFs): synthesis, structure and function," *Acta Crystallographica Section B: Structural Science, Crystal Engineering and Materials,* vol. 70, no. 1, pp. 3-10, 2014.

[125] D. J. Tranchemontagne, J. R. Hunt, and O. M. Yaghi, "Room temperature synthesis of metal-organic frameworks: MOF-5, MOF-74, MOF-177, MOF-199, and IRMOF-0," *Tetrahedron,* vol. 64, no. 36, pp. 8553-8557, 2008.

[126] N. A. Khan, E. Haque, and S. H. Jhung, "Rapid syntheses of a metal–organic framework material Cu 3 (BTC) 2 (H 2 O) 3 under microwave: a quantitative analysis of accelerated syntheses," *Physical Chemistry Chemical Physics,* vol. 12, no. 11, pp. 2625-2631, 2010.

[127] S. H. Jhung, J. H. Lee, J. W. Yoon, C. Serre, G. Férey, and J. S. Chang, "Microwave Synthesis of Chromium Terephthalate MIL-101 and Its Benzene Sorption Ability," *Advanced Materials,* vol. 19, no. 1, pp. 121-124, 2007.

[128] L. R. MacGillivray, *Metal-organic frameworks: design and application*: John Wiley & Sons, 2010.

[129] Y. He, W. Zhou, G. Qian, and B. Chen, "Methane storage in metal–organic frameworks," *Chemical Society Reviews,* vol. 43, no. 16, pp. 5657-5678, 2014.

[130] J. Liu, P. K. Thallapally, B. P. McGrail, D. R. Brown, and J. Liu, "Progress in adsorption-based CO 2 capture by metal–organic frameworks," *Chemical Society Reviews,* vol. 41, no. 6, pp. 2308-2322, 2012.

[131] Y. Yan, X. Lin, S. Yang, A. J. Blake, A. Dailly, N. R. Champness, P. Hubberstey, and M. Schröder, "Exceptionally high H 2 storage by a metal–organic polyhedral framework," *Chemical Communications*, no. 9, pp. 1025-1027, 2009.

[132] B. Van de Voorde, B. Bueken, J. Denayer, and D. De Vos, "Adsorptive separation on metal–organic frameworks in the liquid phase," *Chemical Society Reviews*, vol. 43, no. 16, pp. 5766-5788, 2014.

[133] J. Liu, L. Chen, H. Cui, J. Zhang, L. Zhang, and C.-Y. Su, "Applications of metal–organic frameworks in heterogeneous supramolecular catalysis," *Chemical Society Reviews*, vol. 43, no. 16, pp. 6011-6061, 2014.

[134] T. Zhang, and W. Lin, "Metal–organic frameworks for artificial photosynthesis and photocatalysis," *Chemical Society Reviews*, vol. 43, no. 16, pp. 5982-5993, 2014.

[135] P. Horcajada, T. Chalati, C. Serre, B. Gillet, C. Sebrie, T. Baati, J. F. Eubank, D. Heurtaux, P. Clayette, and C. Kreuz, "Porous metal-organic-framework nanoscale carriers as a potential platform for drug delivery and imaging," *Nature materials*, vol. 9, no. 2, pp. 172, 2010.

[136] Z. Hu, B. J. Deibert, and J. Li, "Luminescent metal–organic frameworks for chemical sensing and explosive detection," *Chemical Society Reviews*, vol. 43, no. 16, pp. 5815-5840, 2014.

[137] W. P. Lustig, S. Mukherjee, N. D. Rudd, A. V. Desai, J. Li, and S. K. Ghosh, "Metal–organic frameworks: functional luminescent and photonic materials for sensing applications," *Chemical Society Reviews*, vol. 46, no. 11, pp. 3242-3285, 2017.

[138] P. Ramaswamy, N. E. Wong, and G. K. Shimizu, "MOFs as proton conductors–challenges and opportunities," *Chemical Society Reviews*, vol. 43, no. 16, pp. 5913-5932, 2014.

[139] S. Qiu, M. Xue, and G. Zhu, "Metal–organic framework membranes: from synthesis to separation application," *Chemical Society Reviews,* vol. 43, no. 16, pp. 6116-6140, 2014.

[140] C. Pettinari, F. Marchetti, N. Mosca, G. Tosi, and A. Drozdov, "Application of metal − organic frameworks," *Polymer International,* vol. 66, no. 6, pp. 731-744, 2017.

[141] R. J. Kuppler, D. J. Timmons, Q.-R. Fang, J.-R. Li, T. A. Makal, M. D. Young, D. Yuan, D. Zhao, W. Zhuang, and H.-C. Zhou, "Potential applications of metal-organic frameworks," *Coordination Chemistry Reviews,* vol. 253, no. 23, pp. 3042-3066, 2009.

[142] S. Kaskel, *The chemistry of metal-organic frameworks: synthesis, characterization, and applications*: John Wiley & Sons, 2016.

[143] N. C. Burtch, H. Jasuja, and K. S. Walton, "Water stability and adsorption in metal–organic frameworks," *Chemical reviews,* vol. 114, no. 20, pp. 10575-10612, 2014.

[144] A. Rezk, A.-D. Raya, S. Mahmoud, and A. Elsayed, "Investigation of Ethanol/metal organic frameworks for low temperature adsorption cooling applications," *Applied energy,* vol. 112, pp. 1025-1031, 2013.

[145] F. Jeremias, D. Fröhlich, C. Janiak, and S. K. Henninger, "Water and methanol adsorption on MOFs for cycling heat transformation processes," *New Journal of Chemistry,* vol. 38, no. 5, pp. 1846-1852, 2014.

[146] B. B. Saha, I. I. El-Sharkawy, T. Miyazaki, S. Koyama, S. K. Henninger, A. Herbst, and C. Janiak, "Ethanol adsorption onto metal organic framework: Theory and experiments," *Energy,* vol. 79, pp. 363-370, 2015.

[147] M. B. Elsheniti, O. A. Elsamni, R. K. Al-dadah, S. Mahmoud, E. Elsayed, and K. Saleh, "Adsorption Refrigeration Technologies," 2018.

[148] J. Ehrenmann, S. K. Henninger, and C. Janiak, "Water Adsorption Characteristics of MIL-101 for Heat-Transformation Applications of MOFs," *European Journal of Inorganic Chemistry,* vol. 2011, no. 4, pp. 471-474, 2011.

[149] J. Yan, Y. Yu, C. Ma, J. Xiao, Q. Xia, Y. Li, and Z. Li, "Adsorption isotherms and kinetics of water vapor on novel adsorbents MIL-101 (Cr)@ GO with super-high capacity," *Applied thermal engineering,* vol. 84, pp. 118-125, 2015.

[150] R. Zhengqiu, L. Quanguo, C. Qun, W. Haiyan, C. Haijun, and Y. Huqing, "Adsorption refrigeration performance of shaped MIL-101-water working pair," *Chinese Journal of Chemical Engineering,* vol. 22, no. 5, pp. 570-575, 2014.

[151] F. Jeremias, D. Fröhlich, C. Janiak, and S. K. Henninger, "Advancement of sorption-based heat transformation by a metal coating of highly-stable, hydrophilic aluminium fumarate MOF," *RSC Advances,* vol. 4, no. 46, pp. 24073-24082, 2014.

[152] B. Shi, A.-D. Raya, S. Mahmoud, A. Elsayed, and E. Elsayed, "CPO-27 (Ni) metal–organic framework based adsorption system for automotive air conditioning," *Applied Thermal Engineering,* vol. 106, pp. 325-333, 2016.

[153] F. Jeremias, V. Lozan, S. K. Henninger, and C. Janiak, "Programming MOFs for water sorption: amino-functionalized MIL-125 and UiO-66 for heat transformation and heat storage applications," *Dalton Transactions,* vol. 42, no. 45, pp. 15967-15973, 2013.

[154] F. Jeremias, A. Khutia, S. K. Henninger, and C. Janiak, "MIL-100 (Al, Fe) as water adsorbents for heat transformation purposes—a promising application," *Journal of Materials Chemistry,* vol. 22, no. 20, pp. 10148-10151, 2012.

[155] S. K. Henninger, F. Jeremias, H. Kummer, and C. Janiak, "MOFs for use in adsorption heat pump processes," *European Journal of Inorganic Chemistry,* vol. 2012, no. 16, pp. 2625-2634, 2012.

[156] S. K. Henninger, H. A. Habib, and C. Janiak, "MOFs as adsorbents for low temperature heating and cooling applications," *Journal of the American Chemical Society,* vol. 131, no. 8, pp. 2776-2777, 2009.

[157] S. K. Henninger, F. Jeremias, H. Kummer, P. Schossig, and H.-M. Henning, "Novel sorption materials for solar heating and cooling," *Energy Procedia,* vol. 30, pp. 279-288, 2012.

[158] C. Janiak, and S. K. Henninger, "Porous coordination polymers as novel sorption materials for heat transformation processes," *CHIMIA International Journal for Chemistry,* vol. 67, no. 6, pp. 419-424, 2013.

[159] C. Janiak, and J. K. Vieth, "MOFs, MILs and more: concepts, properties and applications for porous coordination networks (PCNs)," *New Journal of Chemistry,* vol. 34, no. 11, pp. 2366-2388, 2010.

[160] G. Férey, C. Mellot-Draznieks, C. Serre, F. Millange, J. Dutour, S. Surblé, and I. Margiolaki, "A chromium terephthalate-based solid with unusually large pore volumes and surface area," *Science,* vol. 309, no. 5743, pp. 2040-2042, 2005.

[161] G. Férey, *CRYSTAL CHEMISTRY: From Basics to Tools for Materials Creation*: World Scientific, 2017.

[162] O. Lebedev, F. Millange, C. Serre, G. Van Tendeloo, and G. Férey, "First direct imaging of giant pores of the metal− organic framework MIL-101," *Chemistry of materials,* vol. 17, no. 26, pp. 6525-6527, 2005.

[163] N. A. Khan, I. J. Kang, H. Y. Seok, and S. H. Jhung, "Facile synthesis of nano-sized metal-organic frameworks, chromium-benzenedicarboxylate, MIL-101," *Chemical engineering journal,* vol. 166, no. 3, pp. 1152-1157, 2011.

[164] Y. K. Seo, J. W. Yoon, J. S. Lee, Y. K. Hwang, C. H. Jun, J. S. Chang, S. Wuttke, P. Bazin, A. Vimont, and M. Daturi, "Energy-Efficient Dehumidification over

Hierachically Porous Metal–Organic Frameworks as Advanced Water Adsorbents," *Advanced Materials,* vol. 24, no. 6, pp. 806-810, 2012.

[165] S. Kayal, B. Sun, and A. Chakraborty, "Study of metal-organic framework MIL-101 (Cr) for natural gas (methane) storage and compare with other MOFs (metal-organic frameworks)," *Energy,* vol. 91, pp. 772-781, 2015.

[166] W. Y. Hong, S. P. Perera, and A. D. Burrows, "Manufacturing of metal-organic framework monoliths and their application in CO 2 adsorption," *Microporous and Mesoporous Materials,* vol. 214, pp. 149-155, 2015.

[167] T. Segakweng, "Modulated synthesis of Cr-MOF (MIL 101) for hydrogen storage applications," 2014.

[168] F. Carson, "Development of Metal–Organic Frameworks for Catalysis: Designing Functional and Porous Crystals," Department of Materials and Environmental Chemistry (MMK), Stockkholm University, 2015.

[169] P. Horcajada, S. Surblé, C. Serre, D.-Y. Hong, Y.-K. Seo, J.-S. Chang, J.-M. Greneche, I. Margiolaki, and G. Férey, "Synthesis and catalytic properties of MIL-100 (Fe), an iron (III) carboxylate with large pores," *Chemical Communications*, no. 27, pp. 2820-2822, 2007.

[170] Y.-K. Seo, J. W. Yoon, J. S. Lee, U.-H. Lee, Y. K. Hwang, C.-H. Jun, P. Horcajada, C. Serre, and J.-S. Chang, "Large scale fluorine-free synthesis of hierarchically porous iron (III) trimesate MIL-100 (Fe) with a zeolite MTN topology," *Microporous and Mesoporous Materials,* vol. 157, pp. 137-145, 2012.

[171] J. W. Yoon, Y. K. Seo, Y. K. Hwang, J. S. Chang, H. Leclerc, S. Wuttke, P. Bazin, A. Vimont, M. Daturi, and E. Bloch, "Controlled reducibility of a metal–organic framework with coordinatively unsaturated sites for preferential gas sorption," *Angewandte Chemie,* vol. 122, no. 34, pp. 6085-6088, 2010.

[172] J. Shi, S. Hei, H. Liu, Y. Fu, F. Zhang, Y. Zhong, and W. Zhu, "Synthesis of MIL-100 (Fe) at low temperature and atmospheric pressure," *Journal of Chemistry,* vol. 2013, 2013.

[173] A. García Márquez, A. Demessence, A. E. Platero-Prats, D. Heurtaux, P. Horcajada, C. Serre, J. S. Chang, G. Férey, V. de la Peña-O'Shea, and C. Boissière, "Green Microwave Synthesis of MIL-100 (Al, Cr, Fe) Nanoparticles for Thin-Film Elaboration," *European Journal of Inorganic Chemistry,* vol. 2012, no. 32, pp. 5165-5174, 2012.

[174] W. L. Queen, M. R. Hudson, E. D. Bloch, J. A. Mason, M. I. Gonzalez, J. S. Lee, D. Gygi, J. D. Howe, K. Lee, and T. A. Darwish, "Comprehensive study of carbon dioxide adsorption in the metal–organic frameworks M 2 (dobdc)(M= Mg, Mn, Fe, Co, Ni, Cu, Zn)," *Chemical Science,* vol. 5, no. 12, pp. 4569-4581, 2014.

[175] J.-S. Lee, S. B. Halligudi, N.-H. Jang, D.-W. Hwang, J.-S. Chang, and Y.-K. Hwang, "Microwave synthesis of a porous metal-organic framework, nickel (II) dihydroxyterephthalate and its catalytic properties in oxidation of cyclohexene," *Bulletin of the Korean Chemical Society,* vol. 31, no. 6, pp. 1489-1495, 2010.

[176] S. Chavan, J. G. Vitillo, C. Larabi, E. A. Quadrelli, P. D. Dietzel, and S. Bordiga, "Functionalization of CPO-27-Ni through metal hexacarbonyls: The role of open Ni 2+ sites," *Microporous and Mesoporous Materials,* vol. 157, pp. 56-61, 2012.

[177] M. Tagliabue, C. Rizzo, R. Millini, P. D. Dietzel, R. Blom, and S. Zanardi, "Methane storage on CPO-27-Ni pellets," *Journal of Porous Materials,* vol. 18, no. 3, pp. 289-296, 2011.

[178] E. Haque, and S. H. Jhung, "Synthesis of isostructural metal–organic frameworks, CPO-27s, with ultrasound, microwave, and conventional heating: Effect of synthesis methods and metal ions," *Chemical engineering journal,* vol. 173, no. 3, pp. 866-872, 2011.

[179] S. Cadot, L. Veyre, D. Luneau, D. Farrusseng, and E. A. Quadrelli, "A water-based and high space-time yield synthetic route to MOF Ni 2 (dhtp) and its linker 2, 5-dihydroxyterephthalic acid," *Journal of Materials Chemistry A,* vol. 2, no. 42, pp. 17757-17763, 2014.

[180] M. Gaab, N. Trukhan, S. Maurer, R. Gummaraju, and U. Müller, "The progression of Al-based metal-organic frameworks–From academic research to industrial production and applications," *Microporous and Mesoporous Materials,* vol. 157, pp. 131-136, 2012.

[181] E. Alvarez, N. Guillou, C. Martineau, B. Bueken, B. Van de Voorde, C. Le Guillouzer, P. Fabry, F. Nouar, F. Taulelle, and D. De Vos, "The structure of the aluminum fumarate metal–organic framework A520," *Angewandte Chemie International Edition,* vol. 54, no. 12, pp. 3664-3668, 2015.

[182] R. Wang, L. Wang, and J. Wu, *Adsorption refrigeration technology: theory and application*: John Wiley & Sons, 2014.

[183] L. Wang, Z. Tamainot-Telto, R. Thorpe, R. E. Critoph, S. J. Metcalf, and R. Wang, "Study of thermal conductivity, permeability, and adsorption performance of consolidated composite activated carbon adsorbent for refrigeration," *Renewable energy,* vol. 36, no. 8, pp. 2062-2066, 2011.

[184] S. Hong, O. Kwon, and J. Chung, "Application of an embossed plate heat exchanger to adsorption chiller," *International Journal of Refrigeration,* vol. 65, pp. 142-153, 2016.

[185] H. Niazmand, H. Talebian, and M. Mahdavikhah, "Bed geometrical specifications effects on the performance of silica/water adsorption chillers," *International journal of refrigeration,* vol. 35, no. 8, pp. 2261-2274, 2012.

[186] A. Sharafian, and M. Bahrami, "Assessment of adsorber bed designs in waste-heat driven adsorption cooling systems for vehicle air conditioning and refrigeration," *Renewable and Sustainable Energy Reviews,* vol. 30, pp. 440-451, 2014.

[187] L. Zhang, "Design and testing of an automobile waste heat adsorption cooling system," *Applied Thermal Engineering,* vol. 20, no. 1, pp. 103-114, 2000.

[188] K. D. Sattler, *Handbook of nanophysics: functional nanomaterials*: CRC Press, 2010.

[189] J. Purewal, D. Liu, A. Sudik, M. Veenstra, J. Yang, S. Maurer, U. Müller, and D. J. Siegel, "Improved hydrogen storage and thermal conductivity in high-density MOF-5 composites," *The Journal of Physical Chemistry C,* vol. 116, no. 38, pp. 20199-20212, 2012.

[190] H. Demir, M. Mobedi, and S. Ülkü, "The use of metal piece additives to enhance heat transfer rate through an unconsolidated adsorbent bed," *international journal of refrigeration,* vol. 33, no. 4, pp. 714-720, 2010.

[191] A. A. Askalany, S. K. Henninger, M. Ghazy, and B. B. Saha, "Effect of improving thermal conductivity of the adsorbent on performance of adsorption cooling system," *Applied Thermal Engineering,* vol. 110, pp. 695-702, 2017.

[192] T.-H. Eun, H.-K. Song, J. H. Han, K.-H. Lee, and J.-N. Kim, "Enhancement of heat and mass transfer in silica-expanded graphite composite blocks for adsorption heat pumps: Part I. Characterization of the composite blocks," *International journal of refrigeration,* vol. 23, no. 1, pp. 64-73, 2000.

[193] T.-H. Eun, H.-K. Song, J. H. Han, K.-H. Lee, and J.-N. Kim, "Enhancement of heat and mass transfer in silica-expanded graphite composite blocks for adsorption heat pumps. Part II. Cooling system using the composite blocks," *International Journal of Refrigeration,* vol. 23, no. 1, pp. 74-81, 2000.

[194] K. Fayazmanesh, C. McCague, and M. Bahrami, “Consolidated adsorbent containing graphite flakes for heat-driven water sorption cooling systems,” *Applied Thermal Engineering*, 2017.

[195] B. Huang, A. McGaughey, and M. Kaviany, “Thermal conductivity of metal-organic framework 5 (MOF-5): Part I. Molecular dynamics simulations,” *International Journal of Heat and Mass Transfer*, vol. 50, no. 3, pp. 393-404, 2007.

[196] B. Huang, Z. Ni, A. Millward, A. McGaughey, C. Uher, M. Kaviany, and O. Yaghi, “Thermal conductivity of a metal-organic framework (MOF-5): Part II. Measurement,” *International Journal of Heat and Mass Transfer*, vol. 50, no. 3, pp. 405-411, 2007.

[197] D. Liu, J. Purewal, J. Yang, A. Sudik, S. Maurer, U. Mueller, J. Ni, and D. Siegel, “MOF-5 composites exhibiting improved thermal conductivity,” *international journal of hydrogen energy*, vol. 37, no. 7, pp. 6109-6117, 2012.

[198] Y. Ming, H. Chi, R. Blaser, C. Xu, J. Yang, M. Veenstra, M. Gaab, U. Müller, C. Uher, and D. J. Siegel, “Anisotropic thermal transport in MOF-5 composites,” *International Journal of Heat and Mass Transfer*, vol. 82, pp. 250-258, 2015.

[199] C. Y. Tso, and C. Y. Chao, “Activated carbon, silica-gel and calcium chloride composite adsorbents for energy efficient solar adsorption cooling and dehumidification systems,” *International Journal of Refrigeration*, vol. 35, no. 6, pp. 1626-1638, 2012.

[200] K. Wang, J. Wu, R. Wang, and L. Wang, “Composite adsorbent of CaCl 2 and expanded graphite for adsorption ice maker on fishing boats,” *International Journal of Refrigeration*, vol. 29, no. 2, pp. 199-210, 2006.

[201] Y. I. Aristov, M. Tokarev, G. Cacciola, and G. Restuccia, “Selective water sorbents for multiple applications, 1. CaCl 2 confined in mesopores of silica gel: sorption properties,” *Reaction Kinetics and Catalysis Letters*, vol. 59, no. 2, pp. 325-333, 1996.

[202] Y. I. Aristov, G. Restuccia, G. Cacciola, and V. Parmon, “A family of new working materials for solid sorption air conditioning systems,” *Applied Thermal Engineering,* vol. 22, no. 2, pp. 191-204, 2002.

[203] B. B. Saha, A. Chakraborty, S. Koyama, and Y. I. Aristov, “A new generation cooling device employing CaCl 2-in-silica gel–water system,” *International Journal of Heat and Mass Transfer,* vol. 52, no. 1, pp. 516-524, 2009.

[204] J. Wang, R. Wang, and L. Wang, “Water vapor sorption performance of ACF-CaCl 2 and silica gel-CaCl 2 composite adsorbents,” *Applied Thermal Engineering,* vol. 100, pp. 893-901, 2016.

[205] G. Akiyama, R. Matsuda, H. Sato, A. Hori, M. Takata, and S. Kitagawa, “Effect of functional groups in MIL-101 on water sorption behavior,” *Microporous and Mesoporous Materials*, vol. 157, pp. 89-93, 2012.

[206] N. Ko, P. G. Choi, J. Hong, M. Yeo, S. Sung, K. E. Cordova, H. J. Park, J. K. Yang, and J. Kim, “Tailoring the water adsorption properties of MIL-101 metal–organic frameworks by partial functionalization,” *Journal of Materials Chemistry A,* vol. 3, no. 5, pp. 2057-2064, 2015.

[207] R. Wang, “Performance improvement of adsorption cooling by heat and mass recovery operation,” *International Journal of Refrigeration,* vol. 24, no. 7, pp. 602-611, 2001.

[208] C. Y. Tso, K. C. Chan, and C. Chao, "Experimental investigation of a double-bed adsorption cooling system for application in green buildings."

[209] K. Thu, “Adsorption desalination: theory & experiments,” 2010.

[210] A. Freni, A. Frazzica, B. Dawoud, S. Chmielewski, L. Calabrese, and L. Bonaccorsi, “Adsorbent coatings for heat pumping applications: verification of hydrothermal and mechanical stabilities,” *Applied Thermal Engineering,* vol. 50, no. 2, pp. 1658-1663, 2013.

[211] A. Basile, G. Cacciola, C. Colella, L. Mercadante, and M. Pansini, "Thermal conductivity of natural zeolite-PTFE composites," *Heat Recovery Systems and CHP,* vol. 12, no. 6, pp. 497-503, 1992.

[212] A. Freni, L. Bonaccorsi, L. Calabrese, A. Caprì, A. Frazzica, and A. Sapienza, "SAPO-34 coated adsorbent heat exchanger for adsorption chillers," *Applied thermal engineering,* vol. 82, pp. 1-7, 2015.

[213] L. Pino, Y. Aristov, G. Cacciola, and G. Restuccia, "Composite materials based on zeolite 4A for adsorption heat pumps," *Adsorption,* vol. 3, no. 1, pp. 33-40, 1997.

[214] H. Van Heyden, G. Munz, L. Schnabel, F. Schmidt, S. Mintova, and T. Bein, "Kinetics of water adsorption in microporous aluminophosphate layers for regenerative heat exchangers," *Applied Thermal Engineering,* vol. 29, no. 8, pp. 1514-1522, 2009.

[215] A. Atakan, G. Fueldner, G. Munz, S. Henninger, and M. Tatlier, "Adsorption kinetics and isotherms of zeolite coatings directly crystallized on fibrous plates for heat pump applications," *Applied Thermal Engineering,* vol. 58, no. 1, pp. 273-280, 2013.

[216] L. Schnabel, M. Tatlier, F. Schmidt, and A. Erdem-Şenatalar, "Adsorption kinetics of zeolite coatings directly crystallized on metal supports for heat pump applications (adsorption kinetics of zeolite coatings)," *Applied Thermal Engineering,* vol. 30, no. 11, pp. 1409-1416, 2010.

[217] M. Tatlier, G. Munz, G. Fueldner, and S. K. Henninger, "Effect of zeolite A coating thickness on adsorption kinetics for heat pump applications," *Microporous and Mesoporous Materials,* vol. 193, pp. 115-121, 2014.

[218] A. Frazzica, G. Füldner, A. Sapienza, A. Freni, and L. Schnabel, "Experimental and theoretical analysis of the kinetic performance of an adsorbent coating composition for use in adsorption chillers and heat pumps," *Applied Thermal Engineering,* vol. 73, no. 1, pp. 1022-1031, 2014.

[219] G. Restuccia, A. Freni, and G. Maggio, “A zeolite-coated bed for air conditioning adsorption systems: parametric study of heat and mass transfer by dynamic simulation,” *Applied thermal engineering,* vol. 22, no. 6, pp. 619-630, 2002.

[220] A. J. Howarth, A. W. Peters, N. A. Vermeulen, T. C. Wang, J. T. Hupp, and O. K. Farha, “Best Practices for the Synthesis, Activation, and Characterization of Metal-Organic Frameworks,” *Chemistry of Materials,* vol. 29, no. 1, pp. 26-39, Jan, 2017.

[221] E. Elsayed, A.-D. Raya, S. Mahmoud, A. Elsayed, and P. A. Anderson, “Aluminium fumarate and CPO-27 (Ni) MOFs: characterization and thermodynamic analysis for adsorption heat pump applications,” *Applied Thermal Engineering,* vol. 99, pp. 802-812, 2016.

[222] I. Langmuir, “The adsorption of gases on plane surfaces of glass, mica and platinum,” *Journal of the American Chemical society,* vol. 40, no. 9, pp. 1361-1403, 1918.

[223] S. Brunauer, P. H. Emmett, and E. Teller, “Adsorption of gases in multimolecular layers,” *Journal of the American chemical society,* vol. 60, no. 2, pp. 309-319, 1938.

[224] J. Sun, G. Yu, Q. Huo, Q. Kan, and J. Guan, “Epoxidation of styrene over Fe (Cr)-MIL-101 metal–organic frameworks,” *RSC Advances,* vol. 4, no. 72, pp. 38048-38054, 2014.

[225] E. Elsayed, H. Y. Wang, P. A. Anderson, R. Al-Dadah, S. Mahmoud, H. Navarro, Y. L. Ding, and J. Bowen, “Development of MIL-101(Cr)/GrO composites for adsorption heat pump applications,” *Microporous and Mesoporous Materials,* vol. 244, pp. 180-191, May, 2017.

[226] P. Sahoo, K. Ayappa, M. John, B. Newalkar, and N. Choudary, "Simulation of Methane Adsorption in ANG Storage System."

[227] K. C. Chan, C. Y. Chao, G. Sze-To, and K. S. Hui, “Performance predictions for a new zeolite 13X/CaCl2 composite adsorbent for adsorption cooling systems,” *International Journal of Heat and Mass Transfer,* vol. 55, no. 11-12, pp. 3214-3224, 2012.

[228] M. i. Dubinin, “Physical adsorption of gases and vapors in micropores,” *Progress in surface and membrane science,* vol. 9, pp. 1-70, 1975.

[229] B. B. Saha, E. C. Boelman, and T. Kashiwagi, “Computational analysis of an advanced adsorption-refrigeration cycle,” *Energy,* vol. 20, no. 10, pp. 983-994, 1995.

[230] D. Wang, Z. Xia, J. Wu, R. Wang, H. Zhai, and W. Dou, “Study of a novel silica gel–water adsorption chiller. Part I. Design and performance prediction,” *International Journal of Refrigeration,* vol. 28, no. 7, pp. 1073-1083, 2005.

[231] Y. Liu, and K. Leong, “Numerical study of a novel cascading adsorption cycle,” *International Journal of Refrigeration,* vol. 29, no. 2, pp. 250-259, 2006.

[232] M. Polanyi, “The potential theory of adsorption,” *Science,* vol. 141, no. 3585, pp. 1010-1013, 1963.

[233] F. Goldmann, and M. Polanyi, “Adsorption von Dämpfen an Kohle und die Wärmeausdehnung der Benutzungsschicht,” *Zeitschrift für Physikalische Chemie,* vol. 132, no. 1, pp. 321-370, 1928.

[234] M. Schicktanz, and T. Núñez, “Modelling of an adsorption chiller for dynamic system simulation,” *international journal of refrigeration,* vol. 32, no. 4, pp. 588-595, 2009.

[235] M. Tokarev, B. Okunev, M. Safonov, L. Kheifets, and Y. I. Aristov, “Approximation Equations for Describing the Sorption Equilibrium between Water Vapor and a CaCl~ 2-in-Silica Gel Composite Sorbent,” *RUSSIAN JOURNAL OF PHYSICAL CHEMISTRY C/C OF ZHURNAL FIZICHESKOI KHIMII,* vol. 79, no. 9, pp. 1490, 2005.

[236] G. Restuccia, and G. Cacciola, “Performances of adsorption systems for ambient heating and air conditioning: Performances de systèmes à adsorption pour le chauffage et le conditionnement d'air d'ambiance,” *International Journal of Refrigeration,* vol. 22, no. 1, pp. 18-26, 1999.

[237] S. Waszkiewicz, M. Tierney, and H. S. Scott, “Development of coated, annular fins for adsorption chillers,” *Applied Thermal Engineering,* vol. 29, no. 11, pp. 2222-2227, 2009.

[238] T. Ge, Y. Dai, R. Wang, and Z. Peng, “Experimental comparison and analysis on silica gel and polymer coated fin-tube heat exchangers,” *Energy,* vol. 35, no. 7, pp. 2893-2900, 2010.

[239] H. Niazmand, and I. Dabzadeh, “Numerical simulation of heat and mass transfer in adsorbent beds with annular fins,” *International Journal of Refrigeration,* vol. 35, no. 3, pp. 581-593, 2012.

[240] D. Lefebvre, P. Amyot, B. Ugur, and F. H. Tezel, “Adsorption Prediction and Modeling of Thermal Energy Storage Systems: A Parametric Study,” *Industrial & Engineering Chemistry Research,* vol. 55, no. 16, pp. 4760-4772, 2016.

[241] H. Chua, K. Ng, W. Wang, C. Yap, and X. Wang, “Transient modeling of a two-bed silica gel–water adsorption chiller,” *International Journal of Heat and Mass Transfer,* vol. 47, no. 4, pp. 659-669, 2004.

[242] E. Glueckauf, “Theory of chromatography. Part 10.—Formulæ for diffusion into spheres and their application to chromatography,” *Transactions of the Faraday Society,* vol. 51, pp. 1540-1551, 1955.

[243] E. Gleuckauf, and J. Coates, “The influence of incomplete equilibrium on the front boundary of chromatograms and the effectiveness of separation,” *J Chem Soc,* vol. 1315, pp. e21, 1947.

[244] H. Niazmand, H. Talebian, and M. Mahdavikhah, “Effects of particle diameter on performance improvement of adsorption systems,” *Applied Thermal Engineering,* vol. 59, no. 1, pp. 243-252, 2013.

[245] N. Bimbo, W. Xu, J. E. Sharpe, V. P. Ting, and T. J. Mays, "High-pressure adsorptive storage of hydrogen in MIL-101 (Cr) and AX-21 for mobile applications: cryocharging and cryokinetics," *Materials & Design,* vol. 89, pp. 1086-1094, 2016.

[246] K. Uddin, I. I. El-Sharkawy, T. Miyazaki, B. B. Saha, S. Koyama, H.-S. Kil, J. Miyawaki, and S.-H. Yoon, "Adsorption characteristics of ethanol onto functional activated carbons with controlled oxygen content," *Applied Thermal Engineering,* vol. 72, no. 2, pp. 211-218, 2014.

[247] I. I. El-Sharkawy, K. Uddin, T. Miyazaki, B. B. Saha, S. Koyama, J. Miyawaki, and S.-H. Yoon, "Adsorption of ethanol onto parent and surface treated activated carbon powders," *International Journal of Heat and Mass Transfer,* vol. 73, pp. 445-455, 2014.

[248] I. I. El-Sharkawy, K. Uddin, T. Miyazaki, B. B. Saha, S. Koyama, H.-S. Kil, S.-H. Yoon, and J. Miyawaki, "Adsorption of ethanol onto phenol resin based adsorbents for developing next generation cooling systems," *International Journal of Heat and Mass Transfer,* vol. 81, pp. 171-178, 2015.

[249] I. I. El-Sharkawy, B. B. Saha, S. Koyama, and K. C. Ng, "A study on the kinetics of ethanol-activated carbon fiber: theory and experiments," *International journal of heat and mass transfer,* vol. 49, no. 17-18, pp. 3104-3110, 2006.

[250] L. Yong, and K. Sumathy, "Comparison between heat transfer and heat mass transfer models for transportation process in an adsorbent bed," *International Journal of Heat and Mass Transfer,* vol. 47, no. 8, pp. 1587-1598, 2004.

[251] K. Leong, and Y. Liu, "Numerical modeling of combined heat and mass transfer in the adsorbent bed of a zeolite/water cooling system," *Applied Thermal Engineering,* vol. 24, no. 16, pp. 2359-2374, 2004.

[252] B. B. Saha, A. Chakraborty, S. Koyama, and Y. I. Aristov, “A new generation cooling device employing CaCl2-in-silica gel–water system,” *International Journal of Heat and Mass Transfer,* vol. 52, no. 1-2, pp. 516-524, 2009.

[253] C. Dey, T. Kundu, B. P. Biswal, A. Mallick, and R. Banerjee, “Crystalline metal-organic frameworks (MOFs): synthesis, structure and function,” Acta Crystallographica Section B-Structural Science Crystal Engineering and Materials, 2014.

[254] J. F. Yang, Q. Zhao, J. P. Li, and J. X. Dong, “Synthesis of metal-organic framework MIL-101 in TMAOH-Cr(NO3)(3)-H2BDC-H2O and its hydrogen-storage behavior,” *Microporous and Mesoporous Materials,* vol. 130, no. 1-3, pp. 174-179, May, 2010.

[255] T. Zhao, F. Jeremias, I. Boldog, B. Nguyen, S. K. Henninger, and C. Janiak, “High-yield, fluoride-free and large-scale synthesis of MIL-101 (Cr),” *Dalton Transactions,* vol. 44, no. 38, pp. 16791-16801, 2015.

[256] H. W. B. Teo, A. Chakraborty, and S. Kayal, “Evaluation of CH4 and CO2 adsorption on HKUST-1 and MIL-101 (Cr) MOFs employing Monte Carlo simulation and comparison with experimental data,” *Applied Thermal Engineering,* vol. 110, pp. 891-900, 2017.

[257] X. Zhou, W. Huang, J. Shi, Z. Zhao, Q. Xia, Y. Li, H. Wang, and Z. Li, “A novel MOF/graphene oxide composite GrO@ MIL-101 with high adsorption capacity for acetone,” *Journal of Materials Chemistry A,* vol. 2, no. 13, pp. 4722-4730, 2014.

[258] M. Lammert, S. Bernt, F. Vermoortele, D. E. De Vos, and N. Stock, “Single-and mixed-linker Cr-MIL-101 derivatives: A high-throughput investigation,” *Inorganic chemistry,* vol. 52, no. 15, pp. 8521-8528, 2013.

[259] H. Furukawa, F. Gándara, Y.-B. Zhang, J. Jiang, W. L. Queen, M. R. Hudson, and O. M. Yaghi, “Water adsorption in porous metal–organic frameworks and related

materials," *Journal of the American Chemical Society,* vol. 136, no. 11, pp. 4369-4381, 2014.

[260] E. Elsayed, A.-D. Raya, S. Mahmoud, P. Anderson, A. Hassan, and P. Youssef, "Numerical investigation of MIL-101 (Cr)/GrO composite performance in adsorption cooling systems," *Energy Procedia,* vol. 142, pp. 4131-4137, 2017.

[261] J. Liu, Y. Wang, A. I. Benin, P. Jakubczak, R. R. Willis, and M. D. LeVan, "CO2/H2O adsorption equilibrium and rates on metal− organic frameworks: HKUST-1 and Ni/DOBDC," *Langmuir,* vol. 26, no. 17, pp. 14301-14307, 2010.

[262] S. Chavan, F. Bonino, J. G. Vitillo, E. Groppo, C. Lamberti, P. D. Dietzel, A. Zecchina, and S. Bordiga, "Response of CPO-27-Ni towards CO, N 2 and C 2 H 4," *Physical Chemistry Chemical Physics,* vol. 11, no. 42, pp. 9811-9822, 2009.

[263] H. J. Dakkama, P. G. Youssef, R. K. Al-Dadah, and S. Mahmoud, "Adsorption ice making and water desalination system using metal organic frameworks/water pair," *Energy conversion and management,* vol. 142, pp. 53-61, 2017.

[264] J. W. Yoon, Y. K. Seo, Y. K. Hwang, J. S. Chang, H. Leclerc, S. Wuttke, P. Bazin, A. Vimont, M. Daturi, E. Bloch, P. L. Llewellyn, C. Serre, P. Horcajada, J. M. Greneche, A. E. Rodrigues, and G. Ferey, "Controlled Reducibility of a Metal-Organic Framework with Coordinatively Unsaturated Sites for Preferential Gas Sorption," *Angewandte Chemie-International Edition,* vol. 49, no. 34, pp. 5949-5952, 2010.

[265] J. Shi, S. T. Hei, H. H. Liu, Y. H. Fu, F. M. Zhang, Y. J. Zhong, and W. D. Zhu, "Synthesis of MIL-100(Fe) at Low Temperature and Atmospheric Pressure," *Journal of Chemistry,* 2013.

[266] F. Zhang, J. Shi, Y. Jin, Y. Fu, Y. Zhong, and W. Zhu, "Facile synthesis of MIL-100 (Fe) under HF-free conditions and its application in the acetalization of aldehydes with diols," *Chemical engineering journal,* vol. 259, pp. 183-190, 2015.

[267] J. Dechnik, C. Janiak, and S. De, "Aluminium fumarate metal-organic framework: a super adsorbent for fluoride from water," *Journal of hazardous materials,* vol. 303, pp. 10-20, 2016.

[268] H. W. B. Teo, A. Chakraborty, Y. Kitagawa, and S. Kayal, "Experimental study of isotherms and kinetics for adsorption of water on Aluminium Fumarate," *International Journal of Heat and Mass Transfer,* vol. 114, pp. 621-627, 2017.

[269] S. Karmakar, S. Bhattacharjee, and S. De, "Aluminium fumarate metal organic framework incorporated polyacrylonitrile hollow fiber membranes: Spinning, characterization and application in fluoride removal from groundwater," *Chemical Engineering Journal,* vol. 334, pp. 41-53, 2018.

[270] I. Ahmed, and S. H. Jhung, "Composites of metal–organic frameworks: Preparation and application in adsorption," *Materials today,* vol. 17, no. 3, pp. 136-146, 2014.

[271] X.-W. Liu, T.-J. Sun, J.-L. Hu, and S.-D. Wang, "Composites of metal–organic frameworks and carbon-based materials: preparations, functionalities and applications," *Journal of Materials Chemistry A,* vol. 4, no. 10, pp. 3584-3616, 2016.

[272] Q.-L. Zhu, and Q. Xu, "Metal–organic framework composites," *Chemical Society Reviews,* vol. 43, no. 16, pp. 5468-5512, 2014.

[273] X. Sun, Q. Xia, Z. Zhao, Y. Li, and Z. Li, "Synthesis and adsorption performance of MIL-101 (Cr)/graphite oxide composites with high capacities of n-hexane," *Chemical engineering journal,* vol. 239, pp. 226-232, 2014.

[274] C. Petit, and T. J. Bandosz, "Synthesis, characterization, and ammonia adsorption properties of mesoporous metal–organic framework (MIL (Fe))–graphite oxide composites: exploring the limits of materials fabrication," *Advanced Functional Materials,* vol. 21, no. 11, pp. 2108-2117, 2011.

[275] C. Petit, and T. J. Bandosz, “Exploring the coordination chemistry of MOF–graphite oxide composites and their applications as adsorbents,” *Dalton Transactions,* vol. 41, no. 14, pp. 4027-4035, 2012.

[276] C. Petit, B. Levasseur, B. Mendoza, and T. J. Bandosz, “Reactive adsorption of acidic gases on MOF/graphite oxide composites,” *Microporous and Mesoporous Materials,* vol. 154, pp. 107-112, 2012.

[277] H. Im, and J. Kim, “Thermal conductivity of a graphene oxide–carbon nanotube hybrid/epoxy composite,” *Carbon,* vol. 50, no. 15, pp. 5429-5440, 2012.

[278] N. K. Mahanta, and A. R. Abramson, "Thermal conductivity of graphene and graphene oxide nanoplatelets." pp. 1-6.

[279] N. M. Musyoka, J. Ren, P. Annamalai, H. W. Langmi, B. C. North, M. Mathe, and D. Bessarabov, “Synthesis of a hybrid MIL-101 (Cr)/ZTC composite for hydrogen storage applications,” *Research on Chemical Intermediates,* vol. 42, no. 6, pp. 5299-5307, 2016.

[280] F. Ke, J. Zhu, L.-G. Qiu, and X. Jiang, “Controlled synthesis of novel Au@ MIL-100 (Fe) core–shell nanoparticles with enhanced catalytic performance,” *Chemical Communications,* vol. 49, no. 13, pp. 1267-1269, 2013.

[281] Q. Yang, Q. Zhao, S. Ren, Q. Lu, X. Guo, and Z. Chen, “Fabrication of core-shell Fe3O4@ MIL-100 (Fe) magnetic microspheres for the removal of Cr (VI) in aqueous solution,” *Journal of Solid State Chemistry,* vol. 244, pp. 25-30, 2016.

[282] J. Holman, “Heat transfer, 1986,” *Mc Gran–Hill Book Company, Soythern Methodist University,* 1986.

[283] M. Mahdavikhah, and H. Niazmand, “Effects of plate finned heat exchanger parameters on the adsorption chiller performance,” *Applied Thermal Engineering,* vol. 50, no. 1, pp. 939-949, 2013.

[284] B. B. Saha, E. C. Boelman, and T. Kashiwagi, *Computer simulation of a silica gel-water adsorption refrigeration cycle--The influence of operating conditions on cooling output and COP,* 0001-2505, American Society of Heating, Refrigerating and Air-Conditioning Engineers, Inc., Atlanta, GA (United States), 1995.

[285] A. Elsayed, E. Elsayed, A.-D. Raya, S. Mahmoud, A. Elshaer, and W. Kaialy, "Thermal energy storage using metal–organic framework materials," *Applied Energy,* vol. 186, pp. 509-519, 2017.

[286] B. B. Saha, E. C. Boelman, and T. Kashiwagi, "Computer simulation of a silica gel-water adsorption refrigeration cycle-the influence of operating conditions on cooling output and COP," *Unknown Journal,* vol. 101, no. Pt 2, pp. 348-357, 1995.

[287] H. J. F. Dakkama, "Experimental investigation of MOF adsorption system for ice making, freeze water desalination and cooling applications," University of Birmingham, 2017.

[288] P. G. Youssef, "Experimental and numerical investigation of a new mof based adsorption water desalination system," University of Birmingham, 2017.

[289] Y. I. Aristov, I. S. Glaznev, and I. S. Girnik, "Optimization of adsorption dynamics in adsorptive chillers: loose grains configuration," *Energy,* vol. 46, no. 1, pp. 484-492, 2012.

[290] E. Curley, M. OFlynn, K. McDonnell, T. Addiscott, A. Whitmore, D. Powlson, T. Addiscott, J. Baker, K. Campbell, and H. Johnson, "European Communities (Drinking Water)(No. 2) Regulations 2007," *Journal of Agronomy,* vol. 8, no. 3, pp. pp: 55-72-pp: 55-72, 1991.

[291] W. H. Organization, "Guidelines for drinking-water quality: first addendum to the fourth edition," 2017.

[292] A. M. Elsayed, “Heat Transfer in Helically Coiled Small Diameter Tubes for Miniature Cooling Systems, Degree of Doctor of Philosophy (2011),” *School of Mechanical Engineering, University of Birmingham.*

APPENDIX I: UNCERTAINTY CALCULATIONS

The thermocouples (K type and RTD) and pressure transducers fitted in the system to measure the temperature and pressure in the test facility were previously calibrated [287, 288]. Each pressure transducer was calibrated using a standard vacuum gauge while the thermocouples were calibrated using a water bath and a standard alcohol thermometer [287, 288]. That is why the absolute uncertainty of the calibrated thermocouples and transducers were adopted from [288]. **Table. A-1** shows the absolute uncertainty of the RTD thermocouples. The uncertainty of SCP and SDWP results were calculated using Engineering Equation Solver (EES).

Table. A-1 Absolute uncertainty of RTD thermocouples [288]:

	Absolute uncertainty (°C)
Adsorption bed 1_ inlet water	±0.313
Adsorption bed 1_ outlet water	±0.309
Adsorption bed 1_ inlet water	±0.198
Adsorption bed 1_ outlet water	±0.285
Evaporator_ inlet water	±0.207
Evaporator_ outlet water	±0.179
Condenser_ inlet water	±0.279
Condenser_ outlet water	±0.307

I. Uncertainty of SDWP:

For an experimental result (y) which is a function of (i) independent variables (x_1, x_2, …., x_i), the uncertainty in y can be calculated by **Eq. A-1** [292].

$$U_y = \pm\sqrt{\left[\frac{\partial y}{\partial x_1}U_{x_1}\right]^2 + \left[\frac{\partial y}{\partial x_2}U_{x_2}\right]^2 + \cdots\cdots + \left[\frac{\partial y}{\partial x_i}U_{x_i}\right]^2} \qquad \textbf{(A-1)}$$

As the specific daily water production (SDWP) can be calculated from **Eq. A-2**

$$SDWP = \frac{V_w \times 60 \times 24}{m_a \times No\_cycles \times cycle\_time} \quad \textbf{(A-2)}$$

Where SDWP is the specific daily water production ($m^3\ ton^{-1}\ day^{-1}$), V_w is the collected distilled water (L), $m_{a\ is\ the}$ mass of the adsorbent material (kg), No_cycles are the number of cycles performed to collect V_w and cycle_time is the cycle time (min). The uncertainty in the SDWP can be calculated using **Eq. A-3** where the uncertainty depends on the uncertainty in the volume of the collected water and the adsorbent mass.

$$\frac{U_{SDWP}}{SDWP} = \pm\sqrt{\left[\frac{U_{Vm}}{V_m}\right]^2 + \left[\frac{U_{m_a}}{m_a}\right]^2} \quad \textbf{(A-3)}$$

Where U_{Vm} is the uncertainty in the volume of the collected distilled water, as the volume of collected distilled water was measured using a measuring cylinder with an uncertainty of 0.01 litres and U_{ma} is the uncertainty in the mass of the adsorbent which was weigh using a digital balance with an uncertainty of 0.001 kg. **Table. A-2** shows the absolute uncertainties in SDWP at different chilled water inlet temperatures in case of aluminium fumarate while **Table. A-3** shows the absolute uncertainties in SDWP in case of MIL-100(Fe).

Table. A-2 Uncertainty of aluminium fumarate SDWP at different chilled water inlet temperatures:

Chilled water inlet temperature (°C)	SDWP ($m^3\ ton^{-1}\ day^{-1}$)	Absolute uncertainty ($m^3\ ton^{-1}\ day^{-1}$)	Absolute uncertainty (%)
10	2.63	±0.1578	6
15	4.65		3.39
20	6.83		2.31
29	12.72		1.24

Table. A-3 Uncertainty of MIL-100(Fe) SDWP at different chilled water inlet temperatures:

Chilled water inlet temperature (°C)	SDWP (m^3 ton^{-1} day^{-1})	Absolute uncertainty (m^3 ton^{-1} day^{-1})	Absolute uncertainty (%)
10	4.21	±0.519	12.3
15	9.47		5.48
20	13.85		3.74
29	18.94		2.74

II. Uncertainty of SCP:

The specific cooling power can be calculated using **Eq. A-4**:

$$SCP = \frac{\dot{m}_{chill} C_p (T_{chill\_in} - T_{chill\_out})}{m_a} \quad \textbf{(A-4)}$$

Where SCP is the specific cooling power in W kg^{-1}, C_p is the specific heat capacity of chilled water in J $(K\ kg)^{-1}$, $\dot{m}_{chill}$ is the flowrate of the chilled water in kg s^{-1}, T_{chill_in} and T_{chill_out} are inlet and outlet chilled water temperatures in K and m_a is the adsorbent material mass in kg. The uncertainty in SCP can be calculated from **Eq. A-5** where it depends on the uncertainties in the chilled water flowrate, the chilled water inlet and outlet temperatures and the adsorbent mass.

$$\frac{U_{SCP}}{SCP} = \pm\sqrt{\left[\frac{U_{\dot{m}_{chill}}}{\dot{m}_{chill}}\right]^2 + \left[\frac{U_{T_{chill\_in}}}{T_{chill\_in}}\right]^2 + \left[\frac{U_{T_{chill\_out}}}{T_{chill\_out}}\right]^2 + \left[\frac{U_{m_a}}{m_a}\right]^2} \quad \textbf{(A-5)}$$

Where $U_{\dot{m}\ chill}$ is the uncertainty in the chilled water flowrate, as the flowrate was measured using a flowmeter with an uncertainty of 0.05 L min^{-1}, U_{Tchill_in} is uncertainty in the chilled water inlet temperature while U_{Tchill_out} is uncertainty in the chilled water outlet temperature which are ±0.207 and ±0.179 respectively as shown in **Table. A-1**. U_{ma} is the uncertainty in the

mass of the adsorbent which was weigh using a digital balance with an uncertainty of 0.001 kg. **Table. A-4** shows the absolute uncertainties in SCP at different chilled water inlet temperatures in case of aluminium fumarate while **Table. A-5** shows the absolute uncertainties in SCP in case of MIL-100(Fe).

Table. A-4 Uncertainty of aluminium fumarate SCP at different chilled water inlet temperatures:

Chilled water inlet temperature (°C)	SCP (W kg^{-1})	Absolute uncertainty (W kg^{-1})	Absolute uncertainty (%)
10	64.93	±3.1	4.7
15	136.21		2.2
20	191.18		1.6

Table. A-5 Uncertainty of MIL-100(Fe) SCP at different chilled water inlet temperatures:

Chilled water inlet temperature (°C)	SCP (W kg^{-1})	Absolute uncertainty (W kg^{-1})	Absolute uncertainty (%)
10	89.57	±9.4	10.4
15	226.14		4.1
20	337.20		2.7